UCRL-ID-114972-5

SERS Internship Fall 1995 Abstracts and Research Papers

Beverly Davis

Lawrence Livermore National Laboratory
Livermore, California 94550

May 1996

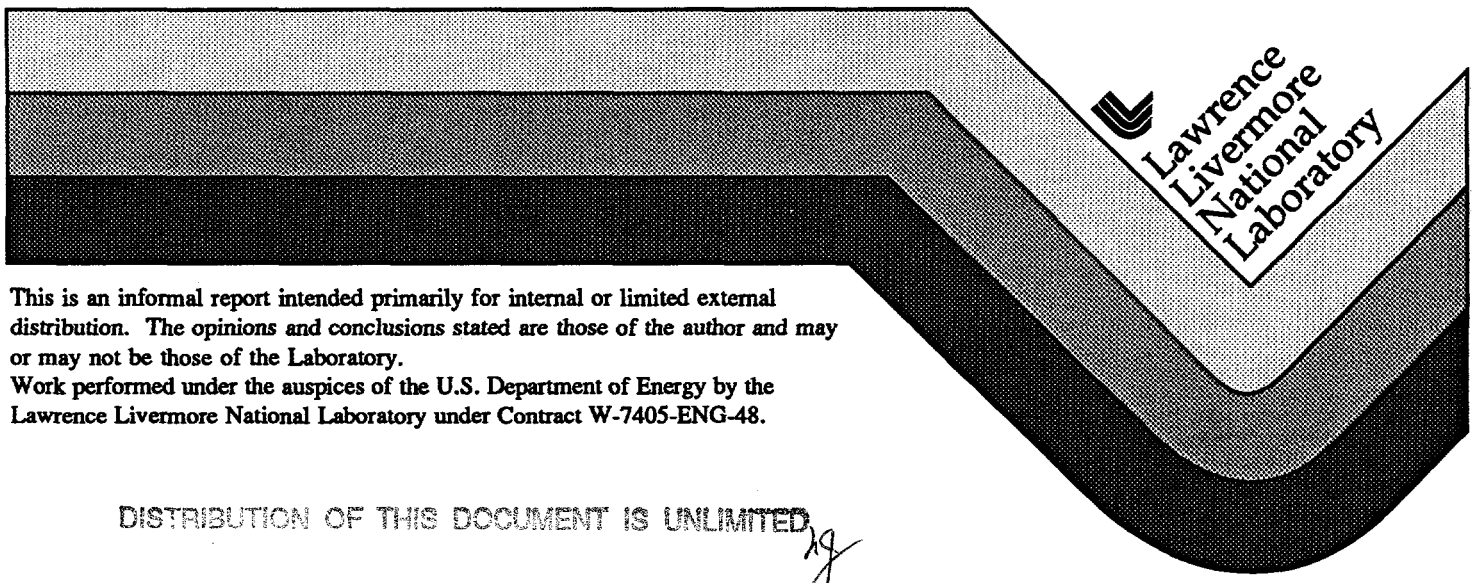

SCIENCE & ENGINEERING
SERS
RESEARCH SEMESTER

NAME/TITLE	PAGE
Marc Abramowitz	
"Developing a Computational Model of Human Hand Kinetics Using AVS"	1
Rodney Agayan	
"Manufacturing High-efficiency, High Damage Threshold Diffraction Gratings with Lift-off Processing"	2
Steven Badelt	
"Magnetic Field Regulation Control System Analysis"	3
Kimberly Bair	
"Volatile Organic Compound (VOC) Retardation in Ground Water"	4
Sarah Connolly	
"Mapping Genes to Human Chromosome 19"	5
Eric Dickenson	
"Transport in Porous Media"	6
Joy Dittmer	
"Directly Incorporating Fluorochromes into DNA Probes by PCR"	7
David Jaffe	
"A Beam Vectoring Trigger for Experiment 910"	8
Kenneth Krovchuck	
"Virtual Supercomputering on Macintosh Desktop Computers"	9
Elizabeth Neroda	
"Boron, Beryllium, and Lithium Partitioning in Olivine"	10
Tri Nguyen	
"Design and Development of Client Database Applications Using Oracle Power Objectives"	11

SCIENCE & ENGINEERING
SERS
RESEARCH SEMESTER

NAME/TITLE **PAGE**

Amy Parsons
"Distributed Computing Support Program's Databases" 12

Patricia Purdue
"The MACHO Project LMC Variable Star Inventory: Aperiodic Blue Variables" 13

Juliet Ricafort
"Mathematical Modeling of the Human Knee Joint" 14

Adam Sanford
"Three Dimensional Computer Vision: Potential Applications with Curvature Tracking" 15

Jason Shaw
"The China Model: Energy Modeling the Modern Dynasty" 16

Kristen Ude
"Understanding Contaminant Transport to Model and Quantify Bioremediation in the Microbial Filters Project" 17

Christopher Veis
"Storm Water Modeling at Lawrence Livermore National Laboratory" 18

Austin Woffington
"Effect of Grain Strength Distribution on Rock Fracture" 19

Brian Wood
"Program Processes of Archiving and Retrieval of Released Documents from the Engineering Resource Center (ERC)" 20

Student Reports i

Developing a Computational Model of Human Hand Kinetics Using AVS*

By:

Marc S. Abramowitz
State University of New York at Binghamton
Binghamton, New York 13902
e-mail: *marc@redhook.llnl.gov*

Mentor:

Karin Hollerbach
Institute for Scientific Computing Research
Lawrence Livermore National Laboratory
Livermore, California 94550
e-mail: *holler@llnl.gov*

In collaboration with:

David Giurintano
Rehabilitation Research Department
Gillis W. Long Hansen's Disease Center
Carville, Louisiana 70721
e-mail: *giurin@resdjg.dnet.lsu.edu*

Abstract

As part of an ongoing effort to develop a finite element model of the human hand at the Institute for Scientific Computing Research (ISCR), this project extended existing computational tools for analyzing and visualizing hand kinetics. These tools employ a commercial, scientific visualization package called AVS.

FORTRAN and C code, originally written by David Giurintano of the Gillis W. Long Hansen's Disease Center, was ported to a different computing platform, debugged, and documented. Usability features were added and the the code was made more modular and readable. When the code is used to visualize bone movement and tendon paths for the thumb, graphical output is consistent with expected results. However, numerical values for forces and moments at the thumb joints do not yet appear to be accurate enough to be included in ISCR's finite element model.

Future work includes debugging the parts of the code that calculate forces and moments and verifying the correctness of these values.

*AVS (Application Visualization System) is a trademark of Advanced Visual Systems, Inc.

Manufacturing High-efficiency, High Damage Threshold Diffraction Gratings with Lift-off Processing

Rodney Agayan
Cornell University
Inertial Confinement Fusion

Abstract

High-efficiency, high damage threshold diffraction gratings fabricated out of multilayers of dielectric materials are needed for the application of chirped-pulse amplification (CPA) in the Petawatt Laser Project. The underlying multilayers are deposited onto a flat substrate by standard e-beam evaporation. The grating structures themselves, however, can either be etched into a plane layer or deposited between a photoresist grating mask which is subsequently lifted off. The latter procedure, although more easily applied to large apertures, requires high-aspect ratio, vertical sidewall photoresist grating masks with, preferably, an overhanging structure to facilitate liftoff. By varying factors in each processing step, sample gratings were fabricated and then characterized.

Using a high-contrast profile photoresist (AZ7710), we have been able to create grating masks with both vertical sidewalls and high-aspect ratios (>4.5). We have also had some encouraging preliminary results in making overhanging structures by including a pre-development chlorobenzene soak in the processing steps. Once these samples are deposited with an oxide and the grating masks lifted off to create the final grating, a more definitive processing method can be developed based on the results.

December 4, 1995
Revision Number 1

Magnetic Field Regulation Control System Analysis*

Steven W. Badelt
Carnegie Mellon University
LLNL Isotope Sciences Division

Abstract

This study comprises (1) an analytical characterization of the Cameca ion microscope's magnetic field regulation circuitry and (2) comparisons between the analytical predictions and the measured performance of the control system. It is the first step in a project to achieve routine field regulation better than 10ppm. The control loop was decomposed into functional subcircuits and simulated in SPICE to determine DC, AC, and transient response. Transfer functions were extracted from SPICE, simplified, and analyzed in MATLAB. Both SPICE and MATLAB simulations were calculated for step inputs, and these results were compared to actual measurements. Magnetic field fluctuations were measured at high mass resolving power. The frequency spectrum of the fluctuations was analyzed by FFT. Difficulties encountered and implications for future work are discussed.

* This research was supported in part by an appointment to the U.S. Department of Energy Science and Engineering Research Semester (hereinafter called SERS) program administered by LLNL under Contract W-7405-Eng-48 with Lawrence Livermore National Laboratory.

Volatile Organic Compound (VOC) retardation in ground water.

Kimberly A. Bair
University of Florida
Environmental Restoration Division

Abstract

This project studies the mechanisms that cause the retardation of Volatile Organic Compounds (VOC) in ground water. Laboratory column and diffusion experiments were run in an effort to determine the contribution of each mechanism to the retarded flow of the VOCs. Retardation factors (Rf) , distribution coefficients (Kd) and diffusion coefficients (Dd) were determined for four VOCs commonly found in ground water. Comparison of two separate column experiments at different velocities shows that retardation is independent of flow velocity. The results from the diffusion experiment are presently being analyzed.

Mapping Genes to Human Chromosome 19

Sarah Connolly
University of Illinois at Urbana-Champaign
Biology and Biotechnology Research Program

For this project, 22 Expressed Sequence Tags (ESTs) were fine mapped to regions of human chromosome 19. An EST is a short DNA sequence that occurs once in the genome and corresponds to a single expressed gene. ^{32}P-radiolabeled probes were made by polymerase chain reaction for each EST and hybridized to filters containing a chromosome 19-specific cosmid library. The location of the ESTs on the chromosome was determined by the location of the ordered cosmid to which the EST hybridized.

Of the 22 ESTs that were sublocalized, 6 correspond to known genes, and 16 correspond to anonymous genes. These localized ESTs may serve as potential candidates for disease genes, as well as markers for future physical mapping.

12/5/95

TRANSPORT IN POROUS MEDIA

Eric Dickenson
University of California at Davis
Environmental Programs Directorate

A novel non-intrusive fluorescence imaging technique is used to study microscopic transport within porous media. The system consists of a column packed with heterogeneous-transparent particles and a refractive index-matched aqueous fluid seeded with fluorescent tracer particles or an organic dye. The flow through the column is illuminated by a planar sheet of laser beam and details of flow and transport through the porous regions can be observed microscopically and qualitative and quantitative transport information can be obtained. Various geometric, flow, and concentration quantities can be determined over a three dimensional volume within the column. The quantities include local and volumetrically averaged porosities, velocity and concentration fields, microscopic and volumetrically averaged dispersive fluxes and the dispersion coefficient. The qualitative and quantitative results will provide a better understanding for modeling of transport in porous media.

Directly Incorporating Fluorochromes into DNA Probes by PCR

Joy Dittmer
Indiana University - Purdue University at Fort Wayne
Health Ecological Assessment Division

Abstract

The object of this study was to produce a directly labeled whole chromosome probe in a Degenerative Oligonucleotide Primed-Polymerase Chain Reaction (DOP-PCR) that will identify chromosome breaks, deletions, inversions and translocations caused by radiation damage. In this study we amplified flow sorted chromosome 19 using DOP-PCR. The product was then subjected to a secondary DOP-PCR amplification. After the secondary amplification the DOP-PCR product was directly labeled in a tertiary PCR reaction with rhodamine conjugated with dUTP (FluoroRed) to produce a DNA fluorescent probe. The probe was then hybridized to human metaphase lymphocytes on slides, washed and counterstained with 4',6-diamino-2-phenylindole (DAPI). The signal of the FluoroRed probe was then compared to a signal of a probe labeled with biotin and stained with avidin fluoroscein isothio cynate (FITC) and anti-avidin FITC.

The results show that the probe labeled with FluoroRed gave signals as bright as the probe with biotin labeling. The FluoroRed probe had less noise than the biotin labeled probe. Therefore, a directly labeled probe has been successfully produced in a DOP-PCR reaction. In future a probe labeled with FluoroRed will be produced instead of a probe labeled with biotin to increase efficiency. Work performed under the auspices of the US DOE contract W-7405-ENG-48 at LLNL.
12/5/95

A Beam Vectoring Trigger for Experiment 910.

David Jaffe
U.C. - Riverside
N-Division Physics

Abstract:

Experiment 910 (e910) is a proton-gold nucleus collision experiment planned to run at the Alternating Gradient Synchrotron at Brookhaven National Laboratory. A gold foil target will be bombarded with high energy protons in an attempt to experimentally verify the existance of the H-dibaryon, a six quark particle permitted by the Standard Model. Strange particle production will also be measured to further understand nucleus-nucleus interactions, where enhanced strange particle production may signal a phase transition in the quark-gluon plasma. My work has been to create a "look up table" for use in the trigger to discriminate between interacting and non-interacting protons. In its final form, this look up table will be a file resident on a CAMAC crate as part of the online data acquisition system, and will contain predicted trajectory data for non-interacting protons of various initial positions and momenta. The table will be created by several programs I have written that work in conjunction with the software simulator eosgx.

version [1]
12-4-95

Virtual Supercomputering on Macintosh Desktop Computers

Ken Krovchuck
Wayne State University
Computations Department - LLNL

Abstract. Many computing problems of today require supercomputer performance, but do not justify the costs needed to run such applications on supercomputers. In order to fill this need, networks of high-end workstations are often linked together to act as a single virtual parallel supercomputer. This project attempts to develop software that will allow less expensive 'desktop' computers to emulate a parallel supercomputer. To demonstrate the viability of the software, it is being integrated with *POV*, a retracing package that is both computationally expensive and easily modified for parallel systems.

The software was developed using the Metrowerks Codewarrier Version 6.0 compiler on a Power Macintosh 7500 computer. The software is designed to run on a cluster of power macs running system 7.1 or greater on an ethernet network. Currently, because of limitations of both the operating system and the Metrowerks compiler, the software is forced to make use of slower, high level communication interfaces. Both the operating system and the compiler software are under revision however, and these revisions will increase the performance of the system as a whole.

December 5, 1995
Revision 1

Boron, Beryllium, and Lithium Partitioning in Olivine

Elizabeth Neroda
Occidental College
Earth Sciences, Experimental Petrology

ABSTRACT

A one atmosphere experimental study was performed to determine the mineral/melt partition coefficients for B, Be, and Li in forsteritic olivine. Two compositions were chosen along the 1350°C isotherm, 1b ($Fo_{17.3}$ $Ab_{82.7}$ An_0, by weight) and 8c (Fo_{30} $Ab_{23.3}$ $An_{47.8}$, by weight) were then combined in equal amounts to form a third composition. Each composition was doped with 25ppm Li, B, Yb, Nb, Zr, Sr, and Hf, 50ppm Sm, and 100ppm Be, Nd, Ce, and Rb. Electron and ion microprobe analyses showed that the olivine crystals and surrounding glasses were homogeneous with respect to major and trace elements. Partition coefficients calculated from these analyses are as follows:
1b: D_B = 4.41 (± 2.3) E-03, D_{Be} = 2.86 (± 0.45) E-03, D_{Li} = 1.54 (± 0.21) E-01,
50/50: D_B = 2.83 (± 0.5) E-03, D_{Be} = 2.07 (± 0.09) E-03, D_{Li} = 1.51 (± 0.18) E-01,
8c: D_B = 6.05 (± 1.5) E-03, D_{Be} = 1.81 (± 0.03) E-03, D_{Li}=1.31 (± 0.09) E-01.
The results of this study will combined with similar data for other minerals as part of a larger study to understand the partitioning behavior of B, Be, and Li in melting of the upper mantle at subduction zones.

Typed on November 30,1995

Design and Development of Client Database Applications, Using Oracle Power Objects

Tri M. Nguyen
Loyola Marymount University
Computations Department
Lawrence Livermore National Laboratory

ABSTRACT

The purpose of this project is to design and to build a suite of client database applications to track work orders and hours spent by employees of the Electronic Services Department. The applications are developed and constructed using Oracle Power Objects. In the object-oriented and integrated environment of this tool, the pre-defined codes are augmented and altered.

Due to bugs and errors in Power Objects itself, only one application has been completed at the current time. As part of an on-going effort, this project should be continued until most of the applications are completed. Costs and benefits of the finished applications can then be evaluated, and a decision can then be made to continue using Power Objects or to use an alternative tool.

Revisions: 2
Date: December 1, 1995

Distributed Computing Support Program's Databases

Amy Parsons
Saint Cloud State University
Computations

ABSTRACT

The Distributed Computing Support Program (DCSP) is the current system for keeping track of computer hardware maintenance throughout the Lawrence Livermore National Laboratory. DCSP consists of four separate Ingres databases each with their own support files. The process of updating and revising the support files, to make the business process more efficient is described in this paper.

The MACHO Project LMC Variable Star Inventory: Aperiodic Blue Variables

Patricia Purdue
Bryn Mawr College
I.G.P.P./Astrophysics

ABSTRACT

The MACHO Project database was searched for aperiodic blue variables in the LMC. Of approximately 250,000 bright blue stars in the region of observation, around 3500 had been flagged as variables or as rejected gravitational microlensing candidates. From a visual inspection of this set, about 400 stars were selected for the catalog. These stars have been categorized by their light curve morphology. Their spatial distribution is presented and correlated with known phenomena.

Analysis of the catalog stars has produced some interesting discoveries. Among some of these variables, unusual color changes were found. Some stars become redder or do not change color when their brightness increases, whereas most stars become bluer if they brighten rapidly. For some stars with relatively long quiescent stages, the light curves were searched for low-level, periodic variability, but no conclusive evidence for such behavior was found.

Typed 12/4/95.

Mathematical Modeling of the Human Knee Joint

Juliet Ricafort

Department of Biomedical Engineering,
University of Southern California

New Technologies Engineering Division
Mechanical Engineering Department
Lawrence Livermore National Laboratory

ABSTRACT

A model was developed to determine the forces exerted by several flexor and extensor muscles of the human knee under static conditions. The following muscles were studied: the gastrocnemius, biceps femoris, semitendinosus, semimembranosus, and the set of quadricep muscles. The tibia and fibula were each modeled as rigid bodies; muscles were modeled by their functional lines of action in space. Assumptions based on previous data were used to resolve the indeterminacy.

THREE DIMENSIONAL COMPUTER VISION: POTENTIAL APPLICATIONS WITH CURVATURE TRACKING

Adam Sanford
Cornell University
Electronics Engineering / Engineering Research Division

The purpose of this project is to develop a method of tracking data points for computer vision systems using curvature analysis. This is of particular importance to fellow researchers at the Lab, who have developed a markerless video computer vision system and are in need of such a method to track data points. A three dimensional viewing program was created to analyze the geometry of surface patches. Virtual surfaces were plotted and processed by the program to determine the Mean and Gaussian Curvature parameters for each point on the surface, thus defining each point's surface geometry type. The same computer processes are then applied to each frame of data acquired by the computer vision system to find surface "landmarks" that hold constant curvature during motion. Preliminary results indicate that curvature analysis shows great promise and could solve the tracking dilemma faced by those in the field of markerless imaging systems.

December 5, 1995 Revision 1

The China Model: Energy Modeling the Modern Dynasty

Jason Shaw
Binghamton University
Energy Research Division

In this paper a node-based microeconomic analysis is used to model the Chinese energy system. This model is run across multiple periods employing Lagrangian Relaxation techniques to achieve general equilibrium. Later, carbon dioxide emissions are added and the model is run to answer the question, "How can greenhouse gas emissions be reduced?"

December 7, 1995 Version 1.2

Understanding Contaminant Transport to Model and Quantify Bioremediation in the Microbial Filters Project.

Kristen Ude
University of Wisconsin - Madison
Lawrence Livermore National Lab, Earth Sciences

The efficacy of *in situ* bioremediation remains difficult to quantitatively demonstrate. One aim of the microbial filters project is to evaluate the *in situ* bioremediation of chlorinated ethenes such as trichloroethylene (TCE). To meet this need, a downhole treatability tool was developed to enable us to assess field biodegradation applications. A tracer lab experiment run in a column of the downhole treatability tool combined with tracer data analyzed from a microbial filters field test were used to understand the flow of water through porous media in the lab and in the field. A spreadsheet template was written to evaluate the contaminant transport equations and predict breakthrough curves of the tracer and TCE. The resulting tracer curve correlated well with experimental data and will lay the foundation for experiments performed with bacteria to assess the extent of bioremediation.

Abstract

Christopher Veis
Montana Tech
Operation and Regulatory Affairs Division

Storm water modeling is important to Lawrence Livermore National Laboratory (LLNL) for compliance with regulations that govern water discharge at large industrial facilities. Modeling is also done to study trend in contaminants and storm sewer infrastructure. The Storm Water Management Model (SWMM) was used to simulate rainfall events at LLNL. SWMM is a comprehensive computer model for simulation of urban runoff quantity and quality in storm and combined sewer systems. Due to time constraints and ongoing research, no modeling was completed at LLNL. With proper information about the storm sewers, a SWMM simulation of a rainfall event on site would be beneficial to storm sewer analyst.

Effect of Grain Strength Distribution on Rock Fracture

Austin Woffington
Diablo Valley College
LLNL Earth Sciences Division

Abstract

This report discloses my contributions to the study of grain strength distribution and its effects in computer modeled rock lattices. Frackrock v35.15 developed by Blair and Cook, was used to model bimodal grain strength distribution and test the lattices under stress. New data was gathered by running trials with a standardized weak grain strength and compared to the original data with a mean weak grain strength. The new data set shows lattice failure to be less predictable with a higher percentage of weak sites. Strain on the lattice is affected by the wide distribution of grain strengths: the closer the grain strengths are to each other, the more predictable they get. Further testing needs to be done on larger lattices, boundary less lattices, and multiple grain strength distributions. This will show the effects of size and stress on the grain distribution strength and will add to advancing our knowledge of how rocks crack and break under stressful conditions.

December 4, 1995 Original Version

Program Processes of Archiving and Retrieval of Released Documents from the Engineering Resource Center (ERC)

Brian K. Wood
University of California, Irvine

Division
Computations/Computations Organization

Abstract

The Purpose of the Engineering Resource Center is to provide a simplified procedure to archive, provide control and distribute newly released engineering data in an electronic medium. The methods used to access these records involve creating a database to populate all newly released engineering data and to construct a graphical user interface in the form of a menu tree using Ingres. From the menu tree, reports were made that queried databases on the Virtual Machine System (VMS) to produce a compiled report of what data was archived and retrieved. Due to the reduction of funds, the project was discontinued and few accomplishments were made. The accomplishments were a creation of tables and forms using SQL (standard query language) converted from Quel that were used to create a final report of what records were archived. The recommendation is to insure that funds be available for projects of importance and that a proper paper trail be implemented for the next SERS student arrival.

Student Reports

Developing a Computational Model of Human Hand Kinematics Using AVS*

Marc S. Abramowitz
State University of New York at Binghamton
Binghamton, NY 13902

Institute for Scientific Computing Research
Lawrence Livermore National Laboratory
Livermore, CA 94550

December 7, 1995

Prepared in partial fulfillment of the requirements of the Science and Engineering Research Semester under the direction of Karin Hollerbach, Research Mentor, at the Lawrence Livermore National Laboratory.

*This research was supported in part by an appointment to the U.S. Department of Energy Science and Engineering Research Semester (hereinafter called SERS) program administered by LLNL under Contract W-7405-Eng-48 with Lawrence Livermore National Laboratory. AVS (Application Visualization System) is a trademark of Advanced Visual Systems, Inc.

Contents

1 Introduction **3**

2 The rigid-body model **3**

3 AVS **4**

4 Methods **4**

5 Results **6**
5.1 The Axis finder module 6
5.2 The Paralysis and Tendon Transfer modules 8
5.3 The Kinematics module 8
5.4 The Kinetics module 9

6 Conclusions & Future Work **11**

List of Figures

1 The AVS Network Editor 5
2 The axis finder 7
3 The control panel for the kinematics module 8
4 An analysis of the thumb using the kinetics module 10

List of Tables

1 Comparison of individual muscle force results from kinetics module with Giurintano's results for 10 N tip pinch with all joint angles set to zero. . . . 12
2 Comparison of joint reaction force magnitude results. 12
3 Comparison of joint reaction moment magnitude results. 12

1 Introduction

It is desirable to develop good computational tools for modeling the mechanics of human joints, because there are many exciting possible applications of such tools in education, prosthetic implants[1], and surgical planning. Computer tools offer scientists and physicians capabilities for calculating forces and moments and other biomechanical data quickly and easily. These tools also offer the ability to visualize the action of bones and tendons using interactive computer graphics. These tools facilitate the analysis of joint function while contributing to our understanding of human anatomy. They also allow us to accurately model and predict the results of impaired motor function and corrective surgeries.

A finite element model of the human hand is currently being developed at the Institute for Scientific Computing Research (ISCR) at the Lawrence Livermore National Laboratory (LLNL)[2]. This finite element model will use NIKE3D, which is a finite element modeling program written at LLNL, along with computerized tomography (CT) scan data obtained from the Non-Destructive Evaluation (NDE) department at LLNL. As a part of this larger project, we are interested in using a rigid body model to:

- Formulate boundary conditions for the finite element model
- Validate the results of the finite element model

The rigid body model we are using for these purposes is based on FORTRAN and C code written by David Giurintano of the Gillis W. Long Hansen's Disease Center in Carville, Louisiana. This code is based on a commercial scientific visualization package called AVS. This paper deals with modifying these programs to further ISCR's own research in finite element modeling of the human hand.

2 The rigid-body model

Given the rotational angles and external forces applied at each joint in question, the model solves for a set of individual muscle forces that would keep the bones in the same static position. One difficulty with this approach is that there are typically many solutions that satisfy the conditions of a given problem. To resolve this indeterminacy, we impose additional conditions that are based on assumptions about hand physiology and mechanics. The validity of the assumptions, therefore, has an important effect on the accuracy of the solutions obtained by the model. The model discussed in this paper makes 3 assumptions about any given static positioning:

1. Stress will be minimized.
2. Moments should be greater than zero.
3. Forces should be greater than or equal to zero

Stress for a muscle is defined as its force divided by its physiological cross-sectional area. These additional conditions are imposed through the optimization of a "cost function" that includes terms for each of the above conditions. The computational model finds a unique solution by finding a set of muscle forces that minimizes the value of the cost function[3].

3 AVS

AVS^{TM} is a scientific visualization package for UNIX workstations that was developed by Advanced Visual Systems, Inc. In modeling of complex systems AVS offers two distinct advantages:

- Built-in capabilities for rendering and viewing of three dimensional objects
- A modular, visually-based programming environment that eases the task of creating complex simulations

AVS can render realistic views of complex three dimensional objects such as bones. At ISCR, we run AVS on Silicon Graphics Iris Indigo workstations that offer built-in hardware support for fast graphics rendering. AVS is able to take advantage of this hardware for speeding up the rendering process. It should be noted, however, that AVS also offers somewhat slower built-in software rendering for machines that do not possess sophisticated graphics hardware. This feature is important because it allows AVS to run on many kinds of platforms. For example, the original code discussed in this paper was developed on ordinary Pentium computers running the SCO UNIX operating system. Substantial performance benefits were realized by porting the code to run on Silicon Graphics workstations.

AVS also offers a modular, visually-based programming environment that eases the task of creating complex simulations. AVS *modules* are small programs that perform one small part within a given simulation. Modules are connected together to form *networks* using the AVS Network Editor (See Figure 1). Each module accepts some input from the user or from another module, performs a small task with that input, and returns appropriate output. In most cases, the output of the module becomes the input of another module. If the module is the last in a chain of modules, it might instead display the output on the screen. One such module is the "Geometry Viewer" which is a built-in module that comes with the AVS package. The input of the Geometry Viewer is data representing three dimensional objects. Its function is to render the objects on the screen. The Geometry Viewer is one of several modules that come with AVS. Although many of these modules are useful for constructing simulations, a given task may often need additional capability specific to that task which is not provided by AVS. To add such capabilities, users may write their own modules using a set of libraries that is provided with the package. Users have the choice of using FORTRAN or C or even a combination of both languages to write AVS modules. The libraries provide the programmer with routines for easily adding a graphical user interface to the module. Also provided are routines for performing manipulations of three dimensional objects such as geometric transformations.

4 Methods

Our work at ISCR has built upon previous AVS modules written by David Giurintano of the Gillis W. Long Hansen's Disease Center in Carville, Louisiana. The original modules were written in C and FORTRAN and were developed for SCO UNIX on IBM PC-compatible computers.

These modules were ported to run under the IRIX operating system used by Silicon Graphics workstations at ISCR. One of the initial problems encountered in compiling and linking the modules for IRIX involved incompatibilities between the COFF and ELF object file formats. The problem was that our version of AVS included COFF libraries, but newer versions of IRIX use the ELF file format. This causes the linker to return an error

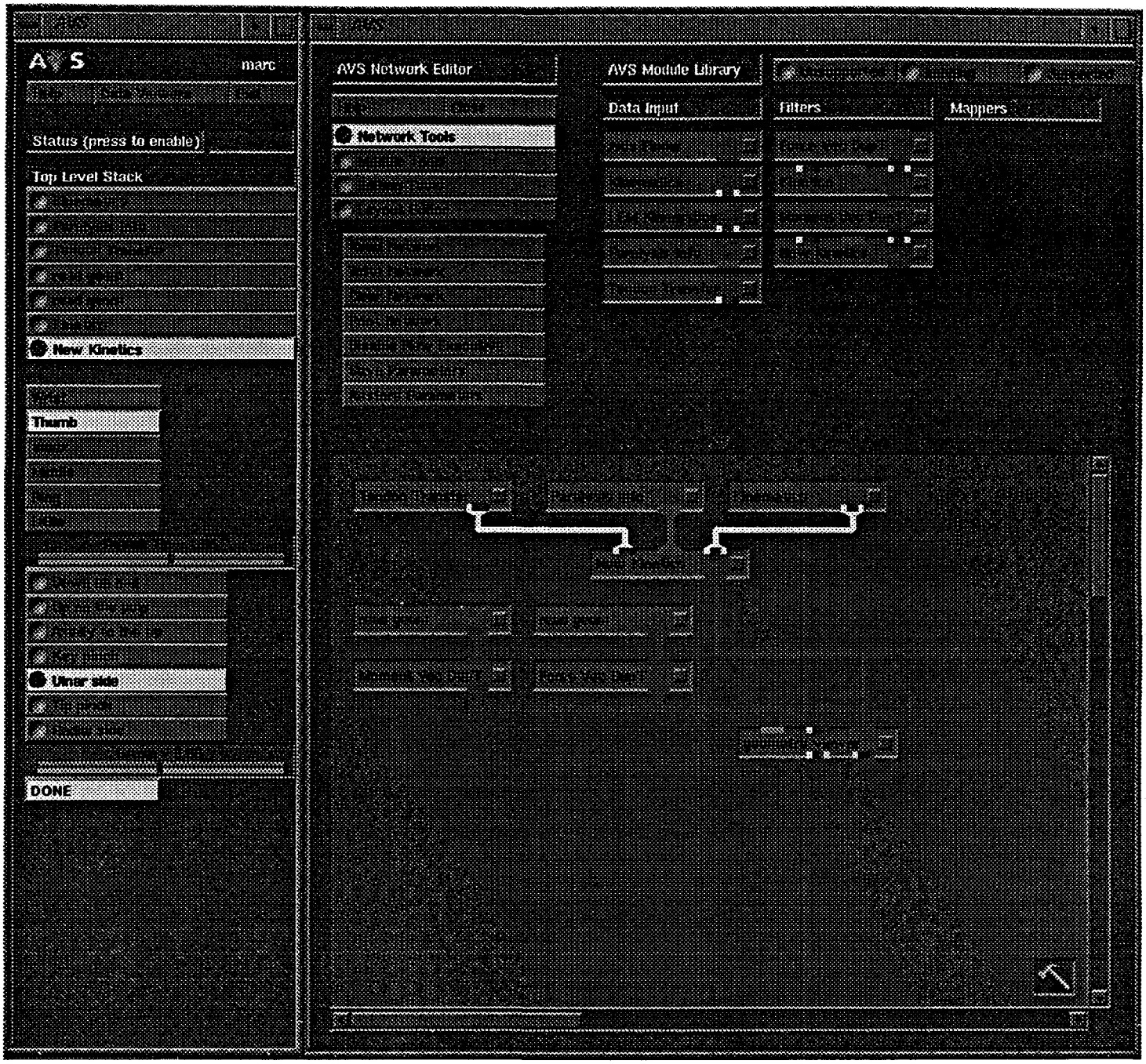

FIG. 1. *The AVS Network Editor*

indicating that COFF and ELF object files may not be linked together. I solved this problem by having our system administrator install the IRIX4 compatibility packages which are included on the CDs that come with the workstations and then adding the following command to my `.cshrc` file:

```
setenv SGI_IRIX4 1
```

This command makes linking possible by forcing the compilers and linkers to consistently use the older COFF object file format supported in earlier versions of the operating system. The compilers used were `f77` (FORTRAN) and `cc` (C). The debugger used was `dbx`.

5 Results

Our first result is that we are now able to compile and link all of the source code for Giurintano's AVS modules. The next two sections describe specific results that were obtained with two of the modules:

- the axis finder module
- the kinetics module

5.1 The Axis finder module

The output of the axis finder is shown in Figure 2. This picture was obtained after porting the code to run on our workstations.

The axis finder module is designed to allow users to interactively determine the location of rotational axes for a given joint. The axis finder allows the user to define as many as three axes for a joint and save them to a log file for later use with other modules.

The steps of the process for finding an axis of a joint follow:

1. Adjust the positions of the red and blue cursors.
2. Draw a line through the cursors representing the axis.
3. Rotate the distal bone around the axis.
4. Repeat 1-3 for the joint until the motion of the bone looks congruent.

Giurintano's original axis finder module ran under SCO UNIX but did not run on our Silicon Graphics workstations. This was due to the fact that there were several bugs in the code. It was written partially in C, but mostly in FORTRAN. This made the code difficult to understand and debug. Several portability problems were introduced by the fact that the module used a mixture of FORTRAN and C. At ISCR, the code for the axis finder was rewritten completely in C to make the program more portable and readable.

The original axis finder was also difficult to use, because the cursors could not be moved directly. The user could only move the cursors by adjusting the three coordinate values with dials. Newer versions of the axis finder were made easier to use by including facilities that allow the user to change the positions of the cursors by simply dragging them with the mouse.

Finally, the axis finder code was very specific to the data set that it was originally developed for, because the dials had a limited range within which they could be adjusted. This limitation made it impossible to determine rotational axes for the knee. ISCR's new version of the axis finder overcomes this limitation by including an extra dial, labeled "Scale", which allows the user to scale the range of possible coordinates for the cursors.

FIG. 2. *The axis finder*

5.2 The Paralysis and Tendon Transfer modules

The paralysis and tendon transfer modules allow the user to model nerve paralysis and corrective surgeries. The paralysis module allows the user to model a hand with a median, ulnar, or combined palsy. The tendon transfer module allows the user to model as many as 4 tendon transfers. The paralysis and tendon transfer modules are required modules, because they supply input to another module called the kinetics module. However, since we are concerned for the time being only with normal hand function, all of our work has been performed with these two modules set to neutral settings (i.e.: no nerve paralysis, no tendon transfers).

5.3 The Kinematics module

The kinematics module allows the user to adjust flexion-extension and abduction-adduction joint angles for the thumb at the carpometacarpal (CMC) and metacarpophalangeal (MCP) joints. The flexion-extension angle at the interphalangeal (IP) joint may also be adjusted. These parameters are adjusted by manipulating sliders on the control panel for the kinematics module. The control panel for the kinematics module is shown in Figure 3.

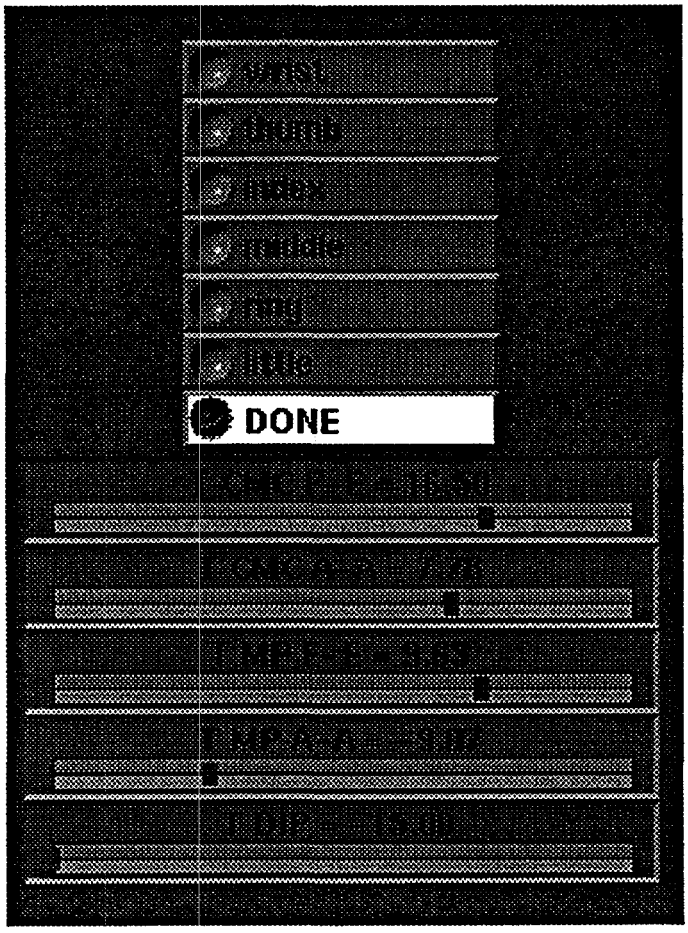

FIG. 3. *The control panel for the kinematics module*

5.4 The Kinetics module

The kinetics module accepts input from three other modules:

- kinematics module
- paralysis module
- tendon transfer module

The kinetics module, when given a static hand position (i.e.: tip pinch, key pinch, etc.) and external applied load, computes forces for each muscle/tendon unit as well as force and moment reactions at each of the three hand joints. In addition, the kinetics module also moves the bones to reflect the choice of joint angles made in the kinematics module and draws the following structures:

- tendon paths
- force and moment vectors for the joint reactions
- applied load vector

Giurintano's original code for the kinetics module did not run on our workstations. After investing considerable work into porting and debugging the code, we are now able to run the module on our workstations and perform analyses on our thumb data set. Figure 4 shows the graphical results of an analysis of the thumb using the kinetics module. Comparison of the graphical output of the simulation with an anatomical reference[4] indicates that simulation results are consistent with expected results. The program also outputs the following numerical results in the form of a log file.

- magnitudes of the individual muscle forces for each of the nine thumb motors
- force and moment vectors for the reactions at each of the three thumb joints

Table 1 compares individual muscle force results from the kinetics module to established results that Giurintano has obtained from a different simulation. It is evident from Table 1 that the results do not match well.

The 2nd and 3rd columns of Tables 2 and 3 show that joint reaction force and moment results from the kinetics module also do not match well with Giurintano's established results. Since joint reaction calculations depend on individual muscle force values, we could not expect the joint reactions to be consistent with established results, given the fact that the muscle force values were already determined to be inconsistent. To verify my hypothesis that inconsistencies in joint reaction results were being caused only by incorrect muscle force values, I temporarily inserted code that forces the module to use Giurintano's established muscle force values.

The results of this "modified kinetics module", in the 4th column of Tables 2 and 3, are highly consistent with Giurintano's results. This fact strengthens our confidence in the correctness of the joint reaction calculation code and emphasizes the need to debug the individual muscle force calculation code.

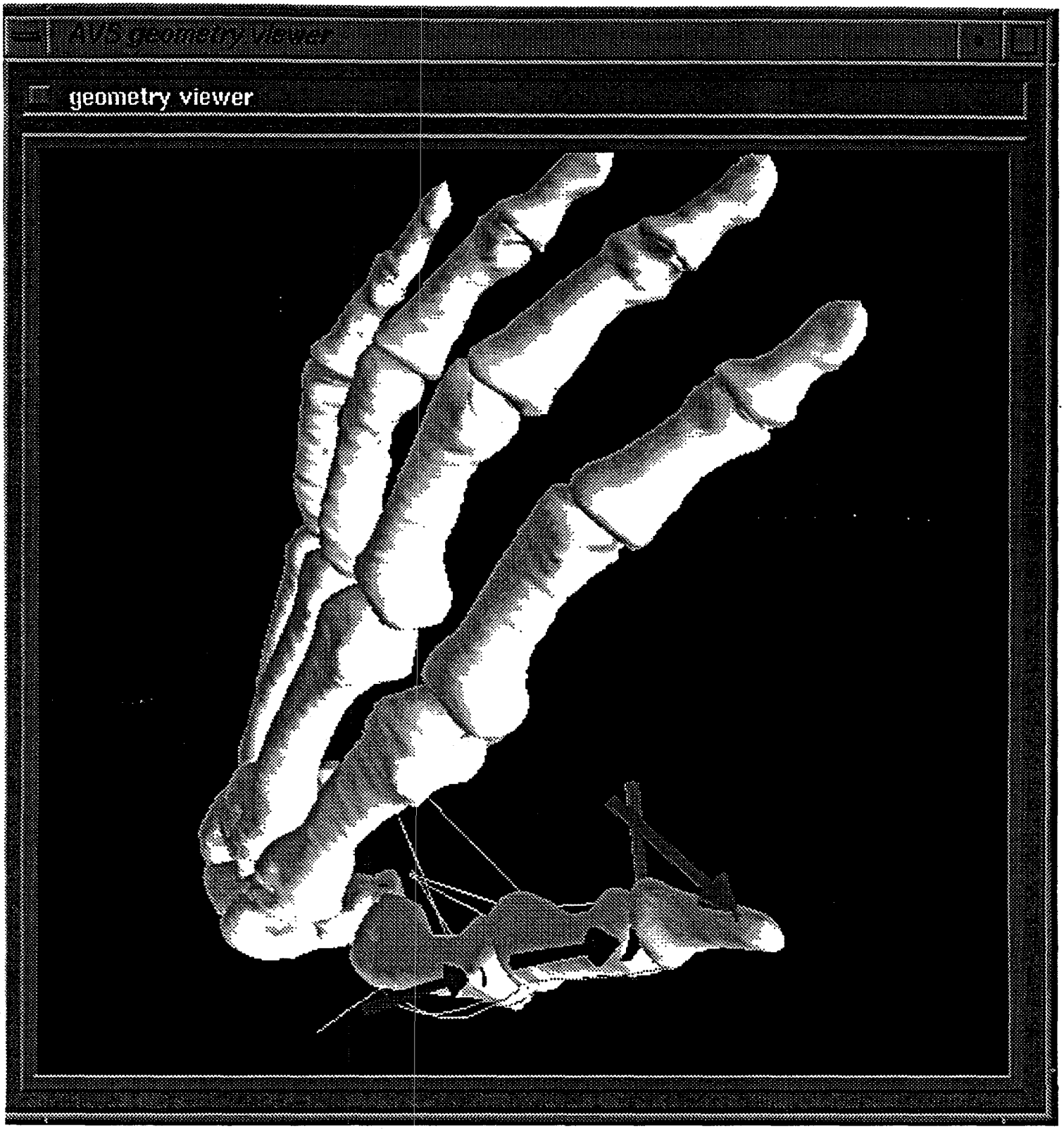

FIG. 4. *An analysis of the thumb using the kinetics module*

6 Conclusions & Future Work

The numerical values for individual muscle forces obtained from the kinetics module do not yet match Giurintano's previous results from past work. Giurintano suggests that this may be due to the fact that different points of reference were used for calculation of moments. Giurintano is currently working on developing a method to remedy this problem so that the results will be in a suitable form for use as inputs to ISCR's finite element model. Although the kinetics module is designed to simulate the entire hand and wrist, so far we have only tested the kinetics module for thumb analyses. Future work is required to test and debug kinetics module code for the entire hand and wrist. Once this is complete, it might be worthwhile to extract the code which performs the calculations from the AVS module and develop text-only kinetics modeling software. One advantage of this software would be the ability to run it independently of AVS, making our work repeatable for institutions that don't own an AVS license.

Towards the end of modeling other parts of the body besides the hand, we are also interested in generalizing the code so that it can be applied to other joints. In particular, Ricafort and Schauer have already begun to formulate a mathematical model of the human knee joint on paper[5]. It is hoped that when this model is completed, we will be able to use the current hand modeling code as the basis for development of a new model of the lower extremities.

References

[1] C. Nielsen, K. Hollerbach, S. Perfect, and K. Underhill. A computational method for comparing the behavior and possible failure of prosthetic implants. *IEEE International Conference of the Engineering in Medicine and Biology Society*, 1995.

[2] K. Hollerbach, K. Underhill, and R.Rainsberger. Automated volumetric grid generation for finite element modeling of human hand jointss. *ASME Bio-engineering Conference*, summer 1995.

[3] D. Giurintano and A. Hollister et. al. A virtual five-link model of the thumb. 1994.

[4] F. Netter. *Atlas of Human Anatomy.* Ciba-Geigy Corp., 1992.

[5] J. Ricafort and D. Schauer. A mathematical model of the human knee joint. *SERS Abstracts and Research Papers*, Fall 1995.

#	Muscle	kinetics module	Giurintano
1	FPL	-2.0261460E-04	2.416722
2	FPB	0.7567608	17.16507
3	EPL	4.6636761E-04	-1.5627980E-02
4	EPB	-2.2397258E-05	-1.5598875E-02
5	OPP	5.1895343E-03	39.81555
6	ADP	17.55579	-4.5162843E-02
7	APL	0.4123430	-4.0476243E-03
8	APB	9.2055276E-04	-1.9551855E-02
9	DI1	2.1207631E-03	-2.7588667E-02

TABLE 1

Comparison of individual muscle force results from kinetics module with Giurintano's results for 10 N tip pinch with all joint angles set to zero.

joint	kinetics module	Giurintano's results	modified kinetics module
CMC	8.335910	49.85252	49.46195
MP	8.205970	12.45917	10.03521
IP	8.900640	8.611233	8.612758

TABLE 2

Comparison of joint reaction force magnitude results.

joint	kinetics module	Giurintano's results	modified kinetics module
CMC	0.3933150	5.387214	5.347664
MP	1.993853	3.777039	3.554528
IP	1.709656	1.590365	1.589850

TABLE 3

Comparison of joint reaction moment magnitude results.

Manufacturing High-efficiency, High Damage Threshold Diffraction Gratings with Lift-off Processing*

Rodney Agayan

Cornell University

Lawrence Livermore Naional Laboratory
Livermore, California 94550

Decmeber 13, 1995

Prepared in partial fulfillment of the requirements of the Science and Engineering Research Semester under the direction of Jerald A. Britten, Research Mentor, at Lawrence Livermore National Laboratory.

*This research was supported in part byh an appointment to the U.S. Department of Energy Science and Engineering Research Semester (hereinafter called SERS) program administered by LLNL under Contract W-7405-Eng-48 with Lawrence Livermore National Laboratory.

Acknowledgements

I would like to thank the University of California, the Lawrence Livermore National Laboratory, and the Department of Energy for giving me the oppurtunity to experience this applied research.

I also thank Jerry Britten, my mentor, for his guidance and support throughout the semester. I thank H. Nguyen, B. Boyd, and C. Hoaglan for their help in the grating lab.

Special thanks go to C. Moore, E. Honea, E. Lindsey, and E. Furst for all of their assistance during the endless hours I spent in the AFM lab.

Abstract

High-efficiency, high damage threshold diffraction gratings fabricated out of multilayers of dielectric materials are needed for the application of chirped-pulse amplification (CPA) in the Petawatt Laser Project. The underlying multilayers are deposited onto a flat substrate by standard e-beam evaporation. The grating structures themselves, however, can either be etched into a plane layer or deposited between a photoresist grating mask which is subsequently lifted off. The latter procedure, although more easily applied to large apertures, requires high-aspect ratio, vertical sidewall photoresist grating masks with, preferably, an overhanging structure to facilitate liftoff. By varying factors in each processing step, sample gratings exhibiting these characteristics were fabricated.

Using a high-contrast profile photoresist (AZ7710), we have been able to create grating masks with both vertical sidewalls and high-aspect ratios (>4.5). We have also had some encouraging preliminary results in making overhanging structures by including a pre-development chlorobenzene soak in the processing steps. Once these samples are deposited with an oxide and the grating masks lifted off to create the final grating, a more definitive processing method can be developed based on the results.

Table of Contents

Acknowledgement i

Abstract ii

1. Introduction 1

2. Procedure 2

2.1 Substrate preparation 3

2.2 Exposure 3

2.3 Preprocessing 5

2.4 Development 5

2.5 Oxide deposition and lift-off 6

3. Results and Analysis 7

4. Conclusions 9

Bibliography 10

1. Introduction

The application of chirped pulse amplification (CPA) (Figure 1) in high power laser systems has required the manufacture of large aperture, high-efficiency, high damage threshold diffraction gratings[1]. At the Lawrence Livermore National Laboratory, we have attempted to fabricate such gratings for a 1000-TW (petawatt) laser system. To achieve such high power with CPA, a laser pulse is often diffracted four times in a typical double-pass compressor. Thus, the diffraction gratings must exhibit both a high efficiency in the m = - 1 order and a high damage threshold to maximize the energy per area that can be tolerated.

Presently, CPA lasers use gold coated photoresist diffraction gratings[2]. However, higher efficiency and higher damage threshold gratings can be made of multilayers of dielectric materials since these do not absorb radiation as does gold[3]. The actual grating structures are often etched into the top layer of a multilayer stack of alternating high and low index of refraction. Another possible method involves creating a photoresist grating mask on top of the multilayer stack and depositing the actual grating material between the structures. The mask is then lifted off by dissolution, leaving ridges of dielectric material in between. An illustration of this process will appear in the next section. This paper presents in detail the processing steps involved in the latter procedure and presents early results of our fabrication experiments.

[1] M. D. Perry and G. Mourou, "High-efficiency multilayer dielectric diffraction gratings."
[2] R. D. Boyd *et al.*, "High-efficiency metallic diffraction gratings for laser applications."
[3] M. D. Perry *et al.*, "High-efficiency multilayer dielectric diffraction gratings."

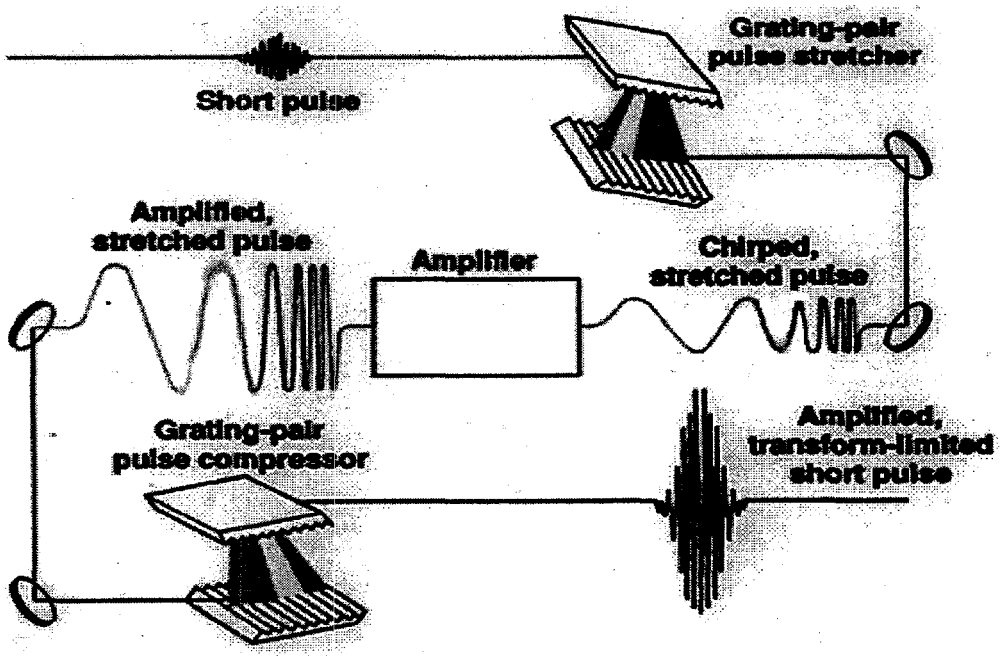

Figure 1. Chirped pulse amplification (CPA) concept

We have been able to construct grating masks that facilitate lift-off. Tall structures with high aspect ratios are preferred for the lift-off process. Structures with an overhang are also favored for they can easily be lifted off to maintain an ideal grating. We show that by using a high-contrast profile resist and including some preprocessing steps, adequate grating masks may be constructed, and the lift-off process is indeed feasible.

2. Procedure

The procedure we use to manufacture high-efficiency diffraction gratings with lift-off processing entails the following steps:

1. Substrate preparation
2. Exposure
3. Preprocessing
4. Development
5. Oxide deposition and lift-off

Variations in processing techniques can affect the shape and overall effectiveness of the grating mask, and thus, influence the efficiency of the

final grating. By adjusting different factors in each processing step, we were able to develop an optimal procedure and create potential grating masks.

2.1 Substrate preparation

The actual diffraction gratings we will use for CPA are created on large, optically flat 80 cm diameter glass substrates layered with dielectric material. However, to analyze the grating mask profiles, microscope slides, 50 × 77 mm, are used. They are first scrubbed in a 3% NaOH detergent solution and later subject to ultrasonic cleaning in the same solution for 30 minutes. After rinsed in distilled water and dried with dry-nitrogen, the substrates are coated with a nominally 1 mm thick AZ7710-series photoresist layer. For small substrates (<12 cm width) the ARC and photoresist layers are applied by spin coating. For larger substrates (≥12 cm width) a meniscus coater[4] is used. When spin coating, photoresist thickness can be controlled either by the solute concentration in the resist solution or by the angular speed of rotation. When applying the resist with a meniscus coater, thickness is again dependent on concentration and on the speed at which the substrate traverses laterally. The photoresist- coated substrates are baked at 70° for 20 minutes, and finally, the back sides are painted with a peelable, black varnish to prevent back reflections during exposure.

2.2 Exposure

The surface relief pattern is holographically produced in the photoresist by exposing the samples to the intersection of two highly collimated laser beams of ultraviolet radiation (Figure 2). The interference pattern is produced by an equal-path, fringe-stabilized interferometer connected in an electronic feedback loop. A lateral-effect photodiode detects the movement of coarse fringes constructed by recombining portions of each laser beam. As a result, an error

[4] W. A. Bookless, ed., "Meniscus Coating."

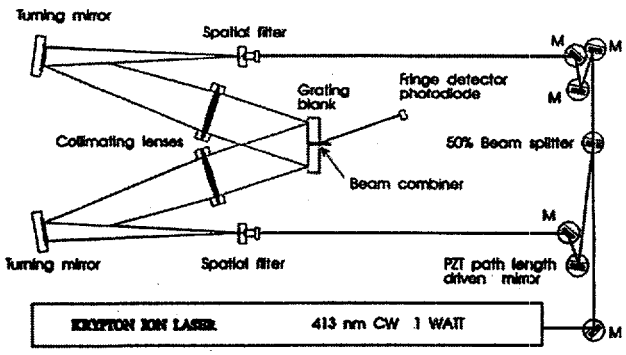

Figure 2. Holographic exposure setup

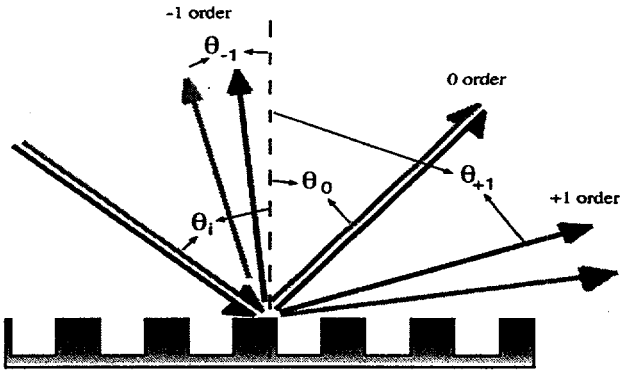

Figure 3. Diffraction equation concept

signal is generated, changing the path length of one arm of the beam. This compensates for any slight vibrations that may occur, thus keeping the fringes locked in place and stabilizing the interference pattern.

The grating equation which relates the incident angle to the angle of diffraction is as follows:

$$\sin\theta_m = \sin\theta_i + \frac{m\lambda}{d} \qquad (1)$$

where θ_i is the incident angle, θ_m is the diffracted angle for order m, λ is the wavelength of incident light, and d is the groove spacing of the grating (Figure 3). If the diffraction grating is to be used at the $m = -1$ order, at the Littrow angle, the grating equation becomes

$$\sin\theta_i = \frac{\lambda}{2d}. \qquad (2)$$

Thus, for a specific incident angle during usage, a certain groove spacing is required. This groove spacing can be achieved by controlling the angles of the exposure beams according to this equation (Figure 4):

$$d = \frac{\lambda_e}{2\sin\theta_e \cos\phi}. \qquad (3)$$

Using equation (2), the groove spacing required for an incident angle of 51.2° of 1053 nm radiation is 675 nm. To achieve this, the exposure angle must be set to 17.8°, assuming the bisector of the angle

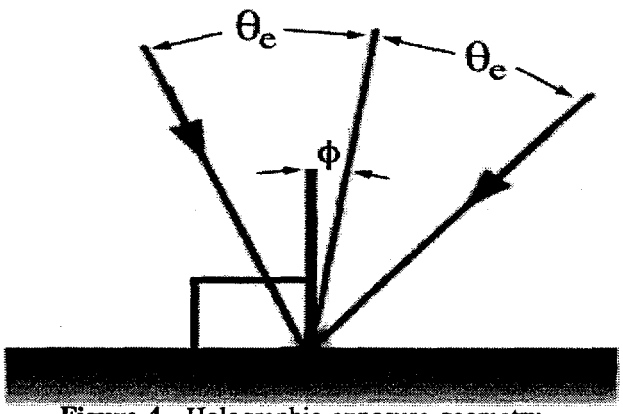

Figure 4. Holographic exposure geometry

between beam vectors is normal to the target grating surface.

Numerous factors influence the exposure time necessary for optimal grating performance. In general, exposure time, often measured as fluence, is inversely related to development time. If a longer development time is desired, the duration of exposure must be shorter. Another factor to be considered is the preferred duty cycle of the grating. For a larger base width, a shorter exposure time may be used. With a high-contrast photoresist, however, there is an exposure fluence threshold under which very little exposed resist will actually dissolve away during development. Fluences we used for lift-off ranged from 130 to 160 mJ/cm^2.

2.3 Preprocessing

To facilitate lift-off, various forms of preprocessing can be utilized[5]. After exposure, our substrates are subject to a chlorobenzene pre-development soak. This fractioning solvent is absorbed in the top surface of the exposed photoresist and serves to inhibit dissolution during development. Consequently, structures with an overhang are produced. The thickness of the overhang layer is affected by the soak time and the impurities in the chlorobenzene. The substrates are again rinsed with distilled water.

2.4 Development

After preprocessing, the samples are brought to the developing station (Figure 5). They are placed in the same exposure holder in the original orientation so that alignment can be maintained for *in situ* development monitoring[6]. A laser beam of

[5] W. M. Moureau, "Semiconductor lithography: principles, practices, and materials."
[6] J. A. Britten *et al.*, "*In situ* end-point detection during development of submicrometer grating structures in photoresist."

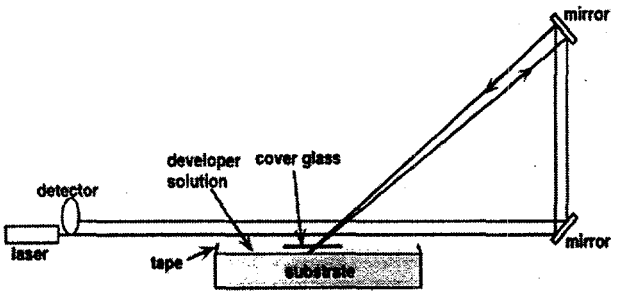

Figure 5. *In situ* development station schematic

unexposing wavelength illuminates the sample at the $m = -1$ order, Littrow angle such that the diffracted beam can be measured with a photodetector. The sample is placed in the reservoir under a wave-suppressing window. At time zero, the sample is immersed in 100% AZ MIF 300 developer. Although development times may vary for each sample, the end-point is determined by the shape of the curve of the monitored diffraction intensity. For tall structures, as the grating emerges, the intensity will cycle through a series of minima and maxima until it finally levels off. At this point, development through the entire photoresist layer has occurred, and the sample can be removed from the developer solution. Further development will merely cause the sidewalls of the gratings structures to dissolve, resulting in a decreased duty cycle. The grating mask sample is then rinsed with distilled water and dried with dry-nitrogen.

2.5 Oxide deposition and lift-off

Once the grating mask has been made, the actual grating itself can be formed. Both small and large substrates can be placed on a magnetron sputtering chamber and undergo oxide deposition. Hafnium oxide is first evaporated at an angle to produce half of a cap at the tips of the grating mask (Figure 6a). Angled evaporation from the other side occurs to produce the other half of the cap (Figure 6b). Oxide evaporation normal to the substrate then deposits the actual grating between the photoresist structures (Figure 6c). The photoresist grating mask is subsequently lifted off by dissolution in 3% NaOH (Figure 6d).

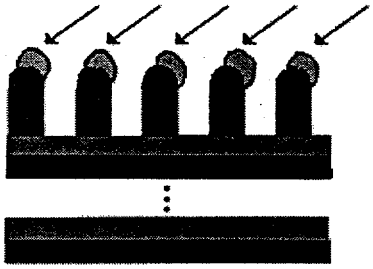

Figure 6a. Angled evaporation of oxide to form half of overghanging cap

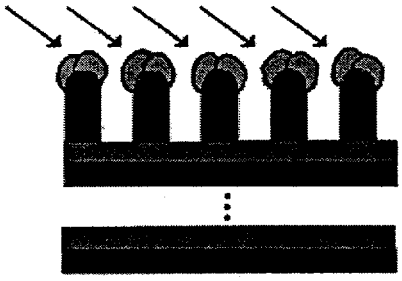

Figure 6b. Angled evaporation of oxide from other side to form other half of cap

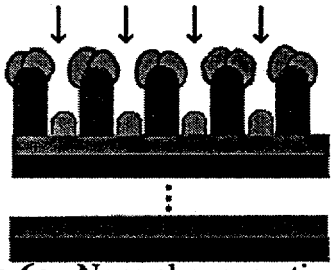

Figure 6c. Normal evaporation of oxide between photoresist grating mask

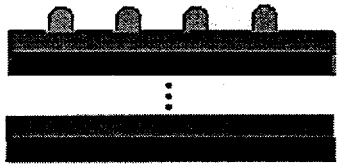

Figure 6d. Photoresist grating mask is lifted off by dissolution

3. Results and Analysis

We have been able to fabricate several different grating masks for the lift-off process (Figures 7-9). Some samples were deposited with an oxide and subsequently stripped of its photoresist grating mask. The samples were then broken and examined with scanning electron microscopy (SEM).

Figure 7 shows SEM's of a grating that was directionally evaporated with scandia. Deep cap-shaped overhangs were created on the scandia samples, and normal evaporation resulted in approximately 250 nm high ridges between the grating masks. After lift-off of the grating mask, scandia ridges remained with excess material along the sides (Figure 7b). These extensions are remnants of the oxide that existed on the sidewalls near the base of the photoresist mask structures. The angle deposited oxide penetrated too deeply into the grating mask, thus producing the final non-ideal grating. These results do show, however, that the lift-off process is possible.

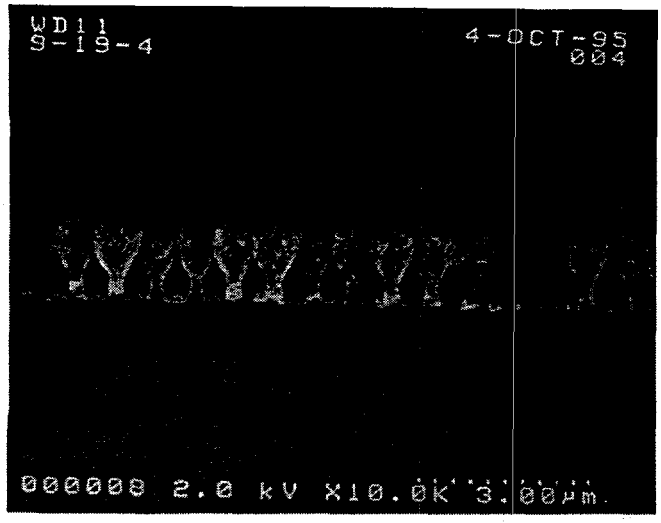

Figure 7a

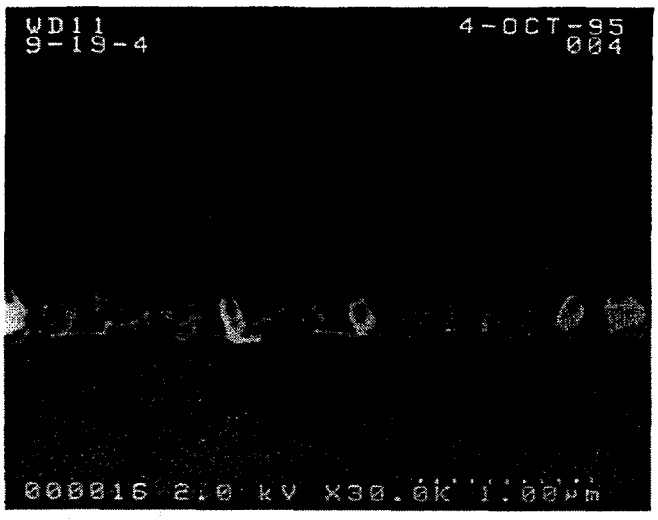

Figure 7b

Figure 8a

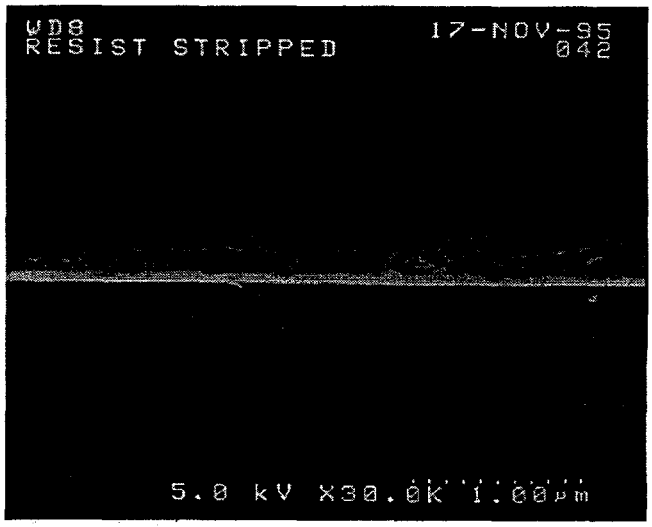

Figure 8b

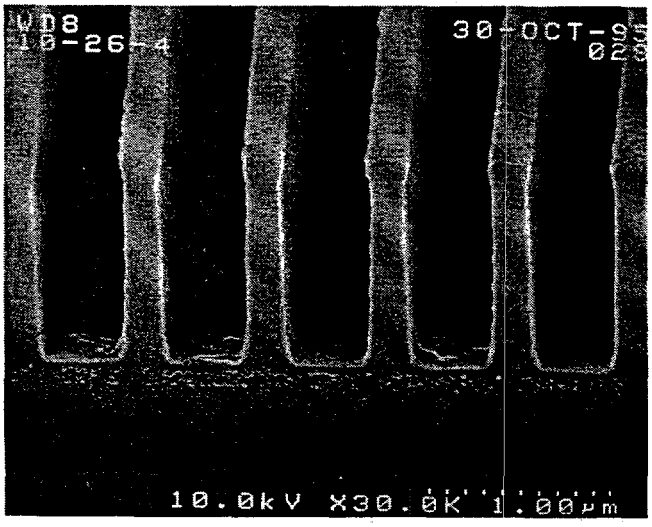

Figure 9a

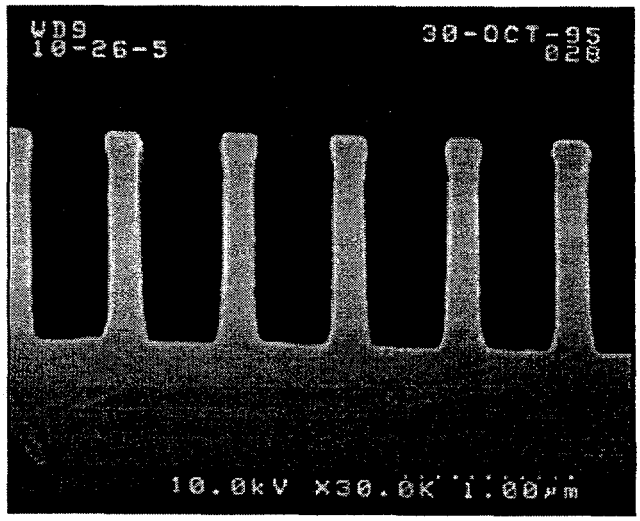

Figure 9b

Figure 8a shows a grating mask magnetron-sputtered with hafnium oxide. A high-contrast photoresist was used to create tall structures with vertical sidewalls. After normal deposition of the oxide, 200 nm high ridges remained between the grating mask structures. After the photoresist mask was stripped, the sample revealed almost no hint of a grating (Figure 8b). The accumulation of oxide on the sidewalls may have again caused problems during lift-off. On this microscope slide sample, the hafnium oxide did not adhere to the underlying surface adequately. This adhesion problem probably would not occur on an actual dielectric surface of high index of refraction.

In hopes of avoiding the sidewall accumulation problem, we attempted to create tall grating masks preprocessed to develop an overhanging structure. Gratings pre-soaked in chlorobenzene exemplify this characteristic, as shown in Figures 9a and b. These structures are 1.2 μm tall with a base width of 0.25 μm. We hope that tall structures such as these, with the appropriate angle of oxide evaporation, will prevent sidewall growth. The high aspect ratio of these structures (>4.5) may also facilitate lift-off by keeping the base of the photoresist clear of oxide. Thus, when the photoresist mask is dissolved, the actual grating material will remain intact.

4. Conclusions

Although the preliminary grating masks we have created did not generate ideal gratings, our limited success does prove that the creation of diffraction gratings by lift-off processing is indeed possible. Each process step contributes significantly to the resulting characteristics of the final grating mask. These characteristics include overall shape, height, basewidth, duty cycle, and adhesion to the substrate surface. We must continue our research to optimize the processing method. Only then will we have the ability to produce grating masks that will provide high-efficiency, high damage threshold diffraction gratings.

BIBLIOGRAPHY

Boyd, R. D., Britten, J. A., Decker, D. E., Shore, B. W., Stuart, B. C., Perry, M. D. and Li, L. "High-eficciency metallic diffraction gratings for laser applications," *Appl. Opt.* **34,** 1697-1706 (1995).

Bookless, W. A. ed. "Meniscus Coating," *Energy and Tech. Rev.* 24-25 (November 1994).

Britten, J. A., Boyd, R. D., Shore, B. W. "*In situ* end-point detection during development of submicrometer grating structures in photoresist," *Opt. Eng.* **34,** 474-479 (1995).

Moreau, W. M. "DQN For Lift-off," *Semiconductor Lithography: Principles, Practices, and Materials*, 573-581 (1988).

Perry, M.D., Boyd, R. D., Britten, J. A., Decker, D. and Shore, B. W. "High-efficiency multilayer dielectric diffraction graitngs," *Opt. Lett.* **20,** 940-942 (1995).

Perry , M. D. and Mourou, G. "Terawatt to Petawatt Subpicosecond Lasers," *Science.* **264**, 917-924 (1994).

Magnetic Field Regulation Control System Analysis*

Steven W. Badelt
Carnegie Mellon University,
Department of Electrical and Computer Engineering

Lawrence Livermore National Laboratory
Isotope Sciences Division
Livermore, California 94550

December 15, 1995

Prepared in partial fulfillment of the requirements of the Science and Engineering Research Semester under the direction of Douglas L. Phinney, PhD., Research Mentor, in the Lawrence Livermore National Laboratory.

* This research was supported in part by an appointment to the U.S. Department of Energy Science and Engineering Research Semester (hereinafter called SERS) program administered by LLNL under Contract W-7405-Eng-48 with Lawrence Livermore National Laboratory.

Magnetic Field Regulation Control System Analysis [1]

Steven W. Badelt [2]

Abstract— This study comprises (1) an analytical characterization of the Cameca ion microscope's magnetic field regulation circuitry and (2) comparisons between the analytical predictions and the measured performance of the control system. It is the first step in a project to achieve routine regulation better than 10ppm.

The control loop was decomposed into functional subcircuits and simulated in SPICE to determine DC, AC, and transient response. Transfer functions were extracted from SPICE, simplified, and analyzed in MATLAB. Both SPICE and MATLAB simulations were calculated for step inputs, and these results were compared to actual measurements. Magnetic field fluctuations were measured at high mass resolving power. The frequency spectrum of the fluctuations was analyzed by FFT. Difficulties encountered and implications for future work are discussed.

I. Introduction

The Cameca IMS-3F ion microscope in operation at the Lawrence Livermore National Laboratory Isotope Sciences Division is a sputtering-source mass spectrometer. It is used for the microcharacterization of solid samples, including trace-element analysis, which requires sensitive measurements. To this purpose, mass resolving powers up to 20,000 (amu/Δamu) are possible with this system. Accuracy of measurements is limited by the regulation of the mass-spectrometry magnetic field. Successful operation at high resolving power requires magnetic field regulation better than 10ppm.

The field regulation control system is an analog closed-loop single-input, single-output circuit. It responds to an input from a DAC by comparing that input to the amplified output of a hall probe which directly measures the magnetic field of the mass-spectrometry magnet. Aside from power supplies and grounds, the regulation circuit is completely independent of all other ion-microscope systems. However, the hall probe does have separate circuitry for temperature and bias current regulation.

The various subcircuits of the system are physically located in two primary areas of the instrument room. The hall probe, its amplifier, and the magnet are adjacent to each other. They are connected to the Field Regulation Chassis, containing all other subcircuits, by a 4m. long cable.

The system suffers from sporadic noise problems in the field regulation loop that prevent high accuracy measurements from being made. The effects of the noise are visually realized when the ion-beam image is created on a phosphor screen. In such an instance, the beam oscillates from side to side on the display. The frequency of this noise is greater than 1hz and less than 60hz (no visual aliasing occurred), and the magnitude is approximately 75ppm. Before measurement of the these field fluctuations was possible, the system inexplicably improved and has not measurably worsened since. It now performs with low amplitude field noise at less than 10ppm. It is assumed, given the previous nature of the system, that the noise may reappear at any time.

If field fluctuations persist in the future, the eventual solution may be to redesign system in part or full. However, it was decided that a systematic approach, first characterizing the entire system, would be best. The initial step in this approach was to simulate the system. From the simulation, clues about system performance were generated, including DC operating points, transfer functions, and transient response. Examining the loop by transfer functions also yielded ideas about stable performance. Noise measurements were taken to establish data for comparison with future performance.

II. Modeling of Functional Subcircuits

Circuit descriptions for input to SPICE were taken from schematics provided by Cameca. The SPICE input deck was created by replicating the feedback loop. Voltage supplies were assumed ideal, and transistor parameters were derived if commercial models were not available. After decomposition of the entire feedback structure, the block diagram in Figure 1 was created. Prior to simulation of the

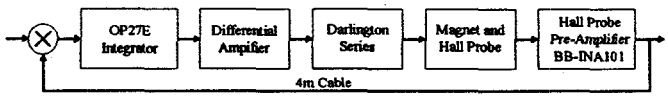

Figure 1: Block diagram of field regulation loop.

1. This research was supported in part by an appointment to the U.S. Department of Energy Science and Engineering Research Semester (hereinafter called SERS) program administered by LLNL under Contract W-7405-Eng-48 with Lawrence Livermore National Laboratory.

2. The author would like to thank Doug Phinney, James Wong, Ian Hutcheon, Tony Laevitas, and the LLNL Isotope Sciences Division for their generous support of this research.

entire feedback loop, each subcircuit was individually analyzed to determine its transfer function as well as AC, DC, and transient characteristics. The functional units were then connected to form the feedback loop for simulation of the total system. The SPICE input decks are included in Appendix A.

For each subcircuit, a transfer function was derived using the .PZ operation in SPICE. Each transfer function was simplified and entered into MATLAB for simulation of the resulting equations (see Appendix B). In each block, poles and zeros were omitted from the system if they were over 100rad/sec. At this frequency, the open loop gain would be attenuated by ~40dB due to the magnet inductance. Simulations including poles and zeros beyond 100rad/sec did not vary in the simulated response in MATLAB. Some Bode plots in this paper do include features above 100rad/sec to show any dominant characteristics of each transfer function.

i. Integrator

The integrator is a single op-amp in non-inverting configuration with an RC series connected for feedback (See Appendix C). As such, the frequency response follows the equation:

$$G_{\text{int}}(s) = \frac{1+0.056s}{0.0011s}$$

In reality, several factors limit the integrator from ideal performance. As can be seen in Figure 2, the effects of slew limit the high-frequency, constant gain of 50 in the ideal integrator beyond 1Mrad/sec. Although the maximum open-loop gain of the OP27E is 100dB, the SPICE model predicts a low frequency gain plateau of 180. The reason for this is unknown, but related to the use of a capacitor in the op-amp feedback loop. In simulations using only a resistor, the gain approached the op-amp's maximum open-loop gain.

The op-amp cannot drive the output beyond supply limits (-15V to 15V). The typical operating range when the loop is undisturbed is between -150mV and 50mV. This means that for 10ppm operation, the noise output of the op-amp must be <1.5uV. The high sensitivity of the instrument becomes particularly evident when examining the formula for integration:

$$\Delta V_{out} = \frac{\left(0.45mV_{output}\right)}{\left(1\text{sec}\right)\left(1uV_{input}\right)}$$

ii. Differential Amplifier

The differential amplifier, as diagrammed in Appendix C, includes a differential pair with output to the darlington series amplified by a separate darlington pair. The two pairs of darlington series were split due to the separate location of each circuit in the chassis. However, their function for current amplification is the same in each case.

The differential pair provides for a 0V input offset and a 18V output offset with a DC gain of 172. Typical input voltages within the range of instrument operation are -150mV to 50mV, with input beyond +/-700mV clipped by input diodes. The output voltage of the differential pair ranges from 0V to 34V (10ppm operation <0.34mV).

The reason for the transistor arrangement above the collector resistor of the output side of the differential pair is unknown. It appears to be put in place to act as a 6.93mA current source. However, this would negate the amplifying of the differential amplifier and exceed the 6.55mA bias current of the differential pair. In SPICE, the differential pair act as would be expected without influence from the 'unknown' current source, which never operates in forward active mode.

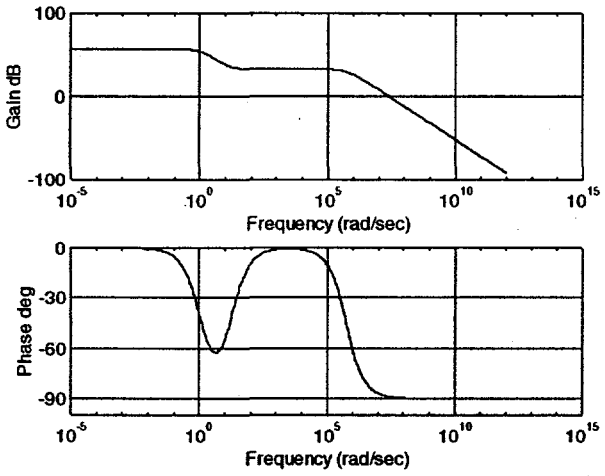

Figure 2: Bode plot of simulated integrator.

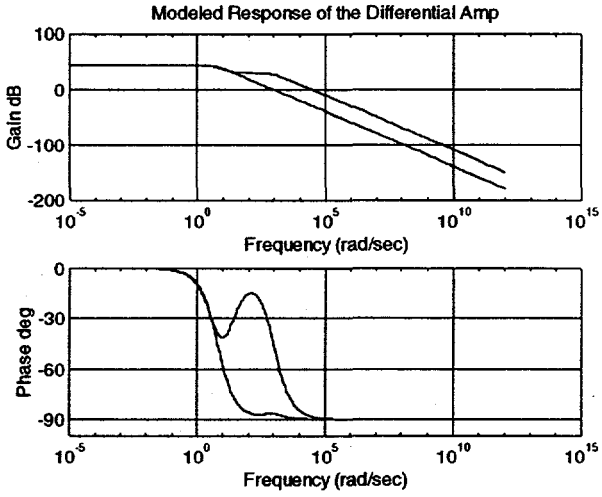

Figure 3: Bode plot of simulated differential amplifier.

The frequency response of the differential pair is modifiable by means of a phase delay-setting potentiometer. The potentiometer is used in series with a capacitor to connect the output of the differential pair to its right-side input. By increasing the resistance of the 47k potentiometer, less negative feedback is applied in the affected frequency range. In Figure 3, the enclosed region represents the possible values for the system bounded by a 100ohm setting (bottom line) and a 47kohm setting (top line). The potentiometer setting affects the stability of the system. A low potentiometer setting (<5k) causes a combination of increased phase delay and attenuation which allows the feedback loop to overshoot when attempting to compensate for the error signal. The result is an unstable system at low potentiometer settings.

The darlington series at the output of the differential pair provide current gain to drive the subsequent darlington series. The combined current gain of both transistors is 400.

iii. Darlington Series

The darlington series after the differential amplifier consists of a single transistor driving the bases of four parallel transistors. The use of four transistors in the second stage permits up to 20A of current to drive the magnet without exceeding the current limit of each individual transistor. The combined current gain of the transistors in parallel is 1400.

As with the other blocks, the transfer function for the darlington series was measured by comparing V_{out}/V_{in}. The derived transfer function had distinguishing characteristics at frequencies much higher than the first pole of the magnet. Consequently, all poles and zeros for the darlington series were neglected. In MATLAB simulation, a constant voltage attenuation of 0.97 was assigned at all frequencies of the transfer function.

iv. Magnet and Hall Probe

The magnet and hall probe were modeled together due the dependency between them.. The hall voltage (V_h) is proportional to the magnetic field which is proportional to the current flowing through the magnet. The magnet was modeled as a single-lump RL series. Using data taken from the magnet, a direct proportional relationship between the magnet current and the resulting hall voltage was created:

$$V_h = -I_{magnet} \times 0.025329$$

V_h is produced within SPICE by a linear current controlled voltage source. Notice that V_h is opposite in polarity from I_{magnet}.

With the large inductance of the magnet, it is not surprising to find that the magnet and hall probe assembly provides a low frequency pole which dominates the system (See Figure 4). It is assume that any high frequency poles and zeros produced by the hall device can be neglected.

v. Hall Probe Pre-Amplifier

The hall probe pre-amplifier buffers the hall probe from any load and applies a gain of 11.667 to V_h, preventing loss of signal integrity from noise and loss along the 4m cable. In the actual system, the hall pre-amp is a BB3629 (Burr-Brown) instrumentation amplifier. No SPICE models exist for the BB3629 and it has been dicontinued. The simulation was instead run with an INA101, Burr-Brown's recommended replacement for the BB3629, for which they provide a SPICE model.

The primary difference in the two amplifiers is that the gain, set by a resistor external to the IC, follows a different equation in each case. Simulation of the INA101 model in SPICE only derived one pole at a frequency much higher than that of the magnet pole. It is assumed that any differences between the current and old amplifier designs

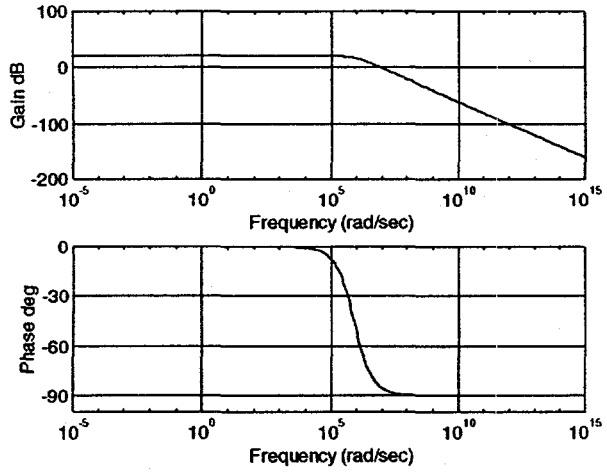

Figure 4: Bode plot of simulated magnet and hall probe.

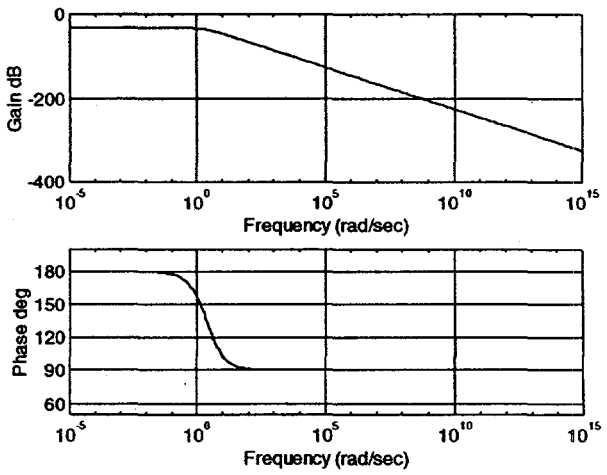

Figure 5:Bode plot of simulated hall pre-amp.

18 bit DAC (0-140)	0.23823
18 bit DAC (0-300)	0.11080
19th bit (0-140)	0.11911
19th bit (0-300)	0.05540
V_h	0.47645

Figure 6: Summing coefficients.

would show up at high frequencies, and the INA101 can be taken as a suitable replacement. Within MATLAB, the pole of the hall pre-amp was neglected, and a constant gain was applied at all frequencies.

vi. Summing Junction

The control system summing junction was realized by a resistive summing junction at the input to the integrator (See Appendix C). The control input is via an 18 bit DAC and an additional, switched '19th' bit supplied by a voltage regulator. Each of these may be switched between two resistors, via a relay, depending on the mass range under inspection on the ion microscope. An additional resistor sums the DAC inputs with V_h, which is opposite in polarity. The coefficients for each input are supplied in Figure 6.

III. Total System Response

After comparing simulated response to expected response of each block, the entire feedback loop was assembled. Modeled step responses in SPICE and MATLAB were compared to the measured step response of a similar Cameca ion microscope at CalTech. No measurements of the system in question were ever made. Plots of the responses are shown for the CalTech, SPICE, and MATLAB measurements in Figures 7-9 respectively (see end of paper for figures). The responses for SPICE were taken at varying values of the phase delay potentiometer, since the actual value was not measured. Simulated values above 10kohms yeilded plots which compared best to the actual data. MATLAB simulations were made using transfer functions for a setting of 32.5kohms.

Though no figures of merit were composed, the SPICE simulated response closely follows that of the actual system on qualitative measures. Each has similar settling time and overshoot. The SPICE was accepted as a reasonable model, since it was being developed to provide ideas on system performance and was not expected to match exactly with all system parameters. The MATLAB simulated step response varies from the actual and SPICE models. The settling time is faster by more than an order of magnitude. It is believed that this difference is due to two factors. The MATLAB analysis, based completely on transfer functions, is dependent on the small signal analysis of the SPICE simulation. In addition, it is not restricted by diode

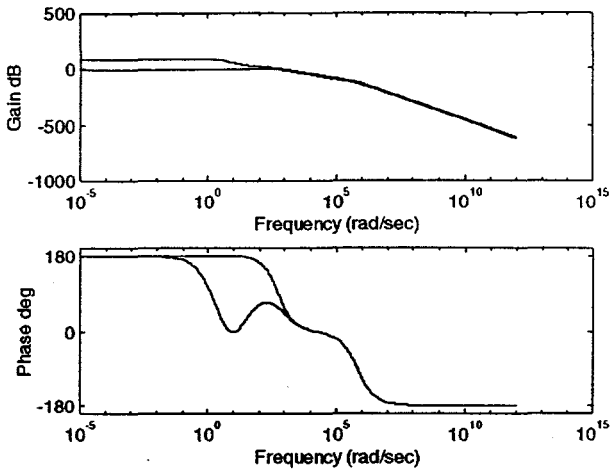

Figure 10: Comparison of open and closed-loop gain.

clipping, saturation of transistors, railing to supply limits, or other system limitations.

Analysis of the closed and open loop transfer functions in MATLAB confirms the effects of feedback on the gain and response of the system. In Figure 10, the open-loop response (top line in gain plot, bottom line in phase plot) and closed-loop response are compared. The feedback limits open loop gain at low frequency, and pushes the dominant pole of the magnet to higher frequency. Examination of the system using the root-locus technique shows that a change in the open-loop gain pushes a zero into the right-half plane. Changes in the phase potentiometer setting did not visibly change the root-locus plot. However, as can be seen in the SPICE step responses (Figure 8), a decrease in the potentiometer setting causes the system to become unstable.

IV. Noise Measurements

Due to the sensitivity of the system and the undesired effects of breaking the control loop, noise measurements were made by measuring fluctuations in the ion beam current detected with the electron multiplier. The beam was partially eclipsed (50%) by the exit slit. Therefore, any fluctuation in the magnetic field would cause the beam to be eclipsed to a greater or lesser extent.

0.1s integrals of electron multiplier counts were taken, and the data were collected by computer. The frequency of measurement was limited to less than 10Hz by the computer setup. Due to computer bus traffic, it is possible that these measurements were not taken at 10Hz. Data has not been taken to determine the accuracy of the computer controlled measurements with respect to time. The data taken were during a period of good beam stability, when the sporadic noise was not present. Therefore, the results may be used as a standard to which future stability measurements may be compared. Conditions during the measurements were recorded for this reason (See Appendix D).

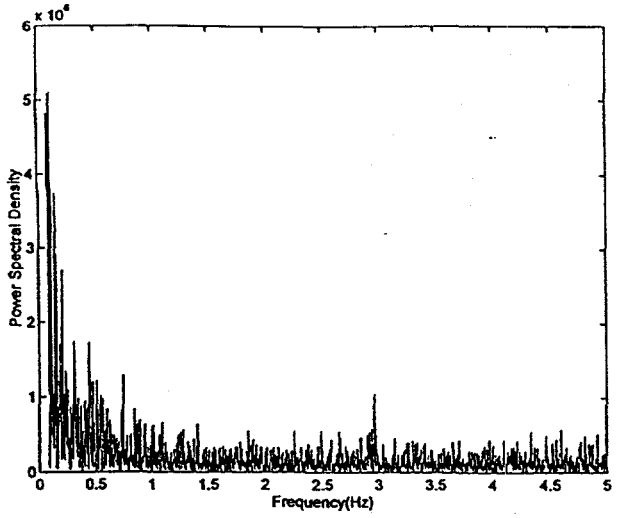

Figure 11: Noise FFT from O^{16}- beam.

Before FFT, a Hanning window was applied to the beam stability data taken with an both Cs- and O^{16}- ion beams. The power spectral density for O^{16}- beam data (1.55×10^4 RMS) is shown in Figure 11. Two sequential measurements were made and the frequency spectra were averaged, reducing the signal to noise ratio by $1/\sqrt{2}$. The average of 4 samples of Cs- data (5.23×10^3 RMS) is shown in Figure 12.

The frequency spectrum in both plots has two salient features, a high amplitude below 1Hz and a peak slightly below 3Hz. The low frequency noise seems to reduce in amplitude as would a simple RL filter (i.e. the magnet). However, the dominant pole of the system in closed- and open-loop transfer functions comes a decade or more after the low frequency noise settles to background. If this characteristic of the noise is from filtering in the system, the transfer function seen by noise entering the loop at different points may not be the same. No noticeable low frequency drift could be seen when looking at an image of the beam. Therefore, the low frequency noise may be coming from variations outside the control loop. One variable on which these noise measurements are highly dependent is the ion source intensity. However, similarities in low frequency noise from both the Cs- and O^{16}- source tests lead credibility that this noise is somewhere in the field regulation loop.

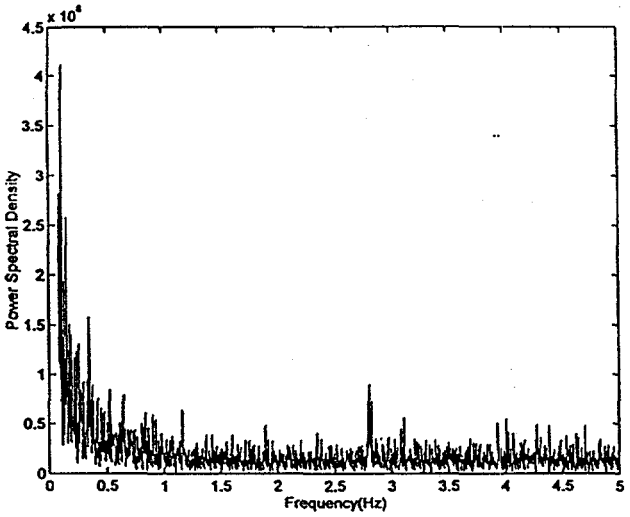

Figure 12: Noise FFT from Cs- beam.

The 3Hz noise is not a function of the transfer function and is within the band in which large amplitude noise (75ppm) was seen prior to measurement. The noise is seen in data taken from beams of both ion species, however there is a difference in frequency of 0.16Hz between the peaks of each beam. If this shift in frequency is not due to system variability, it may be caused by inconsistent timing in computer collection of the data.

V. Difficulties

One of the biggest difficulties encountered was the procurement of appropriate SPICE models, particularly for older transistors. In simulation, delays inserted in the control loop were never accomplished in either SPICE or MATLAB. Delays using the Pade transfer function approximation could not be accurately created at higher order (>5), and lower order models were crude. Test circuits using the delay argument for a controlled voltage source produced delayed signals with glitches.

Measurement of the actual system was complicated by the sensitivity of the system to change. A 4m test cable was created with buffered V_h output and an input from a precision voltage source. Changes in noise levels and system performance were to be studied while a computer read V_h and controlled the precision source accordingly. Unfortunately, the computer could not update the equipment with enough speed to keep the system stable. In addition, the new 4m cable, though created in image of the original, was more susceptible to room noise.

VI. Implications

The Cameca mass-spectrometry magnetic field regulation circuitry has been successfully characterized. In the future, the achieved understanding of the system will assist in the examination of possible noise sources in the system. The data obtained may also be used to create an entirely new control loop, including digital control, or make modifications to the existing system. Irregardless of improvements made, the noise measurements taken set a standard by which present and future performance may be compared.

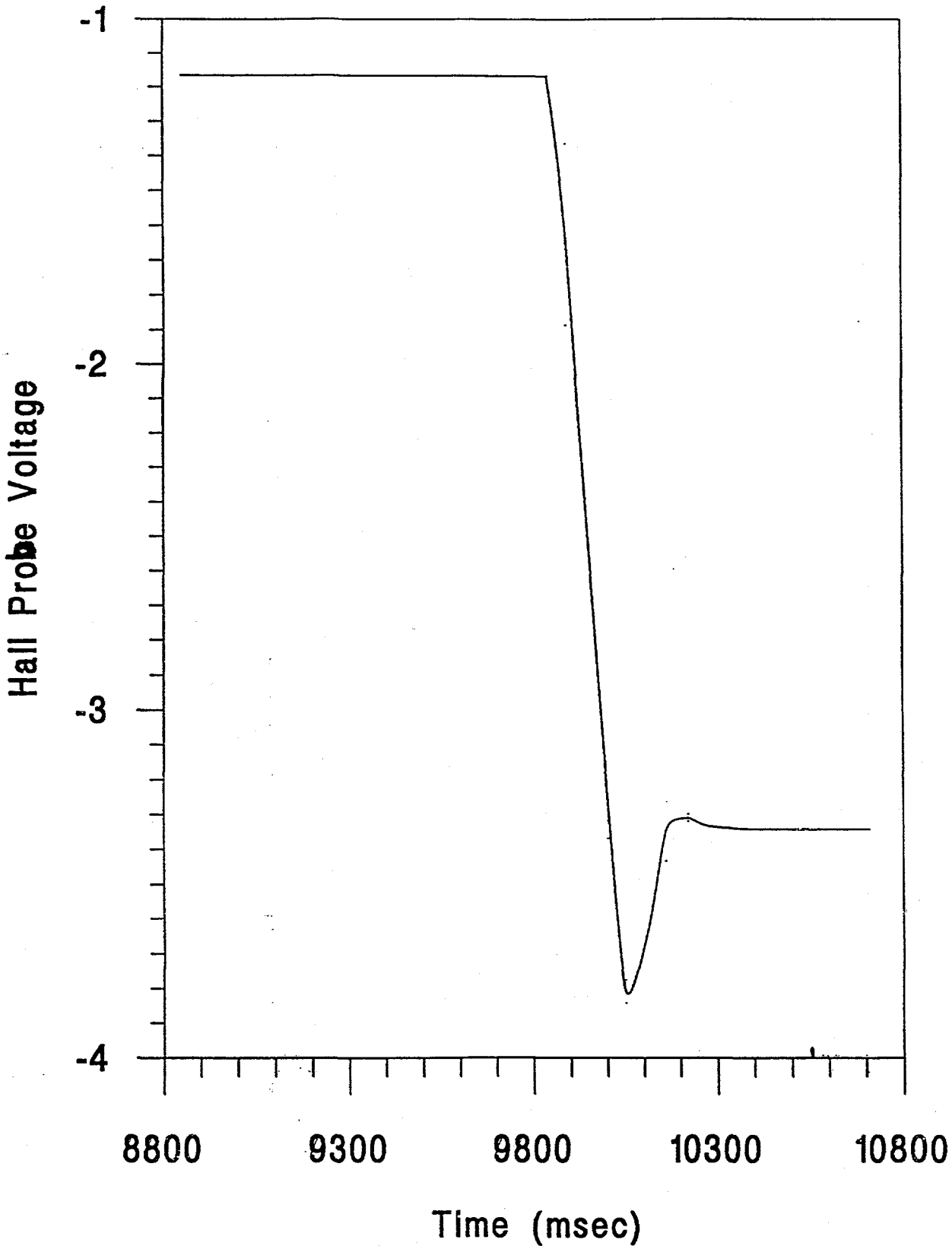

Figure 7: System step response (from CalTech).

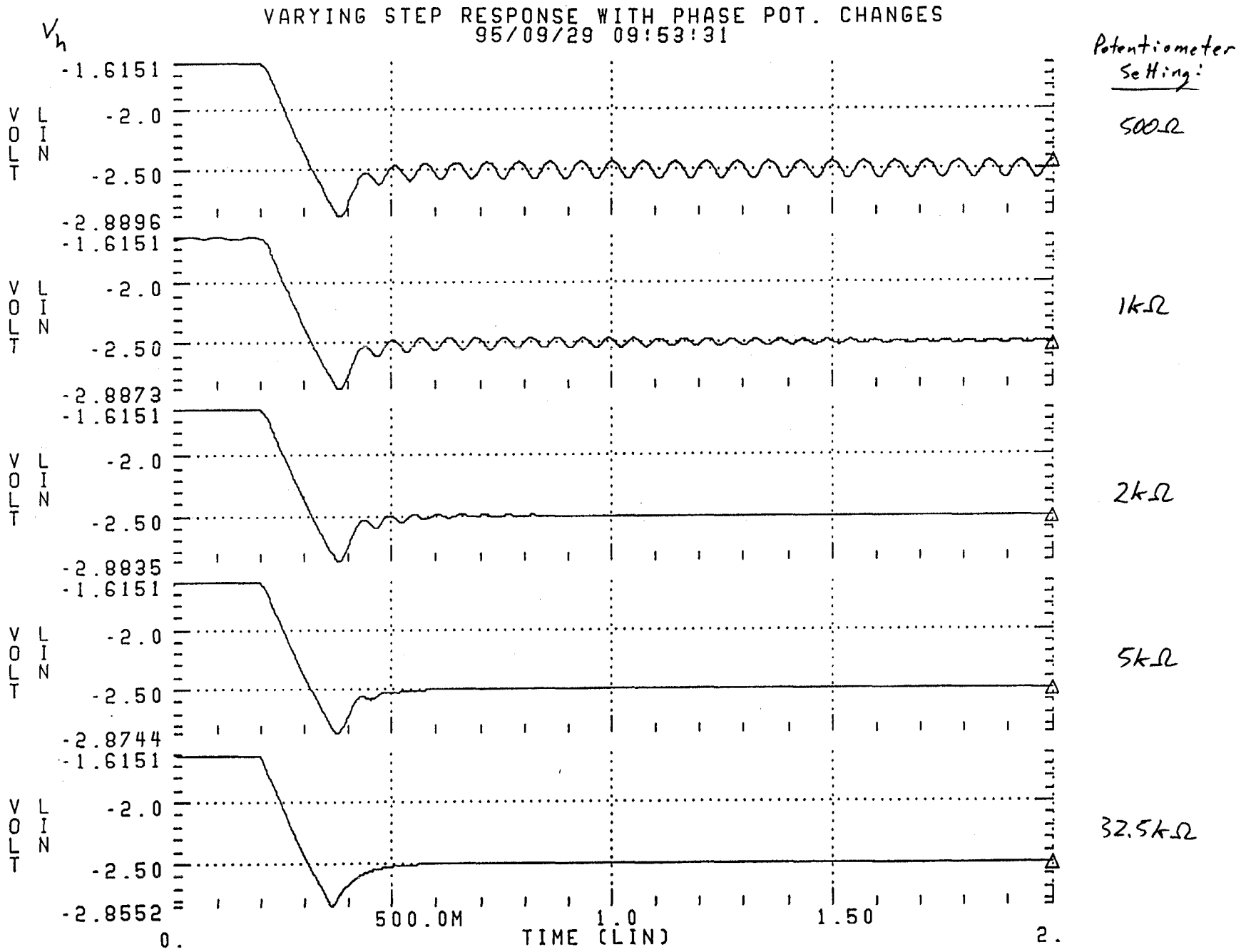

Figure 8: SPICE step response at varying potentiometer values.

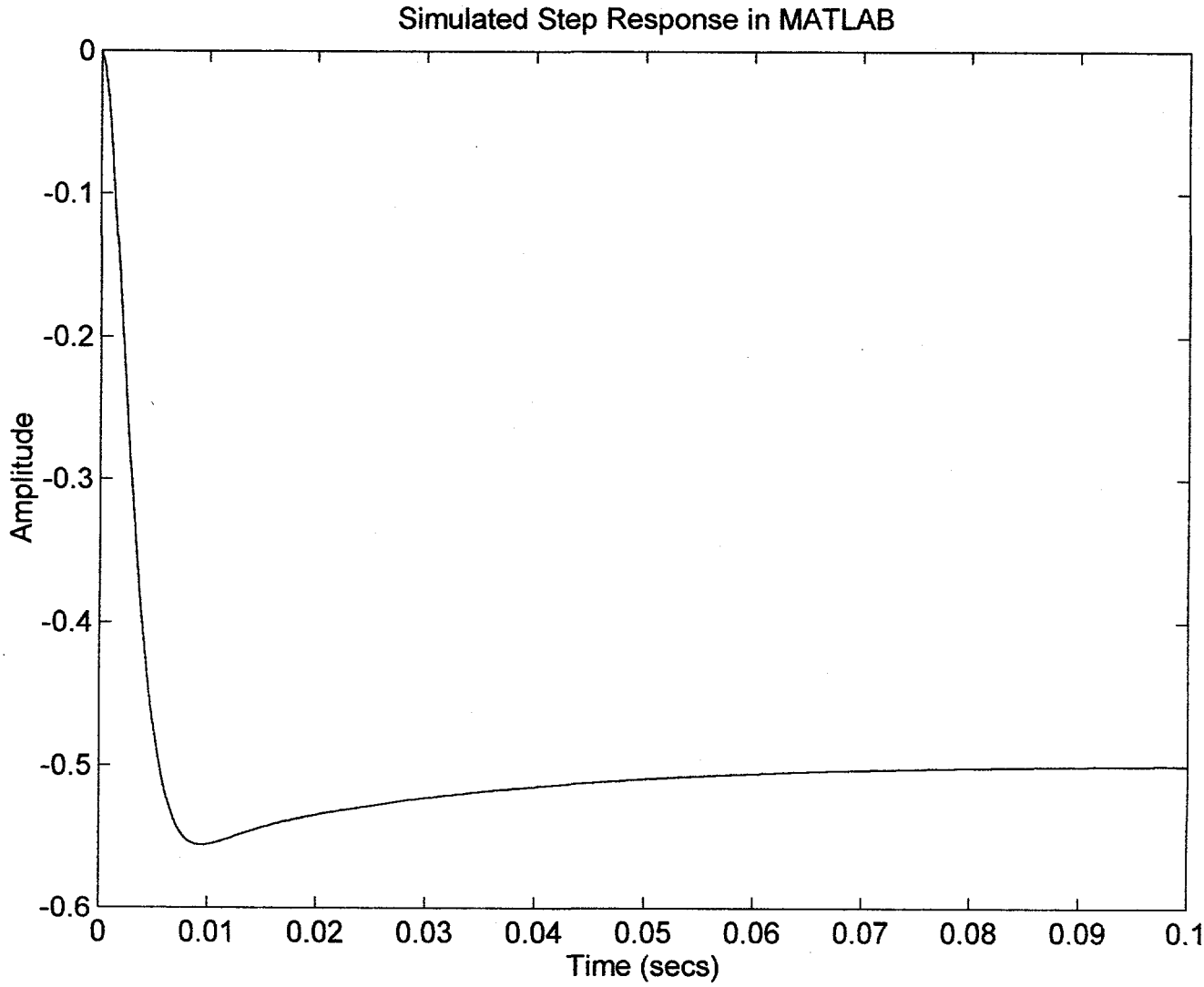

Figure 9: Matlab step response.

Appendix A - Spice Input Deck

The following files inclue the entire code necessary for simulation of the Cameca mass-spectrometry magnet field regulation control system. The first file, 'cameca.sp,' calls all other files. Each of the '*****.sub' files can be used independently for individual inspection. Simulations were run using HSPICE ver. H92 by Meta-Software, Inc.

File: cameca.sp

```
Modeling of the Cameca Magnet System - Rev. 3
* Steven William Badelt
* Lawrence Livermore National Laboratory
* sb6z@andrew.cmu.edu

.option POST          * sets up datafile for GSI and HSPLOT
                      * stores in a binary format
.option brief
.option nomod

.include 'camecabjt.mod'

* subcircuit includes

.include 'regulator.sub'
.include 'magamp.sub'
.include 'maghall.sub'
.include 'hallpre.sub'

.PARAM pot=32.5k        *allows easy change in phase pot value

* ---------------------------------------------------------------
* Total Circuit Response with Feedback
* ---------------------------------------------------------------

Vin   10 0 AC 1.0       * DAC input
Xreg  0  10 20 reg      * regulator chassis:
                *  summing junction
                *  integrator
                *  differential pair
XIm   20 30 mag_amp     *  darlington series
XVh   30 40 mag_hall    *  magnet and hall combined
XPre  40 0 50 hall_pre      *  hall pre-amp

* ---------------------------------------------------------------
* Operators
* ---------------------------------------------------------------
*.OP              * operating point data (DCV)
*.AC dec 5 0.01 1Meg    * bode plot, phase and magnitude
*.TRAN 0.25m 500m       * transient response plots
*.PZ V(50) Vin          * transfer function poles and zeros

.OP

.END
```

File: regulator.sub

```
* Field Regulator Chassis Block
* Steven William Badelt
* Lawrence Livermore National Laboratory

.option brief

.include 'opa27e.mod'
.model D1N4148 D(Is=0.1p Rs=1 CJO=2p Tt=12n Bv=100 Ibv=0.1p)

* ------------------------------------------------------------
* Differential Amplifier Subcircuit
* ------------------------------------------------------------
.SUBCKT reg 1 9900 19
*       |  |   output to darlington series
*       |  input from DAC
*       feedback from hall pre-amp

V15p   1500 0 DC 15volts
V15n   1501 0 DC -15volts
V37p   3790 0 DC 37.9volts
V25p   2500 0 DC 25volts        * SIN 25 2.5 60
                * the poorly regulated magnet
                * power supply
                * 3% at 30Hz

* diodes

Dcr3   6 0 D1N4148
Dcr4   7 6 D1N4148
Dcr5   7 9 D1N4148

* input

*Vdac was replaced by an input from the feedback loop
*Vdac 9900 0 DC 4.321       * 18 bit DAC output 0-5V
                * pos and ground may be flipped

V19bit    9902 0 DC 0     * 19th bit of DAC system
                * pos and ground may be flipped
                * may be turned on and off #V or 0V

R17    9900 2 10k TC=0.001,0.015
R18    0 2 21.5k  TC=0.001,0.015
R19    9902 2 20k  TC=0.001,0.015
R20    0 2 43k  TC=0.001,0.015

R21    1 2 5k     TC=0.001,0.015    * input resistor between op27
                  * and Vh from hall pre-amp

Xa1    2 3 1500 1501 5 OPA27E      * op27e

R32    3 0 5.1k  TC=0.001,0.015    * op27e feedback elements
R16    3 4 249k  TC=0.001,0.015
C11    4 5 0.22uF

R15    5 6 1k  TC=0.001,0.015      * components between op27
C10    6 0 1uF            * and diff. pair
```

```
* Differential Pair

Q4 8 6 7 Q2N4100
R11   1500 8 2.21k  TC=0.001,0.015
Q6 10 9 7 Q2N4100
R10   11 10 4.75k  TC=0.001,0.015
R5 9 0 1k  TC=0.001,0.015
C8 9 20 1uF

Rp1   20 10 pot  TC=0.001,0.015  * 0-47k pot for phase adjustment

* Active load

Q5 11 12 13 Q2N2907
R14   3790 13 1k  TC=0.001,0.015
R13   3790 12 7.5k  TC=0.001,0.015
R12   1500 12 15k  TC=0.001,0.015

* Current Source

Q3 14 15 16 Q2N2222A
R9 7 14 51  TC=0.001,0.015
R6 15 0 15k TC=0.001,0.015
R7 15 1501 15k TC=0.001,0.015
R8 16 1501 1k TC=0.001,0.015

* Beginning of Darlington Cascade

Rfilt 10 17 200 TC=0.001,0.015
Cfilt 17 0 0.1uF

Q2 2500 17 18 Q2N2219A
Q1 2500 18 19 Q2N5320

C7 18 19 0.22uF
R1 19 0 10k TC=0.001,0.015

.ENDS reg

.option brief=0
```

File: magamp.sub

```
* Darlington Series Amplifier Block
* Steven William Badelt
* Lawrence Livermore National Laboratory

.option brief

* ---------------------------------------------------------
* Magnet Amplifier Subcircuit
* ---------------------------------------------------------
.SUBCKT mag_amp 2 8
*     | current output to magnet
*     input from differential amplifier

Vmagsup     1 0   DC 25volts        * try SIN 25 2.5 60
                     * 10% ripple at 60Hz
Qboost      1 2 3 Q2N3772
```

```
Q1     1 3 4 Q2N3772
Q2     1 3 5 Q2N3772
Q3     1 3 6 Q2N3772
Q4     1 3 7 Q2N3772
R1     4 8   0.15 TC=0.001,0.015
R2     5 8   0.15 TC=0.001,0.015
R3     6 8   0.15 TC=0.001,0.015
R4     7 8   0.15 TC=0.001,0.015

.ENDS mag_amp

.option brief=0
```

File: maghall.sub

```
* Magnet and Hall Probe Block
* Steven William Badelt
* Lawrence Livermore National Laboratory

.option brief

* ------------------------------------------------------------
* Magnet and Hall Probe
* ------------------------------------------------------------
.SUBCKT mag_hall 1 9
*       | output to hall pre-amp
*       input from darlington series

Rmag1 1 2 600mohm
Lmag  2 3 0.5           * 34.5mH      * Cameca says its 500mH !
Rmag2 3 8 600mohm
Vmeas 8 0 0volts     * Used to measure current through magnet
            * Only a 0V source can be used to measure
            * current through a point
            * The eight gives me some consecutive
            * node numbers to use if I want to split up
            * the impedence of the magnet into chunks

HVh   9 0 POLY(1) Vmeas 0 -0.025329
            * This is a CCVS.
.ENDS mag_hall

.option brief=0
```

File: hallpre.sub

```
* Hall Pre-Amp Block
* Steven William Badelt
* Lawrence Livermore National Laboratory

.option brief
.include 'ina101.mod'

* ------------------------------------------------------------
* Hall Pre Amp Subcircuit
* ------------------------------------------------------------
.SUBCKT  hall_pre 1 2 3
*       | | output
*       | neg hall probe in
*       pos hall probe in
```

```
* the INA101 is being used instead of the discontinued BB3629CH
* it is the recommended substitute by Burr-Brown
* gain in the BB3629 is determined by the equation 5+(20K/Rgain)
* gain in the INA101 is determined by the equation 1+(40K/Rgain)

Vpos  1500 0 15volts
Vneg  1501 0 -15volts

Rgain 4 5 3.75Kohms

Xopamp   1 2 1500 1501 3 0 4 5 INA101

.ENDS hall_pre

.option brief=0
```

Appendix B - Matlab Script

File: camtf2.m

```
% Transfer Function Model for the Feedback Loop
% The Cameca Secondary Magnet System
%       Steve Badelt
%       Lawrence Livermore National Laboratory
%       L-231 PO Box 808
%       Livermore, CA 94550
%       sb6z@andrew.cmu.edu
%       badelt@sirius.llnl.gov

f = logspace( -5, 12, 500 );
potsamp = [100 32.5e3 47e3];  %values for which potentiometer
                %effects were sampled in SPICE
                %a second order approximation
                %was made to interpolate other
                %values

%------------ Integrator
pole1 = [ -1.0743 ];
zero1 = [ -17.8884 ];
Gop27n = 46.8298*poly(zero1);
Gop27d = poly(pole1);

fbode( Gop27n, Gop27d, f);
[mag,phs,freq] = fbode( Gop27n, Gop27d, f );
subplot(2,1,1);
title('Simple Response of the OP27E Integrator');
dc = mag(1);
figure;

%------------ Differential amplifier
co1 = polyfit(potsamp,[-5.561 -4.065 -4.411],2);
pole1 = polyval(co1,pot)
co2 = polyfit(potsamp,[-1.006e3 -1.01e3 -1.023e3],2);
pole2 = polyval(co2,pot)
co3 = polyfit(potsamp,[-905.4 -29.85 -20.83],2);
zero1 = polyval(co3,pot)
```

```
Gdifn = 23.692e3*poly(zero1);
Gdifd = poly(pole1);
Gdifd = conv( Gdifd, poly(pole2) );

fbode( Gdifn, Gdifd, f);
[mag,phs,freq] = fbode( Gdifn, Gdifd, f );
subplot(2,1,1);
title('Simple Response of the Differential Amplifier');
dc = [dc mag(1)];
mag(1)      % <---- you must check to make sure the
            % DC gain is still 172, may change with
            % the pot values used due to trans funct
figure;

%------------ Darlington Series
Gampn = 0.97;
Gampd = 1;

fbode( Gampn, Gampd, f);
[mag,phs,freq] = fbode( Gampn, Gampd, f );
subplot(2,1,1);
title('Simple Response of the Current Amp');
dc = [dc mag(1)];
figure;

%------------ Magnet and Hall probe
Ghalln = -60.79e-3;
Ghalld = poly(-2.4);

fbode( Ghalln, Ghalld, f);
[mag,phs,freq] = fbode( Ghalln, Ghalld, f );
subplot(2,1,1);
title('Simple Response of the Magnet and Hall Probe');
dc = [dc mag(1)];
figure;

%------------ Hall Pre-amp
pole1 = 1;
Gpren = 11.67;
Gpred = 1;

fbode( Gpren, Gpred, f);
[mag,phs,freq] = fbode( Gpren, Gpred, f );
subplot(2,1,1);
title('Simple Response of the Pre Amp');
dc = [dc mag(1)];
figure; mag(1)

%               Calculations for the Summing Junction

gdacn = 0.23823;
gdacd = 1;
gbackn = 0.47645;
gbackd = 1;

%               The Open Loop
[openn, opend] = series( Ghalln, Ghalld, Gpren, Gpred );
[openn, opend] = series( Gampn, Gampd, openn, opend );
[openn, opend] = series( Gdifn, Gdifd, openn, opend );
[openn, opend] = series( Gop27n, Gop27d, openn, opend );
```

```
%[delayn, delayd ] = pade( 1e-3 , 4);
delayn = 1; delayd = 1;
[loopn, loopd ] = series( delayn, delayd, gbackn, gbackd );

%               The Feedback Loop
[closen, closed] = feedback( openn, opend, loopn, loopd, 1 );

%               The Complete Transfer Function
[closen, closed] = series( gdacn, gdacd, closen, closed );

printsys( closen, closed, 's' );
dc

%printsys( openn, opend, 's' );
figure;
step(closen,closed);    % print step response
```

Appendix C - Schematic of Summing Junction, Integrator, and Differential Amplifier

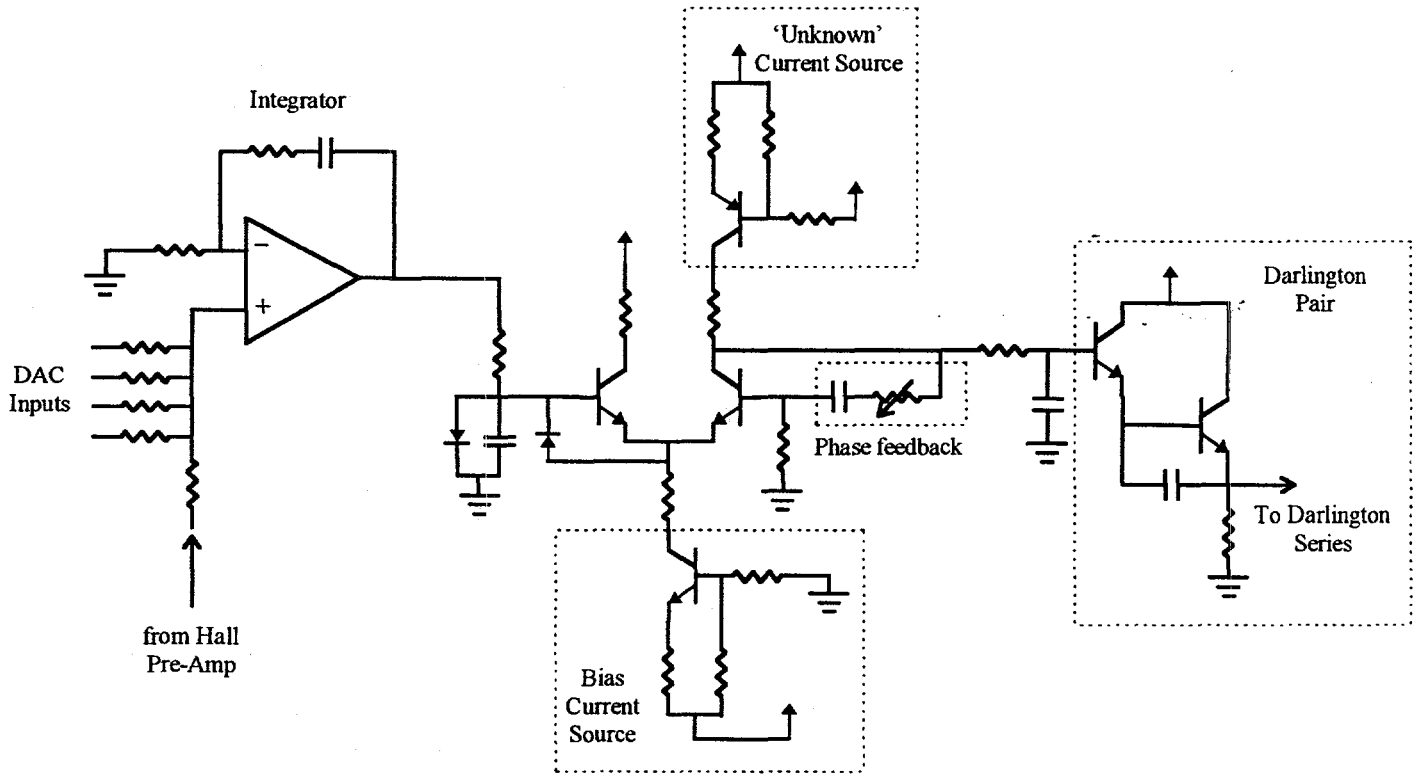

Appendix D - System Specifications for Beam Stability Measurements

Measurement taken Dec. 4, 1995 at 9:23am

Sample:	Al-Cu Grid
Mass width of c.d.	150 microns
Width of F.A. #2	62.5 microns (field of view)
Energy slit width	32.5V
Resolving power	3373
Entrance slit width	1-58
Exit slit width	2 x width of image
Primary beam	O^{16}-
Intensity of primary beam	1.170nA

Appendix E - System Transfer Functions

Block	Transfer Function
Integrator	$\frac{2.62e7(s+17.89)}{(s+1.074)(s+560.8)}$
Differential Amplifier	$\frac{c(s+n1)}{(s+d1)(s+d2)}$ The following coefficients are determined by the potentiometer setting (p) in ohms: $n1 = (-5.63e-7)p^2 + (4.54e-2)p - 9.10e2$ $d1 = (-1.49e-9)p^2 + (9.49e-5)p - 5.57$ $d2 = (-1.65e-8)p^2 + (4.14e-4)p - 1.01e3$ c must set the transfer function equal to 172 at $s = 0$.
Darlington Series	0.97
Magnet and Hall Probe	$\frac{-6.079e-4}{(s+2.4)}$
Hall Probe Pre-Amplifier	$\frac{9.32e6}{(s+798.5e3)}$

Study of the Retardation of VOCs in Ground Water*

Kimberly Bair

University of Florida

Lawrence Livermore National Laboratory
Livermore, California 94550

December 14, 1995

Prepared in partial fulfillment of the requirements of the Science and Engineering Research Semester under the direction of Fred Hoffman, Research Mentor, in the Lawrence Livermore National Laboratory.

* This research was supported in part by an appointment to the U.S. Department of Energy Science and Engineering Research Semester (hereinafter called SERS) program administrated by LLNL under Contract W-7405-Eng-48 with Lawrence Livermore National Laboratory.

CONTENTS

LIST OF ILLUSTRATIONS.....iii

INTRODUCTION.....1

METHODS
Column Experiment.....2

Diffusion Experiment.....2,5

RESULTS
Column experiment.....8

Diffusion experiment.....8,9

DISCUSSION.....9

SUMMARY.....10

REFERENCES.....11

ILLUSTRATIONS

FIGURES

1. Column Experiment Set-Up..... 3
2. Column Retardation Breakthrough And Cleanup Graphs at 4ml/hr.....4
3. Diffusion Experiment Set-Up.....6
4. Diffusion Vial Packing Method Set-Up.....7

TABLES

I. Column Experiment Results.....8

II. Diffusion Experiment Results.....9

Volatile Organic Compound (VOC) retardation in Ground Water.

Kimberly A. Bair
University of Florida
Environmental Restoration Division

Abstract

This project studies the mechanisms that cause the retardation of selected Volatile Organic Compounds (VOC) in ground water. Laboratory column and diffusion experiments were run in an effort to determine the contribution of each mechanism to the retarded flow of the VOCs. Retardation factors (Rf) , distribution coefficients (Kd) and apparent diffusion coefficients (Dd) were determined for four VOCs commonly found in ground water. Comparison of two separate column experiments at different velocities showedthat retardation is independent of flow velocity. Satisfactory results from the diffusion experiment show that the experimental procedures and apparatus proved to be successful.

INTRODUCTION

The remediation of ground water remains difficult due to the retardation or slowed movement of VOCs with respect to the movement of water. In an effort to gain a better understanding of the retardation of VOCs in ground water, experimental research is being conducted to determine the contributions of the various mechanisms causing retardation. According to Piwoni and Banerjee(1989) the absorption into organic sediments in soils, containing greater than 0.1% carbon, tends to dominate the retardation process thereby inhibiting the measurement of other contributors to this process.

This research is focused on adsorption to inorganic materials and diffusion into pore spaces containing immobile water. The use of low organic carbon materials (<0.1%) in the laboratory simplifies the experimental work and simulates the low organic carbon sediments beneath the LLNL Livermore Site. Four VOCs which commonly contaminate ground water were chosen; tetrachloroethylene (PCE), trichloroethylene (TCE), carbon tetrachloride(CCl_4) and chloroform($CHCl_3$). Retardation was measured by running column experiments to determine retardation factors (Rfs) and distribution coefficients (Kds) for the four VOCs. Apparent diffusion coefficients of the four VOCs were measured in a diffusion apparatus designed especially for this purpose. The measurement of the relative contribution of each of the mechanisms involved in the retardation of VOCs will further our understanding of the phenomenon and may inspire new and more effective cleanup technologies.

METHODS- COLUMN

Column experiments were run to determine Rfs and Kds of the four VOCs in ground water. Chloride was used as a conservative tracer and run through a H_2O saturated sand packed column along with a 250ppb solution of premixed VOCs at a rate of 4ml/hr (Figure-1). Influent and effluent samples were taken and analyzed for VOC chemical concentrations. The curves of the chloride tracer and the respective VOCs were then compared to determine breakthrough rates (Figure -2). The Rfs and Kds of the VOCs are calculated from the velocities of the chloride and the contaminant using the equation, taken from(Freeze and Cherry 1979) :

$$R = \frac{Vw}{Vc} = 1 + \frac{\rho b}{n}(Kd)^a$$

where,

Vw=Velocity of the water(Chloride)
Vc= Velocity of the contaminant

$\frac{\rho b}{n}$ = Bulk density of the sand divided by the porosity of the sand, since the same sand is used throughout the column this figure is constant and was calculated to be 5.625 cm^3/g

Kd = Distribution coefficient

The clean-up curves are determined from injecting clean water into the column after contamination. Effluent concentration samples are again taken and analyzed and the calculation process is repeated to determine the Rfs and Kds for the clean-up of the column. The experiment was repeated at twice the velocity (8ml/hr) and the same procedure was followed to determine Rfs and Kds. The results of the experiments are shown in (Table-1).

METHODS-DIFFUSION

For this experiment an instrument was specifically designed to measure the apparent diffusion and tortusity coefficients of the sand and the contaminants (Figure-3). The diffusion block contains 20 cylindrical slots where glass vials uniformly packed with unsieved Oklahoma(OK) #1 sand were placed. The block was covered with a fitted glass plate to prevent volatilization.

Retardation Experiment Setup

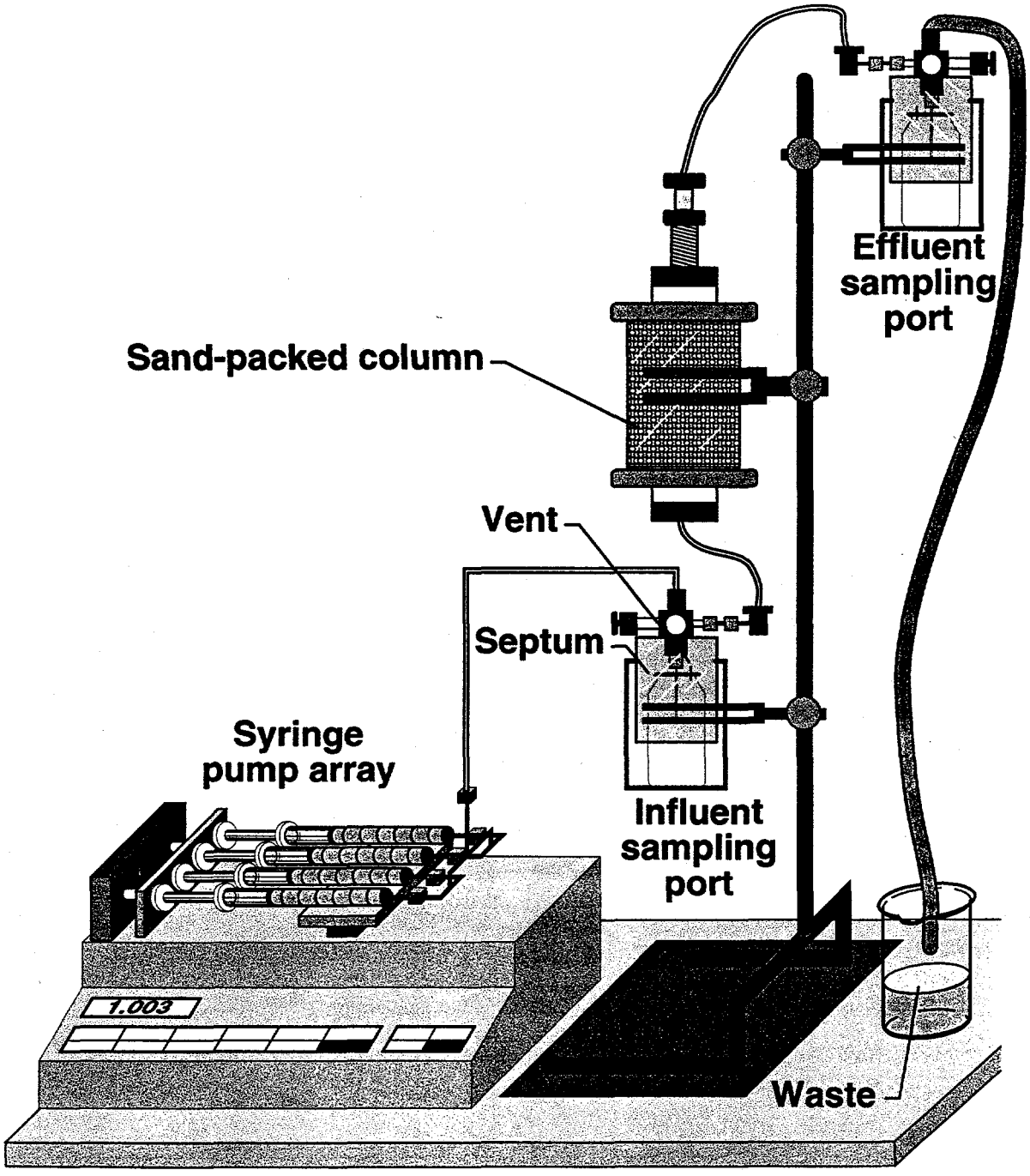

Figure 1. Rendering of the column experiment apparatus showing influent pump, column, and sampling ports.

Column Contaminant Curves

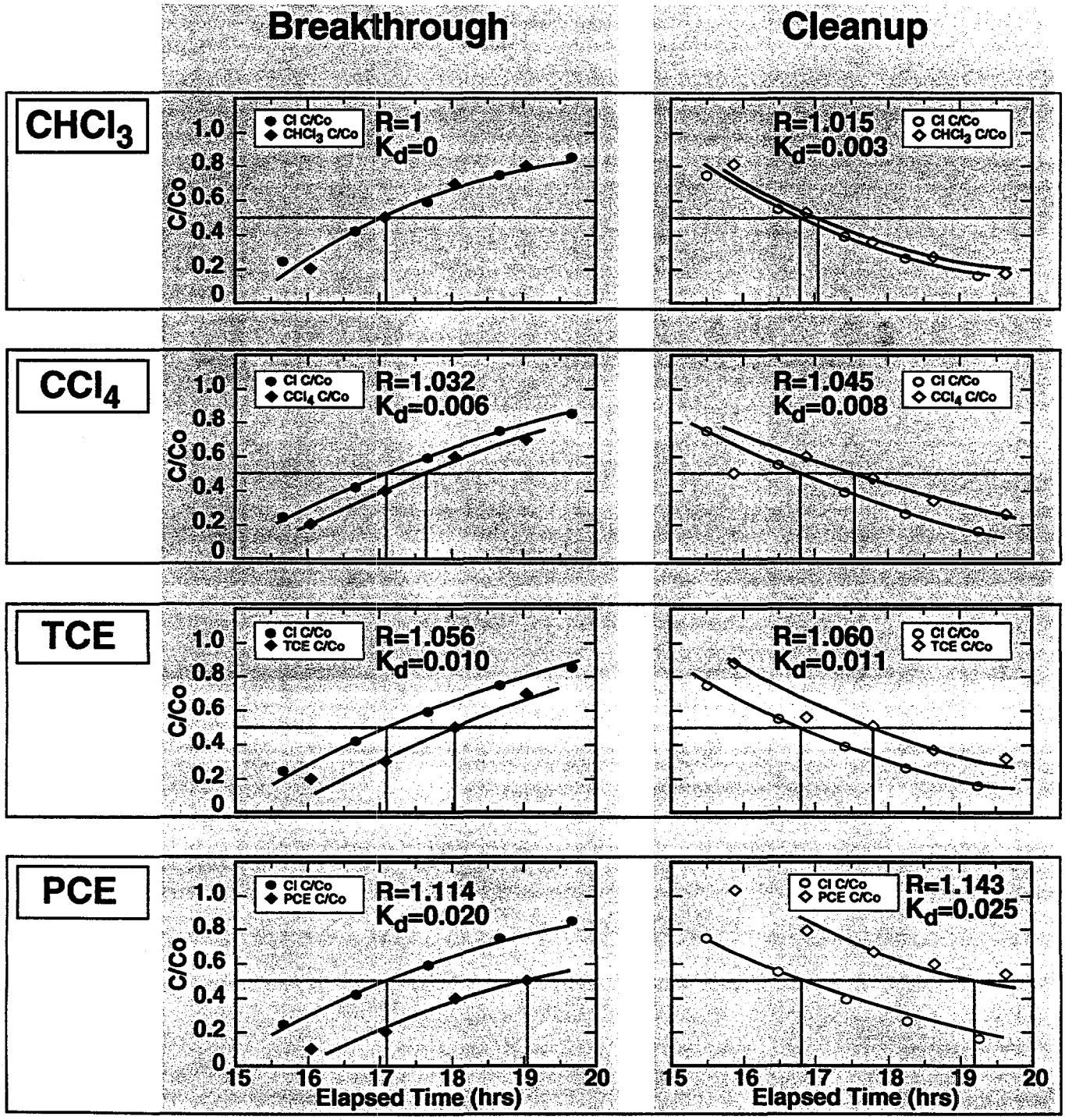

Figure 2. Comparison of Breakthrough and Cleanup curves for each of the contaminants and the tracer during the 4ml/hr run.

The Vials were packed uniformly using a method designed for this experiment. The method involved using a vial packing block and a shaker hooked into a CA valve turned to 1 Bar(15 psi) (Figure-4). From this method the Bulk density(ρb) and porosity (n) were determined for the OK#1 sand used in this experiment. A 250 ppb solution of VOCs was be passed over the vials containing the sand. After a specified amount of time the vials were removed and analyzed for the mass of each contaminant that had diffused into the vial. The mass of each VOC was compared with the results of a model which projects the mass in each vial based on the following equation from (Freeze and Cherry 1979):

$$\frac{C}{C_0} = ERFC\frac{x}{2\sqrt{D^*t}}$$

where,

C = Concentration at time t and location X

C_0 = Initial concentration

$ERFC$ = Complimentary error function

X = Distance at time t

D^* = Apparent diffusion coefficient

t = Time

Since $D^* = Dw(\omega)$

where,

D_w = Diffusion coefficient in water

ω = Tortuosity coefficient

Since the diffusion block contained 4 rows of 5 vials and each row had a separate syringe and solution it was necessary to take an average of daily concentrations for each row , this was the Co used in the model . For calculation purposes the average mass of each contaminant in each of the four rows was used instead of running the model numerous times. The tortuosity coefficient was adjusted in the model until the mass projected by the model equaled the mass reported from the experiment. The calculated tortuosity coefficient provided a measure of the ability of each

Diffusion Experiment Setup

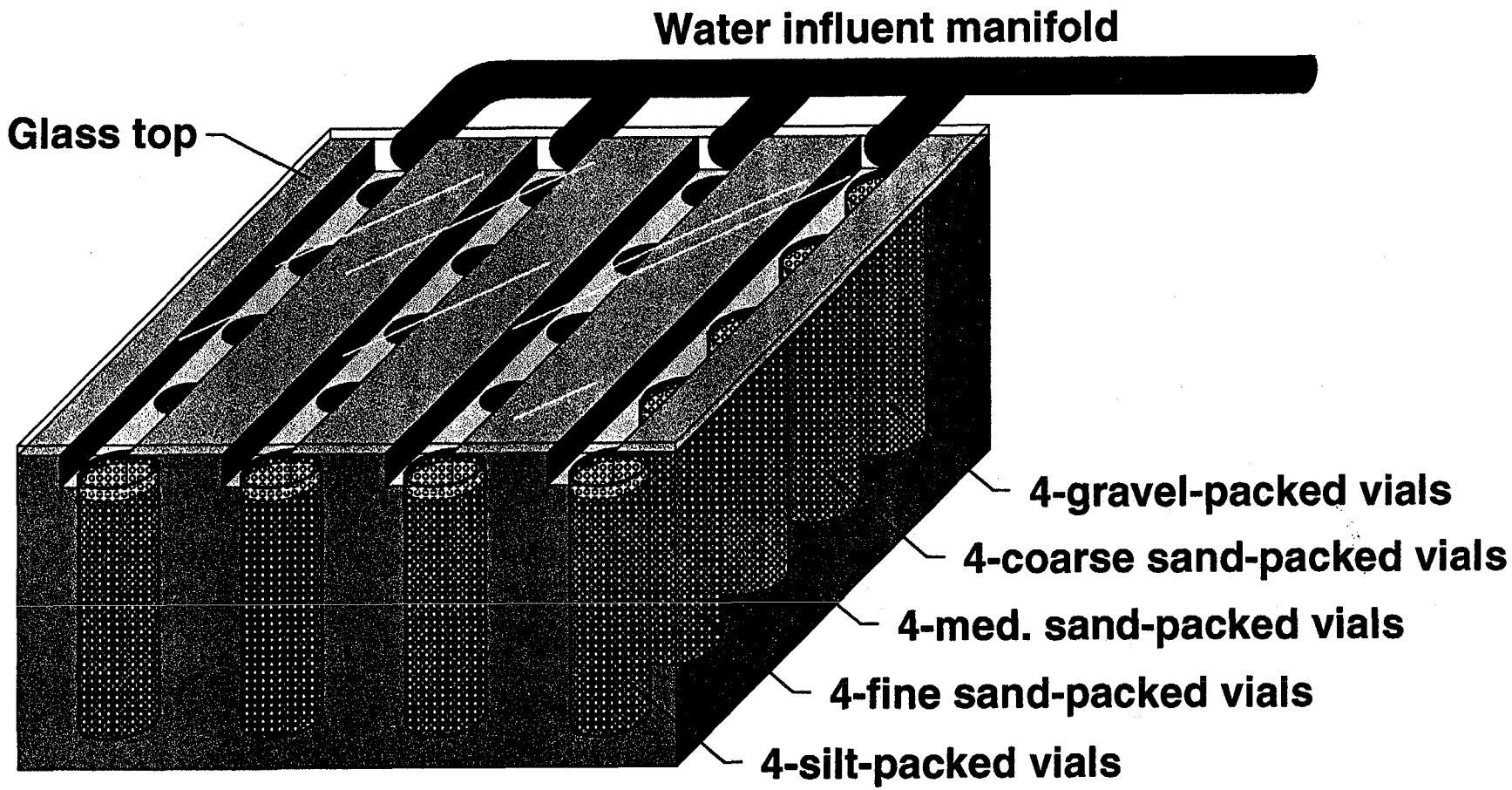

Figure 3. Diagram of influent line into diffusion block with sand packed vials.

Diffusion Vial Packing Method Setup

—Side View—

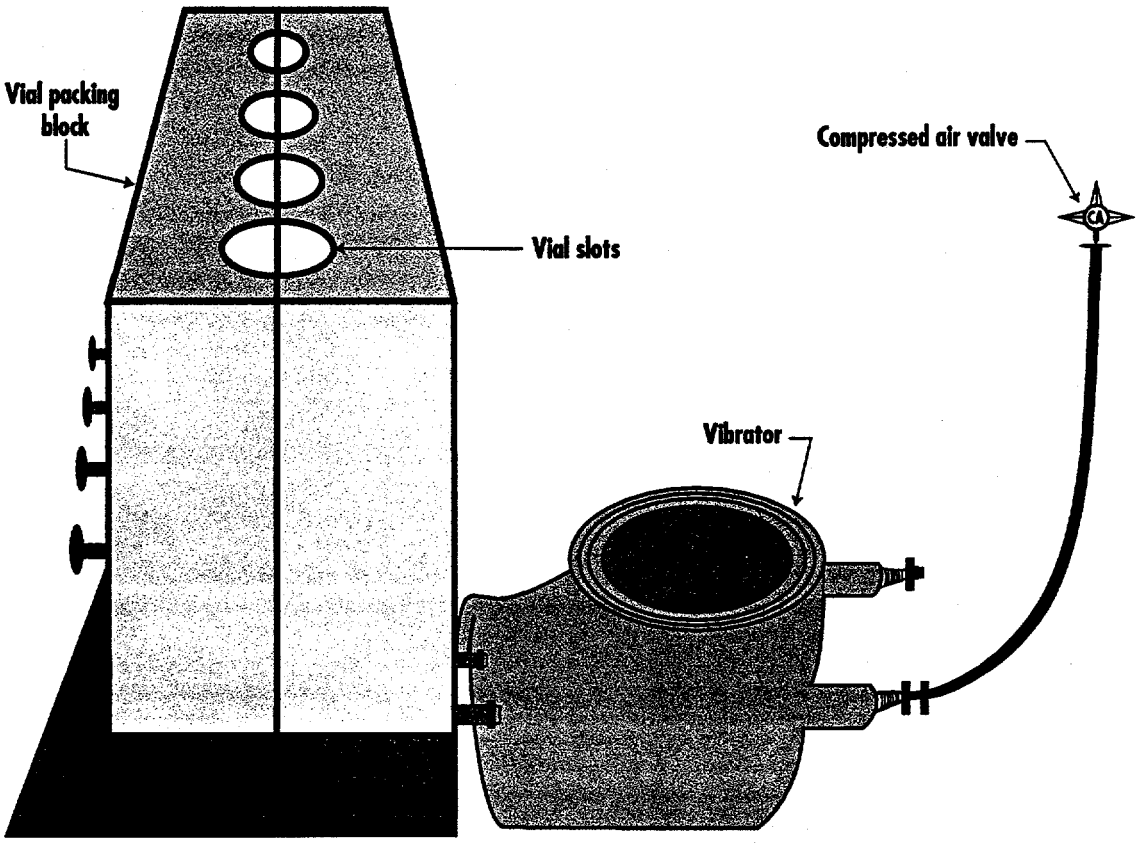

Figure 4. Vial packing setup includes: packing block, vibrator, and compressed air valve.

VOC to diffuse into pores containing immobile water. The modewas used to help us estimate the time for the first experiment: approximately two weeks

RESULTS

Column Experiment

Table I includes a comparison of the results obtained from each of the column experiments. The 4ml/hr run results are located on the left and the 8ml/hr results are located on the right. R= Retardation factor and Kd=Distribution coefficient.

Column Experiment Results (Table-I)

Chemical	R@4ml/hr	Kd@4ml/hr	R@8ml/hr	Kd@8ml/hr
BREAKTHROUGH				
CHCl3	1	0	1	0
CCl4	1.032	0.006	1.12	0.021
TCE	1.056	0.01	1.15	0.027
PCE	1.114	0.02	1.21	0.037
CLEANUP				
CHCl3	1.015	0.003	1.01	0.002
CCl4	1.045	0.008	1.003	0.0006
TCE	1.06	0.011	1.02	0.004
PCE	1.143	0.025	1.12	0.002

Diffusion Experiment

Table II indicates the results obtained from the diffusion experiment. It includes the average mass and daily influent C_0 of each conatminant per row. The average value for each contaminants tortuosity coefficient is located at the bottom of the table.

Diffusion Experiment Results (Table-II)

	CHCL3	CCL4	TCE	PCE
Mass Row D	360	262	309	261
Co Syringe #1 D	259	261	258	239
tortuosity coeff.	0.638	0.363	0.519	0.475
	CHCL3	CCL4	TCE	PCE
Mass Row C	325	282	305	263
Co Syringe #2 C	244	254	240	217
tortuosity coeff.	0.579	0.447	0.587	0.588
	CHCL3	CCL4	TCE	PCE
Mass Row B	312	283	294	249
Co Syringe #3 B	235	237	229	211
tortuosity coeff.	0.575	0.518	0.6	0.556
	CHCL3	CCL4	TCE	PCE
Mass Row A	334	251	300	258
Co Syringe #4 A	229	227	222	208
tortuosity coeff.	0.708	0.442	0.67	0.618
Average tort. coeff.	0.625	0.443	0.594	0.559

DISCUSSION

The first and second column experiments were compared and they indicate that retardation is independent of flow velocity, i.e. there was no significant change in the Rfs nor the Kds when the velocity was doubled for the breakthrough and the clean-up. The results of the two experiments are shown in figure I. The column experiments also showed that chloroform was not retarded. The diffusion model was used to evaluate the data obtained from the diffusion experiment. The tortuosity coefficient for each of the sediments was calculated with the model. Since chloroform was not found to be retarded in the column experiment, any deviation of the tortuosity coefficient calculated for the other VOCs can be considered to be a function of adsorption. The tortuosities of the VOCs decreased as adsorption of the chemicals increased. The actual tortuosity of the sand is .625 which is in complete agreement with values reported in the literature of Fetter (1992) This agreement and the expected results shows the experimental procedures and apparatus to be functioning properly. This experiment may result in a new way to determine Kds for VOCs in variable grain-size sediments.

Summary

The column experiment provided a measure of total retardation and Kds for all of the contaminants. The experiment led to the conclusion that $CHCL_3$ is not retarded in standard laboratory experiments containing low organic carbon materials(< 0.1%). The Rfs and Kds for the contaminants are independent of flow velocity according to the comparison of the column experiments at different velocities. More column experiments will be performed to quantify parameters. The diffusion experiment and model were used to obtain apparent diffusion coefficients for the contaminants . The unretarded flow of the chloroform allowed for the calculation of the tortuosity coefficient of the sand and contaminant and the results seem to be in agreement with previously cited literature. In the next diffusion experiment the OK#1 sand will be replaced with gravel, coarse, medium, fine and silt sizes of sand in an effort to determine the diffusion of the contaminants into sand of varying grain sizes.

BIBLIOGRAPHY

Fetter, C. W. 1992. Contaminant Hydrogeology, (Macmillan College Publishing Company,1994), pp44

Freeze, R. A and J.A. Cherry. 1979. Groundwater. (Pentice-Hall Inc., Englewood Cliffs, NJ.)104,404

Piwoni, Marvin D. and Banerjee, Pinaki. Sorption of volatile organic solvents from aqueous solution onto subsurface solids. Journal of Contaminant Hydrology, 4: 163-179 (1989)

TRANSPORT IN POROUS MEDIA*

Eric Dickenson

University of California at Davis

Lawrence Livermore National Laboratory
Livermore, California 94550

December 13, 1995

Prepare in partial fulfillment of the requirements of the Science and Engineering Research Semester under the direction of Dr. Mehdi Rashidi, Research Mentor, in the Lawrence Livermore National Laboratory.

* This research was supported in part by an appointment to the U.S. Department of Energy Science and Engineering Research Semester (hereinafter called SERS) program administrated by LLNL under Contract W-7405-Eng-48 with Lawrence Livermore National Laboratory.

TRANSPORT IN POROUS MEDIA

Eric Dickenson

Environmental Programs Directorate

ABSTRACT

A novel nonintrusive fluorescence imaging technique is used to study microscopic transport within porous media. The system consists of a column packed with heterogeneous-transparent particles and a refractive index-matched aqueous fluid seeded with fluorescent tracer particles or an organic dye. The flow through the column is illuminated by a planar sheet of laser beam and details of flow and transport through the porous regions can be observed microscopically and qualitative and quantitative transport information can be obtained. Various geometric, flow, and concentration quantities can be determined over a three dimensional volume within the column. The quantities include local and volumetrically averaged porosities, velocity and concentration fields, microscopic and volumetrically averaged dispersive fluxes and the dispersion coefficient. The qualitative and quantitative results will provide a better understanding for modeling of transport in porous media.

TABLE OF CONTENTS

		Page
I.	Introduction	1
II.	Experimental Methods	2
	Table 1. .Experimental Conditions	2
	Figure 1. Experimental Setup	3
	Figure 2. Fluorescence Imaging Configuration	4
	Figure 3. Intensities of dye concentrations at a wavelength of 514 nm	5
III.	Results	6
IV.	Discussion	6
V.	Conclusion	7
VI.	References	8

INTRODUCTION

The study of transport in porous media is of great importance in numerous industrial, environmental, and biological processes. The study has potential applications in series of chemical engineering processes, soil physics and contamination problems, petroleum recovery techniques, and biomedical systems.

This research is a combined theoretical and experimental measurement effort in order to improve our understanding of chemical transport in soils and other porous media. There have been past experimental attempts to measure macroscopic porous-medium properties (Schwartz and Smith, 1953; Harleman and Rumer, 1965; Han et. al., 1985). However, little research has been devoted to experimental observation and characterization of processes within the pore spaces themselves. Microscopic experimental observations of flow and transport behavior in natural, three-dimensional systems, are essentially nonexistent because of the difficulty of obtaining detailed dynamic measurements within the pore spaces of a real medium in a nonintrusive fashion. However, this project involves three-dimensional microscopic measurements of flow and chemical transport performed in a nonintrusive manner.

Both DOE and LLNL are interested in obtaining predictive information regarding the subsurface movement of contaminants and their treatment via bioremediation. Thus, the fundamental goal of the project is to investigate the microscale processes that govern contaminant/chemical transport in porous media to provide the basis for improved modeling of contaminant transport and treatment in natural porous systems.

EXPERIMENTAL METHODS

Experiments are performed in a clear polymethylmethacrylate (PMMA) plastic column of a width and length of 3.0 cm and a height of 7.0 cm. The column is filled with heterogeneous-transparent crystals of diameter approximately 0.15 cm. The system is saturated with an aqueous solution containing either fluorescent-latex microshperes for velocity experiments or fluorescent-organic dye for concentration experiments. Here the fluorescent microspheres and dye are the contaminants.

Before the initiation of experiments, the refractive index for the aqueous solution and crystals are matched at approximately 1.3920 at approximately 20°C and a wavelength of 514.5 nm using a refractometer and temperature control. The column is maintained at this constant temperature by being immersed in a circulating-constant-temperature bath as shown in Figure 1. The refractive index matching of the liquid and crystals allows the porous medium to be free from any scattering and refraction at the solid-liquid interfaces. As shown in Figure 1, the column is saturated with the aqueous solution using a syringe pump at a steady volumetric flow rate. The aqueous solution flows from the bottom to top of the column and the effluent flows to a tank (See Figure 1 & 2). The experiment entails performing six runs at different volumetric flow rates as shown in Table 1. Also, Table 1 lists the temperature, kinematic viscosity, crystal diameter and porosity for the six different runs.

Table 1. Experimental Conditions

Runs	Temperature $\cong$(°C)	Kinematic Viscosity (cm^2/s)	Crystal Diameter $\cong$(cm)	Porosity $\cong$	Volumetric Flow Rate (cm^3/s)
1	20	0.0381	0.15	0.4	0.00095
2	20	0.0381	0.15	0.4	0.00955
3	20	0.0381	0.15	0.4	0.0955
4	20	0.0381	0.15	0.4	0.192
5	20	0.0381	0.15	0.4	0.382
6	20	0.0381	0.15	0.4	0.765

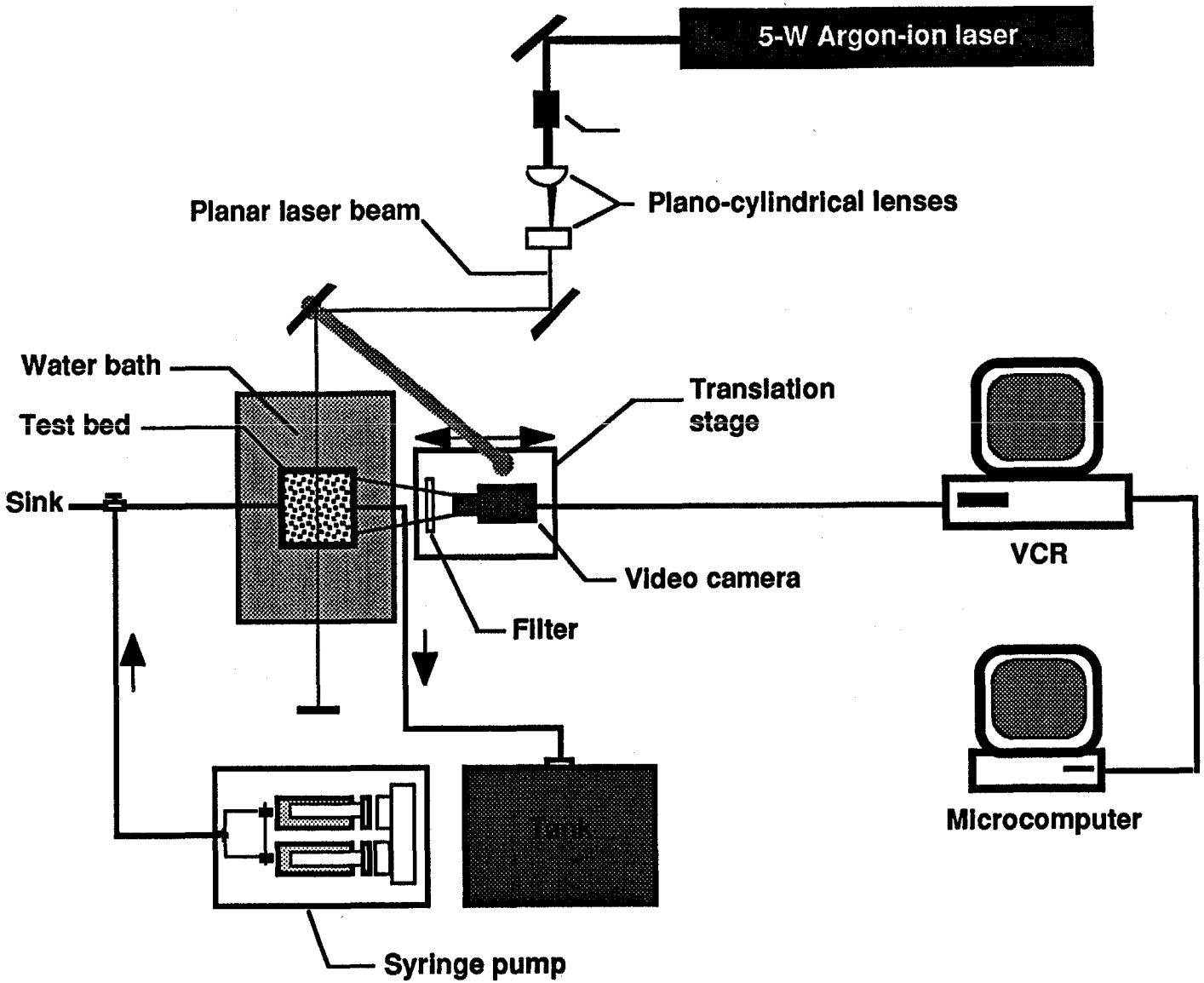

Figure 1. Experimental Setup

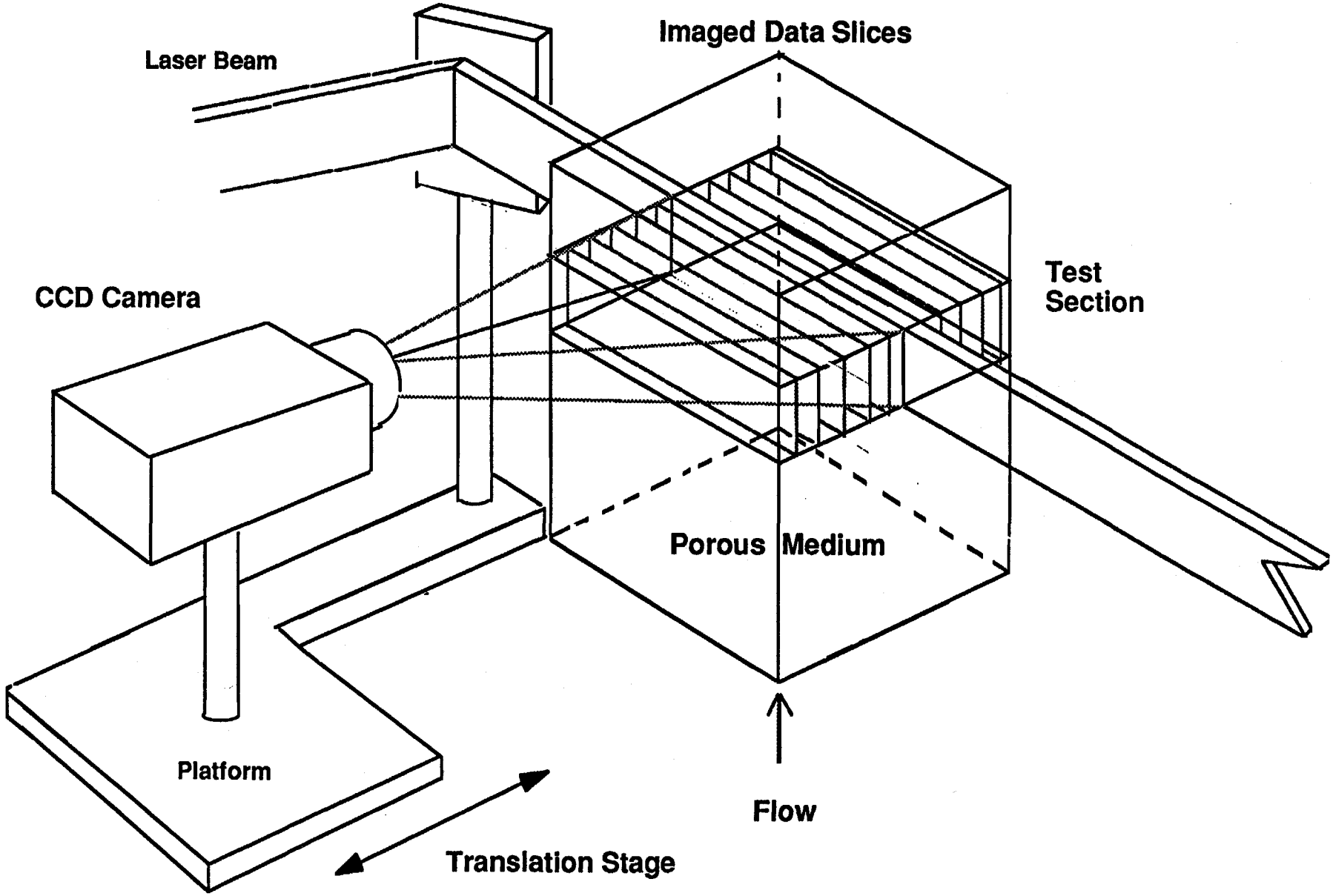

Figure 2. Fluorescence Imaging Configuration

During the experimental runs, planar sections of the observation are illuminated by a coherent Argon-ion laser beam (see Figure 2), operated at 475 nm for velocity measurements and 488 nm for concentration measurements. When illumination occurs, the fluorescent microspheres or dye fluoresces. A CCD camera records fluorescence images at 60 parallel-vertical cross-sections by sweeping back and forth across the column using a translation stage as shown in Figure 2. Approximately ten seconds is required to sweep through all 60 planes within the column. Measurements for each sweep are collected into aggregate blocks of data and used to approximate a snapshot of the system at a single time. At a given time up to 300,000 data points are taken.

The pore-velocity distribution is measured by tracking the motion of the seeded fluorescent microshperes on the 60 parallel vertical cross-sections. Following the velocimetry measurement, the fluorescent-organic dye is introduced and concentration distributions are measured. The dye fluoresces at different intensities and this intensity is correlated with the dye concentration using a fluorimeter. Differing dye concentraions are excited at 488 nm and the emission peaks around 514 nm. Intensities are measured at this wavelength. Figure 3 shows a linear relationship of the fluorescent-dye intensity and dye concentrations between 0-25 $\times 10^{-6}$M. The dye emission peaks at around 514 nm when it fluoresces, so a band pass filter is used on the video camera to pass a narrow range of 514.5 $\pm$5 nm.

Figure 3. Intensities of dye concentrations at a wavelength of 514 nm.

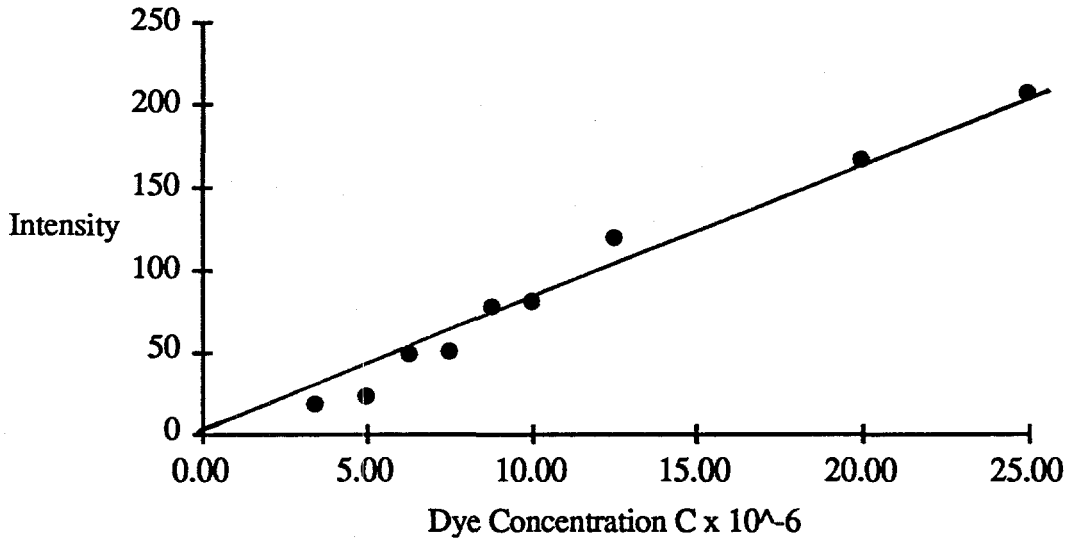

As shown in Figure 1, experimental images are recorded through the video camera by a computer controlled VCR in Hi-8 format. The velocity and concentration measurements are analyzed using image analysis programs developed in OPTMAS (BioScan) software.

RESULTS

The results of the experimental runs are in the process of being analyzed. The measured velocity and concentration fields will provide various geometry and transport quantities, such as volumetrically averaged porosities, microscopic and volumetrically averaged dispersive fluxes and the dispersion coefficient.

DISCUSSION

The liquid used in these experiments is an aqueous solution with sugar, however when the experimental project initiated the proposed liquid to be used differed. The initial liquid consisted of an aqueous solution with trifluoroethanol (CF_3CH_2OH). However, this solution causes polymethylmethacrylate (PMMA) to melt within ten minutes when in contact. Since the column is made of PMMA, the column would melt too if the trifluoroethanol was introduced to the system. The present sugar-aqueous solution does not negatively effect the PMMA column.

Since the liquid medium is water and sugar, the solution is viable for bacteria. Therefore, the measurement techniques used in the experiment will be applied to bacteria transport and this will provide new insight in bioremediation processes.

CONCLUSION

A novel nonintrusive fluorescence imaging technique is used to study microscopic transport within the porous media. Experiments were performed to measure velocity and concentration distributions. These results are being analyzed in order to evaluate volumetrically averaged porosities, velocity and concentration fields, microscopic and volumetrically averaged dispersive fluxes and the dispersion coefficient. This information will lead the next generation of transport models and make better predictions of chemical movement and biological treatment of contaminants in the subsurface.

REFERENCES

Han, N.W., Bhakta, J. and Carbonell R. G., 1985, Longitudinal and lateral dispersion in packed beds: Effect of column length and particle size distribution. *AIChE J.* **31**, 277-288.

Harleman, D. R. E. and Rumer, R. R., 1963, Longitudinal and lateral dispersion in an isotropic porous medium. *J. Fluid Mech.* **16**, 385-394.

Rashidi, M., Peurrung, L., Tompson, A., and Kulp, T., 1994, Experimental Analysis of Pore-Scale Flow and Transport in Porous Media. *Water Resources Research Journal*..

Schwartz, C. E. and Smith, J. M. 1953, Flow distribution in packed beds. *Ind. Eng. Chem.* **45**, 1209-1218.

Whitaker, S., 1986, Flow in porous media I: A theoretical derivation of Darcy's law. *Transport in Porous Media* **1**, 3-25.

Mapping Genes to Human Chromosome 19

Sarah Connolly
University of Illinois at Urbana-Champaign
Lawrence Livermore National Laboratory
Livermore, CA 94550
12/15/95

Prepared in partial fulfillment of the requirements of the Science and Engineering Research Semester under the direction of Dr. Greg Lennon, in the Lawrence Livermore National Laboratory

**This research was supported by an appointment to the U.S. Department of Energy Science and Engineering Research Semester program administered by LLNL under Contract W-7405-Eng-48 with Lawrence Livermore National Laboratory*

Abstract:

For this project, 23 Expressed Sequence Tags (ESTs) were fine mapped to regions of human chromosome 19. An EST is a short DNA sequence that occurs once in the genome and corresponds to a single expressed gene. ^{32}P-radiolabeled probes were made by polymerase chain reaction for each EST and hybridized to filters containing a chromosome 19-specific cosmid library. The location of the ESTs on the chromosome was determined by the location of the ordered cosmid to which the EST hybridized.

Of the 23 ESTs that were sublocalized, 6 correspond to known genes, and 17 correspond to anonymous genes. Five of the anonymous genes have shown strong homologies to other known genes. These localized ESTs may serve as potential candidates for disease genes, as well as detectable markers for future physical mapping.

Introduction:

Goals of the Human Genome Project:

The Human Genome Project is a large coordinated effort, aimed at constructing a detailed map of all three billion base pairs of human DNA. Among the goals of the Human Genome Project are to determine the exact sequence of the genome, to create DNA markers spaced throughout the chromosomes, and to identify the location the genes encoded by this sequence. Since only 10% of the entire genome is estimated to codes for genes, and approximately 100,000 genes reside in the genome, a fast and simple method of locating genes is critical. Identifying the location of genes will provide detectable markers for future physical mapping projects. The localized genes may also serve as candidate genes for various diseases when the approximate location of a diseases gene is known.

Lawrence Livermore National Laboratory focuses its genome effort on chromosome 19. Chromosome 19 is a small, gene-rich chromosome, estimated to contain about 2,000 genes. A high resolution physical map of chromosome 19 has been completed, covering approximately 95% of the chromosome with cosmids contigs. To date, approximately 250 genes have been assigned to these cosmids and mapped to chromosome 19. The mapping effort was continued in this study, with 23 genes more assigned to cosmids of chromosome 19.

Overview of Methods: cDNA mapping

Complementary DNA (cDNA) mapping is a quick method of gene identification and location. A cDNA is a copy of the protein encoding regions of a gene. cDNAs are constructed from mRNA templates in vitro using reverse transcriptase. mRNAs are valuable templates because each mRNA is a continuous stretch of protein-encoding nucleotides that corresponding to a single gene. Constructing a cDNA from an mRNA insures that the cDNA contains only coding information and that it corresponds to a single gene that is expressed in the specific tissue.

Once the cDNA has been made, it is placed in a vector and cloned. Primers are constructed that are capable of selectively amplifying a region of the cDNA by polymerase chain reaction (PCR). PCR is a method used to selectively amplify short regions of DNA. The cDNA primers are 20 base-pair sequences that complement specific regions near the ends of the cDNA sequence. These primers border a target region of the cDNA and allow polymerase to replicate the bordered region repeatedly. The replicated region is called an expressed sequence tag (EST). An EST is a short sequence of DNA that occurs only once in the genome and that corresponds to a single expressed gene. Because an EST sequence is unique in the genome, once it has been mapped to a chromosome it can serve as a physical marker on the chromosome.

Through PCR, the EST is amplified and radiolabeled with ^{32}P to make a probe. A probe is a short stretch of single-stranded DNA whose sequence is complementary to a unique portion of a targeted DNA sequence. The probe is hybridized against filters that contain a chromosome 19-specific cosmid library. Cosmids are 35,000 base pair

segments of chromosome 19 that have been ordered by EcoRI mapping and fluorescence in situ hybridization (FISH). Most of chromosome 19 can be represented by seven cosmid filters.

When a probe is exposed to these cosmid filters, it hybridizes to complementary sequences. The complementary sequence of a probe made from an EST exists in the gene that the EST originated from. The probe will bind to the cosmid that contains the gene, indicating where the gene is located. The hybridized cosmid filters are analyzed by PhosphoImager, and the location of the hybridized probe can be seen on an autoradiogram. The gridded array of the cosmids on the filters allows positive identification of which cosmid the probe hybridized to. The hybridization of the probe to a cosmid indicates that the target gene must be located within that cosmid. To verify the assignment of the gene to the cosmid, the cosmid DNA is used as a template in PCR amplification.

Characteristics of the identified positive cosmids can be found in LLNL databases. If the positive cosmid has been mapped to the chromosome, the location of the gene is known.

Materials and Methods:

(1)Construction of cDNA Primers:

Twenty-three cDNA oligonucleotide primer pairs were either designed during the course of this research or already available through the Genome Data Base. Reference numbers are given in Table 1. The primers were constructed to amplify specific EST sequences.

(2)Amplification of Gene Fragment by Polymerase Chain Reaction:

Using these primers, EST fragments were amplified from human placental DNA by polymerase chain reaction. A Perkin Elmer 9600 machine was used for all PCR reactions. For optimization of the PCR, 50µl reactions were performed using 100ng human placental template DNA, 40pm of each primer pair, 200mM dNTPs, 500mM KCl, 100mM Tris pH 8.3, 0.5 units of Taq polymerase, and varying concentrations of $MgCl_2$. The reactions were run through forty cycles of 94°C for 30 seconds, 54-65°C for 30 seconds, and 94°C for 30 seconds. The specific annealing temperatures (Tm) and $MgCl_2$ concentrations for each EST are given in Table 1.

PCR products were separated by gel electrophoresis on a 1.5% agarose gel with 50µg/µl ethidium bromide. The DNA fragments were visualized by ultra-violet fluorescence, and the sizes of the fragments were determined. The desired fragment was cut from the gel and placed in an eppendorf tube with 10µl of distilled water. The tubes were refrigerated for later use.

(3) Construction of Radiolabeled Probe:

A 25µl PCR radiolabeling reaction was performed using α^{32}P-labeled dCTP and the gel slice as the template. The PCR conditions were consistent with the original PCR conditions. The PCR products were purified using Worthington G-50 minispin columns.

(4) Hybridization of Probe to Cosmid Filters:

High density cosmid filters containing cosmid clones from chromosome 19 were prehybridized for at least two hours at 65°C in a hybridization solution that contained 4M NaCl, 0.5M EDTA, 1M Tris, 5% NA pyrophosphate, 50% dextran sulfate, and 20% SDS. 500µl salmon sperm DNA and 50µg Human Cot-1 DNA were added to block repetitive elements.

The radioactive probes were denatured to single-strands by boiling them for five minutes. They were added to the hybridization mixture and hybridized at 65°C overnight. The filters were then washed twice with a high stringency solution (0.1xSSC-0.1% SDS) for thirty minutes, and once with a low stringency solution (2xSSC-1% SDS) for thirty minutes.

The filters were wrapped and exposed to Molecular Dynamics PhosphoImager cassettes for at least one night. The cassettes were scanned and analyzed for identification of the cosmids positive for hybridizations.

(5) Verification by Polymerase Chain Reaction:

The hybridization of a probe to a cosmid was verified by PCR, using the cDNA primers and the cosmid DNA as template. A 50µl PCR was set up and the products were run through a 1.5% agarose gel. Amplification of a correctly sized fragment from the cosmid DNA served as proof that the EST mapped to that cosmid.

(6) Database Analysis:

The location of cosmids on the chromosome and other attributes of cosmids were available through the LLNL Browser program. This database includes links to information such as similarly EcoRI mapped contigs and cytogenetic band information as determined by FISH. If the positive cosmid was contained in a contig that had been FISH mapped, the location of the EST that hybridize to that cosmid was known.

A sequence homology search was run through the NCBI BLAST database for the anonymous genes to determine if the anonymous sequence matched the sequence of a known gene. Anonymous genes that lack a sequence accession numbers (see Table 2) were not run through BLAST because the sequences were not readily available. For the BLAST analysis, a score of over 200 was considered significant. Only the highest scoring homologous sequence was noted.

Results:

Six known genes and seventeen anonymous genes were mapped to the chromosome. Ten genes mapped to the q arm of chromosome 19 and seven mapped to the p arm, indicating no distinct distribution pattern. The six remaining genes were mapped to cosmids that have not yet been placed on the chromosome. Once these cosmids have been placed on the chromosome, the location of the six genes will be known. Figure 1 is an ideogram of human chromosome 19, showing the approximate locations of the ESTs. Table 2 lists the names of the genes and the cosmids to which each was assigned.

The BLAST search for sequence homologies revealed that five of the anonymous genes had strong matches to characterized genes. The names of the homologous genes and the extent of the homology are listed in Table 3. The nine other anonymous cDNA sequences that were sent through BLAST did not show strong homologies to known genes. These sequences can be considered segments of new, unique genes on chromosome 19.

Chromosome 19

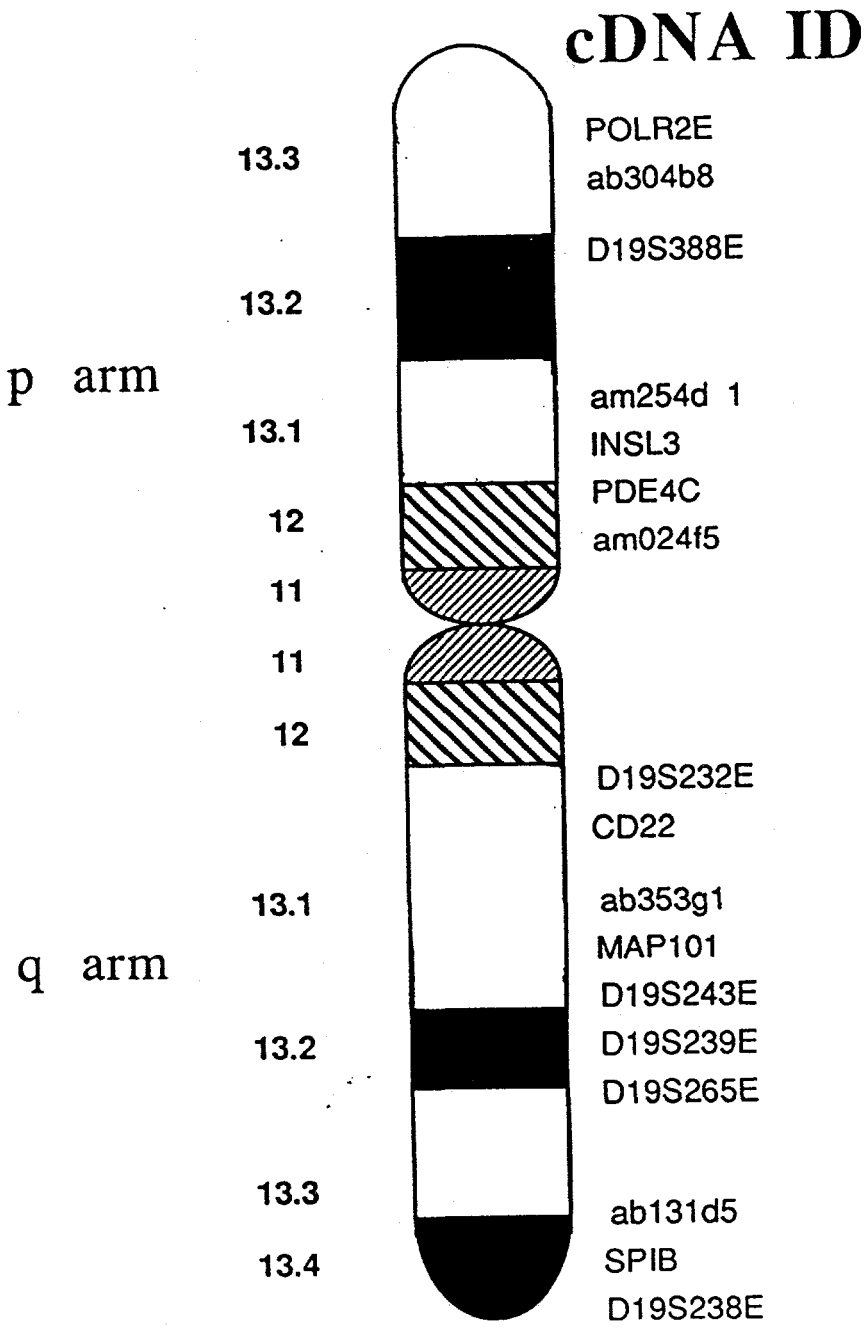

Figure 1: Ideogram of Chromosome 19

Locus	Sequence Accession Number	Genome Database Locus ID	Genome Database PCR probe ID	cDNA ID	Gene Name	Source of PCR Primers and GDB Reference numbers		PCR Optimization Conditions	
								Tm	[MgCl2]
D19S238E	M78256,M79273	G00-130-359	G00-189-000		Anonymous	Polymeropolous	G00-101-107	55	2.0mM
D19S239E	M78106	G00-130-220	G00-188-995		Anonymous	Polymeropolous	G00-101-107	55	2.0mM
D19S265E	M78736	G00-130-834	G00-191-600		Anonymous	Durkin	G00-042-878	60	2.0mM
D19S388E	M85728	G00-139-508	G00-198-958		Anonymous	Maglott	G00-043-830	60	2.0mM
D19S390E	M85570	G00-139-582	G00-199-032		Anonymous	Maglott	G00-043-830	60	2.0mM
D19S819E		G00-130-937	G00-581-496		Anonymous	Polymeropolous	G00-101-107	54	2.0mM
D19S243E		G00-133-968	G00-188-887		Anonymous	Polymeropolous	G00-101-107	55	2.0mM
ab353g1	H11320			47518	Anonymous-LLNL	LLNL		55	2.0mM
ab178c8	R40345			28807	Anonymous-LLNL	LLNL		60	2.0mM
am024f05	T54094, T54185				Anonymous-LLNL	LLNL		60	2.0mM
ab304b8	R59631,R59691			42233	Anonymous-LLNL	LLNL		60	2.0mM
ab389b11	H19436			51303	Anonymous-LLNL	LLNL		60	2.0mM
am254d1	R75610, R75700				Anonymous-LLNL	LLNL		60	2.0mM
ab321b12	H06151,H06152			44051	Anonymous-LLNL	LLNL		60	2.0mM
ab131d5	T77499,R38383			23804	Anonymous-LLNL	LLNL		60	2.0mM
D19S232E		G00-133-858	G00-188-874		Anonymous	Polymeropolous	G00-101-107	60	1.0 mM
D19S234E	M62234	G00-122-882	G00-188-890		Anonymous	Polymeropolous	G00-101-107	55	1.5 mM
CD22-		G00-127-545			CD22 antigen	LLNL		60	2.0mM
INSL3		G00-230-307			Insulin-like 3 (Leydig cell)	LLNL		60	2.0mM
PDE4C	Z46632	G00-132-539			Phosphodiesterase 4C, cAMP specific	LLNL		60	2.0mM
POLR2E		G00-250-743			Polymerase (RNA) II polypeptide E	LLNL		60	2.0mM
SPIB		G00-374-517			Spi-B transcription factor	LLNL		60	2.0mM
MAP101					Map 101	Ross, David		60	1.0 mM

Table 1: References and PCR Conditions

Locus/EST	Location on Chromosome	Positive Cosmid IDs
D19S238E	19q13.4	24602, 25446, 16251
D19S239E	19q13.2	16651, 24533, 25361
D19S265E	19q13.2	26165, 26630, 26834, 27577, 28943, 30006, 30012, 30563, 31696, 32336
D19S388E	19p13.2-13.3	20259
D19S390E		25056
D19S819E		17025
D19S243E	19q13.2	18930, 23864, 24762, 25796
ab353g1	19q13.1	31418, 31710
ab178c8		21915
am024f05	19p12-13.1	29957, 30465, 30777, 31164, 31165, 33114, 34330
ab304b8	19p13.3	21834, 22077
ab389b11		22115
am254d1	19p13.1	16351
ab321b12		15616
ab131d5	19q13.3-13.4	16450
D19S232E	19q13.11	20520, 21363
D19S234E		22986, 24563
CD22-	19q13.1	16661, 18534, 18536, 24202
INSL3	19p13.2-p12	19847, 25186, 25196
PDE4C	19p12-13.1	19896, 22037
POLR2E	19p13.3	15978, 23821
SPIB	19q13.3-q13.4	20372, 24917
MAP101	19q13.1	16584, 19754, 24590

Table 2: EST Locations

Locus	Homologous Gene Name	GDB ID	SCORE
ab321b12	Human Natural Killer Cell Enhancing Factor	L19185	1632
D19S239E	H. sapiens HZF4 mRNA for Zinc Finger	X78927	1433
D19S388E	Human Interleukin 11	M81890	810
ab131d5	Human Tristetraproline mRNA	M63625	703
D19S238E	Human Retinoblastoma Susceptability	L11910	264

Table 3: BLAST search results

Conclusions:

The twenty-three ESTs that were localized to chromosome 19 in this study may now serve as detectable landmarks on the physical map of the chromosome. The mapping of these ESTs will aid in further physical mapping projects. ESTs can be used to find pairs of overlapping clones in the construction of contig maps of chromosomes. In addition, the anonymous ESTs may serve as candidate genes for various diseases when the approximate location of a disease gene has been determined by genetic linkage techniques. Further study is needed to determine the location of the six genes that mapped to cosmids that were not currently mapped to the chromosome. The homologies found for five of the anonymous genes may deserve further inquiry also. Eventually, a metric ordering of these ESTs will be determined, based on the locations of these cosmids on the chromosome.

References:

Cooper, Necia ed. (1992) *Los Alamos Science: The Human Genome Project* . Number 20: 108-140.

Mohrenweiser, H.W., S.Tsuijimoto, K. Tynan, J. Lamerdin, and A.V. Carrano (1995) Unique sequence STSs for 21 cytogenetically mapped loci on human chromosome 19. *Cytogenet Cell Genet* **71:** 58-61.

Mohenrenweiser HW, Swartz A, Johnson K: *Report of the Committe on the Genetic Constitution of Chromosome 19 in Cuicchia AJ, Pearson PL (eds):Human Gene Mapping 1993*, pp.575-597 (Johns Hopkins University Press, Baltimore 1994).

Pappas, George J., Michael H. Polymeropolous, John M. Boyle, and Jeffery M. Trent (1995) Regional Assignment by Hybrid Mapping of 36 Expressed Sequence Tags (ESTs) on Human Chromosome 6. *Genomics* **25:** 124-128.

Directly incorporating fluorochromes into DNA probes by PCR increases the efficience of fluorescence *in situ* hybridization*

Joy Dittmer

Indiana University - Purdue University
Fort Wayne, Indiana 46805

Lawrence Livermore National Laboratory
Livermore, California 94550

12/13/95

Prepare in partial fulfillment of the requirements of the Science and Engineering Research Semester under the direction of Joe Lucas, Research mentor, in the Lawrence Livermore National Laboratory.

*This research was supported in part by an appointment to the U.S. Department of Energy Science and Engineering Research Semester (hereinafter called SERS) program administered by LLNL under Contract W-7405-Eng-48 with Lawrence Livermore National Laboratory.

Directly Incorporating Fluorochromes into DNA Probes by PCR Increases the efficiency of fluorescence *in situ* hybridization

Joy Dittmer
Indiana University - Purdue University at Fort Wayne
Division: Health Ecological Assessment
Mentor: Joe Lucas

Abstract

The object of this study was to produce a directly labeled whole chromosome probe in a Degenerative Oligonucleotide Primed-Polymerase Chain Reaction (DOP-PCR) that will identify chromosome breaks, deletions, inversions and translocations caused by radiation damage. In this study we amplified flow sorted chromosome 19 using DOP-PCR. The product was then subjected to a secondary DOP-PCR amplification. After the secondary amplification the DOP-PCR product was directly labeled in a tertiary PCR reaction with rhodamine conjugated with dUTP (FluoroRed) to produce a DNA fluorescent probe. The probe was then hybridized to human metaphase lymphocytes on slides, washed and counterstained with 4',6-diamino-2-phenylindole (DAPI). The signal of the FluoroRed probe was then compared to a signal of a probe labeled with biotin and stained with avidin-fluorescein isothiocyanate (FITC) and anti-avidin (FITC).

The results show that the probe labeled with FluoroRed gave signals as bright as the probe with biotin labeling. The FluoroRed probe had less noise than the biotin labeled probe. Therefore, a directly labeled probe has been successfully produced in a DOP-PCR reaction. In the future a probe labeled with FluoroRed will be produced instead of a probe labeled with biotin to increase efficiency and reduce noise.

Introduction

Fluorescence *in situ* hybridization (FISH) is a technique which allows visual identification of specific chromosomes or portions of chromosomes through fluorescence microscopy. This technique is performed using a DNA probe specific for a desired chromosome and a glass slide which contains a spread of metaphase chromosomes that are prepared by standard cytogenetic methods. The probe is a short piece of DNA, usually between 300-500 base pairs, which is produced from flow sorted chromosomes. Both the target DNA and the probe are denatured by heating which causes the melting of the DNA double helix. The target DNA and the probe are mixed and the strands are allowed to recombine. The probe reanneals to the target at locations where the base pairs are complementary, forming a double stranded hybrid molecule. Usually the probe is an indirectly labeled probe which requires excess washing and staining. But in this experiment the DNA probes are directly incorporated with fluorochrome conjugated bases. Using directly labeled probes decreases the effort required for post-hybridization washings and omits the time consuming staining process that is required for an indirectly labeled probe.

Materials and Methods

The chromosomes were flow sorted and isolated as described previously (Breneman et al., 1993). Briefly, chromosomes were stained with two fluorescent dyes, Hoechst 33258 (HO) and Chromomycin A 3 (CA3). The dyes caused the chromosomes to fluoresce differently when passed through a dual-laser cell sorter, producing a bi-variant, HO vs CA3 flow karyotype. The dye in the chromosomes excited differently because the size and base-pair composition of each chromosome is different. The chromosomes were then

flow sorted at a rate of 5-10/sec. One thousand chromosomes were sorted into each PCR tube.

Metaphase slides were prepared by the method of Evans et al., (1971). Briefly T lymphocytes were cultured from whole blood, arrested in metaphase with colcemid, harvested and fixed to glass slides with 3:1 methanol/acetic acid.

Whole chromosome probes were prepared using flow sorted chromosomes that were amplified by DOP-PCR. The primer (5'OHCCGACTCGAGNNNNNN NATGTGGOH-3') used was a 22 mer universal primer with a 6 nucleotide long degenerated region that represents all possible 6 nucleotide combinations. For the initial amplification the flow sorted chromosomes served as a template and were combined with the following: 50 ul 2 x Master Mix (25 U Taq DNA polymerase in 20mM Tris HCl, 100 mM KCl, 3mM $MgCl_2$, Brij®35, 0.01% (v/v), 0.4mM dATP, 0.4mM dGTP, 0.4mM dCTP, 0.4mM dTTP, final pH 8.3) 5 ul (40 uM) DOP-PCR primer, 45 ul water (Boehringer Mannheim). PCR was performed on a 480 thermal cycle as follows: 5 minutes at 95°C followed by 5 cycles of 1 minute at 94°C, 1.5 minute at 30°C, a 3 minute transition from 30-72°C and a 3 minute extension at 72°C. This was followed by 35 cycles of 1 minute at 94°C, 1 minute at 62°C and 2 minute at 72°C. Followed by a 7 minute extension at 72°C (Telenius et al., 1992). A secondary DOP-PCR was performed using the conditions described above and the following reagents: 50 ul Master Mix, 5 ul DOP-PCR primer, 2 ul primary template, and 43 ul water.

The DOP-PCR fragments were either directly labeled in a tertiary DOP-PCR reaction that contained fluorochromes or by random priming. The fragments that were directly labeled in a tertiary DOP-PCR reaction used the conditions described above and the following reagents: 5 ul 10 x buffer (Perkin Elmer), 2.5 ul 40 uM DOP-PCR primer, 30.5 ul water, 5 ul secondary template,

5.5 ul dNTPs with FluoroRed(200 uM each of dATP, dCTP, and dGTP, 100uM dTTP plus 0.04nM of FluoroRed), 1.5 ul Taq. The total reaction volume was 50 ul. The DOP-PCR fragments were indirectly labeled by random priming using the BioPrime DNA labeling system (Gibco BRL) to prepare biotinylated. That was done by combining 25-100ng of DNA with 19 ul of water and denaturing the solution for 5 minutes at 100°C. Immediately following the denaturing 5 ul of 10 x dNTP, 20 ul of 2.5 x random primers solution, and 4 ul of water was added. This mixture was mixed briefly and then 1 ul of Klenow fragment (40 U/ul) was added. This solution was incubated for 1-4 hours at 37°C. Then 5 ul of stop buffer was added to stop the reaction.

The hybridization was performed as described previously (Lucas et al., 1992). Briefly, metaphase chromosomes were denatured in 70% formamide, 2 x SSC at 70°C for 2-10 minutes. The slides were then dehydrated in a 70-85-100 % ethanol series and air dried. The probe mix was prepared by combining 2 ul of probe, 7 ul of probe master mix (50% formamide, 10% dextran sulfate, 2 x SSC, pH 7.0), and 1 ul cot-1 DNA. This probe mix was denatured for 5 minutes at 70°C. The probe mix was applied to a slide, covered with cover glass and sealed with rubber cement. The slide was then placed in a 37 °C incubator overnight. The cover glass was then removed and the slide was washed three times at 45°C in 50 % formamide/2xSSC, pH 7, once in 2xSSC and once in PN buffer. The slide was washed in each solution for 5 minutes. The directly labeled probe was then counterstained with DAPI, covered with cover glass and viewed under a fluorescent microscope (see figures 1 and 2). The probe that was indirectly labeled by random priming had to be stained with one layer of FITC-conjugated avidin and one layer of anti-avidin-FITC. (Avidin and anti-avidin were obtained from Vector Laboratories Inc., Burlingame CA.) The indirectly labeled probe was then counterstained with

DAPI, covered with cover glass and viewed under a fluorescent microscope (see figures 3 and 4).

Results

In this experiment our objective was to produce a directly labeled whole chromosomes probe in a DOP-PCR reaction. We began the experiment trying to indirectly label using bio-16-dUTP in a PCR reaction. But we never obtained a good, clean signal using biotin conjugated to dUTP. The next thing we tried was directly labeling with FluoroGreen (fluoroscein-11-dUTP) in a PCR reaction. Again, we never obtained a good, bright, clean signal using FluoroGreen. However, the signal obtained using FluoroGreen was brighter and cleaner than the signal obtained when the biotinylated probe was used. The final type of fluorochrome that we tried was FluoroRed. When FluoroRed was attached to the probe in PCR the signal was bright and clean. The next experiment conducted was to determine the optimal amount of FluoroRed needed for each reaction. We tried using the following ratios of FluoroRed to dTTP: 1:5, 1:6 and 1:7. Both the 1:5 and the 1:6 ratio had good clean signals. We concluded that the 1:6 ratio was more cost efficient, because the signal looked the same, but used less FluoroRed. Finally, we compared a directly labeled FluoroRed probe, generated by PCR, to an indirectly biotinylated probe generated by random priming. We compared the signal that each probe gave. The probe with FluoroRed gave a good, bright, clean signal with less noise than the indirectly biotinylated probe.

Discussion

Directly labeling the probe in PCR was more efficient than random priming of DOP-PCR products. Directly labeling the probe in PCR eliminates the time required for random priming (1-4 hours) and for staining the slide (2-3 hours.). One disadvantage to directly labeling in PCR was that another

PCR program was required to label the DNA. Another, more important, advantage to the use of fluorochrome-labeled DNA was that when hybridized it produced less noise (non-specific signals) than biotin labeled probes. Therefore, a directly labeled probe has been successfully produced in a DOP-PCR reaction. In the future a probe labeled with FluoroRed will be produced instead of a probe labeled with biotin to increase efficiency and reduce noise.

Acknowledgments

I would like to thank Francesca Hill for her guidance and friendship. I would also like to thank Joe Lucas for supervising the project; Tore Straume and Hung He for their technical assistance; and Lynn Wilder for her encouragement. This work was performed under the U.S. Department of Energy, Science and Engineering Semester program administered by Lawrence Livermore National Laboratory under contract W - 7405-Eng-48.

References

Breneman J., Ramsey M., Lee D., Eveleth G., Minkler J., Tucker J. (1993) The development of chromosome-specific composite DNA probes for the mouse and their application to chromosome painting. *Chromosoma* 102 : 591-598

Evans J., Buckton K., Hamilton G., Carothers A. (1979) Radiation-induced chromosome aberrations in nuclear-dockyard workers. *Nature* 277 : 531-534

Lucas J., Awa A., Straume T., Poggensee M., Kodama Y., Nakano M., Ohtaki K, Weier H., Pinkel D., Gray J., Littlefield G. (1992) Rapid translocation frequency analysis in humans decades after exposure to ionizing radiation. *International Journal of Radiation Biology* 62 : 53-63

Telenius H., Pelmear A., Tunnacliffe A., Carter N., Behmel A., Malcolm A., Ferguson-Smith M., Nordenskjold M., Pfragner R., Ponder B. (1992)

Cytogenetic analysis by chromosome painting using DOP-PCR amplified flow-sorted chromosomes. *Genes, Chromosomes & Cancer* 4 : 257-263

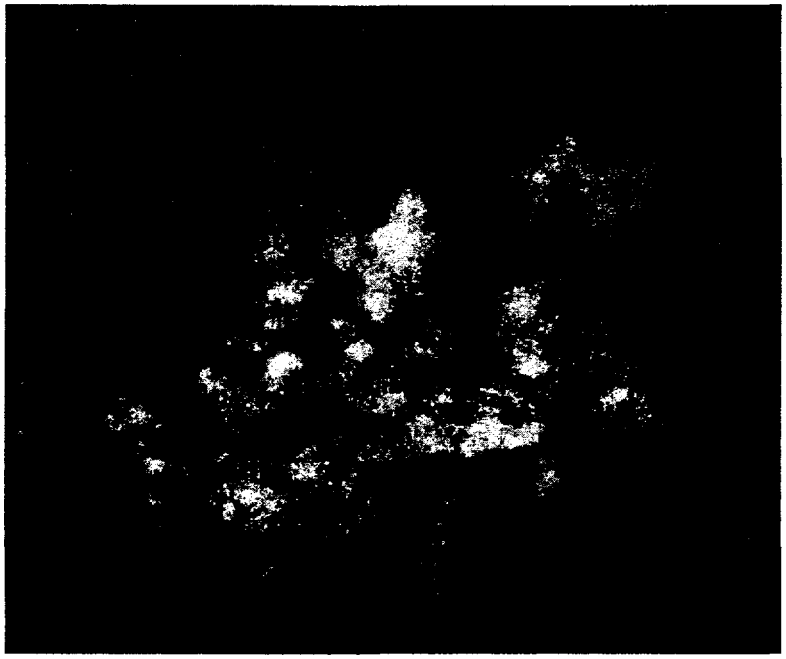

Figure # 1:

Metaphase spread hybridized with DOP-PCR chromosome 19 that was directly labeled in PCR with FluoroRed.

Figure # 2:

Metaphase spread hybridized with DOP-PCR chromosome 19 that was directly labeled in PCR with FluoroRed .

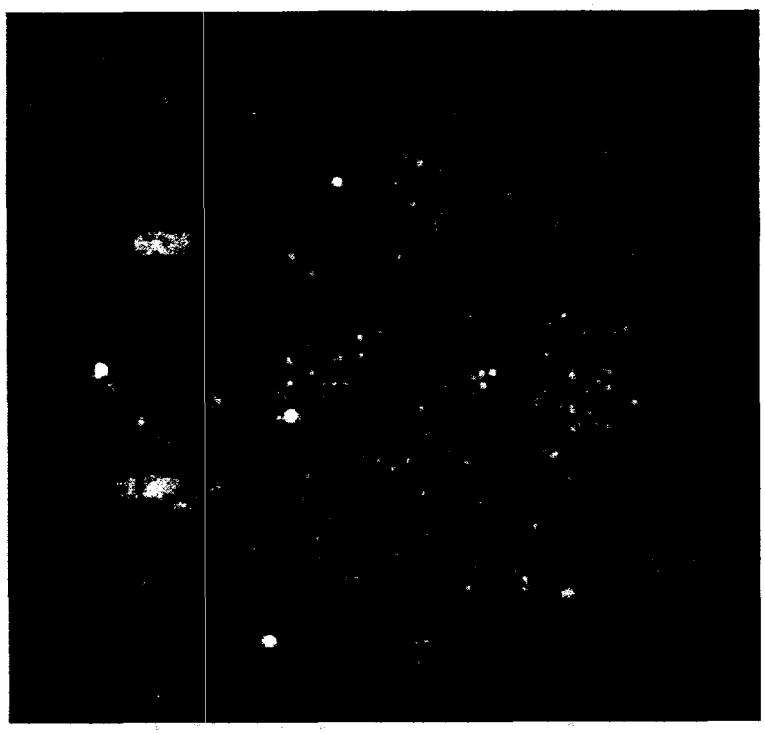

Figure # 3:

Metaphase spread hybridized with DOP-PCR chromosome 19 that was biotinylated.

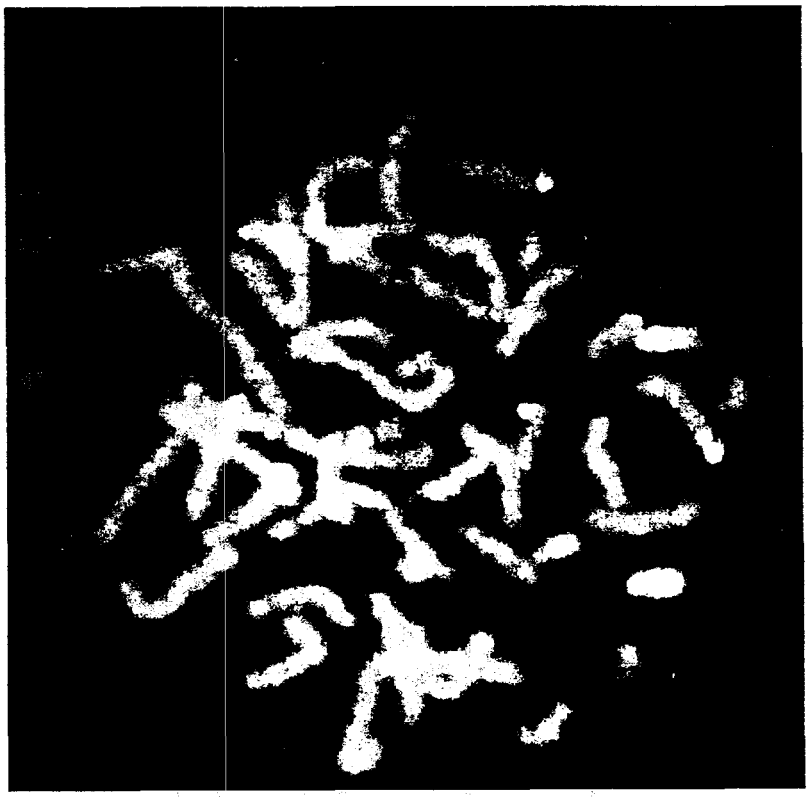

Figure # 4:

Metaphase spread hybridized with DOP-PCR chromosome 19 that was biotinylated.

A Beam Vectoring Trigger for E910.*

David Jaffe
U.C. - Riverside

Lawrence Livermore National Laboratory
Livermore, CA 94550

Prepared in partial fulfillment of the requirements of the Science and Engineering Research Semester under the direction of Dr. Ron Soltz, Research Mentor, in the Lawrence Livermore National Laboratory.

* This work was supported in part by an appointment to the U.S. Department of Energy Science and Engineering Research Semester (hereinafter called SERS) program administered by LLNL under Contract W-7405-Eng-48 with Lawrence Livermore National Laboratory.

I. Introduction.

From a hardware perspective, e910 is comprised primarily of the EOS TPC, along with several wire chambers and TOF walls. To discriminate between interacting and non-interacting protons, the trigger will use data readout from three wire chambers to characterize a track of the proton as it traverses the experimental apparatus. Chambers 1 and 2 (my designations) are located upstream of the target and magnet. Data from these instruments tell us the origin and initial momenta of the incoming protons. Chamber 3 is located downstream of the target, just inside the magnet. A hit on this chamber tells us what the trajectory of the proton was after it passed through the gold foil. If the proton doesn't interact with the gold foil, then its trajectory is simply a function of its initial position and momenta, and the magnetic field. Using this fact we can construct a simple, low level trigger to detect these non-interacting protons. Based on the data from chambers 1 and 2, we calculate where the proton will hit chamber 3, *if it does not interact.* If the actual hit matches the predicted hit, we know that the proton did not interact, and we veto the event. There is a slight probability that a particle produced in an interaction will give us an erroneous veto by hitting chamber 3 in the location we expect a non-interacting proton, but it is low enough to be acceptable. To implement this trigger, we need a very fast way of

comparing the hits on chambers 1 and 2 to hits on chamber 3, and deciding whether or not the proton interacted. And so we have decided to do all of these calculations in advance, using the software simulator "e910gx". By running thousands of non-interacting protons through the simulator, we can create a table of possible trajectories for non-interacting protons of expected initial positions and momenta. The trigger can then simply compare its hit data to that in the table and make a quick comparison.

II. E910gx.

The e910gx simulator contains a complete experimental setup, that can be modified by adding, removing, or moving the various detectors. More importantly, it gives the user complete control of all physics processes involved in the experiment. For our purposes, we have turned all interaction and decay processes off. This way we are sure that the trajectories we get through the simulator are all those of non-interacting particles. We have modified the original e910gx code to include two COMIS hooks. These hooks can be set by the user to point to user defined COMIS routines. The first of these hooks, "cs_event", is executed at the beginning of every event, and is used to define the particle type, and its initial position and momenta. The second, "cs_step", is executed at the end

of every step of the particle as it traverses the experiment. These hooks are defined from the e910gx command line as follows:

e910gx> cs_event COMIS_event_routine.f

e910gx> cs_step COMIS_step_routine.f

III. Software.

In order to actually use e910gx and create the lookup table, I have written the following FORTRAN programs, including the COMIS routines that correspond to the above mentioned hooks:

particles.f

jaf_event.f

jaf_step.f

jaf_out.f

assignwires.f

spreads.f

All of these files are documented in the following sections.

A. Particles.f.

The program particles.f generates a text file called "10000particles" containing the initial particle data, i.e. particle type, initial position, and

initial momenta, with one particle's worth of data per line. At present there are 10000 particles worth of data in this file, hence the name. Each line is formatted like so:

gpid ox oy oz px py pz

The integer gpid is the GEANT particle ID code. Here it is set to 14, for protons. But this data is not used. The variables ox, oy, and oz are real, and are the coordinates of the particle vertex (initial position) in cm. The variables px, py, and pz are also real, and are the initial momenta of the protons in GeV. At the gold foil target, we wanted the beam to be a 4 mm square spot with momenta ranging from -0.1 to 0.1 in the x and y directions, and 18.4 to 18.6 in the z direction. So the program first defines the target position and momenta randomly from within these ranges, and then calculates a corresponding initial position, with oz defined to be -420 for all particles. The number of particles generated, the ranges of allowed momenta, and oz, are all parameterized for easy modification.

B. Jaf_event.f.

Jaf_event.f is the COMIS routine I wrote to correspond with the hook cs_event.f. This routine is executed at the beginning of each event. The first time it is called, it allocates memory for future HBOOK operations via

a call to HLIMIT, and opens the file "10000particles". It then, and for each subsequent call, reads in a line of data from that file and tells e910gx the initial position and momenta of the input particle. At this point the particle is defined as a proton, by defining the mass and charge numbers (A, and Z) to be 1. The variable gpid is not used. WARNING: since there are only 10000 particles worth of data in the input file, no more than 10000 protons may be fired in a single run.

C. Jaf_step.f.

Jaf_step.f is the COMIS routine that corresponds to the hook cs_step. This routine is called after each step that the protons take on their trajectory through the experiment. The first time it is called, it opens a new file "jaf.ntup", and books a column-wise Ntuple. This Ntuple stores the event number, track number, and initial momenta of each proton, as well as the exact position of the proton when it hits each of the three wire chambers. For each step, jaf_step.f first determines if this is the first step of a new proton. If so, the event and track numbers are defined, along with the initial momenta. It then determines whether the proton has crossed a chamber in the last step. If so, exactly where it hit the chamber is calculated and stored in the Ntuple. The z-positions of the chambers are defined here and parameterized for easy relocation.

D. Jaf_out.f.

At the end of each run, this COMIS routine is called to save the Ntuple to the file "jaf.ntup", and close both it and the file "10000particles".

E. Assignwires.f.

This FORTRAN program takes the position data of the wire chamber hits in the Ntuple, and calculates wire numbers. This data is added to the Ntuple as a new variable. The wire pitches, and center wire number are parameterized for easy modification.

F. Spreads.f.

This is the final program that actually creates the lookup table we need for our trigger. This program goes through the Ntuple, and calculates a range of possible wire hits, or spread, on chamber 3 for each pair of wire hits on chambers 1 and 2. Once we have these spreads, we need but store them in a new file, and we have our lookup table. As of yet, a format has not been defined for this table. But once we have the needed data, the actual creation of the table is pretty trivial.

IV. Conclusion.

All of these programs, along with their corresponding makefiles, are located on the physgi0x computers at Brookhaven National Laboratory in the ~jaffe/run910 directory. In the same directory is a script file "jaf_run.inp". Using this file, the user can, in one command, start e910gx, define the COMIS hooks, and start a run, resulting in a filled Ntuple, containing the position data of the wire chamber hits. The user then runs assignwires and spreads, and the lookup table is created in three commands. Each of these programs is extensively documented internally to aid in their use and modification by other users.

Virtual Supercomputering on Macintosh Desktop Computers

Ken Krovchuck
Wayne State University
Computations Department - LLNL

Prepared in partial fulfillment of the requirements of the Science and Engineering Research Semester under the direction of John Wade, Research Mentor, in the Lawrence Livermore National Laboratory.

*This research was supported in part by an appointment to the U.S. Department of Energy and Engineering Research Semester (hereinafter called SERS) program administered by LLNL under Contract W-7405-Eng-48 with Lawrence Livermore National Laboratory.

Abstract. Many computing problems of today require supercomputer performance, but do not justify the costs needed to run such applications on supercomputers. In order to fill this need, networks of high-end workstations are often linked together to act as a single virtual parallel supercomputer. This project attempts to develop software that will allow less expensive 'desktop' computers to emulate a parallel supercomputer. To demonstrate the viability of the software, it is being integrated with *POV*, a retracing package that is both computationally expensive and easily modified for parallel systems.

The software was developed using the MetroWerks CodeWarrier Version 6.0 compiler on a Power Macintosh 7500 computer. The software is designed to run on a cluster of Power Macs running system 7.1 or greater on an ethernet network. Currently, because of limitations of both the operating system and the Metrowerks compiler, the software is forced to make use of slower, high level communication interfaces. Both the operating system and the compiler software are under revision however, and these revisions will increase the performance of the system as a whole.

December 12, 1995
Revision 2

Introduction

The wide availability of networked desktop computers has made them a viable option to supercomputers. The power of a large numbers of small computers can be combined to provide speeds comparable to larger, more expensive parallel computers. The maximum speed, however, is limited by the bandwidth of the network, and is also a function of the type of application involved.

Currently, several library interfaces are available for Unix workstations that allow them to emulate a parallel machine. A very popular and freely available interface is known as PVM, or Parallel Virtual Machine. This interface has been ported to supercomputers such as the Cray T3D. Since it is available on both workstations and supercomputers, programmers are able to test and debug code on the less expensive workstations, and then run the production version on a supercomputer. PVM is not available for Macintosh desktop computers. These computers are more widely available than Unix workstations in many workplaces The newer models also provide nearly the same computational power, particularly with respect to floating point operations.

This paper will describe the initial development of a software package designed to create a virtual parallel machine when run across a network of Macintosh computers. This software is called the Parallel Chicken Interface[1], hereafter referred to as PCI. As a proof of concept, this software was combined with a ray tracing package called Pov-Ray. The result, called Parallel Pov, distributes the ray-tracing processes across a network, significantly improving the time required to complete a ray-traced image.

AppleTalk

The Macintosh OS provides networking support through an interface and specification known as AppleTalk. AppleTalk provides an interface to the network, insulating applications from the type of network used, whether it be ethernet, a token network, or other network standard. AppleTalk provides both a low level interface and higher level interfaces to the network. The low level interface simply provides a method to send and receive packets over the network. There is

[1] This name comes from a common analogy used to describe parallel computers, A supercomputer, (the bull) is able to do much more work than a single parallel processor (the chicken), but given a large number of chickens, the total work that can be done can exceed that of the bull.

no checking to see if the packets actually arrive, or arrive more than once. Order of the packets is also not guaranteed. This interface, known as Data Delivery Protocol, or DDP, is also the fastest method of sending packets, (excluding calls made directly to the network hardware). The high level interfaces provide error checking, and packet ordering. They also allow data to be sent as bidirectional streams. These interfaces are known as ADSP, (AppleTalk Data Stream Protocol) and ASDSP (AppleTalk Secure Data Stream Protocol) . Using DDP requires procedures that are called during interrupt time, this in turn requires that the procedures have assembly language entry and exit points which save and restore the CPU registers. This code must be emulated 68020 code on the Power Macintosh computers. The compiler used to develop the PCI software , (MetroWerks CodeWarrier 6.0,) does not allow mixing of 680xx assembly language with PPC601 C language code. In order to utilize the speed of the Power Macintosh computers, applications must used the native, PPC601 instruction set. This has forced the initial version of PCI to use the slower, (but simpler) ADSP AppleTalk interface.

Preemptive Threads

Prior to the introduction of a high speed, RISC based Macintosh computer (Power Macintosh), Apple Computer developed a OS extension known as the thread manager. The thread manager allowed for both cooperative, and preemptive threads. The thread manager does not support preemptive threads on the new Power Macintosh computers, however. Also, a new OS extension, OpenDoc, is being developed that will not be compatible with multithreaded programs. This has led Apple Computer to withdraw support for the preemptive capability of the thread manager and to only support cooperative threads. Cooperative threads require that a program make an explicit call in order for tasks to be switched. Threads must also be executing in the same program space; threads cannot yield time to other processes running on the same machine. This leaves little reason for PCI to make use of threads. Instead, PCI uses a polling loop to determine what process needs to be serviced next. If no process needs service, PCI yields time to other programs running on the machine, which is handled by a mechanism that is separate from the thread manager.

The next version of the Macintosh operating system will allow true, preemptive multitasking. PCI could be updated to use that mechanism at that time, if it proves to be more efficient.

PCI.

PCI, in its final form, will be a library interface that can be linked with programs that wish to use a parallel architecture. It will provide a message passing interface which is purposely similar to the ones provided by PVM and MPI. The similarity will allow programs (or at least their algorithms) to be ported to a Macintosh platform running PCI. Also, many supercomputers are designed to make use of message passing software, and a similar interface to the MPI standard would allow PCI programs, or even PCI itself, to be easily ported to large parallel machines. The PCI interface consists mostly of Send and Receive calls, which are use for the passing of messages to other processes. Other procedures would be provided for the spawning and killing of tasks, determining the ID of a task, and for sending and receiving blocking messages, etc.

The current version of PCI is implemented only enough to allow for the development of Parallel Pov. This was done so that the limitations of the hardware and Mac OS could be well understood before the interface design was frozen. Currently PCI provides for sending and receiving of non-blocking messages to any other process, but does not allow for multicasts. Also, process creation and destruction are not implemented. A small library for building lists of processes is provided, which allows for easier handling of multiple tasks in a non-preemptive environment.

Parallel Pov

Parallel Pov, developed as a test program for PCI, is organized around a master-slave architecture. Two separate programs exist. The pov-master, and one or more pov-slaves. The pov-master is the only program that actually interacts with the user. The pov-slaves, except for initial startup, are controlled internally by the pov-master. There can be up to 254 pov-slaves running simultaneously, though the bandwidth of the network will probably make this impractical.

The general operation of the pov-master program is the same as the original Pov-Ray program, where the user cycles through phases of editing the text description file of the scene to be

rendered, and actually rendering the scene. The internal operation of both the pov-master and the pov-slave is considerably different from Pov-Ray.

When a pov-slave program first starts up, it calls routines from PCI which initialize the network interface, and publish the identity of the application to the network. The program then finishes its normal initialization, and makes an asynchronous call instructing the operating system to wait for a connection request. The program waits at this point until the pov-master establishes a connection with it.

When the pov-master program first starts, it scans the network looking for any other program that identifies itself as type 'chick', which corresponds to pov-slave processes which published their identity during initialization. Since this scan is currently done only at startup, all of the pov-slave programs must be started before pov-master is started, otherwise they will be ignored by the pov-master program. Once the identity of all of the processes is received, the master opens a connection with each of those processes (one per pov-slave).

A different list is maintained for each of the different possible states that a processes might be in. Whenever a response is received from a process , it is moved to the list that corresponds to its new state, for example, a process that responds to a connection request would be moved from the WaitingToConnect list to the ReadyForCommand list. Every network call is made in asynchronous mode, a feature of the Macintosh operating system that allows the program to continue operation while the network call is taking place (true multitasking is not available with this OS). The master program polls the status of each of these calls, and responds to them only when they have been completed by the operating system. This allows the master program to service the slave processes in an arbitrary order.

When the user has finished editing the image description file and issues a render command, the master slave program parses the file looking for syntax errors, and if there are none, sends a copy of the text file across the network to each slave process. It also sends a copy of the currently selected options. Once a process has received a copy of the description file, the master sends it a set of coordinates describing the area that needs to be rendered. Each slave process renders a

different portion of the image, and returns the result. The master then assembles these pieces into the final image. Theoretically, a speed up that is linear to the number of processors involved is possible, though the top speed of the network, and the constant time spent parsing the data file will reduce the overall speed of the system. Ray tracing is an ideal parallel processing job, since the bulk of the processing time is spent rendering pixels, and the computations for each pixel are independent of neighboring pixels. It was for these reasons that the application was chosen as an initial test-bed for the PCI software.

Implementing Parallel Pov

Even though Parallel-Pov was selected for its easy modification, some portions of the code have proven to be difficult to port to PCI. For example, Pov-Ray provides a mechanism to increase the quality of an image though anti-aliasing. For anti-aliasing to work, whenever a pixel differs significantly from either the pixel to the left of it or above it, that pixel is resampled. Resampling is done at random points very close to to the original pixel. These points are then averaged together to determine the new value of the pixel. The adjacent pixel that caused the anti-aliasing is also resampled. This has the effect of blending the color of the two pixels together, and reduces the jagged edges commonly seen on rasterized images. For PCI however, adjacent pixels are not necessarily known by the process that is calculating the current pixel. That process must also be able to change the value of the neighboring pixel. The most obvious solution to this problem would be to have the process send a message to the appropriate process asking for the value of the pixel. The sending process would then be forced to wait for an answer, or wait for the other process to actually calculate the value of that pixel. Both of these solutions can seriously degrade the performance of the rendering. A better solution would be for the process to ignore the anti-aliasing completely, and allow a separate, clean up process to scan areas that have already been completely rendered, and determine if any of those pixels need to be anti-aliased. That process would be able to adjust the pixels without waiting for any other task to complete.

Another difficulty in implementation occurs with the parsing of the file. Before rendering of the image begins, the text file describing the image is parsed and converted into a structure more

usable by the ray tracing engine. Currently, this process is executed redundantly by each process. The algorithm used by Pov-Ray is not yet fully understood (by the author of PCI, at least), and the resulting data structure the parser produces is complex. Also, the parsing is not easily separated into discrete, separate tasks. Attempting to distribute the work would result in a large amount of message passing that would easily bottleneck the network. Instead, the entire text of the description file is sent to each process. The size of the description file is less than the resulting data structure, so transmission of the text can actually be faster that the transmission of the data structure. The current method was chosen for its simplicity of implementation. The other options should be more fully investigated, however, before any final solution is determined.

A third problem in modifying Pov-Ray results from the memory requirements of the rendering. While rendering, each pixel is saved as a set of 4 double precision values, for red, green, blue, and alpha channel data. For large images, this results in a very large buffer to hold all of the pixel values. Pov-Ray does not actually do this. Instead, only the enough information to allow for anti-aliasing to work is held in memory. This is the current and previous line rendered. Once one line is rendered it is stored onto disk and the memory is released. Ideally, Parallel-Pov would store the entire frame buffer. Since each process can return image data at varying times (the time required to render a pixel is not constant), some data can arrive out of sequence with other data. Storing the entire frame buffer allows for easy resequencing of the data. If memory requirements do not allow for this, virtual memory can be used, or synchronization points can be set up where all processes wait until a line of the image is completely rendered. Both of these options would slow the rendering process. The current version of Parallel-Pov buffers the entire image, but the pixel data is reduced to the accuracy of the displaying monitor, which is significantly less than four double float values normally stored.

The development of PCI and Parallel Pov has shown that a virtual machine interface for desktop computers is indeed possible, though the performance of such a system is not yet competitive with existing workstation implementations. This situation may change once the Macintosh platform is more fully ported to the RISC architecture, and emulated calls to the networking interface are no longer necessary. Continued development of PCI would provide an excellent

experimental platform for designing parallel programming models, however. Problems that PCI and other message passing systems such as PVM do not address are the problems with parallel programming itself. Programmers are still forced to deal with the complexities of balancing the work load across the different processes evenly. This is partly due to the fact that these PCI and PVM are interfaces to C language programs, a language that was never designed for parallel computing. Development in this area is needed in order for parallel programs to be written in a more productive way.

Boron, Beryllium, and Lithium Partitioning in Olivine*

Elizabeth Neroda

Occidental College
Departments of Chemistry and Geology

Earth Sciences and IGPP-GEO Divisions
Lawrence Livermore National Laboratory
Livermore, California 94550

This paper was prepared in partial fulfillment of the requirements of the Science and Engineering Research Semester under the direction of Frederick Ryerson, James Brenan, and Henry Shaw, Research Mentors, in the Lawrence Livermore National Laboratory.

* This research was supported in part by an appointment to the U.S. Department of Energy Science and Engineering Research Semester (herein after called SERS) program administered by LLNL under Contract W-7405-Eng-48 with Lawrence Livermore National Laboratory.

ABSTRACT

A one atmosphere experimental study was performed to determine the mineral/melt partition coefficients for B, Be, and Li in forsteritic olivine. Two compositions were chosen along the 1350°C isotherm of the forsterite-albite-anorthite ternary phase diagram, 1b ($Fo_{17.3}$ $Ab_{82.7}$ An_0, by weight) and 8c (Fo_{30} $Ab_{23.3}$ $An_{47.8}$, by weight) were then combined in equal amounts to form a third composition. Each composition was doped with 25ppm Li, B, Yb, Nb, Zr, Sr, and Hf, 50ppm Sm, and 100ppm Be, Nd, Ce, and Rb. Electron and ion microprobe analyses showed that the olivine crystals and surrounding glasses were homogeneous with respect to major and trace elements. Partition coefficients calculated from these analyses are as follows:

1b: D_B = 4.41 (± 2.3) E-03, D_{Be} = 2.86 (± 0.45) E-03, D_{Li} = 1.54 (± 0.21) E-01,

50/50: D_B = 2.83 (± 0.5) E-03, D_{Be} = 2.07 (± 0.09) E-03, D_{Li} = 1.51 (± 0.18) E-01,

8c: D_B = 6.05 (± 1.5) E-03, D_{Be} = 1.81 (± 0.03) E-03, DLi = 1.31 (± 0.09) E-01.

The results of this study will be combined with similar data for other minerals as part of a larger study to understand the partitioning behavior of B, Be, and Li in melting of the upper mantle at subduction zones.

INTRODUCTION

Convergent plate boundaries are the primary area of interest in studying the mass and chemical recycling processes of the Earth. At mid-ocean ridges oceanic crust is formed by up welling of the mantle. As the crust moves away from the ridge it reacts hydrothermally with the ocean incorporating water into its structure and layers of sediment are deposited on top of it. When the altered oceanic crust and sediments are subducted into the mantle, they dehydrate releasing a chemical rich fluid into the overlying mantle wedge. The influx of this fluid into the mantle lowers its melting point, and approximately 10-20% of the mantle melts. The melt and fluid, rise to the surface and are erupted at island arc volcanoes. (Figure 1)

Boron, beryllium, and lithium are enriched in oceanic sediments and altered oceanic crust relative to their abundance in the mantle. (Figure 2) ^{10}Be is created by cosmic ray interactions with the atmosphere, it is extracted from the atmosphere and incorporated into clay-rich oceanic sediments. Due to ^{10}Be's short half-life of 1.5Myr, both the mantle and oceanic crust are essentially ^{10}Be-free. All three elements are found in arc volcanics indicating that there is a sediment derived component in island arc magmas. The ratio of B/Be is a commonly used geochemical indicator of this slab contribution. The B/Be ratios measured in arc volcanics are assumed to be preserved from the original slab fluid, and not altered or fractionated in any way by the mantle. The goal of this study was to determine how olivine, the main constituent of the mantle, partitions these three elements.

EXPERIMENTAL

Starting Compositions

Starting materials were chosen to be representative of basaltic compositions. Two compositions were chosen along the 1350°C isotherm of the forsterite-albite-anorthite ternary phase diagram of WATSON (1977) (Figure 3). These compositions were chosen so that the

experiment would be temperature independent and compositionally dependent. The two compositions 1b ($Fo_{17.3}$ $Ab_{82.7}$ An_0, by weight) and 8c (Fo_{30} $Ab_{23.3}$ $An_{47.8}$, by weight) were synthesized by repeated fusion and grinding of an initial oxide/carbonate mix. Equal portions of the two starting materials were combined to make a third (50/50) composition. Trace elements (Be, Yb, Nb, Zr, Sr, Hf, Sm, Nd, Ce, and Rb in dilute HNO_3, Li as Li_2CO_3 in HCl) were added to the glasses and ground under ethanol then dried at 400°C. Boron (as H_3BO_3 in H_20) was added after drying to prevent B vaporization.

Liquidus Determinations

A one atmosphere furnace and Pt/Pt10%Rh thermocouple were calibrated to the melting point of gold. The undoped starting glasses were loaded into Pt capsules, welded shut, and inserted into the furnace. Experiments were conducted as follows: 1) the capsules were heated to 1450°C and held for 1 hour to ensure homogeneity of the melt; 2) the temperature was decreased at 60°C/hr to 1350°C; 3) the capsules were held at 1350°C for 1 hour; 4) the run was quenched by dropping the capsules into water; 5) the capsules were opened and oil mounts were made of the glasses. The oil mounts were examined for any crystal growth. This procedure was repeated at varying final temperatures until crystal growth was observed in all three compositions.

Partitioning Experiments

The doped glasses were loaded in Pt capsules, welded shut, and inserted into the furnace. Experiments were conducted as follows: 1) the capsules were heated to 1450°C and held for 1 hour; 2) the temperature was decreased at 60°C/hour to 1353°C; 3) the temperature was decreased at 0.2°C/hour to 1349°C; 4) the capsules were held isothermal for 1hour in the first run and for four days in the second run; 5) the run was quenched by dropping the capsules into water. (Figure 4) The purpose of this protocol was to minimize nucleation density and promote the slow growth of a few, large crystals that would be adequate for ion microprobe analysis. (Figure 5)

ANALYSIS

Major element analyses of the starting materials and run products used a JEOL Superprobe 733 electron microprobe with a 15μm defocused beam and a beam current of 10nA on crystals and 5nA on glasses to prevent Na loss. Synthetic mineral standards were used, and raw X-ray intensities were converted to oxide weight percents using the Bence-Albee method . Reported errors are one standard deviation in the average of several spots.(Table 1)

Trace elements were measured using the Cameca IMS-3F ion microprobe at LLNL using a 15-50nA O^- primary beam. For each sample, multiple spots on each phase were analyzed, and the results averaged. Trace element concentrations were determined by comparing the ^{30}Si-normalized isotopic ratios of the samples to those of silicate and glass standards. Partition coefficients were calculated from the ratio of the average ^{30}Si-normalized count rate of an isotope in the forsterite to the average of the ^{30}Si-normalized count rate in the glass, correcting for differences in Si contents. (Tables 2-4)

RESULTS

The data from the electron microprobe and ion microprobe analyses showed that the crystals and glasses were homogeneous with respect to major and trace elements. All partition coefficents were calculated from the ^{30}Si-corrected ion microprobe data. The partition coefficient of an isotope between a mineral and the coexisting melt is defined by the ratio of the concentration of the isotope in the mineral and the melt.

$$D_{mineral\text{-}melt} = [i]_{mineral}/[i]_{melt}$$

The partition coefficients for each of the compositions and an overall average are summarized in Table 5. Figures 6-8 show that there is no compositional dependance on the partitioning behavior of boron, beryllium, or lithium.

A comparison of D vs. the experiment duration (Figure 9) yields horizontal lines for each of the elements. This shows that the experiment is not time dependent, the experiment reached equilibrium, and that the experiment is reproducible. Because the experiment is not time dependent, the partition coefficients for olivine are locked into the system after the slow cooling step, holding the system isothermal has little effect on the outcome.

A comparison of $D_{olivine}$ and $D_{clinopyroxene}$ (Figure 10) shows that olivine has a higher partition coefficient for all three elements than clinopyroxene. Using these partition coefficients, and the assumption that orthopyroxene fractionates elements similar to olivine, a partial melting curve (Figure 11) was calculated using the following equation:

$$C_{melt}/C_{total} = 1/(X_{melt} + D_{bulk}X_{solid})$$

where X_{melt}= the melt fraction (10 or 20%), X_{solid} = solid fraction (90 or 80%), and D_{bulk} = the bulk partition coefficient :

$$D_{bulk} = D_{olivine}X_{olivine} + D_{orthopyroxene}X_{opx} + D_{clinopyroxene}X_{cpx}$$

assuming $X_{ol} = 60\%$, $X_{opx} = 30\%$, and $X_{cpx} = 10\%$.

This partial melting curve shows that boron and beryllium are not fractionated relative to each other during mantle melting and lithium is only slightly fractionated relative to both boron and beryllium.

CONCLUSIONS

The results for olivine/melt partitioning of B, Be, and Li have been presented and are summarized in Table 5. This new set of partitioning data has expanded the information on how boron, beryllium, and lithium behave during mantle melting. By combining this data, with that of clinopyroxene, it has been shown that B and Be are not fractionated relative to each other, thus preserving their original slab derived ratio. The assumption that the B/Be ratio can be used as a geochemical indicator of slab derived components in arc magmas, has been verified.

FURTHER STUDIES

In order to finish this study the ion microprobe analyses of the heavy trace elements needs to be completed. The partition coefficients for the heavy trace elements will then be compared to the partition coefficients of B, Be, and Li to see if there is any correlation between their partitioning behavior in olivine.

The next logical step is to determine the partition coefficients of B, Be, and Li in orthopyroxene so a more accurate partial melting curve can be created. Then continue and determine the partition coefficients of B, Be, and Li in other mantle minerals such as amphibole and garnet.

ACKNOWLEDGMENTS

I would like to thank my mentors Frederick Ryerson, James, Brenan, and Henry Shaw for all of their help in completing this project. A special thanks to James, who spent many hours in the lab helping me learn about experimental petrology. I would also like to thank Bill Minarik and Dan Farber for their help in and out of the lab, to Ian Hutcheon for use of his clean lab, and to Doug Phinney for his help in analyzing my samples on the ion microprobe.

I would like to thank the Department of Energy's Science and Engineering Research Semester at Lawrence Livermore National Laboratory, for the opportunity to participate in their program and conduct this research.

BIBLIOGRAPHY

Agee C.B., Walker D. (1990) Aluminum partitioning between olivine and ultrabasic silicate liquid to 6GPa. *Contrib Mineral Petrol.* **105**, 243-254

Baker M.B., Hirchmann M.M., Ghiorso M.S., Stolper E.M. (1994) Compositions of low-degree partial melts of peridotite: Results from experiments and thermodynamic calculations. *Nature*. submitted October 13, 1994

Beattie P. (1993) Uranium-thorium disequilibria and partitioning on melting of garnet peridotite. *Nature*. **363**, 63-65

Beattie P. (1994) Systematics and energetics of trace-element partitioning between olivine and silicate melts: Implications for the nature of mineral/melt partitioning. *Chem. Geol.* **117**, 57-71

Blundy J., Wood B. (1994) Prediction of crystal-melt partition coefficients from elastic moduli. *Nature*. **372**, 452-454

Brenan J.M., Shaw H.F., Ryerson F.J., Phinney D.L. (1995) Experimental Determination of Trace Element Partitioning between Pargasite Amphibole and Synthetic Hydrous Andesitic Melt. *Earth Planet. Sci. Lett.*

Chaussidon M., Libourel G. (1993) Boron Partitioning in the upper mantle: An experimental ion probe study. *Geochim. Cosmochim. Acta.* **57**, 5053-5062

Jurewicz A.J., Watson E.B. (1988) Cations in Olivine Part 1: Calcium partitioning and calcium-magnesium distribution between olivines and coexisting melts, with petrologic applications. *Contrib Mineral Petrol.* **99**, 176-185

Jurewicz A.J., Watson E.B. (1989) Erratum - Cations in Olivine Part 1: Calcium partitioning and calcium-magnesium distribution between olivines and coexisting melts, with petrologic applications. *Contrib Mineral Petrol.* **102**, 255

Jurewicz A.J., Watson E.B. (1988) Cations in Olivine Part 2: Diffusion in olivine xenocrysts, with applications to petrology and mineral physics. *Contrib Mineral Petrol.* **99**, 186-201

Lundstrom C.C., Shaw H.F., Ryerson F.J., Phinney D.L., Gill J.B., Williams Q. (1994) Compositional controls on the partitioning of U, Th, Ba, Pb, Sr, and Zr between clinopyroxene and haplobasaltic melts: implications for uranium series disequilibria in basalts. *Earth Planet. Sci. Lett.* **128**, 407-423

O'Nions R.K., Powell R. The Thermodynamics of Trace Element Distribution, Thermodynamics in Geology, D. Reidel Publishing Company, Dordrecht, Holland, copyright 1977, 349-363

Ryan J.H., Langmuir C.H. (1987) The sytematics of lithium abundances in young volcanic rocks. *Geochim. Cosmochim Acta.* **51**, 1727-1741

Ryan J.H., Langmuir C.H. (1987) Beryllium sytematics in young volcanic rocks: Implications for ^{10}Be. *Geochim. Cosmochim Acta.* **52**, 237-244

Ryan J.H., Langmuir C.H. (1992) The sytematics of boron abundances in young volcanic rocks. *Geochim. Cosmochim Acta.* **57**, 1489-1498

Ryan J.H., Langmuir C.H., A Preliminary Study of Li, Be, and B Mineral/Melt Partitioning in Oceanic Basalts. not yet submitted to *Geochimica Cosmochimia Acta*

Ryan J.G., Morris J., Tera F., Leeman W.P., Tsvetkov A. (1995) Cross-Arc Geochemical Variations in the Kurile Arc as a function of Slab Depth. *Science.* **270**, 625-627

Shaw H.F., Brenan J.M., Ryerson F.J., Experimental constraints on fluid compositions at convergent boundaries. 1995 Proposal to DOE Office of Basic Energy Sciences

Watson E.B. (1979) Calcium content of forsterite coexisting with silicate liquid in the system Na_2O-CaO-MgO-Al_2O_3-SiO_2. *Am. Min.* **64**, 824-829

Watson E.B. (1977) Partitioning of manganese between forsterite and silicate liquid. *Geochim. Cosmocim. Acta.* **41**, 1363-1374

Figure 1

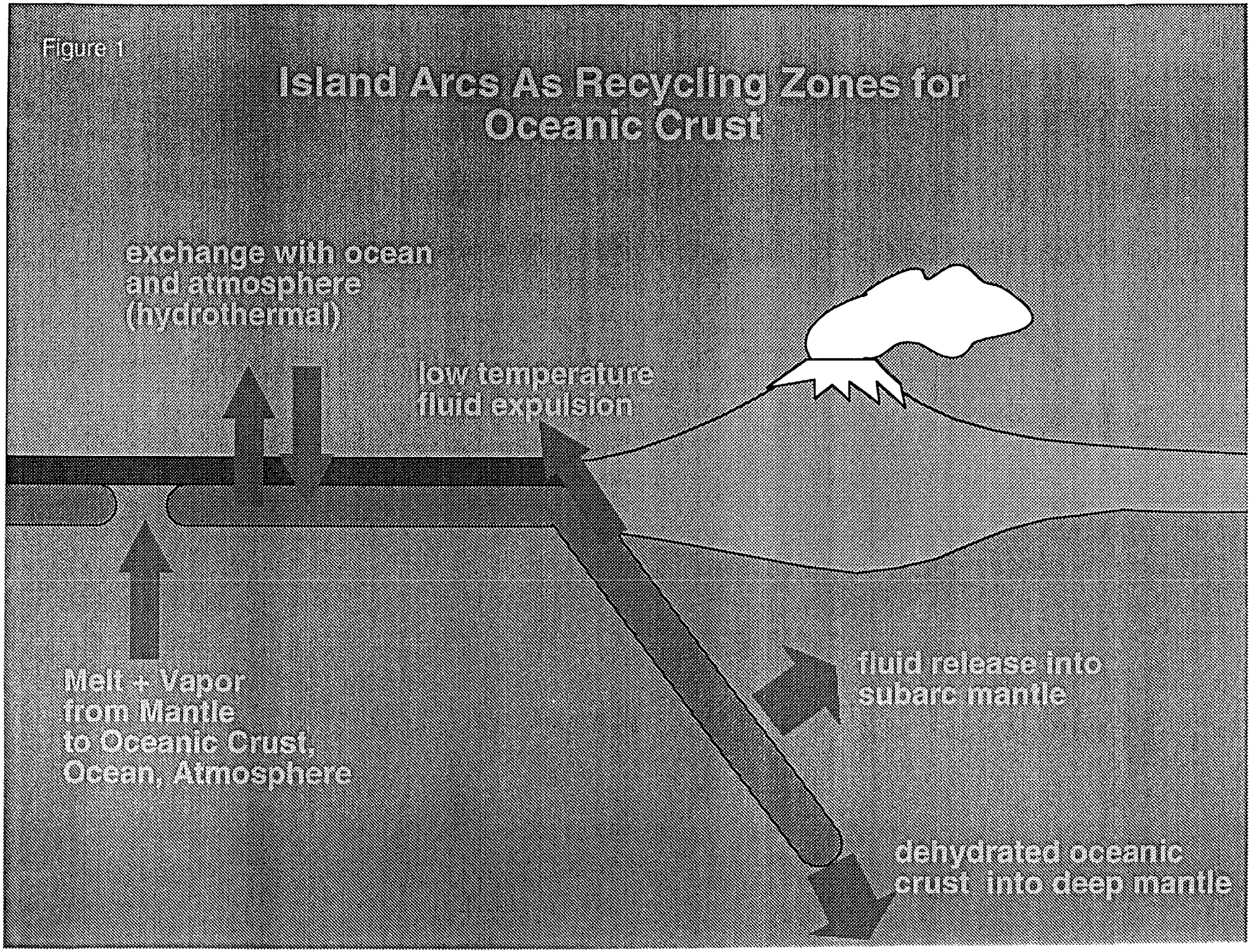
Island Arcs As Recycling Zones for Oceanic Crust
exchange with ocean and atmosphere (hydrothermal)
low temperature fluid expulsion
Melt + Vapor from Mantle to Oceanic Crust, Ocean, Atmosphere
fluid release into subarc mantle
dehydrated oceanic crust into deep mantle

Figure 2

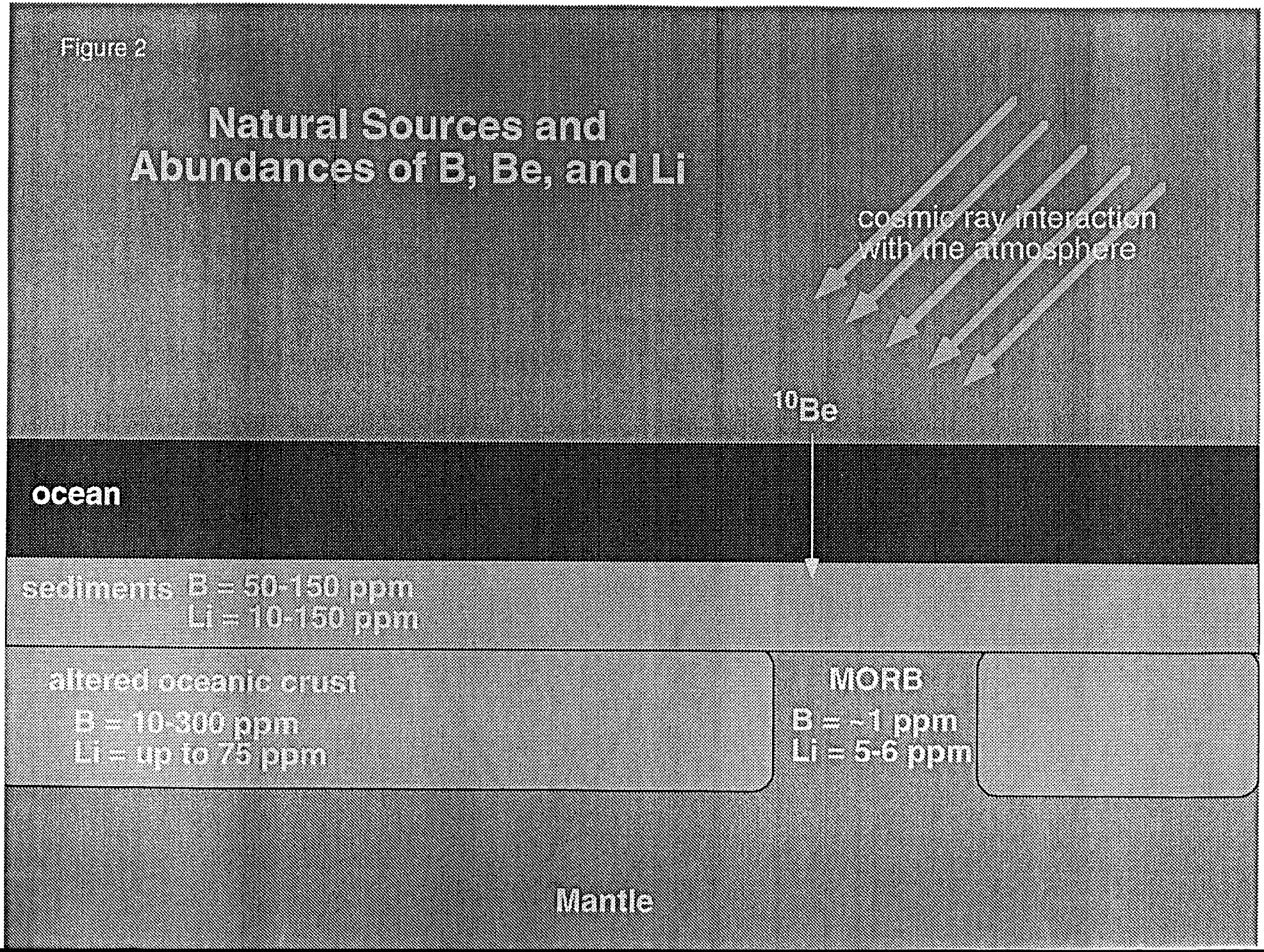
Natural Sources and
Abundances of B, Be, and Li
cosmic ray interaction
with the atmosphere
^{10}Be
ocean
sediments B = 50-150 ppm
Li = 10-150 ppm
altered oceanic crust
B = 10-300 ppm
Li = up to 75 ppm
MORB
B = ~1 ppm
Li = 5-6 ppm
Mantle

Figure 3

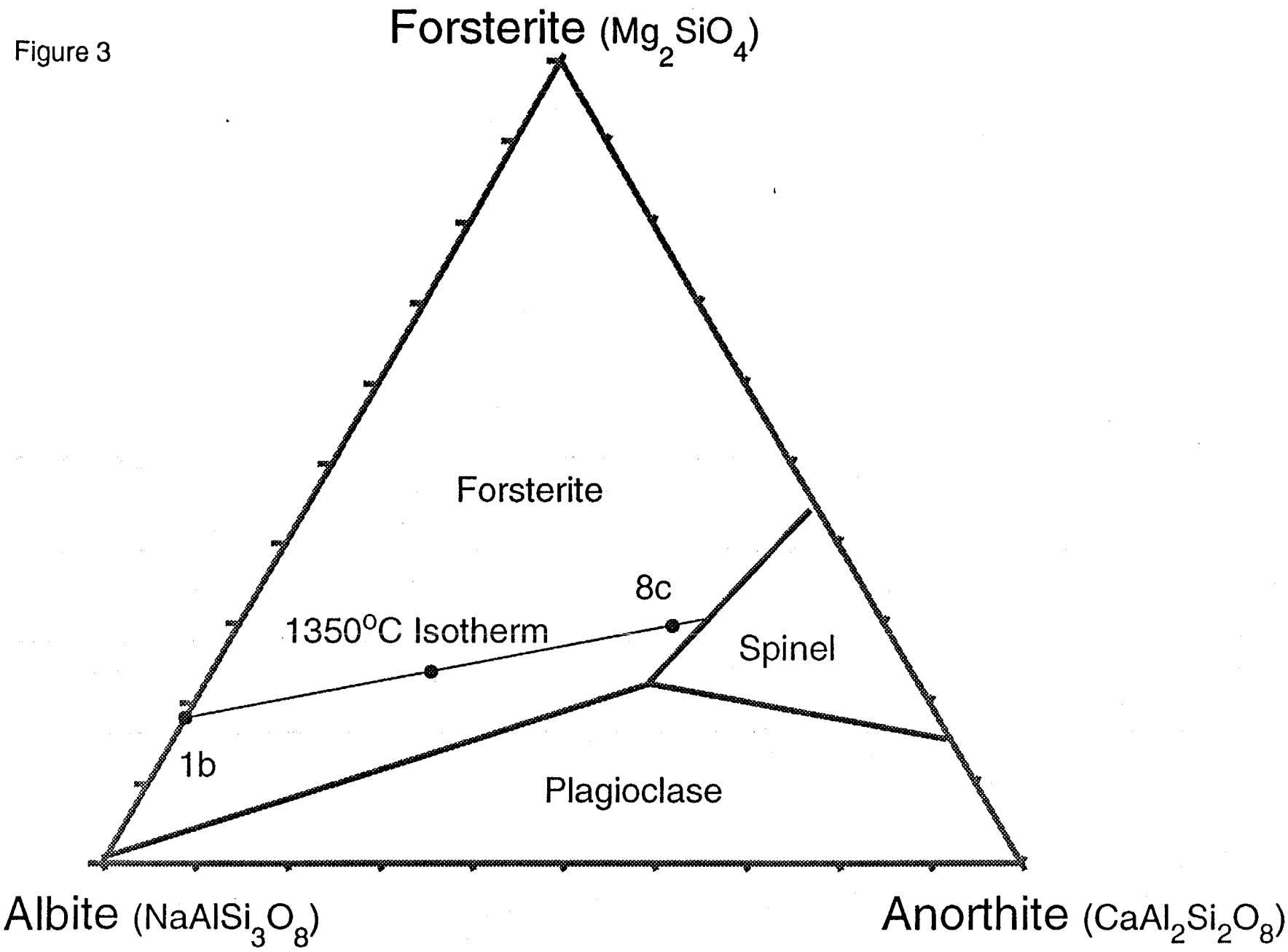

(Watson, 1977)

Figure 4

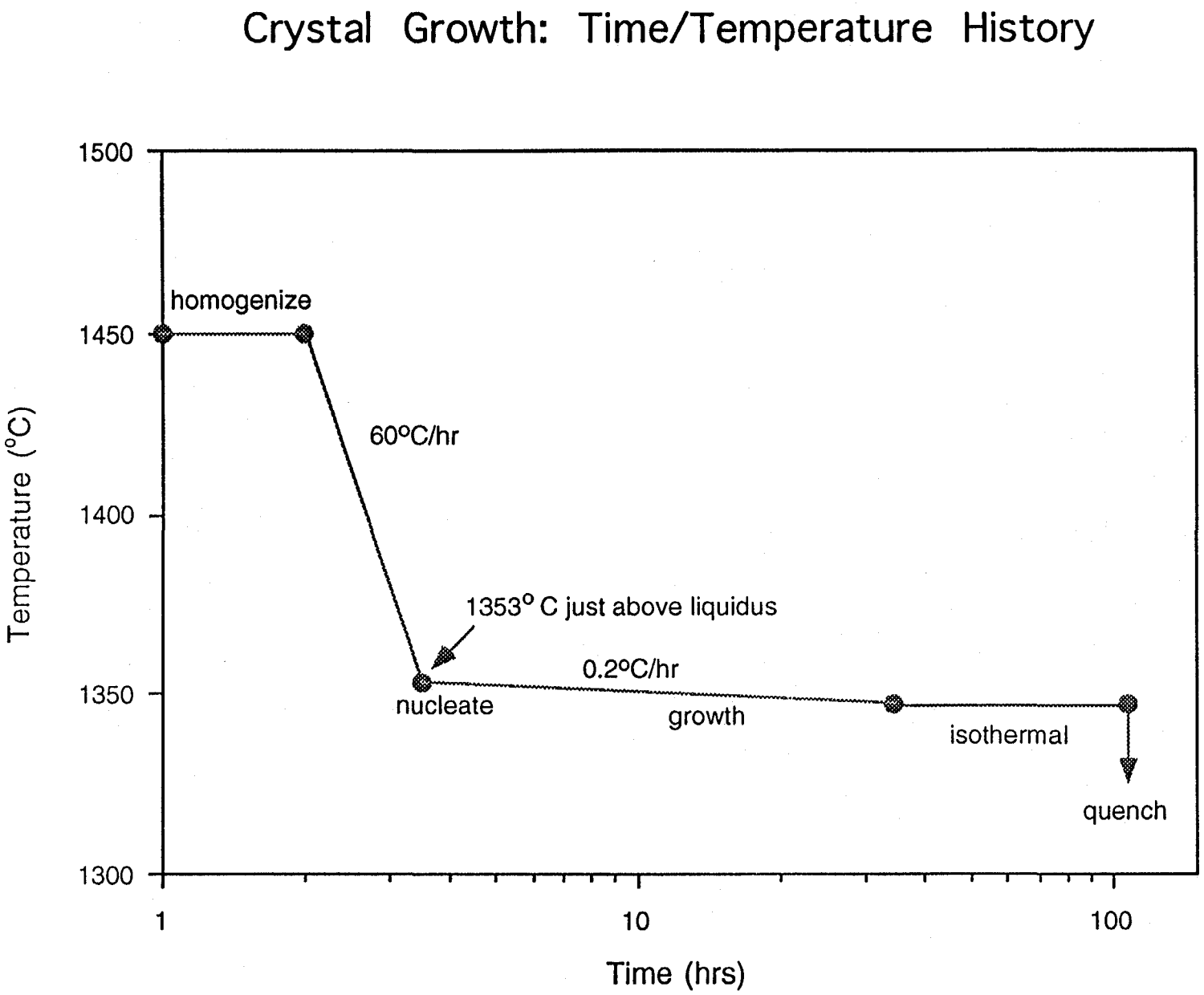

This method minimizes nucleation density and maximizes the slow growth of a few large crystals.

Figure 5

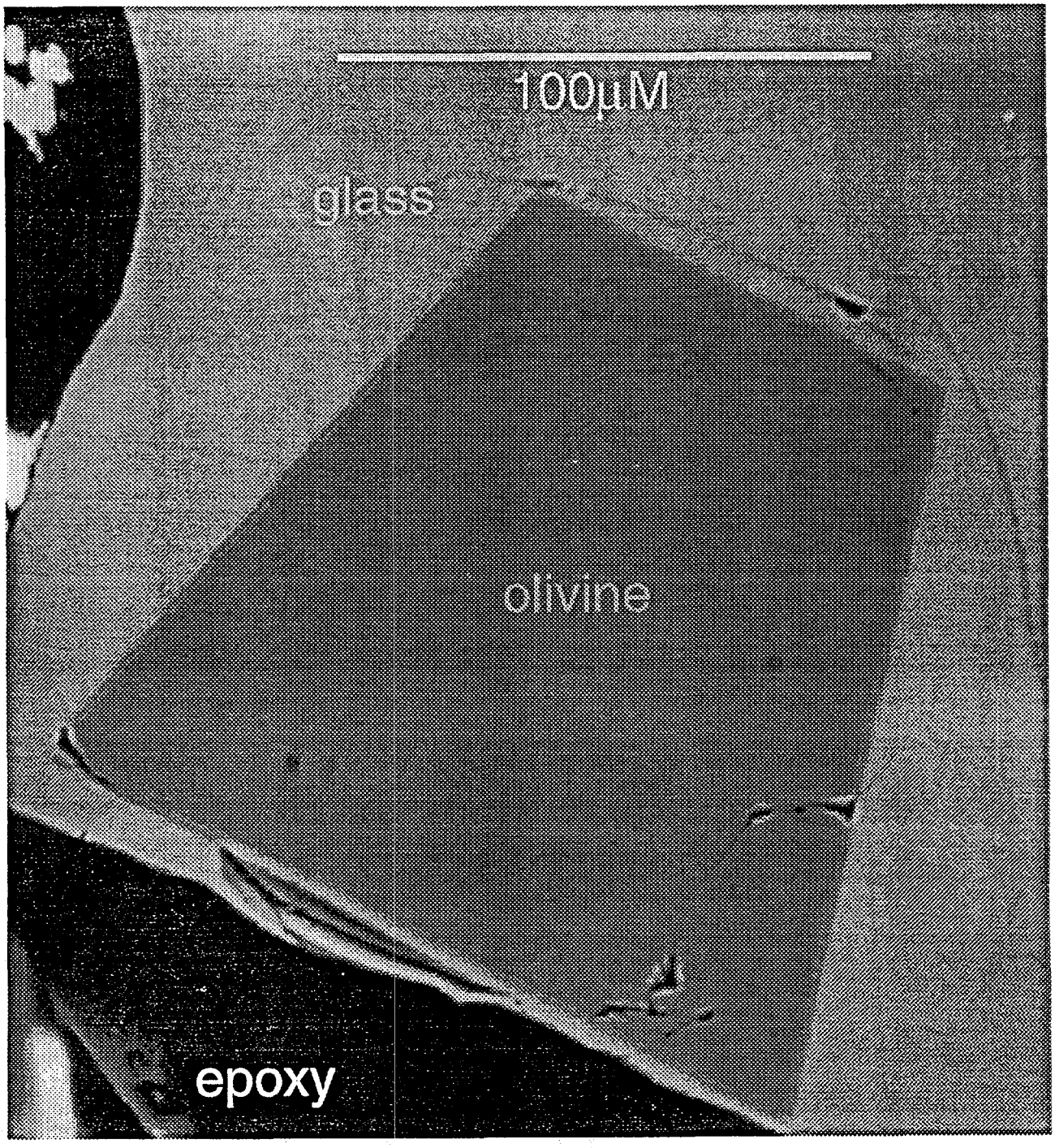

Figure 6

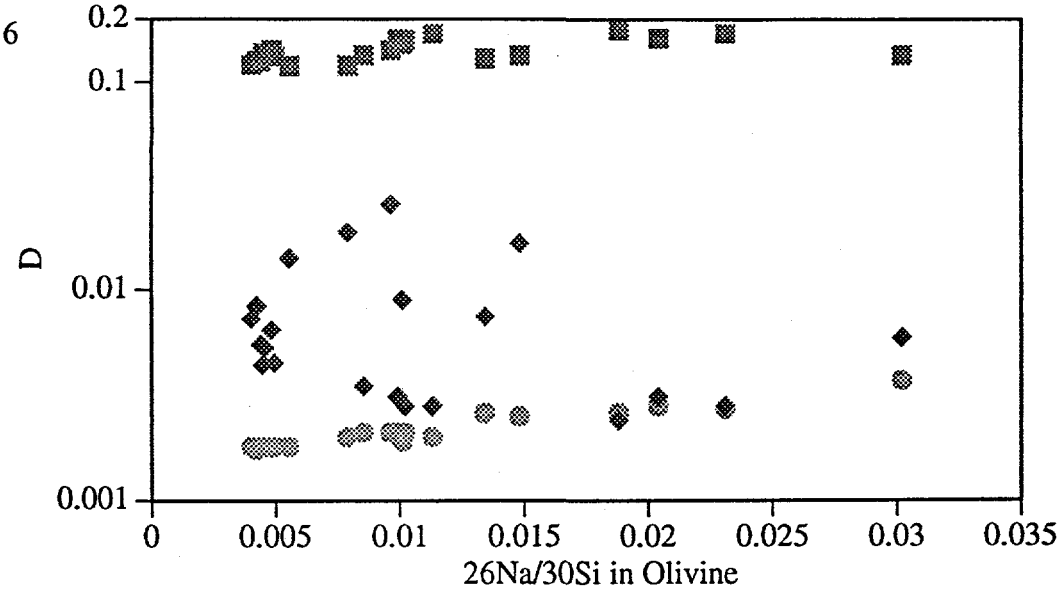

Squares = D_{Li}
Diamonds = D_B
Circles = D_{Be}

Figure 7

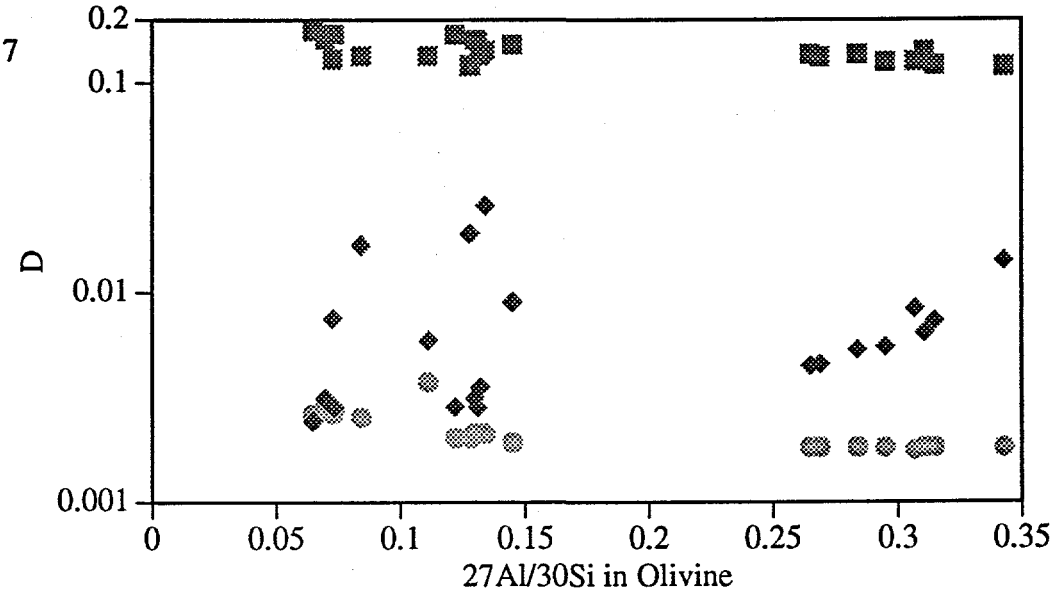

Figure 8

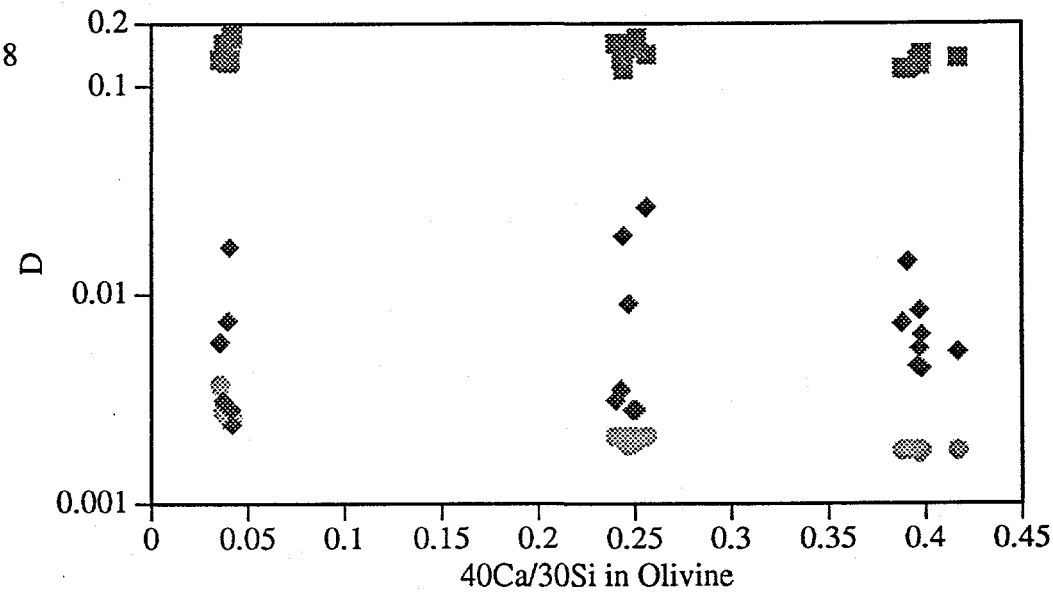

Figure 9

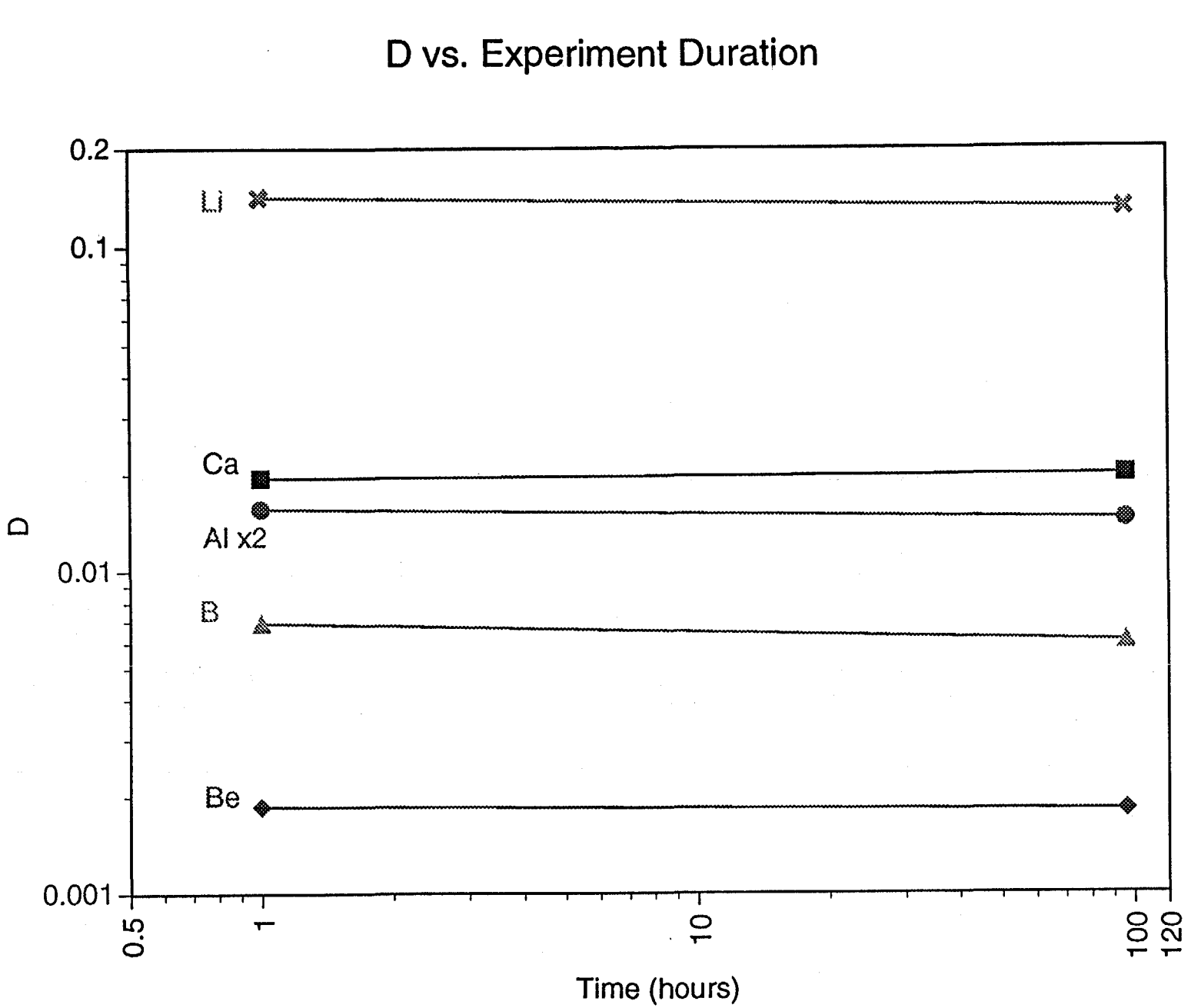
D vs. Experiment Duration
0.2
0.1
0.01
0.001
D
Li
Ca
Al x2
B
Be
0.5
1
10
100
120
Time (hours)

Figure 10

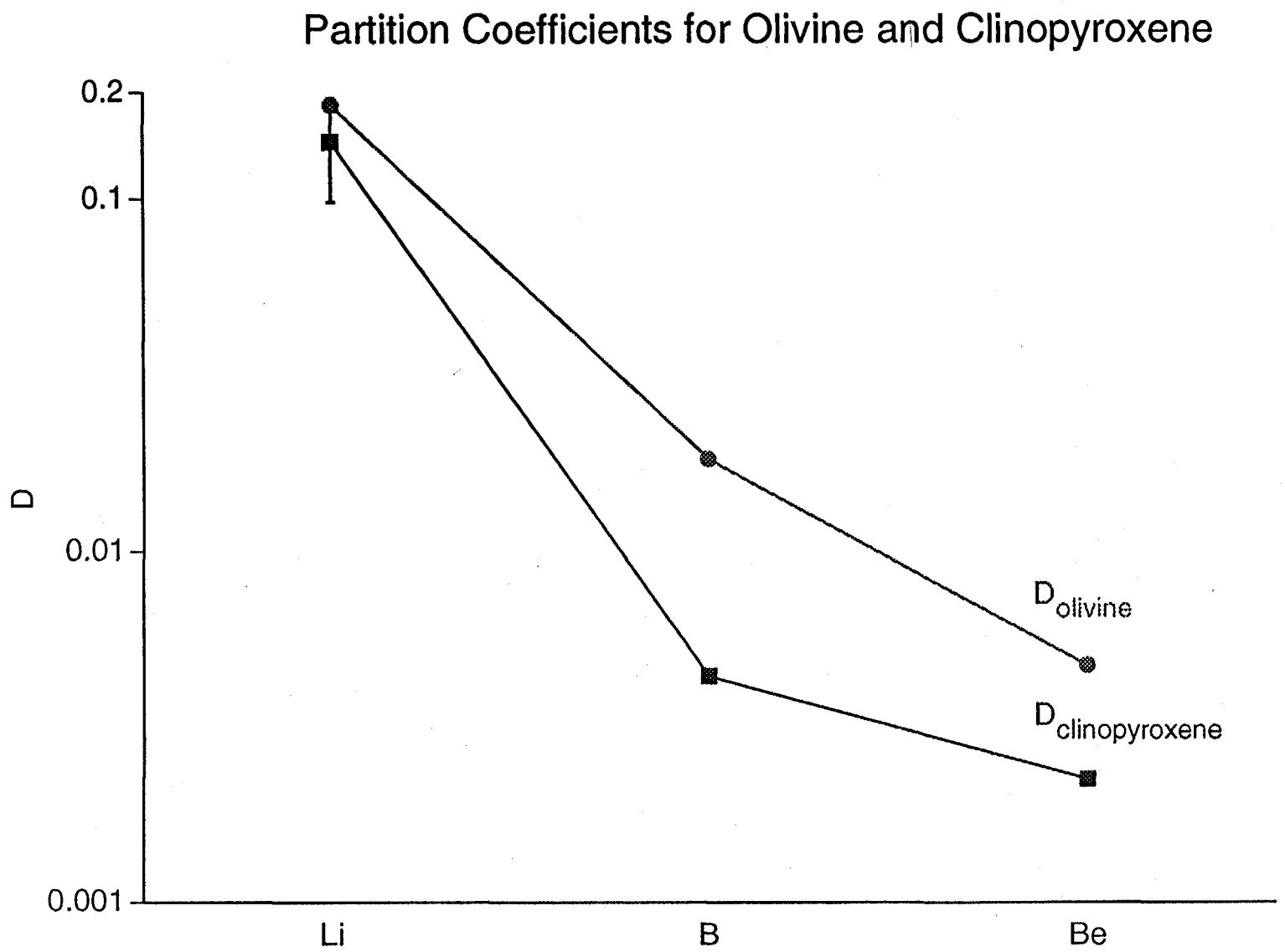
Partition Coefficients for Olivine and Clinopyroxene
0.2
0.1
0.01
0.001
D
Li
B
Be
$D_{olivine}$
$D_{clinopyroxene}$
(D_{cpx}, Lundstrom)

Figure 11

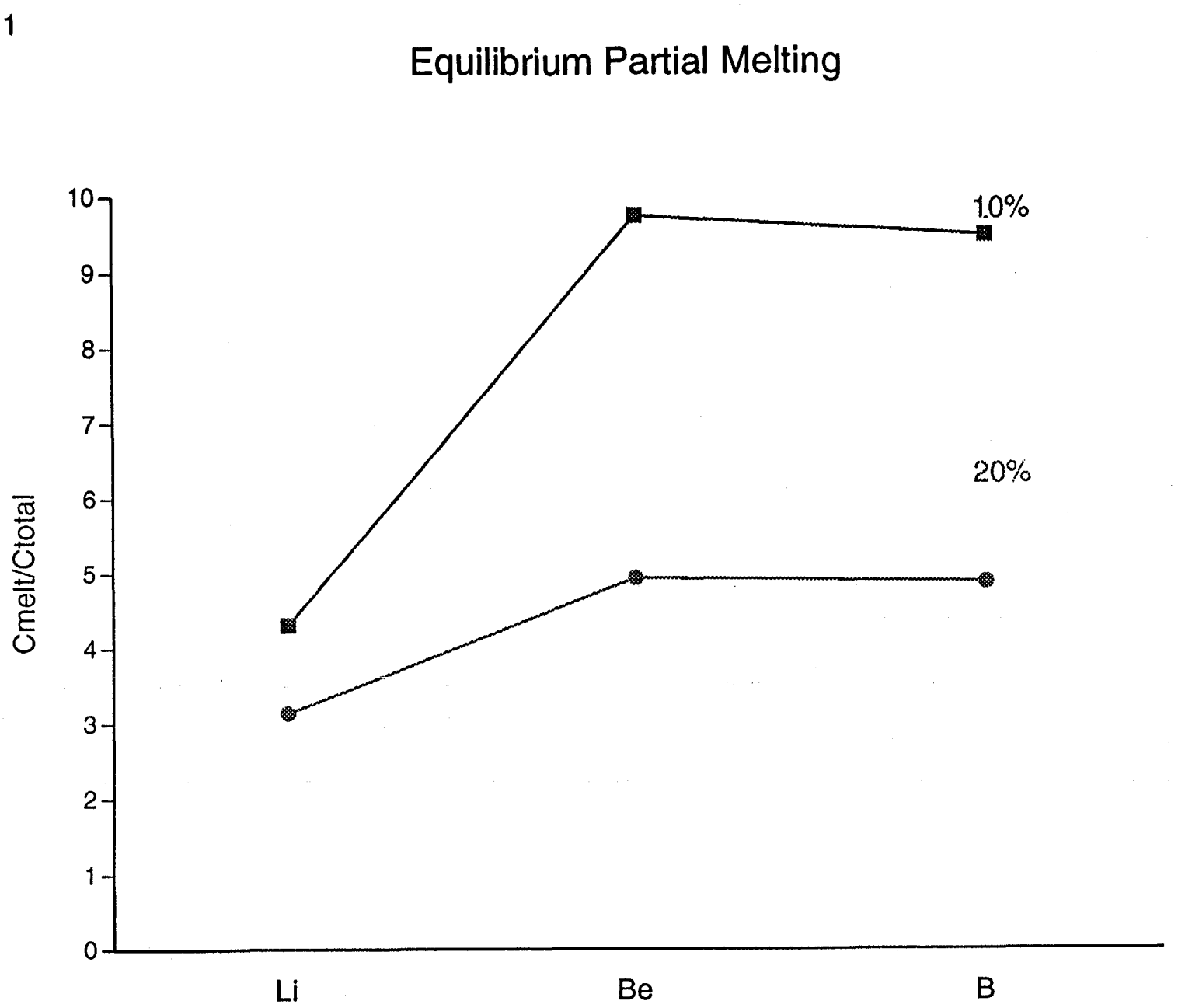
Equilibrium Partial Melting
Cmelt/Ctotal
10
9
8
7
6
5
4
3
2
1
0
1.0%
20%
Li
Be
B

Table 1

Major Element Compositons in Starting Materials and Run Products

1b Composition :

oxide	starting material	glass	olivine
SiO_2	65.62 (± 0.66)	64.93 (± 0.36)	42.86 (± 0.25)
MgO	7.37 (± 0.11)	8.61 (± 0.17)	57.06 (± 0.63)
Al_2O_3	16.99 (± 0.40)	16.76 (± 0.26)	0.05 (± 0.01)
CaO	0.05 (± 0.03)	0.05 (± 0.01)	0.01 (± 0.01)
Na_2O	9.97 (± 0.07)	9.65 (± 0.20)	-

8c Composition :

oxide	starting material	glass	olivine
SiO_2	49.16 (± 0.65)	49.16 (± 0.41)	42.77 (± 0.39)
MgO	16.67 (± 0.23)	15.58 (± 0.22)	56.81 (± 0.30)
Al_2O_3	21.50 (± 0.20)	22.62 (± 0.40)	0.18 (± 0.04)
CaO	9.81 (± 0.21)	9.80 (± 0.19)	0.19 (± 0.02)
Na_2O	2.86 (± 0.05)	2.83 (±0.05)	-

50/50 Composition :

oxide	starting material	glass	olivine
SiO_2	58.13 (± 0.72)	56.75 (± 0.35)	42.88 (± 0.28)
MgO	11.39 (± 0.19)	12.67 (± 0.21)	56.49 (± 0.35)
Al_2O_3	18.80 (± 0.34)	19.39 (± 0.18)	0.078 (± 0.008)
CaO	4.76 (± 0.14)	4.81 (± 0.06)	0.12 (± 0.01)
Na_2O	6.93 (± 0.13)	6.38 (± 0.09)	-

Table 2 1b*-2													
	RATIO O N=>	6.4	7li	9be	11b	16o	23na	26mg	27al	30si	40ca	25Mg16O	42ca
Glass													
C:\DATA\BETH\DR95N28A.006	30si	0.00E+00	1.21E-02	2.35E-02	2.15E-02	3.39E-01	9.33E+00	8.94E-01	2.08E+01	1.00E+00	6.91E-02		8.15E-04
C:\DATA\BETH\DR95N28A.006	Sigma	INF	1.25E-04	1.76E-04	1.68E-04	7.64E-04	1.11E-02	1.47E-03	2.41E-02	1.60E-03	3.08E-04		9.80E-06
C:\DATA\BETH\DR95N28A.006	%Error	INF	1.04%	0.75%	0.78%	0.23%	0.12%	0.16%	0.12%	0.16%	0.45%		1.20%
C:\DATA\BETH\DR95N28A.007	30si	0.00E+00	1.16E-02	2.21E-02	2.13E-02	2.81E-01	9.98E+00	8.33E-01	2.21E+01	1.00E+00	6.71E-02	2.54E-03	9.59E-04
C:\DATA\BETH\DR95N28A.007	Sigma	INF	1.18E-04	1.64E-04	1.61E-04	6.53E-04	1.14E-02	1.34E-03	2.46E-02	1.54E-03	2.91E-04	1.76E-05	1.07E-05
C:\DATA\BETH\DR95N28A.007	%Error	INF	1.02%	0.74%	0.75%	0.23%	0.11%	0.16%	0.11%	0.15%	0.43%	0.69%	1.12%
C:\DATA\BETH\DR95N28A.00A	30si	0.00E+00	1.26E-02	2.42E-02	2.23E-02	3.59E-01	9.33E+00	8.96E-01	2.64E+01	1.00E+00	6.90E-02	2.39E-03	7.97E-04
C:\DATA\BETH\DR95N28A.00A	Sigma	INF	1.14E-04	1.58E-04	1.52E-04	7.05E-04	9.89E-03	1.31E-03	2.71E-02	1.43E-03	2.74E-04	4.83E-05	1.16E-05
C:\DATA\BETH\DR95N28A.00A	%Error	INF	0.90%	0.66%	0.68%	0.20%	0.11%	0.15%	0.10%	0.14%	0.40%	2.07%	1.46%
C:\DATA\BETH\DR95N28A.00B	30si	0.00E+00	1.26E-02	2.43E-02	2.20E-02	3.47E-01	9.65E+00	8.86E-01	2.14E+01	1.00E+00	7.04E-02	2.58E-03	7.66E-04
C:\DATA\BETH\DR95N28A.00B	Sigma	INF	1.18E-04	1.65E-04	1.57E-04	7.17E-04	1.06E-02	1.36E-03	2.30E-02	1.48E-03	2.88E-04	5.33E-05	1.19E-05
C:\DATA\BETH\DR95N28A.00B	%Error	INF	0.94%	0.68%	0.71%	0.21%	0.11%	0.15%	0.11%	0.15%	0.41%	2.07%	1.55%
C:\DATA\BETH\DR95N28A.00E	30si	1.49E-11	1.28E-02	2.45E-02	2.24E-02	3.53E-01	9.41E+00	8.99E-01	2.67E+01	1.00E+00	6.97E-02	2.42E-03	7.97E-04
C:\DATA\BETH\DR95N28A.00E	Sigma	1.69E-07	1.24E-04	1.73E-04	1.66E-04	7.56E-04	1.08E-02	1.43E-03	2.97E-02	1.55E-03	2.99E-04	2.70E-05	8.96E-06
C:\DATA\BETH\DR95N28A.00E	%Error	>1000000%	0.97%	0.71%	0.74%	0.21%	0.12%	0.16%	0.11%	0.15%	0.43%	1.12%	1.12%
C:\DATA\BETH\DR95N28A.004	30si	-7.24E-09	1.20E-02	2.40E-02	2.19E-02	3.06E-01	9.89E+00	8.56E-01	2.14E+01	1.00E+00	6.65E-02	2.43E-03	7.49E-04
C:\DATA\BETH\DR95N28A.004	Sigma	-1.05E-11	1.29E-04	1.84E-04	1.76E-04	7.41E-04	1.22E-02	1.48E-03	2.57E-02	1.66E-03	3.12E-04	1.85E-05	7.41E-06
C:\DATA\BETH\DR95N28A.004	%Error	0.14%	1.08%	0.77%	0.80%	0.24%	0.12%	0.17%	0.12%	0.17%	0.47%	0.76%	0.99%
C:\DATA\BETH\DR95N29A.005	30si	-6.01E-10	1.25E-02	2.52E-02	2.19E-02	3.54E-01	9.26E+00	9.09E-01	2.12E+01	1.00E+00	7.11E-02	2.29E-03	7.89E-04
C:\DATA\BETH\DR95N29A.005	Sigma	-2.64E-12	1.70E-04	2.43E-04	2.26E-04	1.05E-03	1.47E-02	1.99E-03	3.27E-02	2.14E-03	4.17E-04	2.75E-05	9.57E-06
C:\DATA\BETH\DR95N29A.005	%Error	0.44%	1.36%	0.96%	1.03%	0.30%	0.16%	0.22%	0.15%	0.21%	0.59%	1.20%	1.21%
	Average		1.23E-02	2.40E-02	2.19E-02	3.34E-01	9.55E+00	8.82E-01	2.29E+01	1.00E+00	6.90E-02	2.44E-03	8.10E-04
	Std Dev		4.03E-04	9.64E-04	4.06E-04	2.95E-02	2.92E-01	2.73E-02	2.55E+00	0.00E+00	1.66E-03	1.06E-04	6.90E-05
	% Std Dev		3.28%	4.02%	1.85%	8.82%	3.06%	3.10%	11.14%	0.00%	2.41%	4.33%	8.51%
							Calc MgO/Mg=	4.17E-04		Corrected Ca/Si	6.64E-02		4.43E-04
							Meas MgO/Mg=	2.77E-03					
Olivine													
C:\DATA\BETH\DR95N28A.008	30si	0.00E+00	2.51E-03	9.26E-05	5.60E-04	4.54E-01	1.48E-02	1.12E+01	8.43E-02	1.00E+00	4.08E-02	5.37E-03	4.88E-03
C:\DATA\BETH\DR95N28A.008	Sigma	INF	1.93E-05	2.02E-06	5.12E-06	7.63E-04	1.15E-04	1.10E-02	2.84E-04	1.33E-03	1.93E-04	2.23E-05	2.06E-05
C:\DATA\BETH\DR95N28A.008	%Error	INF	0.77%	2.18%	0.91%	0.17%	0.78%	0.10%	0.34%	0.13%	0.47%	0.42%	0.45%
C:\DATA\BETH\DR95N28A.009	30si	0.00E+00	2.43E-03	9.49E-05	2.51E-04	4.15E-01	1.34E-02	1.12E+01	7.30E-02	1.00E+00	3.97E-02	5.17E-03	4.46E-03
C:\DATA\BETH\DR95N28A.009	Sigma	INF	2.28E-05	2.01E-06	3.26E-06	7.05E-04	1.07E-04	1.07E-02	2.57E-04	1.30E-03	1.87E-04	2.15E-05	1.99E-05
C:\DATA\BETH\DR95N28A.009	%Error	INF	0.94%	2.11%	1.30%	0.17%	0.80%	0.10%	0.35%	0.13%	0.47%	0.41%	0.44%
C:\DATA\BETH\DR95N28A.00C	30si	0.00E+00	3.31E-03	9.53E-05	8.10E-05	4.80E-01	1.88E-02	1.13E+01	6.50E-02	1.00E+00	4.21E-02	5.43E-03	4.69E-03
C:\DATA\BETH\DR95N28A.00C	Sigma	INF	3.73E-05	2.44E-06	2.25E-06	9.42E-04	1.55E-04	1.32E-02	2.94E-04	1.58E-03	2.34E-04	2.67E-05	2.48E-05
C:\DATA\BETH\DR95N28A.00C	%Error	INF	1.13%	2.56%	2.78%	0.20%	0.82%	0.12%	0.45%	0.18%	0.56%	0.49%	0.53%
C:\DATA\BETH\DR95N28A.00D	30si	0.00E+00	3.20E-03	9.74E-05	9.30E-05	4.97E-01	2.31E-02	1.13E+01	7.35E-02	1.00E+00	4.13E-02	5.19E-03	4.43E-03
C:\DATA\BETH\DR95N28A.00D	Sigma	INF	3.70E-05	2.87E-06	2.81E-06	1.12E-03	2.00E-04	1.54E-02	3.65E-04	1.84E-03	2.70E-04	3.04E-05	2.80E-05
C:\DATA\BETH\DR95N28A.00D	%Error	INF	1.16%	2.95%	3.02%	0.23%	0.87%	0.14%	0.50%	0.18%	0.65%	0.59%	0.63%
C:\DATA\BETH\DR95N29A.001	30si	0.00E+00	2.51E-03	1.34E-04	1.96E-04	4.00E-01	3.02E-02	1.10E+01	1.11E-01	1.00E+00	3.57E-02	4.54E-03	4.22E-03
C:\DATA\BETH\DR95N29A.001	Sigma	INF	2.36E-05	4.21E-06	5.09E-06	6.08E-04	1.43E-04	9.37E-03	2.86E-04	1.15E-03	1.56E-04	1.77E-05	5.29E-05
C:\DATA\BETH\DR95N29A.001	%Error	INF	0.94%	3.15%	2.60%	0.15%	0.47%	0.08%	0.26%	0.11%	0.44%	0.39%	1.25%
C:\DATA\BETH\DR95N29A.002	30si	0.00E+00	3.02E-03	1.03E-04	1.04E-04	4.48E-01	2.04E-02	1.12E+01	6.99E-02	1.00E+00	3.74E-02	4.77E-03	4.22E-03
C:\DATA\BETH\DR95N29A.002	Sigma	INF	2.47E-05	2.03E-06	2.04E-06	7.20E-04	1.29E-04	1.05E-02	2.45E-04	1.26E-03	1.76E-04	2.00E-05	4.13E-05
C:\DATA\BETH\DR95N28A.002	%Error	INF	0.82%	1.97%	1.97%	0.16%	0.63%	0.09%	0.35%	0.13%	0.47%	0.42%	0.98%
	Average		2.83E-03	1.03E-04	1.45E-04	4.49E-01	2.01E-02	1.12E+01	7.95E-02	1.00E+00	3.95E-02	5.08E-03	4.44E-03
	Std Dev		3.92E-04	1.55E-05	7.46E-05	3.69E-02	6.11E-03	1.00E-01	1.68E-02	0.00E+00	2.45E-03	3.50E-04	1.93E-04
	% Std Dev		13.86%	15.08%	51.51%	8.22%	30.41%	0.89%	21.12%	0.00%	6.22%	6.89%	4.35%
SiO2 in glass =	64.58	Si Ratio=	0.66738928				Calc MgO/Mg=	3.91E-04		Corrected Ca/Si	6.04E-03		5.36E-05
SiO2 in Olivine =	43.1						Meas MgO/Mg=	4.53E-04					
											6.67E-03		
Partition Coefficients	D		1.536E-01	2.865E-03	4.410E-03	8.964E-01	1.405E-03	8.494E+00	2.322E-03		8.089E-02		8.089E-02
	Std Dev		2.188E-02	4.470E-04	2.273E-03	1.081E-01	4.295E-04	2.739E-01	5.546E-04		5.394E-03		7.730E-03
	% Std Dev		14.24%	15.61%	51.54%	12.06%	30.57%	3.22%	23.88%		6.67%		9.56%

Table 3	50-50													
	RATIO D Ni=>	6.4	7li	9be	11b	16o	23na	26mg	27al	30si	40ca	25mg+o	42ca	
Glass														
B:\DR95N29A.006	30si	0.00E+00	1.07E-02	3.23E-02	1.30E-02	3.90E-01	5.00E+00	1.75E+00	2.63E+01	1.00E+00	6.97E+00	1.11E-02	4.66E-02	
B:\DR95N29A.006	Sigma	NF	1.66E-04	2.90E-04	1.82E-04	1.17E-03	8.72E-03	3.49E-03	4.26E-02	2.25E-03	1.19E-02	1.69E-04	3.52E-04	
B:\DR95N29A.006	%Error	NF	1.55%	0.90%	1.41%	0.30%	0.17%	0.20%	0.16%	0.23%	0.17%	1.52%	0.75%	
B:\DR95N29A.00C	30si	0.00E+00	1.04E-02	3.28E-02	1.31E-02	4.36E-01	5.02E+00	1.75E+00	2.67E+01	1.00E+00	7.11E+00	5.25E-03	4.69E-02	
B:\DR95N29A.00C	Sigma	NF	8.85E-05	6.33E-05	3.49E-05	9.62E-04	6.68E-03	2.66E-03	3.31E-02	1.72E-03	9.23E-03	8.84E-05	2.69E-04	
B:\DR95N29A.00C	%Error	NF	0.85%	0.19%	0.27%	0.22%	0.13%	0.15%	0.12%	0.17%	0.13%	1.68%	0.58%	
B:\DR95N29A.00D	30si	0.00E+00	1.05E-02	3.28E-02	1.32E-02	4.36E-01	5.07E+00	1.76E+00	2.68E+01	1.00E+00	7.14E+00	4.69E-03	4.69E-02	
B:\DR95N29A.00D	Sigma	NF	9.00E-05	1.07E-04	6.50E-05	9.70E-04	6.81E-03	2.70E-03	3.35E-02	1.73E-03	9.35E-03	8.42E-05	2.72E-04	
B:\DR95N29A.00D	%Error	NF	0.85%	0.33%	0.49%	0.22%	0.13%	0.15%	0.12%	0.17%	0.13%	1.80%	0.58%	
B:\DR95N30A.005	30si	0.00E+00	9.96E-03	3.04E-02	1.29E-02	3.86E-01	5.44E+00	1.69E+00	2.64E+01	1.00E+00	7.04E+00	3.41E-03	4.69E-02	
B:\DR95N30A.005	Sigma	NF	1.42E-04	2.49E-04	1.61E-04	1.03E-03	8.35E-03	3.01E-03	3.80E-02	1.99E-03	1.06E-02	4.15E-05	3.13E-04	
B:\DR95N30A.005	%Error	NF	1.42%	0.82%	1.25%	0.27%	0.15%	0.18%	0.14%	0.20%	0.15%	1.22%	0.67%	
B:\DR95N30A.003	30si	0.00E+00	1.07E-02	3.27E-02	1.35E-02	3.88E-01	5.54E+00	1.71E+00	2.67E+01	1.00E+00	7.02E+00	3.32E-03	4.68E-02	
B:\DR95N30A.003	Sigma	NF	1.14E-04	2.01E-04	1.28E-04	8.05E-04	6.59E-03	2.38E-03	2.98E-02	1.55E-03	8.22E-03	4.48E-05	2.43E-04	
B:\DR95N30A.003	%Error	NF	1.06%	0.62%	0.95%	0.21%	0.12%	0.14%	0.11%	0.16%	0.12%	1.35%	0.52%	
B:\DR95N30A.004	30si	0.00E+00	1.00E-02	3.06E-02	1.30E-02	3.82E-01	5.46E+00	1.69E+00	2.64E+01	1.00E+00	7.03E+00	3.39E-03	4.71E-02	
B:\DR95N30A.004	Sigma	NF	1.34E-04	2.36E-04	1.52E-04	9.65E-04	7.88E-03	2.83E-03	3.58E-02	1.88E-03	9.97E-03	3.89E-05	2.95E-04	
B:\DR95N30A.004	%Error	NF	1.33%	0.77%	1.17%	0.25%	0.14%	0.17%	0.14%	0.19%	0.14%	1.15%	0.63%	
	Average		1.04E-02	3.19E-02	1.31E-02	4.03E-01	5.26E+00	1.72E+00	2.66E+01	1.00E+00	7.05E+00	5.19E-03	4.69E-02	
	Std Dev		3.35E-04	1.13E-03	2.18E-04	2.55E-02	2.50E-01	2.99E-02	2.18E-01	0.00E+00	6.34E-02	3.00E-03	1.50E-04	
	% Std Dev		3.22%	3.53%	1.67%	6.32%	4.76%	1.73%	0.82%	0.00%	0.90%	57.73%	0.32%	
							Calc MgO/Mg=	-1.04E-04		Corrected Ca/Si	7.05E+00		4.70E-02	
							Meas MgO/Mg=	3.01E-03						
							Meas 42Ca/40Ca=	6.65E-03		true 42Ca/40Ca=6.67E-03				
Olivine														
B:\DR95N29A.007	30si	0.00E+00	2.27E-03	9.21E-05	5.02E-05	4.46E-01	1.02E-02	1.13E+01	1.31E-01	1.00E+00	2.49E-01	5.23E-03	6.01E-03	
B:\DR95N29A.007	Sigma	NF	2.30E-05	1.46E-06	1.08E-06	5.47E-04	6.92E-05	6.02E-03	2.62E-04	9.63E-04	3.80E-04	4.84E-05	5.30E-05	
B:\DR95N29A.007	%Error	NF	1.01%	1.59%	2.15%	0.12%	0.68%	0.07%	0.20%	0.10%	0.15%	0.94%	0.88%	
B:\DR95N29A.008	30si	0.00E+00	2.28E-03	9.10E-05	5.48E-05	4.63E-01	9.91E-03	1.14E+01	1.30E-01	1.00E+00	2.40E-01	5.11E-03	5.80E-03	
B:\DR95N29A.008	Sigma	NF	2.90E-05	1.82E-06	1.41E-06	7.03E-04	8.55E-05	1.01E-02	3.27E-04	1.21E-03	4.67E-04	6.12E-05	6.52E-05	
B:\DR95N29A.008	%Error	NF	1.27%	2.00%	2.58%	0.15%	0.86%	0.09%	0.25%	0.12%	0.19%	1.20%	1.13%	
B:\DR95N29A.009	30si	0.00E+00	2.43E-03	8.71E-05	5.03E-05	4.42E-01	1.13E-02	1.11E+01	1.22E-01	1.00E+00	2.51E-01	4.91E-03	5.80E-03	
B:\DR95N29A.009	Sigma	NF	2.14E-05	1.28E-06	9.71E-07	4.89E-04	6.53E-05	7.11E-03	2.26E-04	8.65E-04	3.43E-04	4.30E-05	4.67E-05	
B:\DR95N29A.009	%Error	NF	0.88%	1.47%	1.93%	0.11%	0.58%	0.06%	0.19%	0.09%	0.14%	0.88%	0.81%	
B:\DR95N29A.00A	30si	0.00E+00	1.92E-03	9.11E-05	6.31E-05	4.92E-01	8.53E-03	1.14E+01	1.32E-01	1.00E+00	2.43E-01	5.29E-03	6.12E-03	
B:\DR95N29A.00A	Sigma	NF	2.83E-05	1.95E-06	1.62E-06	7.81E-04	6.46E-05	1.08E-02	3.53E-04	1.29E-03	5.01E-04	6.65E-05	7.16E-05	
B:\DR95N29A.00A	%Error	NF	1.47%	2.14%	2.57%	0.16%	0.99%	0.10%	0.27%	0.13%	0.21%	1.26%	1.17%	
B:\DR95N29A.00E	30si	0.00E+00	1.72E-03	8.72E-05	3.42E-05	5.05E-01	7.90E-03	1.14E+01	1.28E-01	1.00E+00	2.44E-01	5.41E-03	6.38E-03	
B:\DR95N29A.00E	Sigma	NF	1.57E-05	3.52E-06	2.20E-06	7.34E-04	7.51E-05	9.98E-03	3.19E-04	1.19E-03	4.64E-04	6.21E-05	6.74E-05	
B:\DR95N29A.00E	%Error	NF	0.91%	4.03%	6.44%	0.15%	0.95%	0.09%	0.25%	0.12%	0.19%	1.15%	1.06%	
B:\DR95N30A.001	30si	0.00E+00	2.03E-03	9.00E-05	4.80E-05	4.00E-01	9.62E-03	1.11E+01	1.34E-01	1.00E+00	2.56E-01	4.71E-03	5.75E-03	
B:\DR95N30A.001	Sigma	NF	2.69E-05	1.27E-06	9.24E-07	4.46E-04	5.88E-05	6.87E-03	2.33E-04	8.43E-04	3.38E-04	4.10E-05	4.53E-05	
B:\DR95N30A.001	%Error	NF	1.33%	1.41%	1.92%	0.11%	0.61%	0.06%	0.17%	0.08%	0.13%	0.87%	0.79%	
B:\DR95N30A.002	30si	0.00E+00	2.16E-03	8.50E-05	1.62E-04	4.59E-01	1.01E-02	1.12E+01	1.45E-01	1.00E+00	2.47E-01	5.02E-03	5.96E-03	
B:\DR95N30A.002	Sigma	NF	3.02E-05	1.34E-06	1.85E-06	5.30E-04	6.53E-05	7.58E-03	2.63E-04	9.16E-04	3.59E-04	4.60E-05	5.02E-05	
B:\DR95N30A.002	%Error	NF	1.39%	1.57%	1.14%	0.12%	0.65%	0.07%	0.18%	0.09%	0.15%	0.92%	0.84%	
	Average		2.12E-03	8.91E-05	5.01E-05	4.58E-01	9.65E-03	1.13E+01	1.32E-01	1.00E+00	2.47E-01	5.10E-03	5.97E-03	
	Std Dev		2.46E-04	2.63E-06	9.48E-06	3.45E-02	1.12E-03	1.24E-01	6.83E-03	0.00E+00	5.36E-03	2.39E-04	2.23E-04	
	% Std Dev		11.60%	2.96%	18.93%	7.52%	11.56%	1.10%	5.27%	0.00%	2.17%	4.68%	3.73%	
SiO2 in glass =	56.4	Si Ratio=	0.74113475				Calc MgO/Mg=	4.03E-04		Corrected Ca/Si	2.15E-01		1.43E-03	
SiO2 in Olivine =	41.8						Meas MgO/Mg=	4.53E-04						
Partition Coefficients	D		1.510E-01	2.068E-03	2.835E-03	8.422E-01	1.360E-03	4.839E+00	3.671E-03		2.257E-02		2.265E-02	
	Std Dev		1.818E-02	9.527E-05	5.387E-04	8.275E-02	1.700E-04	9.939E-02	1.956E-04		5.296E-04		6.485E-04	
	% Std Dev		12.04%	4.61%	19.00%	9.83%	12.50%	2.05%	5.33%		2.35%		2.75%	

Table 4 8c*-2													
	RATIO D N=>	6.4	7li	9be	11b	16o	23na	26mg	27al	30si	40ca	42ca	
Glass													
C:\DATA\BETH\DR95N27A.003	30si	0.00E+00	1.79E-02	3.49E-02	3.57E-03	4.28E-01	2.38E+00	2.77E+00	3.62E+01	1.00E+00	1.62E+01	1.07E-01	
C:\DATA\BETH\DR95N27A.003	Sigma	INF	1.31E-04	1.84E-04	5.81E-05	7.60E-04	2.75E-03	3.14E-03	3.57E-02	1.37E-03	1.62E-02	3.34E-04	
C:\DATA\BETH\DR95N27A.003	%Error	INF	0.73%	0.53%	1.63%	0.18%	0.12%	0.11%	0.10%	0.14%	0.10%	0.31%	
C:\DATA\BETH\DR95N27A.004	30si	0.00E+00	1.89E-02	3.45E-02	3.74E-03	3.80E-01	2.77E+00	2.59E+00	3.55E+01	1.00E+00	1.60E+01	1.06E-01	
C:\DATA\BETH\DR95N27A.004	Sigma	INF	1.35E-04	1.84E-04	4.23E-05	7.07E-04	3.15E-03	2.97E-03	3.51E-02	1.38E-03	1.61E-02	3.33E-04	
C:\DATA\BETH\DR95N27A.004	%Error	INF	0.72%	0.53%	1.13%	0.19%	0.11%	0.11%	0.10%	0.14%	0.10%	0.32%	
C:\DATA\BETH\DR95N27A.009	30si	0.00E+00	1.81E-02	3.50E-02	3.64E-03	4.31E-01	2.43E+00	2.76E+00	3.64E+01	1.00E+00	1.62E+01	1.07E-01	
C:\DATA\BETH\DR95N27A.009	Sigma	INF	1.70E-04	2.38E-04	4.38E-05	9.82E-04	3.61E-03	4.02E-03	4.61E-02	1.77E-03	2.08E-02	4.30E-04	
C:\DATA\BETH\DR95N27A.009	%Error	INF	0.94%	0.68%	1.20%	0.23%	0.15%	0.15%	0.13%	0.18%	0.13%	0.40%	
C:\DATA\BETH\DR95N27A.00A	30si	0.00E+00	1.78E-02	3.51E-02	3.74E-03	4.31E-01	2.34E+00	2.75E+00	3.65E+01	1.00E+00	1.60E+01	1.07E-01	
C:\DATA\BETH\DR95N27A.00A	Sigma	INF	1.91E-04	2.71E-04	4.38E-05	1.11E-03	3.96E-03	4.56E-03	5.26E-02	2.01E-03	2.34E-02	4.88E-04	
C:\DATA\BETH\DR95N27A.00A	%Error	INF	1.07%	0.77%	1.17%	0.26%	0.17%	0.17%	0.14%	0.20%	0.15%	0.46%	
C:\DATA\BETH\DR95N27A.00B	30si	-1.67E-14	1.78E-02	3.56E-02	3.73E-03	4.34E-01	2.31E+00	2.74E+00	3.66E+01	1.00E+00	1.61E+01	1.07E-01	
C:\DATA\BETH\DR95N27A.00B	Sigma	-2.85E-07	1.91E-04	2.73E-04	4.37E-05	1.12E-03	3.92E-03	4.55E-03	5.27E-02	2.01E-03	2.35E-02	4.88E-04	
C:\DATA\BETH\DR95N27A.00B	%Error	>1000000%	1.07%	0.77%	1.17%	0.26%	0.17%	0.17%	0.14%	0.20%	0.15%	0.46%	
C:\DATA\BETH\DR95N27A.00C	30si	0.00E+00	1.82E-02	3.55E-02	3.71E-03	4.22E-01	2.31E+00	2.78E+00	3.66E+01	1.00E+00	1.60E+01	1.06E-01	
C:\DATA\BETH\DR95N27A.00C	Sigma	INF	1.95E-04	2.75E-04	3.84E-05	1.11E-03	3.96E-03	4.65E-03	5.32E-02	2.03E-03	2.37E-02	4.91E-04	
C:\DATA\BETH\DR95N27A.00C	%Error	INF	1.07%	0.77%	1.06%	0.26%	0.17%	0.17%	0.15%	0.20%	0.15%	0.46%	
C:\DATA\BETH\DR95N28A.003	30si	0.00E+00	1.75E-02	3.52E-02	3.65E-03	4.72E-01	2.33E+00	2.80E+00		1.00E+00	1.63E+01	1.08E-01	
C:\DATA\BETH\DR95N28A.003	Sigma	INF	1.03E-04	1.48E-04	4.69E-05	6.45E-04	2.16E-03	2.53E-03		1.09E-03	1.20E-02	2.67E-04	
C:\DATA\BETH\DR95N28A.003	%Error	INF	0.59%	0.42%	1.28%	0.14%	0.09%	0.09%		0.11%	0.08%	0.25%	
C:\DATA\BETH\DR95N28A.004	30si	0.00E+00	1.76E-02	3.48E-02	3.73E-03	4.58E-01	2.32E+00	2.80E+00		1.00E+00	1.63E+01	1.08E-01	
C:\DATA\BETH\DR95N28A.004	Sigma	INF	9.59E-05	1.36E-04	4.38E-05	5.85E-04	1.99E-03	2.34E-03		1.01E-03	1.20E-02	2.47E-04	
C:\DATA\BETH\DR95N28A.004	%Error	INF	0.54%	0.39%	1.17%	0.13%	0.09%	0.08%		0.10%	0.07%	0.23%	
	Average		1.80E-02	3.51E-02	3.69E-03	4.32E-01	2.40E+00	2.75E+00	3.63E+01	1.00E+00	1.61E+01	1.07E-01	
	Std Dev		4.50E-04	3.55E-04	6.13E-05	2.68E-02	1.57E-01	6.82E-02	4.23E-01	0.00E+00	1.13E-01	7.21E-04	
	% Std Dev		2.50%	1.01%	1.66%	6.20%	6.56%	2.48%	1.16%	0.00%	0.70%	0.68%	
										40/42=	6.62E-03		
										true 40,42=	6.67E-03		
Olivine													
C:\DATA\BETH\DR95N27A.005	30si	0.00E+00	2.47E-03	7.18E-05	6.01E-05	4.90E-01	5.55E-03	1.14E+01	3.43E-01	1.00E+00	3.91E-01	6.78E-03	
C:\DATA\BETH\DR95N27A.005	Sigma	INF	3.12E-05	4.06E-06	3.72E-06	1.83E-03	9.29E-05	2.55E-02	1.45E-03	3.03E-03	1.58E-03	8.02E-05	
C:\DATA\BETH\DR95N27A.005	%Error	INF	1.26%	5.66%	6.19%	0.37%	1.67%	0.22%	0.42%	0.30%	0.40%	1.18%	
C:\DATA\BETH\DR95N27A.006	30si	0.00E+00	2.93E-03	7.27E-05	2.70E-05	4.39E-01	4.82E-03	1.12E+01	3.11E-01	1.00E+00	3.98E-01	6.63E-03	
C:\DATA\BETH\DR95N27A.006	Sigma	INF	3.10E-05	1.54E-06	9.39E-07	6.42E-04	5.82E-05	9.45E-03	5.16E-04	1.14E-03	6.02E-04	6.60E-05	
C:\DATA\BETH\DR95N27A.006	%Error	INF	1.06%	2.12%	3.48%	0.15%	1.17%	0.08%	0.17%	0.11%	0.15%	1.00%	
C:\DATA\BETH\DR95N27A.007	30si	0.00E+00	2.61E-03	7.08E-05	3.56E-05	4.50E-01	4.24E-03	1.12E+01	3.07E-01	1.00E+00	3.97E-01	6.83E-03	
C:\DATA\BETH\DR95N27A.007	Sigma	INF	3.03E-05	1.58E-06	1.12E-06	6.76E-04	5.47E-05	9.81E-03	5.31E-04	1.18E-03	6.23E-04	6.94E-05	
C:\DATA\BETH\DR95N27A.007	%Error	INF	1.16%	2.23%	3.14%	0.15%	1.29%	0.09%	0.17%	0.12%	0.16%	1.02%	
C:\DATA\BETH\DR95N27A.00D	30si	0.00E+00	2.73E-03	7.34E-05	1.91E-05	4.64E-01	4.96E-03	1.14E+01	2.69E-01	1.00E+00	3.96E-01	7.05E-03	
C:\DATA\BETH\DR95N27A.00D	Sigma	INF	3.02E-05	1.57E-06	7.99E-07	6.73E-04	5.77E-05	9.69E-03	4.77E-04	1.15E-03	6.07E-04	6.88E-05	
C:\DATA\BETH\DR95N27A.00D	%Error	INF	1.11%	2.13%	4.18%	0.15%	1.16%	0.09%	0.18%	0.12%	0.15%	0.98%	
C:\DATA\BETH\DR95N27A.00E	30si	0.00E+00	2.82E-03	7.11E-05	1.88E-05	4.47E-01	4.49E-03	1.13E+01	2.65E-01	1.00E+00	3.98E-01	7.29E-03	
C:\DATA\BETH\DR95N27A.00E	Sigma	INF	3.20E-05	1.60E-06	8.24E-07	6.83E-04	5.70E-05	9.87E-03	4.92E-04	1.20E-03	6.33E-04	7.27E-05	
C:\DATA\BETH\DR95N27A.00E	%Error	INF	1.13%	2.25%	4.38%	0.15%	1.27%	0.09%	0.19%	0.12%	0.16%	1.00%	
C:\DATA\BETH\DR95N27A.00F	30si	0.00E+00	2.59E-03	7.21E-05	2.34E-05	4.79E-01	4.38E-03	1.13E+01	2.95E-01	1.00E+00	3.97E-01	7.31E-03	
C:\DATA\BETH\DR95N27A.00F	Sigma	INF	4.58E-05	1.71E-06	9.72E-07	7.57E-04	5.97E-05	1.06E-02	5.56E-04	1.27E-03	6.70E-04	7.72E-05	
C:\DATA\BETH\DR95N27A.00F	%Error	INF	1.77%	2.37%	4.16%	0.16%	1.36%	0.09%	0.19%	0.13%	0.17%	1.06%	
C:\DATA\BETH\DR95N28A.001	30si	0.00E+00	2.81E-03	7.32E-05	2.23E-05	3.81E-01	4.57E-03	1.10E+01	2.84E-01	1.00E+00	4.17E-01	6.87E-03	
C:\DATA\BETH\DR95N28A.001	Sigma	INF	3.62E-05	1.31E-06	7.19E-07	5.03E-04	4.62E-05	7.81E-03	4.12E-04	9.63E-04	5.24E-04	5.67E-05	
C:\DATA\BETH\DR95N28A.001	%Error	INF	1.29%	1.78%	3.23%	0.13%	1.01%	0.07%	0.14%	0.10%	0.13%	0.83%	
C:\DATA\BETH\DR95N28A.002	30si	0.00E+00	2.50E-03	7.25E-05	3.11E-05	5.53E-01	4.03E-03	1.13E+01	3.15E-01	1.00E+00	3.88E-01	6.99E-03	
C:\DATA\BETH\DR95N28A.002	Sigma	INF	3.29E-05	1.25E-06	8.19E-07	6.08E-04	4.18E-05	7.76E-03	4.22E-04	9.28E-04	4.82E-04	5.51E-05	
C:\DATA\BETH\DR95N28A.002	%Error	INF	1.31%	1.73%	2.63%	0.11%	1.04%	0.07%	0.13%	0.09%	0.12%	0.79%	
	Average		2.68E-03	7.22E-05	2.53E-05	4.64E-01	4.63E-03	1.13E+01	2.98E-01	1.00E+00	3.98E-01	6.97E-03	
	Std Dev		1.64E-04	9.32E-07	6.28E-06	4.64E-02	4.77E-04	1.34E-01	2.58E-02	0.00E+00	8.74E-03	2.40E-04	
	% Std Dev		6.12%	1.29%	24.81%	10.00%	10.29%	1.19%	8.63%	0.00%	2.20%	3.45%	
SiO2 in glass =	48.67	Si Ratio=	0.8814465										
SiO2 in Olivine =	42.9						MgO/Mg=	4.02E-04		Corrected Ca/Si	3.65E-01	2.44E-03	
Partition Coefficients	D		1.314E-01	1.814E-03	6.050E-03	9.471E-01	1.702E-03	3.613E+00	7.248E-03		1.997E-02	2.012E-02	
	Std Dev		8.691E-03	2.975E-05	1.504E-03	1.115E-01	2.077E-04	9.937E-02	6.312E-04		4.607E-04	7.066E-04	
	% Std Dev		6.62%	1.64%	24.87%	11.77%	12.21%	2.75%	8.71%		2.31%	3.51%	

Table 5 Summary			
D	7li	9be	11b
composition			
1b*-2	1.536E-01	2.865E-03	4.410E-03
50-50*-2	1.510E-01	2.068E-03	2.835E-03
8c*-2	1.314E-01	1.814E-03	6.050E-03
average	1.453E-01	2.249E-03	4.432E-03
1-sigma	1.214E-02	5.484E-04	1.608E-03

Design and Development of Client Database Applications, Using Oracle Power Objects*

Tri M. Nguyen

Loyola Marymount University

Computations Department
Lawrence Livermore National Laboratory
Livermore, California 94550

December 12, 1995

Prepare in partial fulfillment of the requirements of the Science and Engineering Research Semester under the direction of John Wade and Young Seiden, Research Mentors, in the Lawrence Livermore National Laboratory.

* This research was supported in part by an appointment to the U.S. Department of Energy's Science and Engineering Research Semester (hereinafter called SERS) program administered by LLNL under Contract W-7405-Eng-48 with Lawrence Livermore National Laboratory.

Design and Development of Client Database Applications, Using Oracle Power Objects

Tri M. Nguyen
Loyola Marymount University
Computations Department
Lawrence Livermore National Laboratory

ABSTRACT

The purpose of this project is to design and to build a suite of client database applications to track work orders and hours spent by employees of the Electronic Services Department. The applications are developed and constructed using Oracle Power Objects. In the object-oriented and integrated environment of this tool, the pre-defined codes are augmented and altered.

Due to bugs and errors in Power Objects itself, only one application has been completed at the current time. As part of an on-going effort, this project should be continued until most of the applications are completed. Costs and benefits of the finished applications can then be evaluated, and a decision can then be made to continue using Power Objects or to use an alternative tool.

Table of Contents

Abstract iii

1. Introduction 1
- 1.1 Overview 1
- 1.2 Problem Definition 1
- 1.3 Requirements 2

2. Background 4
- 2.1 Business Procedures 4
- 2.2 Current Database 6
- 2.3 System Components & Interfaces 8
- 2.4 Computer-Human Interface 12

3. Methods & Tools Used 15
- 3.1 Automation & Object-Oriented Principles 15
- 3.2 Properties of PO Objects 18
- 3.3 Methods of PO Objects 20
- 3.4 Design & Development Methodology 22

4. Sample Iterations of Development Cycle 23
- 4.1 Adding a New Feature - Altering the Framework 25
- 4.2 Testing the Alterations 27
- 4.3 Debug & Analyze 29

5. Results 31
- 5.1 Accomplishments 31
- 5.2 Works in Progress 31

6. Conclusions & Recommendations 32
- 6.1 Significance of Accomplishments 32
- 6.2 Next Steps 32

Bibliography 33

Acknowledgments 34

List of Illustrations

Figure 1	3
Figure 2	5
Figure 3	7
Figure 4	9
Figure 5	11
Figure 6	14
Figure 7	17
Figure 8	19
Figure 9	21
Figure 10	24
Figure 11	26
Figure 12	28
Figure 13	30

1. Introduction

1.1 Overview

For small companies or departments, keeping track of employees and jobs is relative easy. In these situations, paper forms and punch cards could be appropriate. However, as companies and departments grow in size -- in terms of personnel and orders -- the method of tracking just mentioned becomes daunting and time-consuming. This scenario applies to the Electronic Services and Electronic Manufacturing Departments at Lawrence Livermore National Laboratory. The systems of these two departments have already moved from paper forms to electronic forms. However, there are some problems with the current systems. The project described in this paper addresses these problems and upgrades to the current electronic forms. In particular, this paper will discuss the problems, background, methods & tools, development cycle, and results of the project. The problems and requirements will be defined in the next two sub-sections.

1.2 Problem Definition

The customers are the Electronic Services (ES) Department and Electronic Manufacturing (EM) Department. In particular, the project described in this paper focuses on the Electronic Services Department, but both departments have similar protocols and systems. So, solutions implemented for one department can be easily transported to the other department. The crux of the customers' demands and the project is to construct a front-end application, which runs on a Macintosh computer and

connects to an Oracle 7 server. The purpose is to maintain records of hours spent by ES employees on jobs and work orders. Ultimately, the upgrades will track jobs and work orders from creation to completion.

1.3 Requirements

The following list is a detailed view of the requirements for the problem:

- Target applications run on Macintosh desktop computers
- Connect to an Oracle 7 (DEC/OSF Unix) server
- Functionalities & features specified by mentor(s) & communities of users (employees)
- Controls & presentations with graphical user interfaces (GUIs)
- Consistency with previous versions, especially the current version

See Figure 1.

Figure 1 presents and encapsulates a simplified view of the problem and requirements defined so far. The requirements will be more clear after the background is covered.

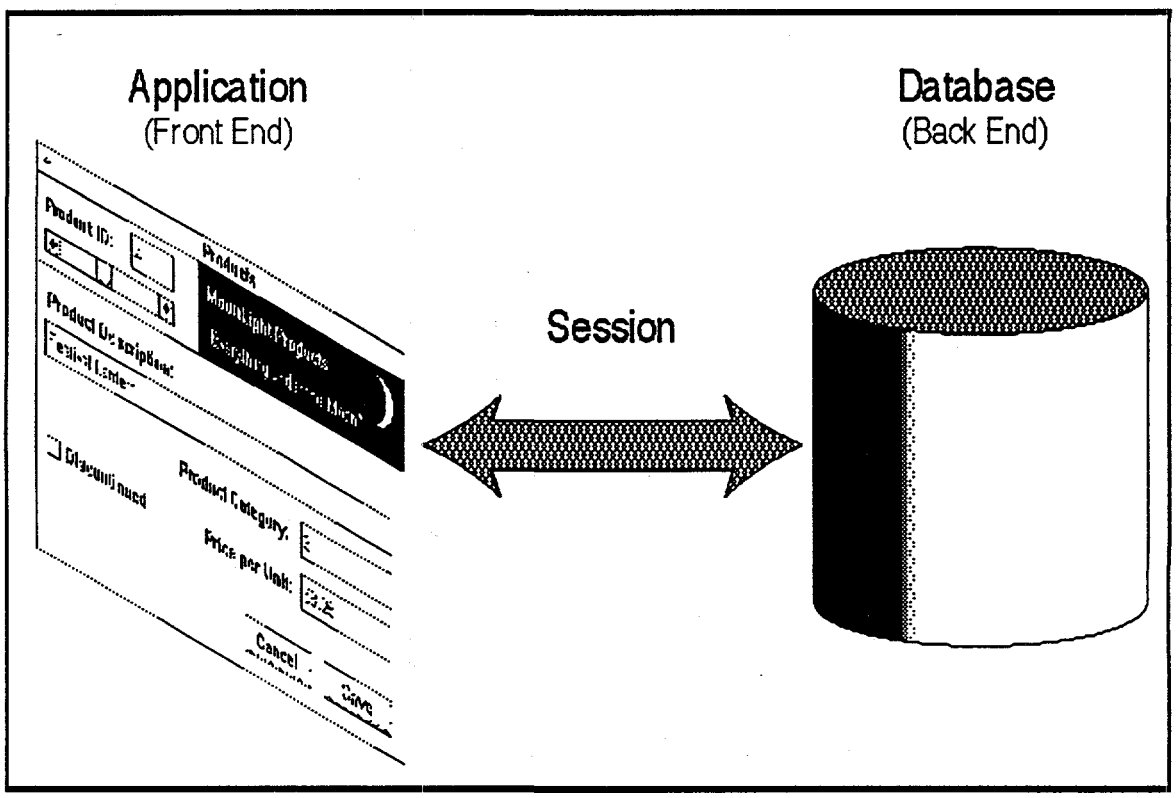

Figure 1: Simplified view of problem & requirements (Roberts, *Getting Started with Oracle Power Objects, Version 1.0*)

2. Background

To see how the problems and requirements fit into the overall picture, some background will now be provided. In particular, the business procedures, current database, system components & interfaces, and issues of computer-human interface will be discussed.

2.1 Business Procedures

In this sub-section, the business procedures of the ES Department -- i.e. what a typical ES employee performs -- will be described. Here are the events that occur:

- Jobs and work orders are created (because an electronic component or part needs repair or service)
- Employees perform the job or work order
- Employees log hours spent performing specific work orders
- Accounts are charged for labor performed
- Employees are paid accordingly
- Work orders are completed

To log these activities, an employee must enter the data in the following electronic form: time card application. See Figure 2.

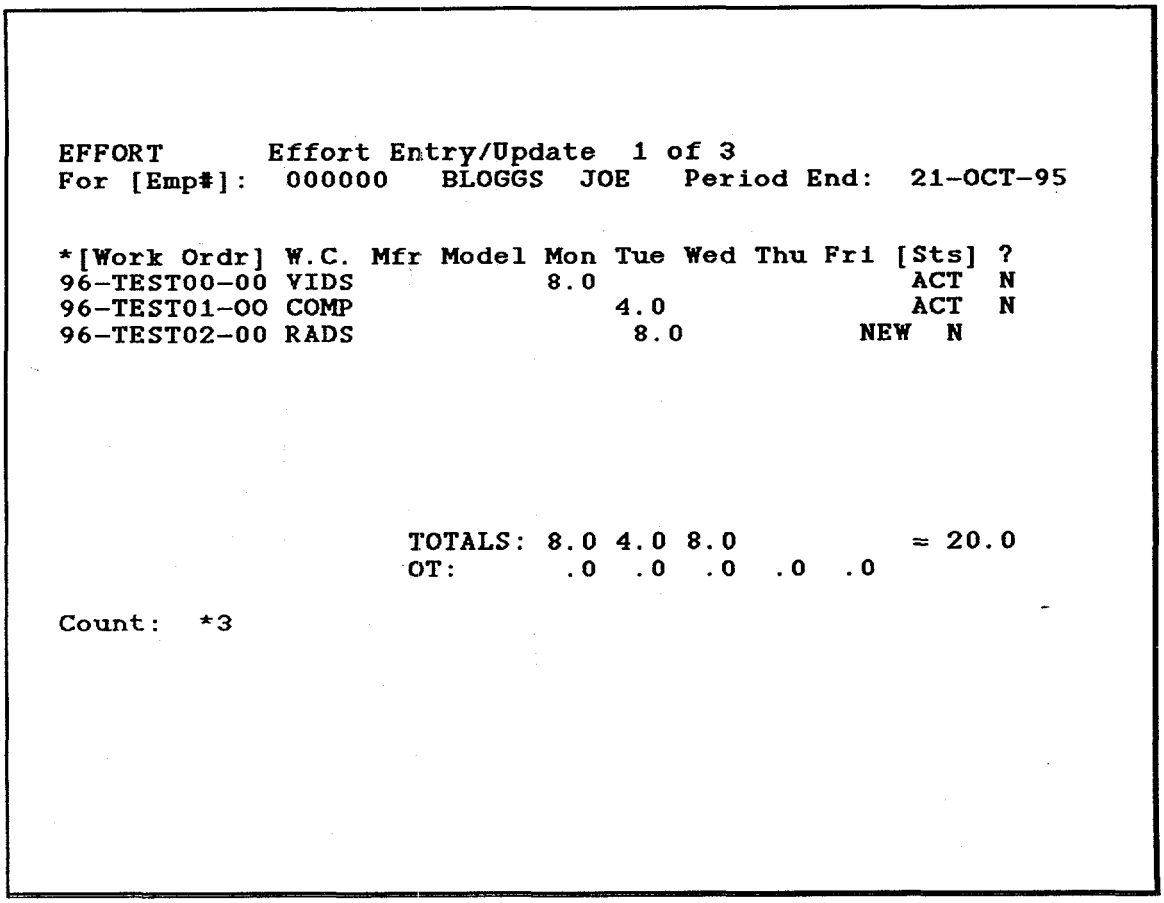

Figure 2: Current character-based application.

The current electronic form is character-based. Evidently, the character-based presentation is not intuitive and not easy to use. To enter time, employees must navigate through fields and forms using the keyboard. Thus, employees delay time entry and logging their work. As a result, records are not updated and maintained properly.

2.2 Current Database

The current system has a database and applications to manipulate the data. In this sub-section, the focus is on the database, which is the server that applications of this project must connect to and access data from. As typical with any database, the current database has the following elements:

- Tables
  - Structure records of data
- Keys
  - Identifying fields in tables
- Joins
  - Relationships between tables

Figure 3 contains a snapshot of table snippets, which are used in the current working applications.

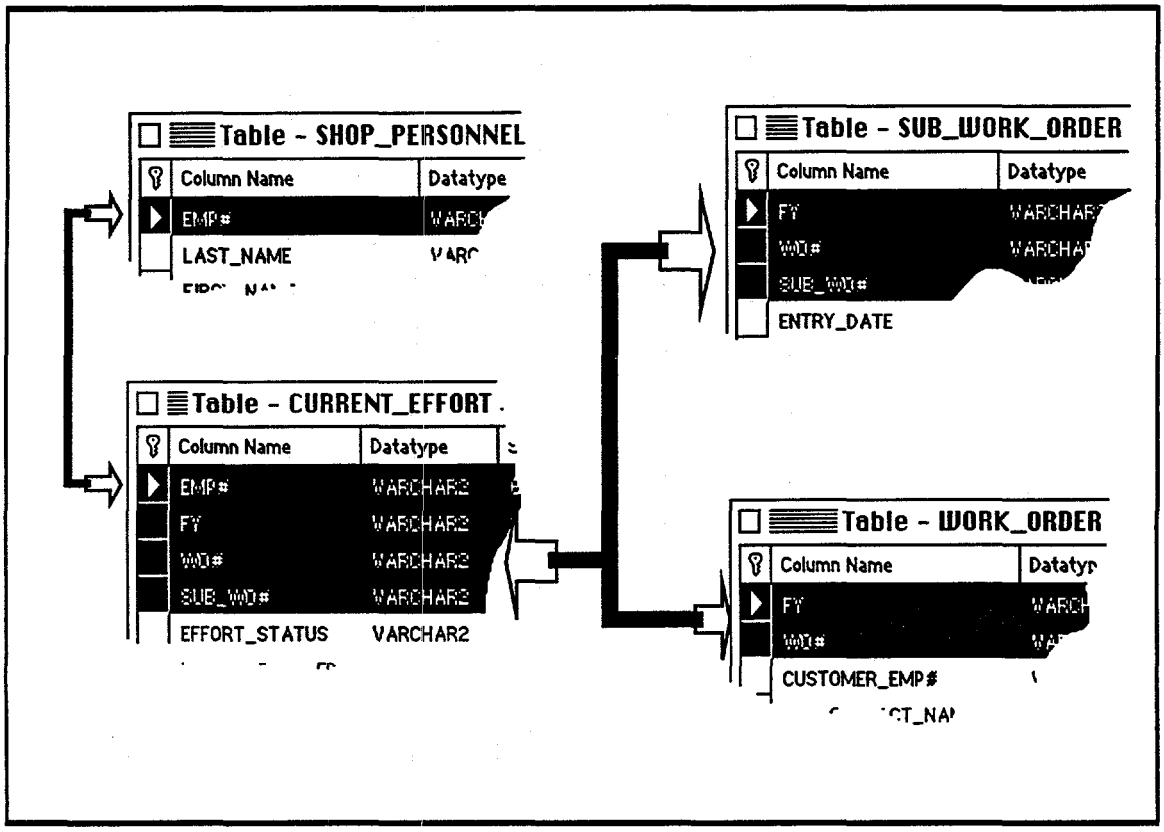

Figure 3: Sample database tables.

Figure 3 contains snippets of 4 tables: SHOP_PERSONNEL, CURRENT_EFFORT, SUB_WORK_ORDER, AND WORK_ORDER. The table, SHOP_PERSONNEL, contains information about employees, such as employee number. The table, CURRENT_EFFORT, contains information about hours spent by employees performing certain jobs and work orders. The tables, SUB_WORK_ORDER and WORK_ORDER, contain information about jobs and work orders. As illustrated in Figure 3, the field, EMP#, is the key for the table, SHOP_PERSONNEL. The keys: FY, WO#, and SUB_WO#, represent the relationships between the tables: CURRENT_EFFORT, SUB_WORK_ORDER, and WORK_ORDER.

2.3 System Components & Interfaces

The current system includes other elements besides the database. Also, the applications of the current system are all server-based. Figure 4 illustrates the server principles and components.

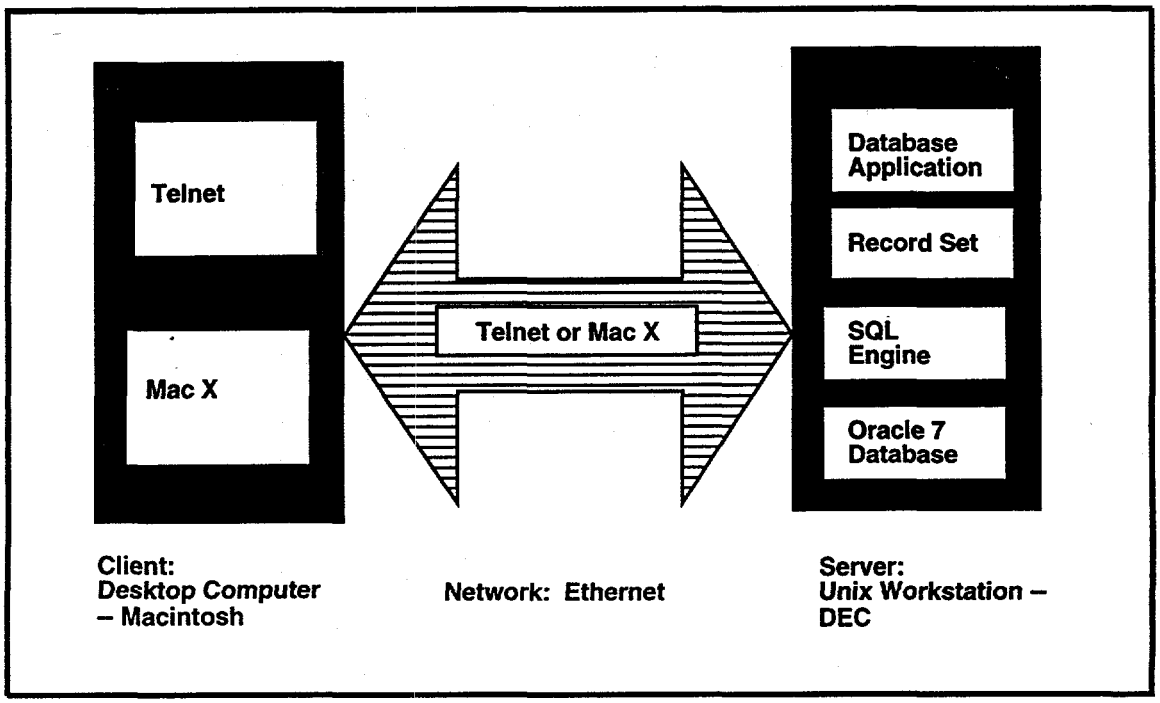

Figure 4: Model of server applications.

With the model as presented in Figure 4, all of the applications reside on the Oracle 7 server. The employees still use desktop computers to launch the applications and enter data. However, the desktop computers are just 'dumb terminals'. There are two main disadvantages with this paradigm. The network will be slowed down by the 'heavy traffic'. In other words, all transactions and commands, such as entering and leaving fields, are transmitted across the network, and the server processes all of those transactions and commands. The server will likewise be slowed down, because it must run the applications as well as maintain the data.

The applications produced in this project changed paradigms. The server still maintains the data, but the applications reside on the client, desktop computers. The client-server paradigm has the following elements:

- Oracle 7: Database back-end & server
- SQL Engine: Accepts & performs database commands
- SQL*Net: Network
- Record set: Local copies of data
- User application: client front-end

Figure 5 illustrates the client-server principles and components.

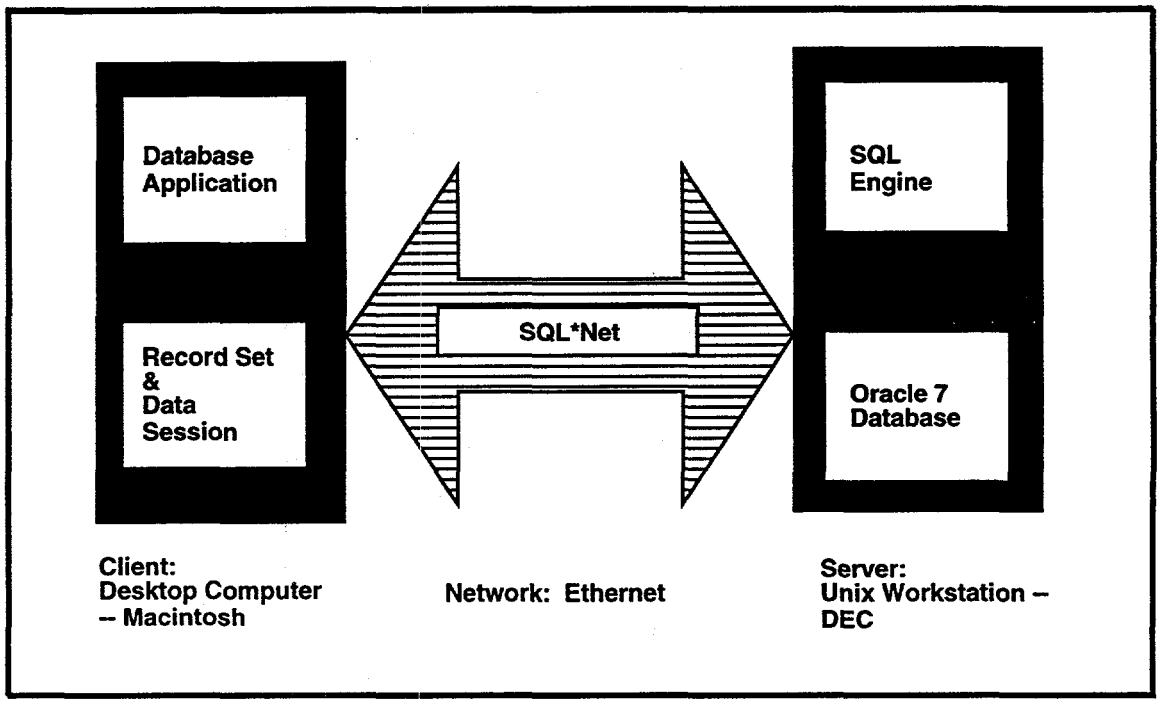

Figure 5: Client-server principles & components.

The client-server paradigm avoids the disadvantages of the previous paradigm. The client computer runs the application locally. The client computer also keeps and manipulates local copies of data, and it contacts the server only when it needs to read new data or when it needs to commit changed data. Thus, network traffic is minimized, and the server only has to maintain the data. Overall, the upgrades to the current system involved two changes: (1) moving the user interfaces from character-based presentations to graphical user interfaces, and (2) moving the applications from the server to the clients.

2.4 Computer-Human Interface

There are other issues that have to be addressed in the design and development process. In particular, this sub-section will deal with the issues of computer-human interface (CHI) -- i.e. appearance and look of the application's GUIs. The following listing itemizes only a small subset of CHI issues encountered in the project:

- Easy to use
- Intuitive
  - Meet expectations of users
- Nice & clean presentation
- Paths of navigation

The first three items are obvious. ES employees should concentrate on servicing the electronic components and parts, not on using the database applications -- especially the time card application. The last item needs some explanation. Paths of navigation (PON) are traversals between states, especially between fields and forms. One example of PON is default buttons and "safest path". For destructive actions, the default button should be

'CANCEL', not 'OK', but for normal actions, the default button can direct toward expected and common actions. In the time card application, there are at least five buttons: 'ADD JOB', 'PRINT', 'QUIT', 'ROLLBACK', & 'COMMIT'. The only action that might qualify as being destructive is 'QUIT', which ends the application. Since none of the five buttons are really destructive, the five buttons can be classified as normal and common actions. Most of the time, the users will enter time and then commit the data. Thus, in the time card application, the default button is 'COMMIT'. Note the default button of the form in Figure 6. Another subtle CHI issued dealt in the time card is the way the widgets are drawn. Fields that are 'read-only' are drawn as standard controls; fields that can be manipulated by user are drawn as 3-D controls. Note how the widgets of the application in Figure 6 are drawn.

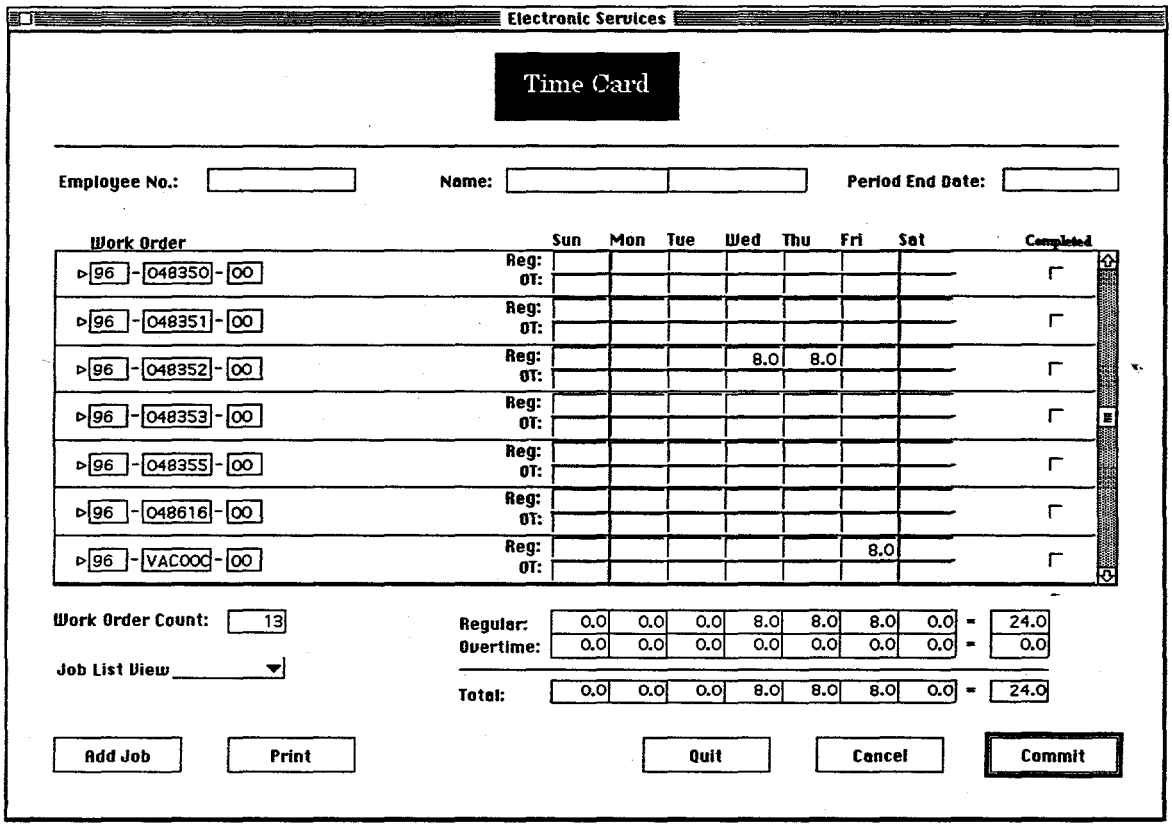

Figure 6: Before alteration.

3. Methods & Tools Used

The tool used to design and develop the client database applications is Oracle Power Objects (PO). The tool has the following elements:

- Framework
  - Properties
  - Methods
- Integrated & object-oriented setting
  - Object hierarchy
  - Event-driven & triggers
  - Automatic query & default processing

The next three sub-sections will further discuss the elements of Power Objects.

3.1 Automation & Object-Oriented Principles

In Power Objects, each widget or graphical component is considered as an object -- even the application itself. See Figure 7. Therefore, in some aspects, Power Objects is "object-oriented". Under the object-oriented ideology, each object has properties and methods. Objects can be embedded in other objects.

Also, some widgets, called bindable objects, have automatic queries. In other words, the bindable widget only has to be linked to a table in the database. When the applications or forms are launched, the record sets, which are managers of local copies of data, populate the widgets with data from the database. For forms with nested levels of embedded, the automatic queries follow a top-down approach. In other words, the application queries for the top-most object in the hierarchy of Figure 7. Then, it queries

for objects on the lower levels. There is a similar element in the automatic event-handling mechanism of PO. Events are handled automatically from a bottom-up approach. For controls, the event or message is passed to the controls themselves.

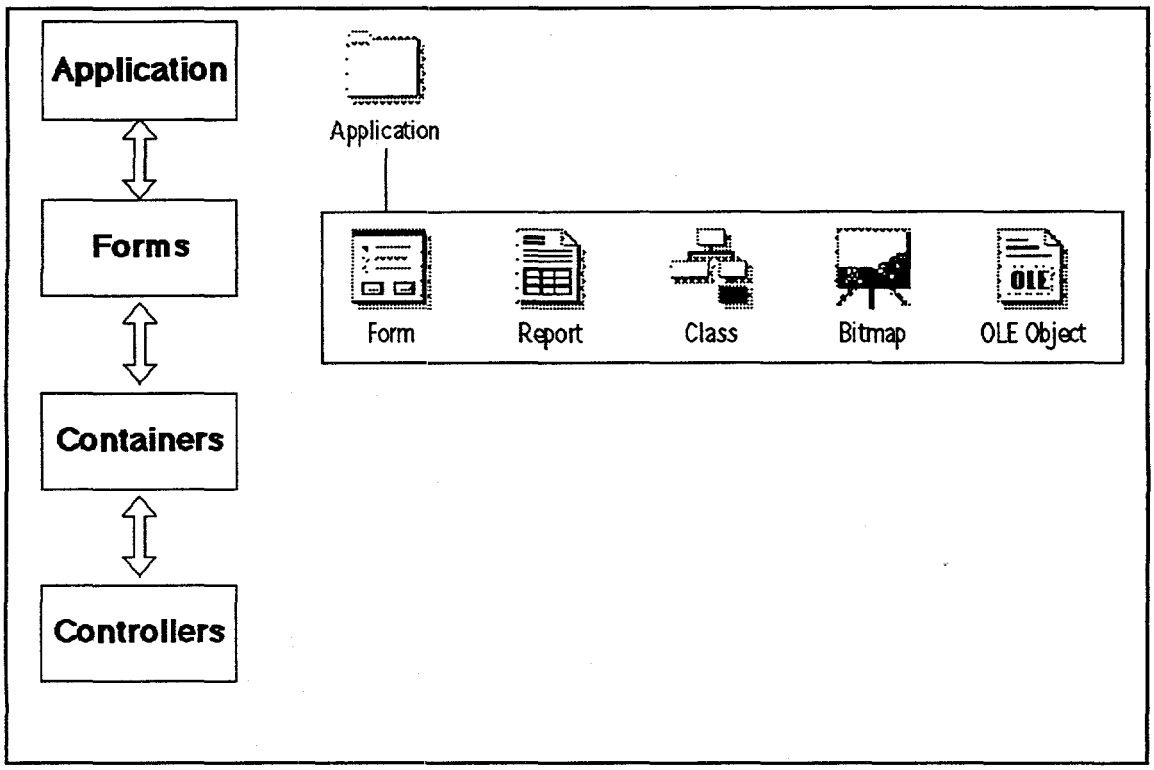

Figure 7: Hierarchy & event-handling flow of PO objects & widgets (Roberts, *Getting Started with Oracle Power Objects, Version 1.0*).

3.2 Properties of PO Objects

As mentioned before, PO has some object-oriented principles -- e.g. properties and methods. Each object has properties, which are accessed through property sheets as illustrated in Figure 8. The properties for a repeater display is given in Figure 8. The first, third, and fifth sections of the repeater display's property sheet determine how the widget is displayed. The second section determines how the repeater display is linked to other objects in the same form or application. The fourth section determines how the repeater display is linked to tables in the database.

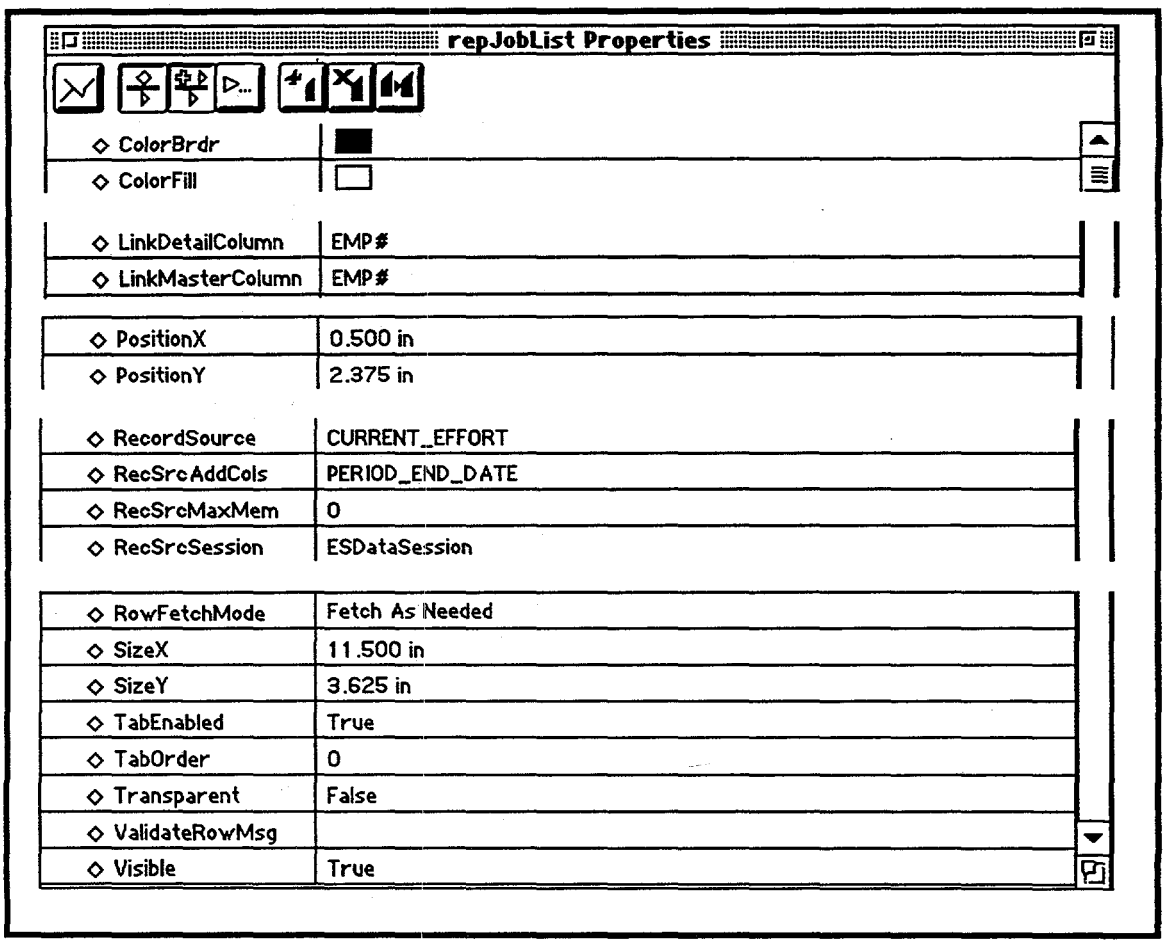

Figure 8: Example properties of a repeater display.

3.3 Methods of PO Objects

Objects in Power Objects have methods to complement the properties, especially for handling events. As mentioned before, events are handled using a bottom-up approach. However, methods can be used for other purposes also, as illustrated in Figure 9. In that figure, the method, udmGetSQLPeriodEndDate(), does not handle events. Instead, it determines the next period end date based on the server's current date. The method, udmGetSQLPeriodEndDate(), is called from within the method, QueryMasters(). In other words, methods can call other methods.

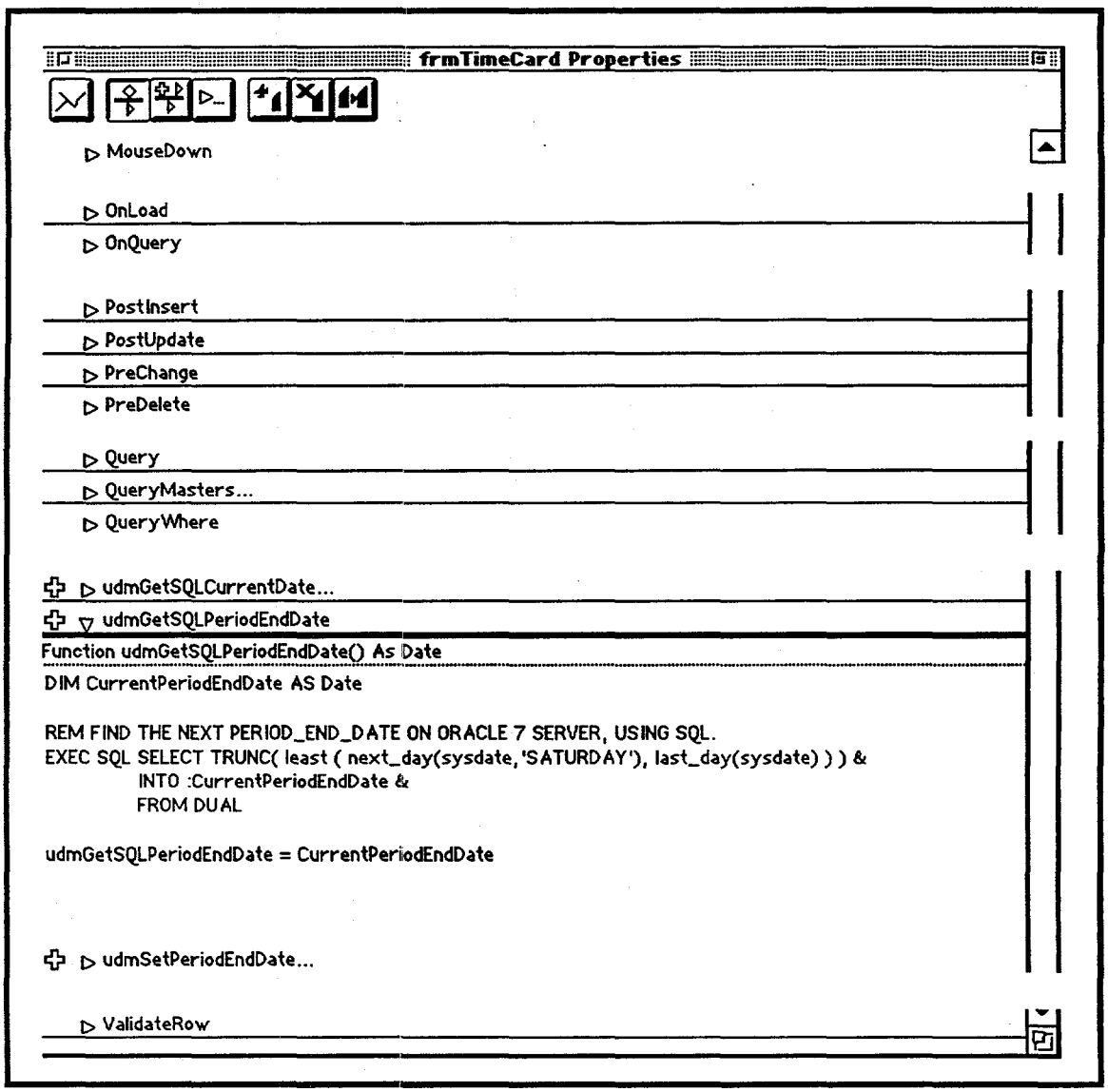

Figure 9: Example methods of a form.

3.4 Design & Development Methodology.

For the application produced in this project, application objects were created. Then, forms were drawn, and containers and controls were 'dropped' onto the forms. Finally, links, properties, and methods were added to the appropriate objects.

4. Sample Iteration of Development Cycle

Since the problems and requirements are now defined and some background has been given, a sample iteration of the development cycle can be shown. In this iteration, a new feature will be added. In particular, the application at the initial state looked like Figure 10. The next feature to be added to that form is a field inside the repeater display. Note that the time card application in Figure 10 has a blank space between the work order number and the time of each day. A field will be added to display the work center of each work order.

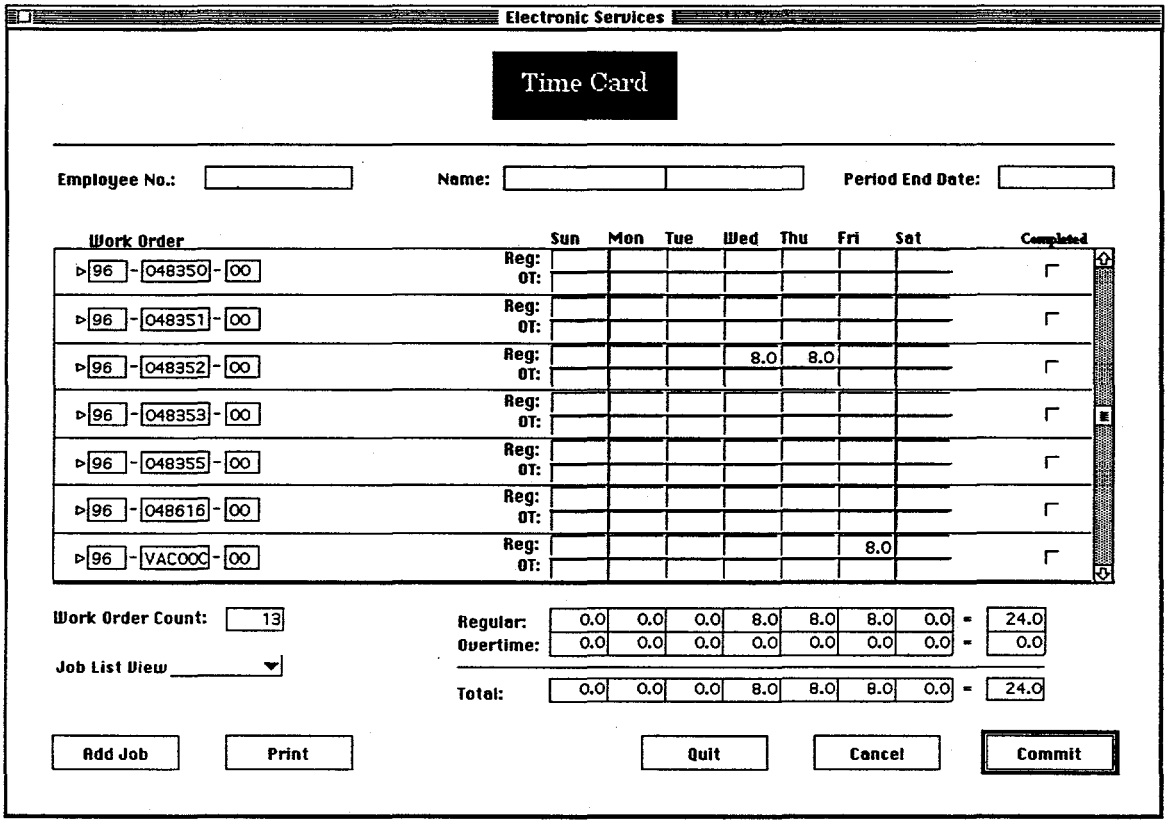

Figure 10: Before alteration.

4.1 Adding a New Feature - Altering the Framework

First, since a 'look-up' field is needed, a text-field is drawn inside the repeater display, repJobList. The newly drawn field is named, fldWorkCenter, because it will display the work center information of each work order. Moreover, repJobList, contains fldWorkCenter. To add a feature into the form, the framework of fldWorkCenter. must be altered. See Figure 11. The method of 'SQLLookUp' is augmented to the property of 'DATASOURCE' of text-field, fldWorkCenter.

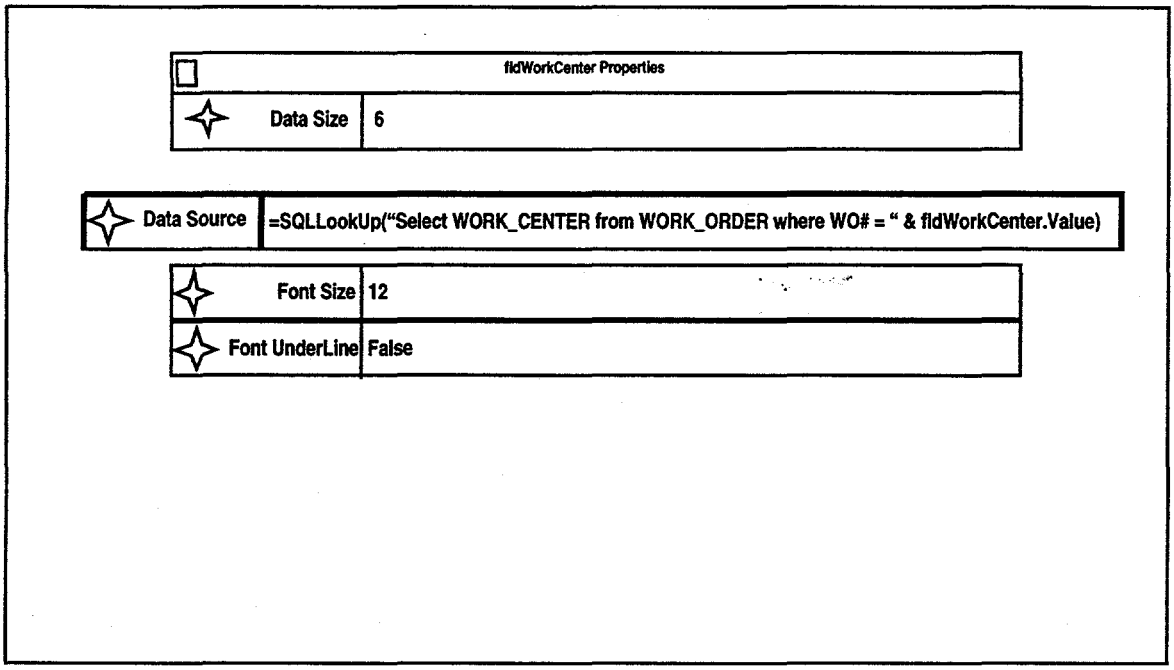

Figure 11: Altered framework of field fldWorkCenter.

4.2 Testing the Alteration

After the feature has been added, the application is tested. Figure 12 shows the new feature in a trial-run. Every feature that has been added up to this point must then be tested again to make sure that the new feature does not interfere with the previous features and existing architecture. However, there is a possibility that some errors can slip by this testing process, and they could be passed on to the communities of users.

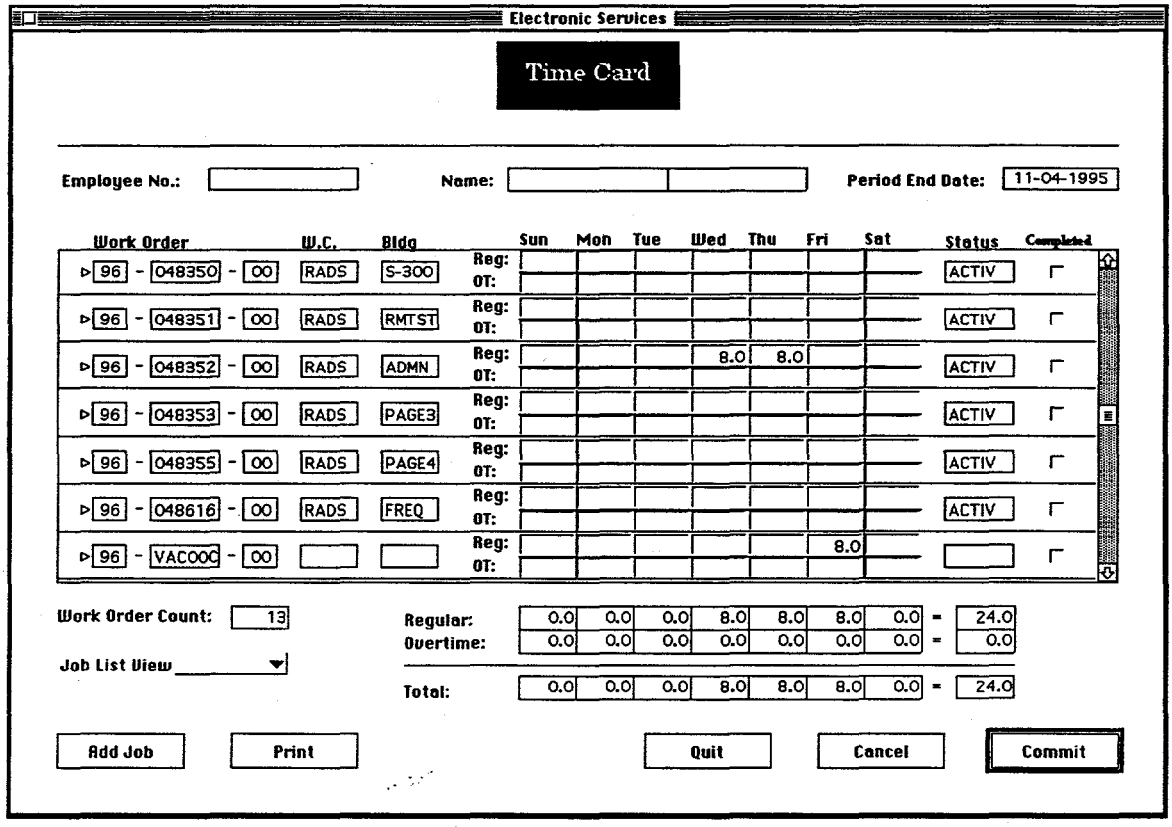

Figure 12: Testing form with new feature.

4.3 Debug & Analyze

In this case, there are no perceivable errors with the new added feature. However, in other iterations, there were errors. If there are any bugs and errors, then they are noted. Then, possible solutions are proposed. Each possible solution is implemented, until the best solution is found. In other words, in cases of bugs and errors, development is reiterated over the same cycle until problems of that feature are solved. In this case of a 'SQLLookUp' field, there are no errors -- so the cycle is iterated for the next feature. Nonetheless, work on this iteration is documented as shown in Figure 13.

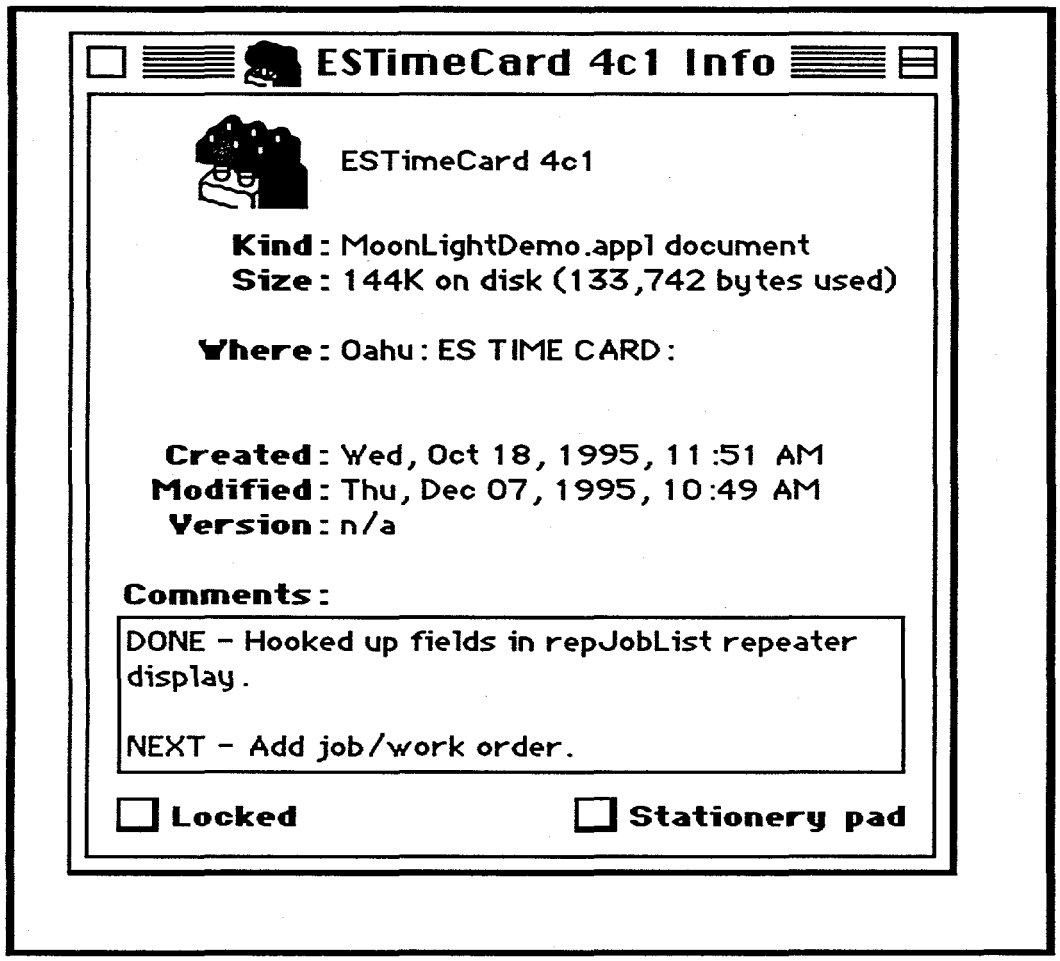

Figure 13: Documenting accomplishment -- successful new feature.

5. Results

5.1 Accomplishments

Only one application, time card/time entry, has been completed. The finished application looks similar the one presented in Figure 12. The completed application has the basic features, and it satisfies the requirements.

5.2 Works in Progress

The time card/time entry application is being updated for advanced features. Furthermore, documentation for future developers is being written, and the architecture is being restructured for easy maintenance. Most importantly, the job/work order application is being designed.

6. Conclusions & Recommendations

6.1 Significance of Accomplishments

Developing client database applications with Oracle Power Objects is not as fast as planned. Version 1.0 of Power Objects was used in this project. (Version 1 of most software applications are known to have bugs and errors.) Power Objects is an unstable tool. Also, applications produced by Power Objects are slow, and they do not have a 'native Macintosh look and feel'. However, the application produced by Power Objects seem to be stable.

6.2 Next Steps

The next step is to complete the application for job/work order entry. The advanced and optional features for both applications: time card entry and work order entry, should also be completed. After that step, the applications should be integrated into a suite. Then, a similar suite should be built for the Electronic Manufacturing Department. A library or repository should be developed to maximize reuse of similar objects. Finally, the benefits and costs of using Oracle Power Objects must be evaluated. If Power Objects Version 2 is unstable and the costs of development using Power Objects is high, then alternative tools must be considered.

Bibliography

Roberts, Christopher Getting Started with Oracle Power Objects, Version 1.0 Redwood City, California:Oracle Corporation 1995 p. 27 & 37

Acknowledgments

I would like to thank John Wade and Young Seiden, my mentors, for giving me the opportunity to work at LLNL. I wool like to thank Kerry Bobo, an Oracle expert and the creator of the current system, for providing detailed information on the current systems and answers to my questions.

Distributed Computing Support Program's Databases*

Amy Parsons

Saint Cloud State University

Lawrence Livermore National Laboratory
Livermore, California 94550

December 1, 1995

Prepared in partial fulfillment of the requirements of the Science and Engineering Research Semester under the direction of John Wade and Young Seiden, Mentors, at the Lawrence Livermore National Laboratory.

*This research was supported in part by an appointment to the U.S. Department of Energy Science and Engineering Research Semester (hereinafter called SERS) program administered by LLNL under contract W-7405-Eng-48 with Lawrence Livermore National Laboratory.

ABSTRACT

The Distributed Computing Support Program (DCSP) is the current system for keeping track of computer hardware maintenance throughout the Lawrence Livermore National Laboratory. DCSP consists of four separate Ingres databases each with their own support files. My project was to update the support files to make the business process more efficient.

HISTORY

The DCSP database started as a single elementary database with one vendor. Later, when there came a time to add a new vendor, the database could not handle the addition. At this point, the choice was made to make a carbon copy of the existing database instead of making one robust database. They now had two database systems: one for DEC and one for Sun. The two databases grew in separate directions. Later, a need to add two more vendors came. Once again the decision was made to make a carbon copy of the two existing databases. There are now four separate database systems: DEC, Telos (a carbon copy of DEC), Sun, and Grumman (a carbon copy of Sun).

The original plan was for a SERS Computation student to make one robust database that included all four vendors. My project was to finish writing and testing all of the Ingres Report-Writer scripts and to make an efficient SQL script that created the temporary tables that are used to run the monthly reports. However, seven weeks into the semester the budget was cut and along with the budget went the project. My new project was to take the old DCSP system and make it more efficient and user friendly.

OVERVIEW

DCSP runs monthly reports, but before the reports can be done the pre-report work must be completed. The pre-report work consists of entering the data into the corresponding

four databases. (The data is collected over a month and entered as the first step in the pre-report work when convenient.) The next step is to update the command files to reflect the current date. This needs to be done in various places in several files. (Thirty-eight files need to be modified with the new date, the date is changed a total of 144 times.) In the old system, this was done manually. The user would have to use a text editor (such as VI) and manually change all the dates. They could not use a find and replace method because not all the dates in the files needed to be changed. Reducing the amount of time to do the pre-report work is one of the updates made.

After the pre-report work had been completed they could finally run the reports. To run the reports they would have to first run a command file. The file would run a QUEL script which created the temporary tables used to run the reports. Then, for each of the reports (eight for DEC and Telos and nine for Sun and Grumman), they would have to run another command file for each of the reports. This process was cut down so it would be more automated.

The reports themselves also needed updating. The reports still reflected "adjustments" which is a form of payment that DCSP no longer practices. The "adjustments" needed to be removed from the reports. In some reports, the format of the report was not appealing and was changed to make the report easier to read. In other cases, some of the information needed on the reports was not included and was updated to included all necessary data.

ACCOMPLISHMENTS

The first user requirement that was accomplished was the updating of the actual reports. The "adjustment" columns were removed. The reports are in the form of Ingres Report-Writer Scripts, to remove the "adjustment" column the scripts for the reports had to be modified. The "adjustment" was also used in the report to figure the grand total of the

price. Since the adjustment method is no longer practiced, the initial price and the grand total price were always the same. The grand total price could also be deleted from all of the report-writer scripts. Changes were made to the following files (a total of twenty files):

DEC/Telos	Sun/Grumman
deqsumm (231)	newssumm (221)
deqacct (232)	newsacct (222)
deqadd (233)	newsadd (223)
deqaddc (233a)	newsaddcon (223a)
deqsummacc (237)	newsummacct (227)

The next change to the Report-Writer scripts were on the contact reports. The contact reports can be any where from fifty to one hundred pages. The report prints the contact and then lists all of the hardware associated with that contact. On the DEC/Telos side each contact had its own page, however, if the contact had more than a page of information it would continue printing on the next page. However, it would not reprint the contact name and thus might lead to confusion. The contact report-writer scripts were modified to include a single if statement in the .page section that would reprint the contact name and avoid confusion. On the Sun/Grumman side, each contact does not get their own page. Information for a contact usually runs on to a second page. Here to, the contact was not printed on the second page, which led to confusion. To correct this, the same thing was done to the .page sections of the report writer scripts (a single if statement was added). The change was done to the following reports (total of four reports):

DEC/Telos	Sun/Grumman
deqsuppl (230)	newssuppc (224)

The goal for changing the command files was to cut down on the number of manual changes to the files. To do this, I used several techniques. First, I cut down on the number of changes in the deq.com (twelve changes) and the newsun.com (nine changes) files. The first idea was to use UNIX's command substitution. This did not work because

the files are QUEL command files and therefore, can only use QUEL commands. QUEL provides variables and prompts only when using embedded QUEL. So, I created a temporary table with one column which was a date field. The next line in the script is an append that adds a date to the table. This date needs to be changed by the user every month. The rest of the file then refers to the table to get the date, instead of the date directly. The table is destroyed at the end of the file and in the beginning of the file. The destroy at the beginning of the file was done to insure the integrity of the tables. If the command file did not completely execute, when it is re-ran, the table will not contain old dates. This insured the accuracy of the reports.

The next update was to find a way to reduce the number of changes in the command files that run the reports. There are three changes to each file and a total of thirty-four reports that are ran each month. I tried UNIX command substitution. This worked in changing to the correct directory. It did not work in the place that I most wanted it to, in the Ingres Report command. In the Report-Writer scripts it prompts the user for a date. There are two ways the user can handle the prompt. They can run the report and wait for the prompt to appear on the screen and then type in the correct date or in the Ingress Reports command they can specify the date. The later is what has been chosen as the preferred method. In the command files, every month they needed to change the date in the Ingres Report command to reflect the new date. Because this is a Ingres command a UNIX command substitution did not work.

A solution was to take the command files and combine them into two files. Therefore, they do not need to edit several files. Doing this also cut down on the number of changes they had to make. In each of the separate command files, UNIX commands are used to create a new directory for this months reports and then changes to the new directory. Since they

only have two files now they only need to make this change twice (instead of nine times in each system).

RESULTS

I was unable to find a way for the user to get around to changing the date parameter in the Ingres Report command. To run the reports the users need to edit a total of nine files and change the date fifty times. Originally they needed to edit thirty-eight files and change the date 144 times.

The MACHO Project LMC Variable Star Inventory: Aperiodic Blue Variables

Patricia Purdue

Bryn Mawr College

Lawrence Livermore National Laboratory
Livermore, California 94550

December 13, 1995

Prepared in partial fulfillment of the requirements of the Science and Engineering Research Semester under the direction of Kem Cook, Research Mentor, in the Lawrence Livermore National Laboratory.

* This research was supported in part by an appointment to the U.S. Department of Energy Science and Engineering Research Semester (hereinafter called SERS) program administered by LLNL under Contract W-7405-Eng-48 with Lawrence Livermore National Laboratory.

The MACHO Project LMC Variable Star Inventory: Aperiodic Blue Variables

Patricia Purdue

Abstract

The MACHO Project database was searched for aperiodic blue variables in the LMC. Of approximately 250,000 bright blue stars in the region of observation, around 3500 had been flagged as variables or as rejected gravitational microlensing candidates. From a visual inspection of this set, about 400 stars were selected for the catalog. These stars have been categorized by their light curve morphology. Their spatial distribution is presented and correlated with known phenomena.

Analysis of the catalog stars has produced some interesting discoveries. Among some of these variables, unusual color changes were found. Some stars become redder or do not change color when their brightness increases, whereas most stars become bluer if they rapidly brighten. For some stars with relatively long quiescent stages, the light curves were searched for low-level, periodic variability, but no conclusive evidence for such behavior was found.

1 Introduction

MAssive Compact Halo Objects (MACHOs) may account for a significant amount of the dark matter in the Milky Way. Finding these MACHOs and determining how much they contribute to the mass of the galaxy is the primary goal of the MACHO Project. Millions of stars in the Large Magellanic Cloud (LMC), Small Magellanic Cloud, and the bulge of the Milky Way are being monitored to detect gravitational microlensing events caused by MACHOs. The nightly monitoring of these stars has also created an excellent database for variable star research.

When a MACHO passes near the line of sight to a background star, the MACHO's gravitational field acts as a lens. As a result, two images of the source star appear; however, these often cannot be resolved independently since the separation is less than a milliarcsecond for a halo object mass of less than thousands of solar masses. Thus, the effect is a transient brightening called gravitational microlensing. The transient nature of the phenomenon is due to the relative motions of the source star, the MACHO, and the solar system. The brightening is achromatic and is expected to be symmetrical because the apparent motions of the components are constant over the time span of the event.

The MACHO Project nightly monitors millions of stars in an effort to detect microlensing events. The resulting database provides a vast amount of variable star data to be explored. In this paper, we present a catalog of about 400 LMC aperiodic blue variables selected from the approximately 250,000 bright blue stars in the region of observation.

The catalog stars have been classified by their light curve morphology. For example, some of the light curves are relatively constant with one to a few episodes of brightening (bumpers), some are constant with sections of "flickering," and some have step-like changes (steppers).

Preliminary analysis of the catalog stars produced some interesting information. Some unusual color changes were discovered for the bumpers and steppers. In particular, bumpers become redder when their brightness increases, and steppers do not appear to change color. For the bumpers which have relatively long quiescent stages, some of the light curves were searched for low-level, periodic variability, but no conclusive evidence for such behavior was found.

2 Procedures

The MACHO project has the dedicated use of the 1.27m Great Melbourne telescope at Mount Stromlo, Australia. Every night, fields of the LMC, or sometimes the bulge of the Milky Way and the Small Magellanic Cloud, are observed; a beam splitter allows two passbands of CCD data to be collected simultaneously. The V_{MACHO} passband is $440 - 590$ nm, and the R_{MACHO} passband is $590 - 790$ nm.

Most of the catalog was produced by selecting stars which had been flagged as potential microlensing candidates; their light curves triggered a microlens filter and could be moderately well fit by a microlensing curve. From the set of 3991 potential microlensing events, the light curves of the 561 stars that were bright (14.0 mag $< V_{MACHO} <$ 18.0 mag) and blue ($V_{MACHO} - R_{MACHO} < 0.3$) were inspected visually, and those that appeared to be aperiodic variables (382) were selected. Eighteen aperiodic blue stars were also selected from around 3000 bright blue stars which had been flagged as variable (but had not necessarily been flagged as microlensing candidates).

The stars in the catalog were visually inspected and classified according to their light curve morphology. The categories were: stars with one to a few prominent "bumps" (called bumpers, with constant or variable baseline), "flickering" stars (where the flickering starts from the baseline or on a plateau), stars with flat plateaus, and stars with step-like changes in their light curves (called steppers).

Several types of preliminary analysis were accomplished. Light curves of the color ratios were made for representatives of each group. The catalog stars were correlated with known phenomena, using the SIMBAD database.

For the bumpers with long quiescent stages, 20 randomly selected light curves were searched for low-level, periodic variations of 0.1 to 30 days, using a C program that attempts to phase the data to periods within the given interval using a supersmoother fit (Friedman 1984). In addition, the supersmoother fit was subracted out of the data for each, and the residuals were phased with the same program.

3 Data

The light curves of the catalog stars were classified according to their light curve morphology. It should be noted that these categories are only a preliminary attempt to classify the stars in the catalog. In some cases, the boundaries between categories are indefinite, and the categorization is subjective. The categories are as follows:

(1) **Sporadic bumpers with constant baseline.** These are characterized by having long periods of quiescence with occasional episodes of rapid brightening, followed by a slower decline to the previous level. The magnitude of these stars increase by about 20-40%. The rise takes place over a span of 10-20 days, with the entire "bump" episode usually lasting on the order of 100 days (see Fig. 1).

(2) **Sporadic bumpers with variable baseline.** These stars are much the same as the bumpers described above, but their baselines are variable (see Fig. 2).

(3) **Flickering stars with constant baseline.** These stars have episodes of rapid variation and stages of quiescence. The baseline during "flickering" is the same as the baseline during quiescence (see Fig. 3). The episodes of flickering may last hundreds of days, while the individual cycles of rise and decline are on the order of 10-20 days.

(4) **Flickering stars with plateau baseline.** These are much the same as the above flickering stars, but the baseline during an episode of flickering is 20-40% brighter than the baseline during quiescence (see Fig. 4).

(5) **Stars with long plateaus.** The light curves of these stars are characterized by long spans of increased but relatively constant magnitude. These stages of increased magnitude, about 20-40% above the baseline, generally last for about 100-200 days (see Fig. 5).

(6) **Steppers.** These stars are characterized by long periods of quiescence punctuated by abrupt changes in magnitude. The magnitude increases by 30-50% and is constant before and after the change, which usually occurs over a span of less than 20 days (see Fig. 6).

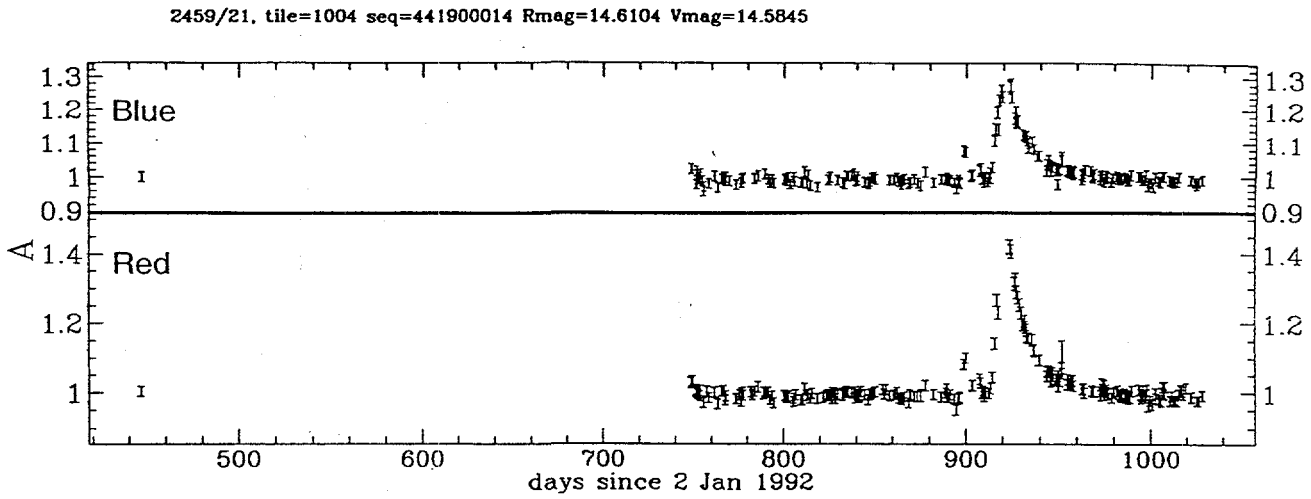

Fig. 1. Light curve of a sporadic bumper with constant baseline.

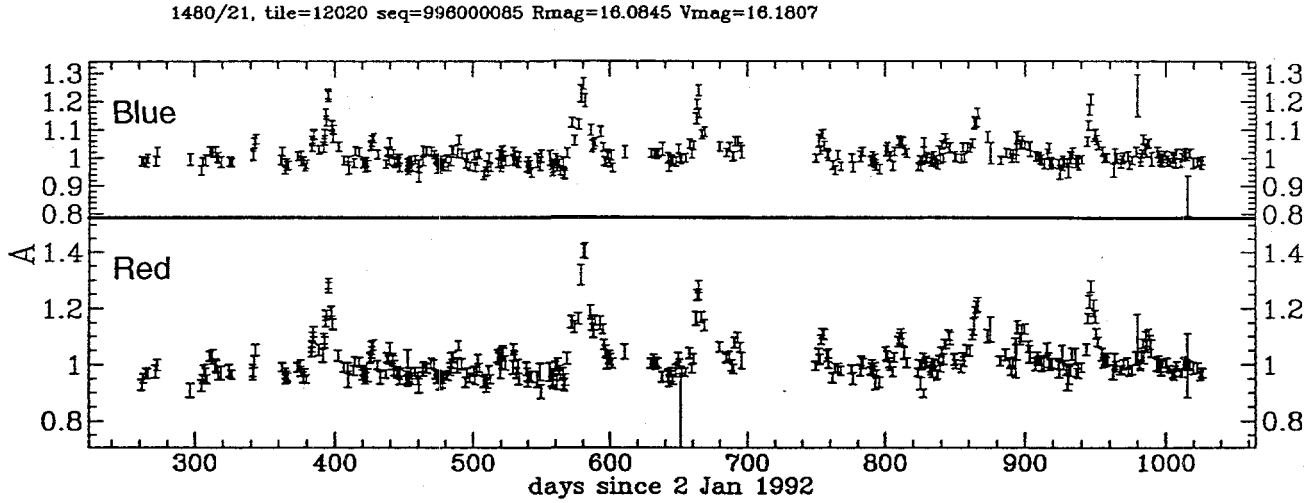

Fig. 2. Light curve of a sporadic bumper with variable baseline.

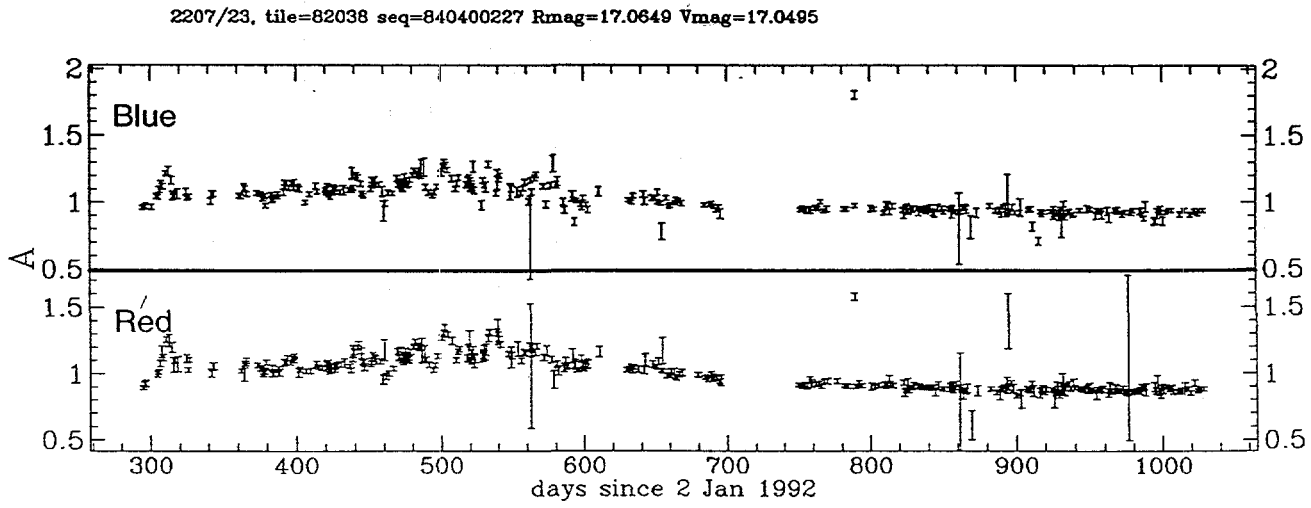

Fig. 3. Light curve of a flickering star with constant baseline.

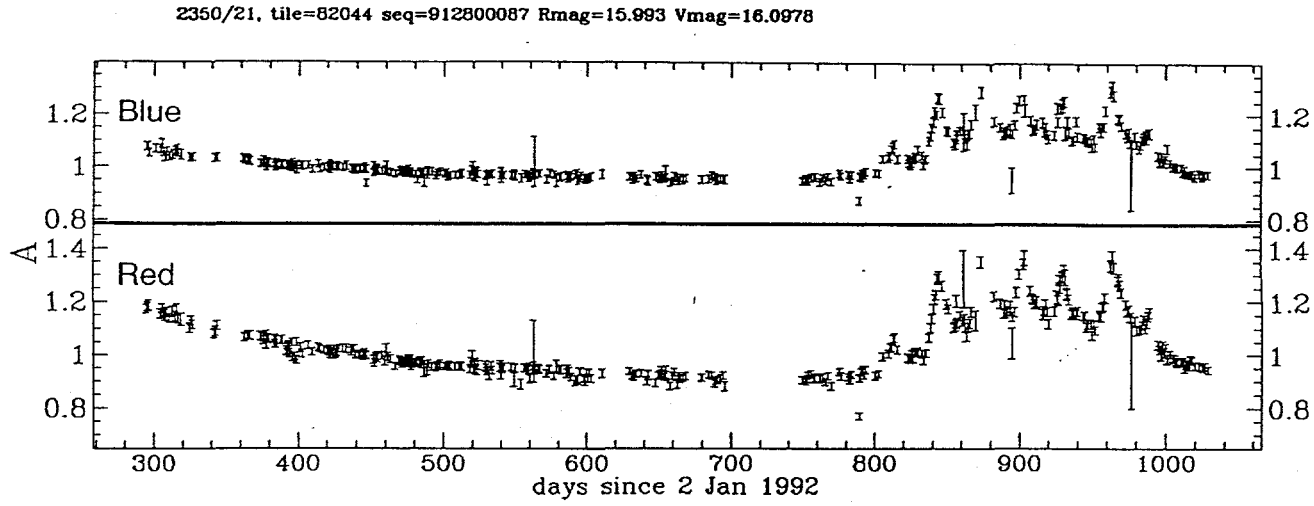

Fig. 4. Light curve of a flickering star with plateau baseline.

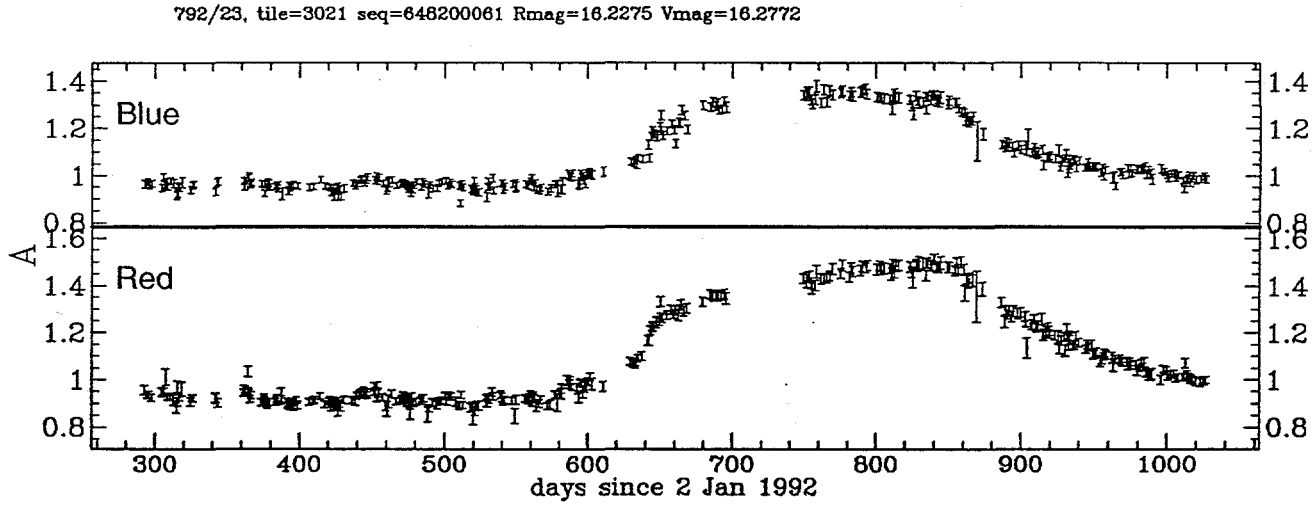

Fig. 5. Light curve of a star with long plateau.

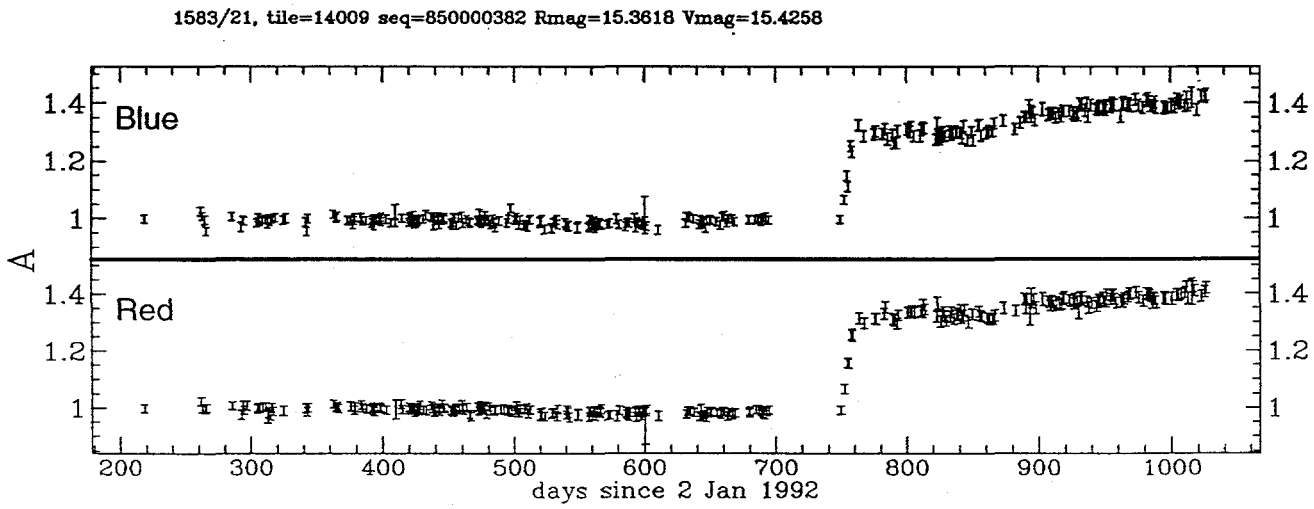

Fig. 6. Light curve of a stepper.

Not all of the stars in the catalog fall into one of these categories, and some display very unusual behavior. For example, the light curve in Fig. 7 appears similar to that of some eclipsing binaries, but the period is not entirely regular. Another example is shown in Fig. 8; here, the star varied with a regular period and with an overall downward trend, then it stopped varying and became constant. Additional data shows that this star later resumes its variations, this time with an upward trend.

Currently, attempts are being made to correlate the catalog stars with known phenomena, as listed in the SIMBAD database. There is an interesting correlation with supernova 1987A. Several objects, which form a ring around 1987A, show dramatic increases in magnitude around 1000 days (late September 1994). Since the correlation process is still in progress, there is little more to report at this time.

About 20 bumpers with constant baselines were tested for low-level periodic variability. When the results of the first tests were inconclusive, the data were fit by a supersmoother curve. This was then subtracted out of the data, and the residuals were phased. No conclusive evidence for low-level periodic behavior was found. An example of a typical result from the phasing program is shown in Fig. 9.

Representatives of each of the categories of catalog stars were selected and their color light curves plotted. Many of the steppers displayed little or no color change during the change in magnitude (see Fig. 10). Most of the bumpers became redder during "bumps" (see Fig. 11).

4 Discussion

The primary result of this project is the compilation of a catalog of aperiodic blue variables in the LMC. In the course of accomplishing this, some unusual and very distinctive light curves were discovered. Many of these are quite different from any previously studied stars and are in need of further study; the two stars whose light curves are shown in Fig. 7 and Fig. 8 are examples of this.

Another discovery involves the color changes of some of the catalog stars. When most variable stars brighten rapidly, they become hotter and bluer. Bumpers, however, are unusual in that they seem to become redder when their brightness increases. This would mean that their temperature drops

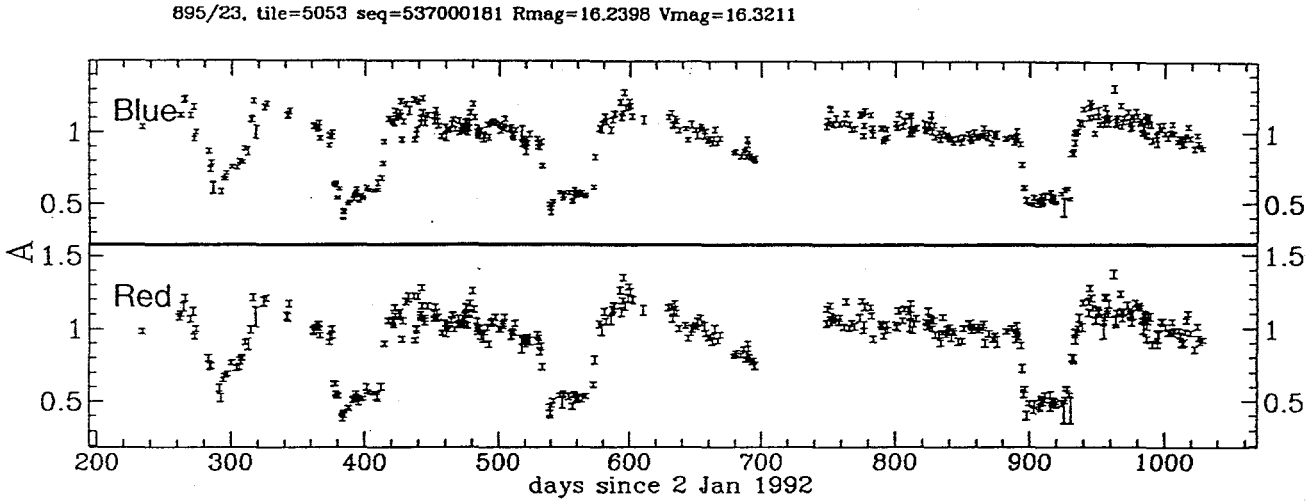

Fig. 7. Example of an unusual light curve; possible eclipsing binary.

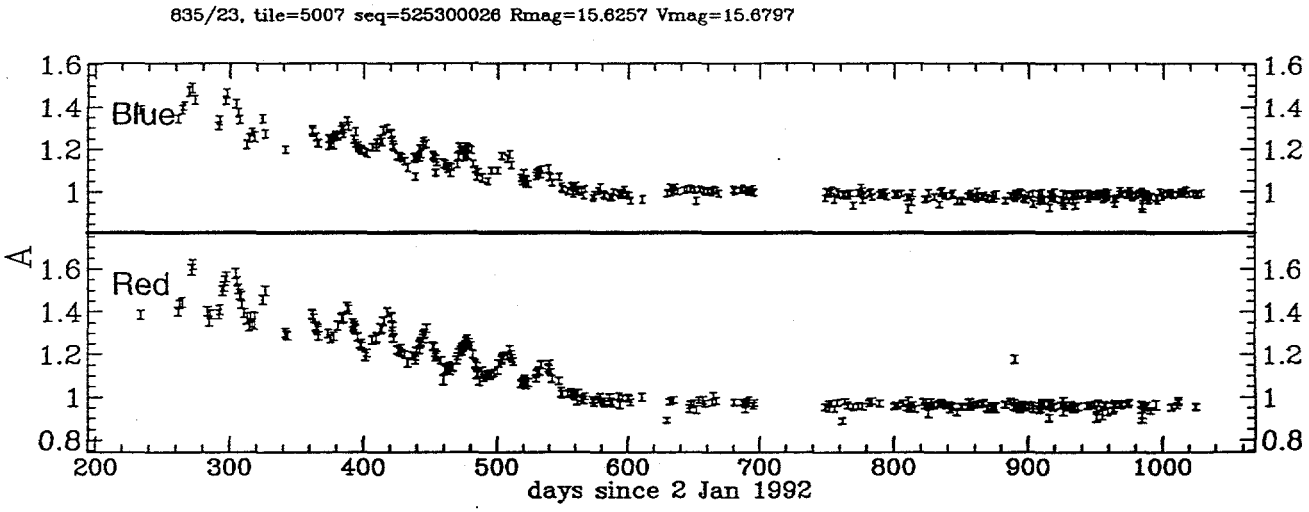

Fig. 8. Example of an unusual light curve.

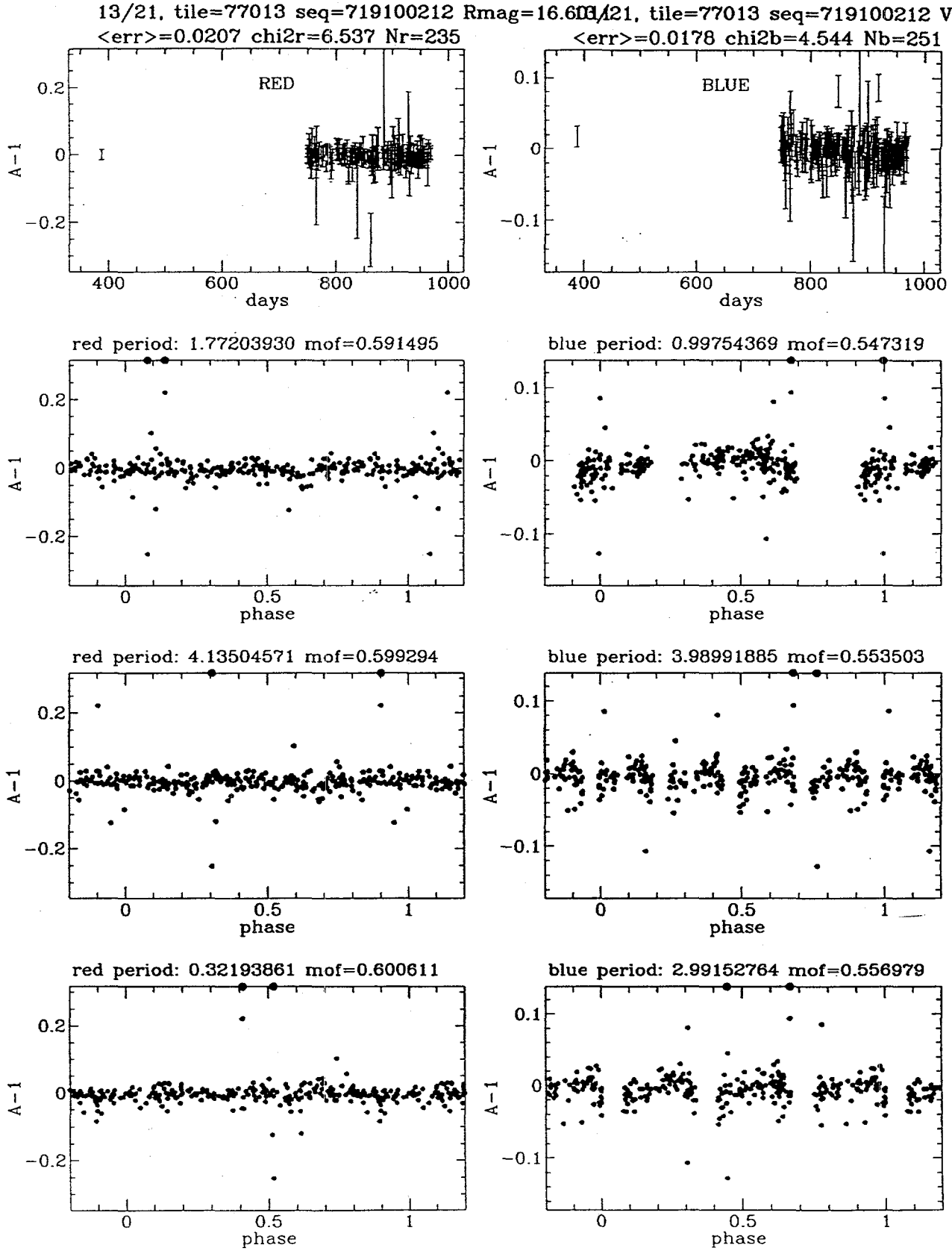

Fig. 9. Typical result of the phasing program. Red and blue light curves are shown in the top panels, phased with the top three periods in the following panels.

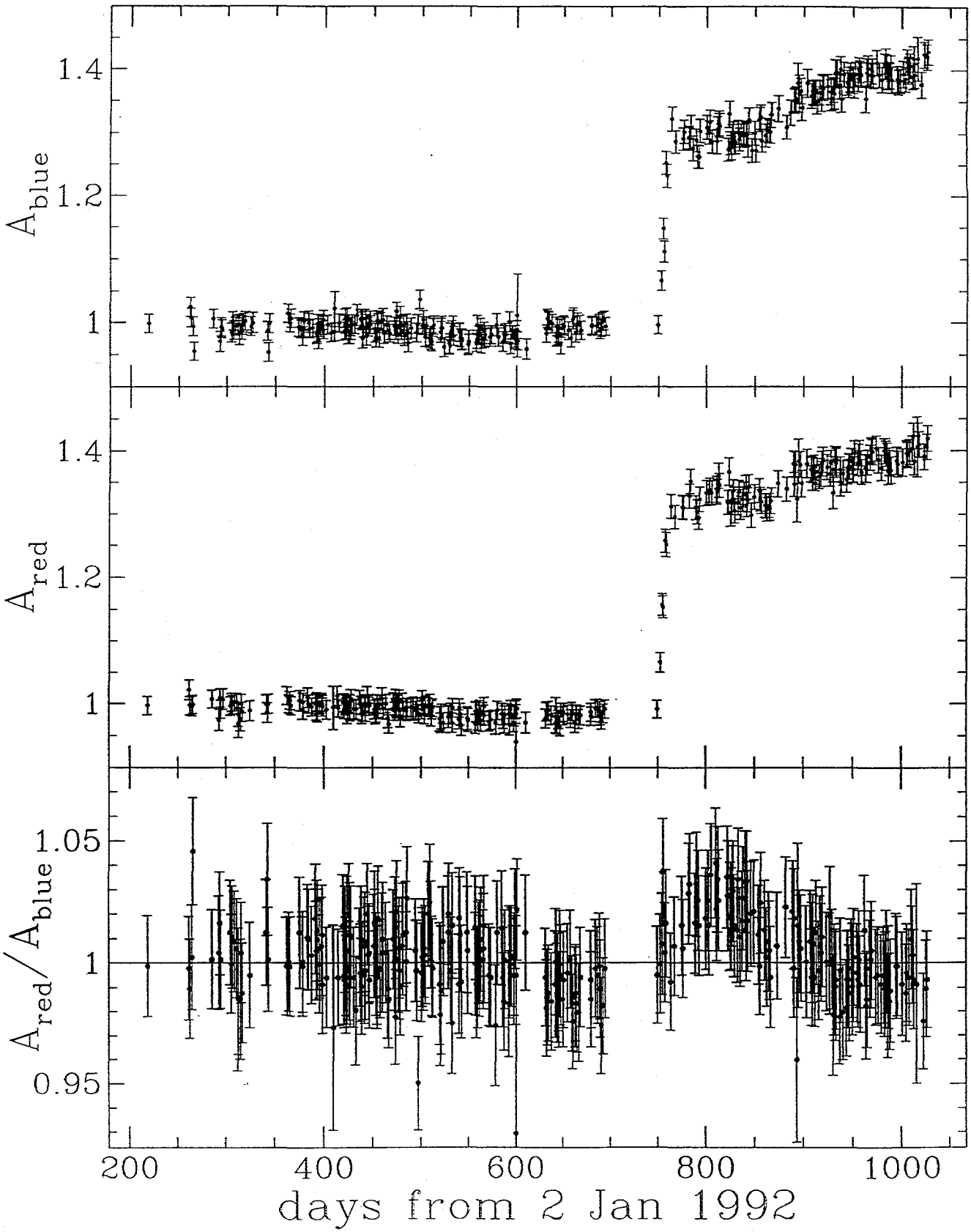

Fig. 10. Color curve of a stepper. The blue and red light curves are the top two panels. The bottom panel is the ratio of red to blue magnitude.

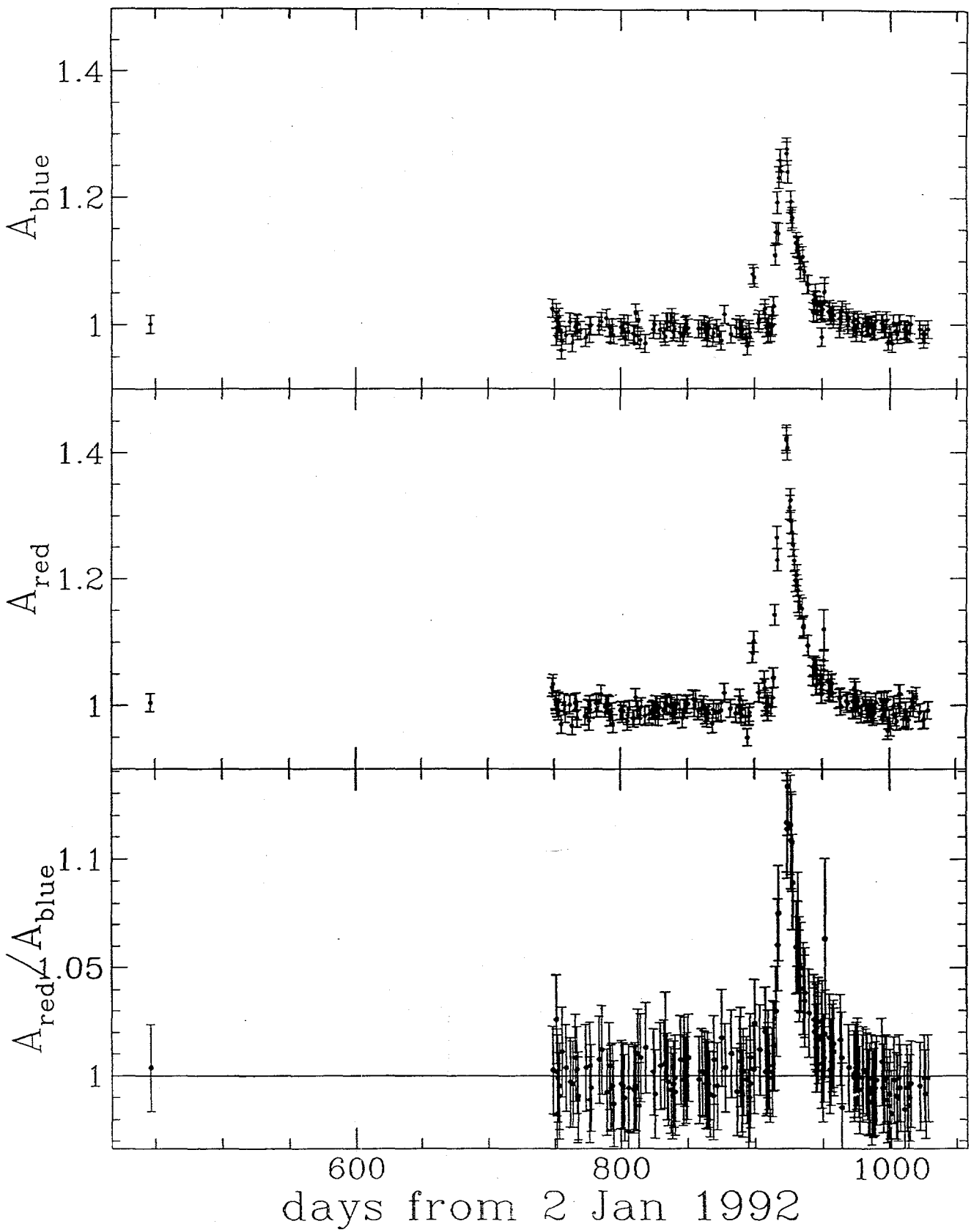

Fig. 11. Color curve of a bumper. The blue and red light curves are the top two panels. The bottom panel is the ratio of red to blue magnitude.

during the outburst. However, it is also possible that increased H-α emissions would cause the R_{MACHO} magnitudes to appear larger.

Some of the steppers display a different form of unusual color behavior; their color does not appear change when the brightness varies. In other words, they seem to be remaining at the same surface temperature, even though the stars are becoming brighter.

At this point in the search for low-level periodic variability, we have been unable to find evidence of such behavior in the quiescent stages of bumpers' light curves. This is unexpected, since most current theories on the causes of variability in this type of star predict low-level variations. For example, Sterken (1989) states that such low-level variations are present in normal supergiants and have been found in all luminous blue variables that have sufficiently accurate observations. In addition, the two competing theories on the causes of variations in Be stars predict periodicity of some type. Rotational modulation predicts single periodicity, and non-radial pulsation predicts multiperiodicity (see, for example, Baade & Balona 1994). Thus, it is unexpected that periodic variations have not been found in the stars in this catalog.

5 Conclusions

A catalog of approximately 400 aperiodic blue variables in the LMC was produced from the MACHO database. A preliminary classification of the catalog stars was attempted, based on the morphology of their light curves. Currently, the stars' positions are being correlated with known phenomena. Examination of the stars' color light curves shows that many steppers and bumpers display unusual color behavior. In a search for low-level periodic variability among bumpers with long quescient stages, there was an unexpected lack of conclusive evidence for such behavior. As a result, many of the stars in the catalog are in need of further study.

References

[1] Baade, D. 1987. "Be Stars as Nonradial Pulsators," in *Physics of Be Stars*, eds. Arne Slettebak and Theodore P. Snow (New York: Cam-

bridge University Press), 361-383.

[2] Baade, D., and Balona, L.A. 1994. "Periodic Variability of Be Stars: Nonradial Pulsation or Rotational Modulation?" in *Pulsation, Rotation, and Mass Loss in Early-Type Stars*, IAU Symp. 162, eds. L.A. Balona *et al.* (Boston: Kluwer Academic Publishers), 311-324.

[3] Balona, L.A. 1990. "Short-Period Variability in Be Stars," *Monthly Notices of the Royal Astronomical Society* 245, 92-100.

[4] Friedman, Jerome H. 1984. "A Variable Span Smoother," Laboratory for Computational Statistics Technical Report No. 5, SLAC PUB-3477.

[5] Moskalik, Pawel. 1995. "New Results on Pulsating OB Stars," *Astrophysical Applications of Stellar Pulsation*, ASP Conf. Series 83, eds. R.S. Stobie and P.A. Whitlock, 44-55.

[6] Percy, John R. 1987. "Observations of Rapid Variability in Be Stars," in *Physics of Be Stars*, eds. Arne Slettebak and Theodore P. Snow (New York: Cambridge University Press), 49-65.

[7] Sterken, C. 1989. "Photometric Variability of Luminous Blue Variables in Quiescent State," in *Physics of Luminous Blue Variables*, eds. Kris Davidson *et al.* (Boston: Kluwer Academic Publishers), 59-66.

[8] Waelkens, C. 1991. "Slowly Pulsating B Stars," *Astronomy & Astrophysics* 246, 453-468.

Mathematical Modeling of the Human Knee Joint*

Juliet Ricafort

Department of Biomedical Engineering,
University of Southern California

Lawrence Livermore National Laboratory
Livermore, CA 94550

December 13, 1995

Prepared in partial fulfillment of the requirements of the Science and Engineering Research Semester under the direction of Dale Schauer, Research Mentor, at Lawrence Livermore National Laboratory.

* This research was supported in part by an appointment to the U.S. Department of Energy Science and Engineering Research Semester (herein after called SERS) program administered by LLNL under **Contract W-7405-Eng-48** with Lawrence Livermore National Laboratory.

ABSTRACT

A model was developed to determine the forces exerted by several flexor and extensor muscles of the human knee under static conditions. The model was used to evaluate muscle tension and joint load for two static postures: the standing position and the position of the knee in an automobile simulation. The following muscles were studied: the gastrocnemius, biceps femoris, semitendinosus, semimembranosus, and the set of quadricep muscles. The rules of rigid body mechanics were employed to formulate force equilibrium equations for two rigid bodies: Rigid body 1 included the pelvis, femur and patella; Rigid body 2 included the tibia, fibula, and the collective bones of the foot. Planar motion at the knee joint was assumed. The selected muscles were modeled by their functional lines of action in space, which connected their points of origin to their points of insertion. Assumptions based on previous muscle tension data were used to resolve the indeterminacy.

INTRODUCTION

Musculoskeletal models provide the means for estimating individual muscle forces, stresses, and joint loads. Clinical applications of such models include modeling prosthetics to determine the change in joint load, and observing the effects of changes in muscle strength, size, and point of attachment, as well as loss of muscle functionality. Documented in this report is an illustrative description of the modeling technique used to evaluate selected flexor and extensor muscles of the knee in various static postures.

METHOD

Using the rules of rigid body mechanics, a static model of the knee joint was developed. We modeled the knee in two postures: (1) the standing position (full extension at the knee, 0 degrees of flexion) and (2) the knee in the position taken when a subject is seated in an automobile with the foot pressed against the brake pedal (35 degrees of flexion at the knee).

The individual skeletal components included in the model are the pelvis, femur, patella, tibia, fibula, and the collective bones of the foot. The following assumptions were made:
(1) Motion of the fibula with respect to the tibia is negligible.
(2) Rotation about the hip and ankle joint is not considered for the purpose of this model. Rotation occurs only at the knee joint.

(3) The patella was assumed to be fixed with respect to the femur. The position of the patella was determined as a function of the knee flexion angle.

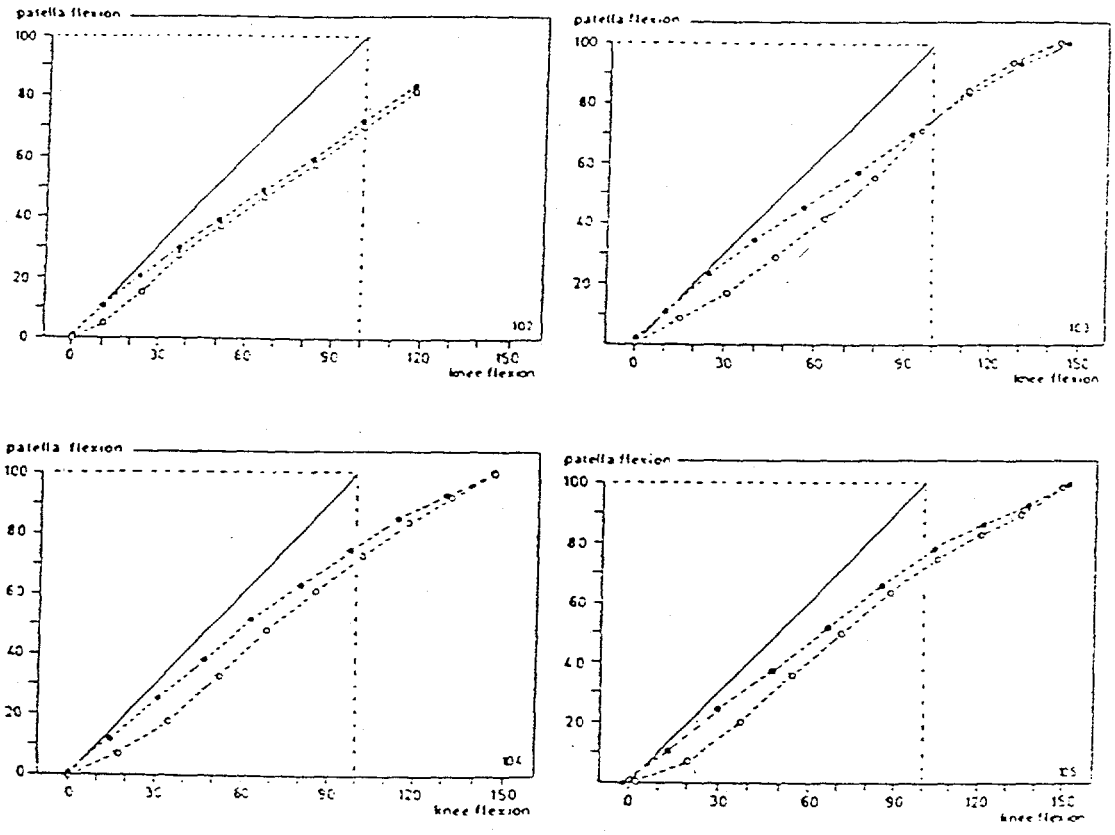

figure 1:

Patellar flexion as a function of knee flexion. (A. Van Kampen (1990) The Three Dimensional Tracking Pattern of the Human Patella)

(4) The knee is assumed to be a hinge joint, with motion occuring only in the sagittal plane.

Taking the above assumptions into account, two rigid bodies were considered. Rigid body 1 collectively includes the geometries of the pelvis, femur, and patella; Rigid body two includes the geometries of the tibia, fibula, and the collection of foot bones. Rigid body 1 will herein be referred to as the femur; Rigid body 2 will herein be referred to as the tibia.

With over 30 flexor and extensor muscles crossing the knee joint, selective muscle modeling is necessary to keep the problem of redundancy to a minimum. Data taken from the literature was used to select those muscles whose force contribution seemed most significant. The following muscles were selected: the gastrocnemius, rectus femoris,

vastus intermedius, vastus lateralis, vastus medialis, semitendinosus, semimembranosus, and biceps femoris muscles.

For each of the muscles selected, single points representing the origin and insertion sites of each of the muscles were determined. Ambiguity was involved in assigning single points to muscles that attached to bone over a wide region. In these cases, we assumed that the midpoint of the region was the attachment point.

We modeled the muscles by their functional lines of action in space, defined by the line that connects the point of origin to the corresponding point of insertion. Muscles with more than one distinct component, or those with complex tendon paths, were modeled using multiple lines. In modeling the gastrocnemius muscle, which is comprised of two heads, we represented each head with a single line of action originating from the corresponding femoral condyle and inserting into the calcaneus bone of the foot (see figure 9).

Muscle	figure no.	force reference no.
Semitendinosus	2	1
Semimembranosus	3	2
Biceps Femoris	4	3
Rectus Femoris	5	4
Vastus Lateralis	6	5
Vastus Medialis	7	6
Vastus Intermedius	8	7
Gastrocnemius (medial)	9	8
Gastrocnemius (lateral)	9	9

table 1:

Muscle lines of action

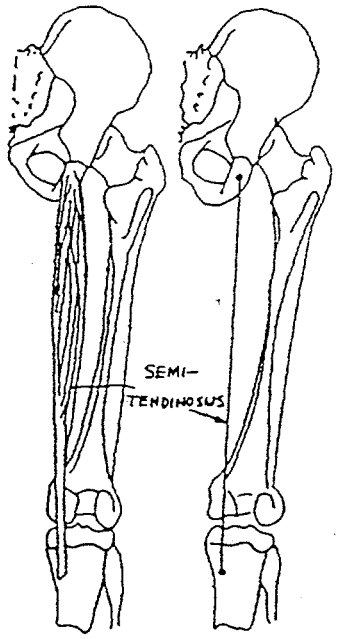

figure 2:

Line of Action for Semitendinosus*

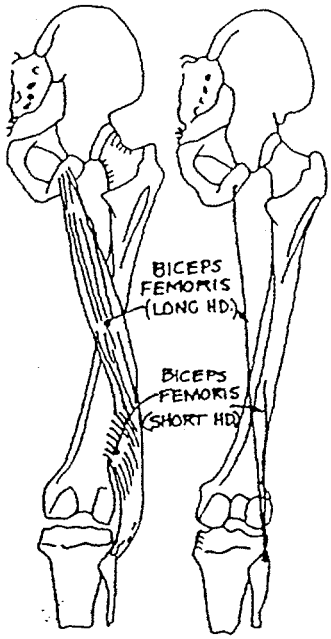

figure 4:

Line of Action for Biceps Femoris*

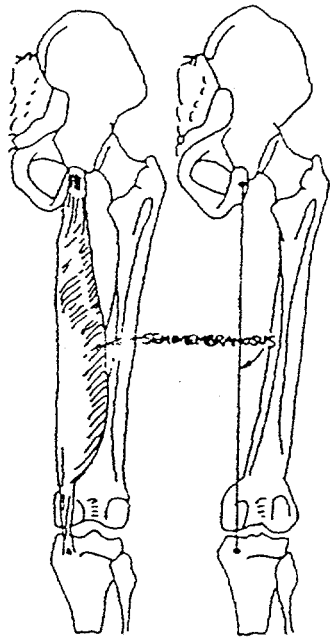

figure 3:

Line of Action for Semimembranosus*

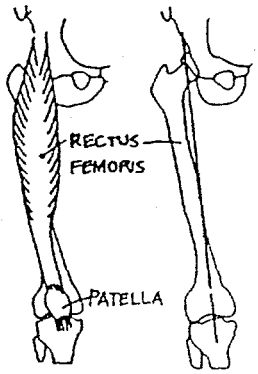

figure 5:

Line of Action for Rectus Femoris*

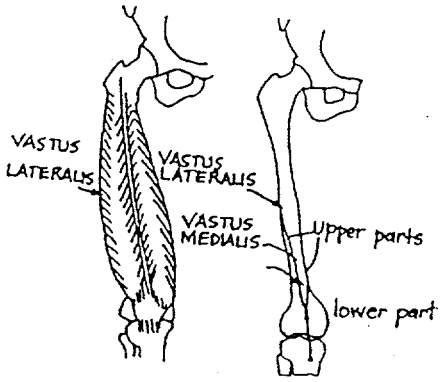

figure 6:

Line of Action for Vastus Lateralis*

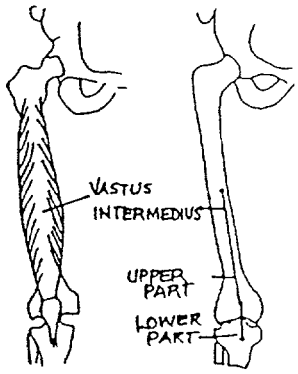

figure 8:

Line of Action for Vastus Intermedius*

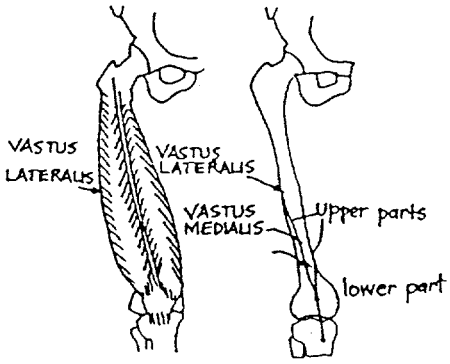

figure 7:

Line of Action for Vastus Medialis*

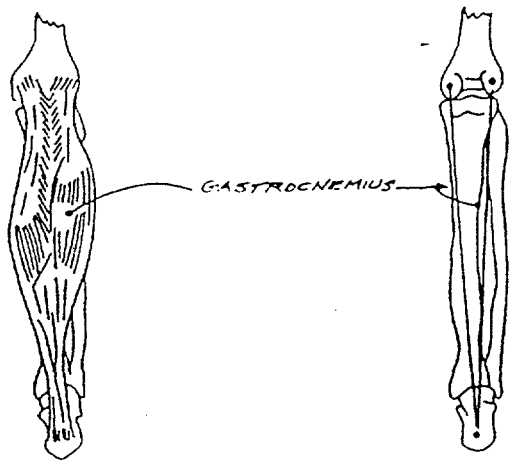

figure 9:

Lines of Action for Gastrocnemius*

* A. Seireg and R.J. Arkivar (1973) A Mathematical Model for Evaluations of forces in Lower Extremities of the Musculo-Skeletal System.

For each position modeled, the magnitude, direction, and point of application of an applied load was specified. In modeling the standing position, the magnitude of the applied load was specified as 344 N, acting down on the femoral head. This force magnitude value corresponds to the force produced by one-half of the body weight of a 70kg subject. In modeling the automobile situation, a force of 200 N acting perpendicular to the bottom of the calcaneus bone of the foot was applied, simulating the force of the brake pedal on the bottom of the foot.

Free body diagrams included the force vectors of the muscle tensions, the joint and ground reaction forces, the weights of the rigid bodies, and the applied load. Using the free body diagrams, we formulated force and moment equilibrium equations. A set of force component equations for each segment was developed, as well as a moment equation describing rotation about the knee joint. The following table and diagram indicates the reference axes used in formulating the force component equations:

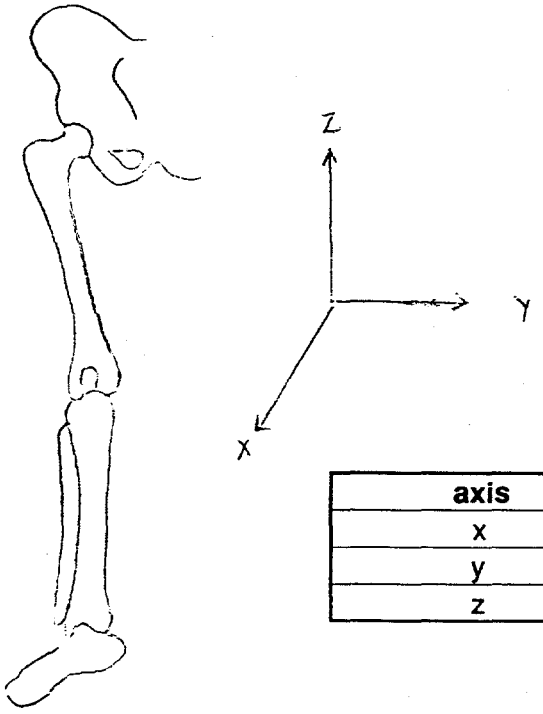

axis	positive direction	negative direction
x	anterior	posterior
y	medial	lateral
z	upward	downward

figure 10:

Reference Axes

Our equation set consisted of six force component equations and one moment equation with a total of 10 unknowns (9 forces from muscle lines of action and one joint reaction force). In order to resolve the redundancy problem, the following assumptions were made:

(1) The forces produced by the medial and lateral heads of the gastrocnemius are equal in magnitude.

(2) The forces produced by the quadricep muscles (rectus femoris, vastus lateralis, vastus intermedius, vastus medialis) are equal in magnitude.

RESULTS

Free-body diagrams for both the femur and the tibia were constructed for both the standing and the automobile simultation positions.

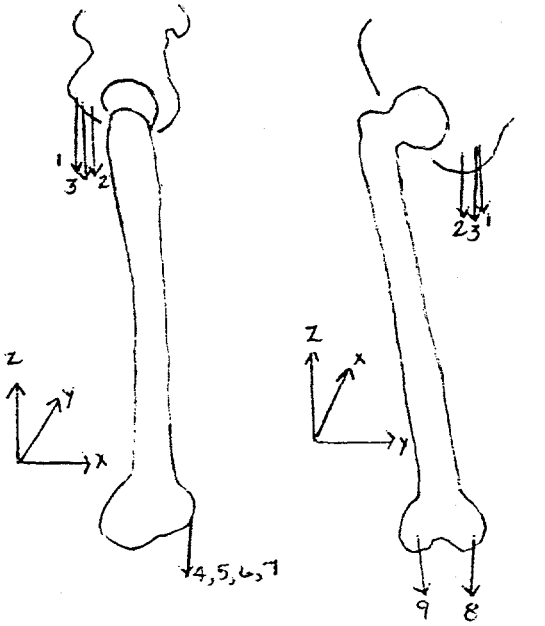

figure 11:
Free-body diagram for the femur, standing position

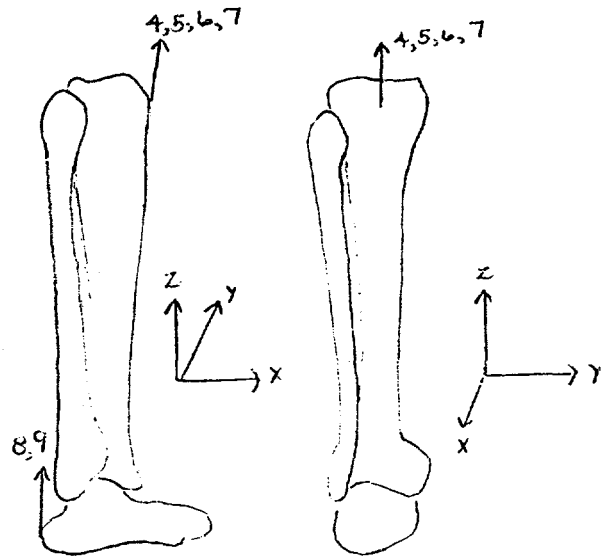

figure 12:
Free-body diagram for the tibia, standing position

Force equilibrium equations and a moment equation were formulated to describe the forces at each segment and rotation about the knee joint, respectively. The following equations were formulated for the standing position.

Force equilibrium equations for femur:

$$\Sigma F_X = F_{X1} + F_{X2} + F_{X4} + F_{X5} + F_{X6} + F_{X7} - (F_{X3} + F_{X7} + F_{X8} + F_{X9}) + R_X = 0$$

$$\Sigma F_Y = F_{Y4} + F_{Y7} + F_{Y9} + (F_{Y1} + F_{Y2} + F_{Y3} + F_{Y5} + F_{Y6} + F_{Y8} + R_Y = 0$$
$$\Sigma F_Z = -(F_{Z1} + F_{Z2} + F_{Z3} + F_{Z4} + F_{Z5} + F_{Z6} + F_{Z7} + F_{Z8} + F_{Z9)} + F_A + R_Z - W_F = 0$$

Force equilibrium equations for tibia:

$$\Sigma F_X = F_{X3} + F_{X7} + F_{X8} + F_{X9} - (F_{X1} + F_{X2} + F_{X4} + F_{X5} + F_{X6} + F_{X7}) - R_X = 0$$
$$\Sigma F_Y = F_{Y1} + F_{Y2} + F_{Y3} + F_{Y5} + F_{Y6} + F_{Y8} - (F_{Y4} - F_{Y7} - F_{Y9}) - R_Y = 0$$
$$\Sigma F_Z = F_{Z1} + F_{Z2} + F_{Z3} + F_{Z4} + F_{Z5} + F_{Z6} + F_{Z7} + F_{Z8} + F_{Z9} - R_Z - W_Z = 0$$

Moment equation describing rotation about the knee joint:

$$\Sigma M = F_1d_1 + F_2d_2 + F_3d_3 + F_4d_4 + F_5d_5 + F_6d_6 + F_7d_7 + F_8d_8 + F_9d_9 + W_F + F_A = 0$$

CONCLUSION

Applications. Determining muscle tensions and joint reaction forces in various postures is an immediate application of the model. Using the method outlined, several static situations (e.g. leaning, squatting, rising from a chair) can be modeled. The results of the standing and automobile situations will be used as boundary conditions for a finite element model of the human knee joint.

The concepts and equations developed for this model may be used as input for a computational model of the human knee joint. Specifically, a computational model can be used to solve for muscle forces using the optimization technique. One can use the model to analyze the effects of changes in muscle attachment points.

Suggestions for Improvement. Several changes can be made to improve the accuracy of the model.

- The data used to formulate the results presented in this paper exhibited considerable variability. Muscle length, moment arm length, and cross sectional area values vary between subjects. For the purpose of this model, data was obtained from several sources in the literature.

- The attachment of muscle to bone may occur over a variable region, making the task of assigning an origin and/or insertion point an ambiguous one. Lines of action should closely reflect the true physiological function of the muscle. Therefore, choosing a

point of origin and a point of insertion should involve careful consideration of the muscles' kinetic characteristics.

- The assumptions made when reducing the number of unknown variables may not accurately reflect true physiological behavior of the muscles. EMG analyses and verification of the proposed assumptions should be performed before calculating muscle forces.

- Straight-line modeling does not account for the curvature of tendon paths. To take into account those muscle which wrap around bones, second and third order equations should be employed. With straight line modeling, the muscle's true tendon path is not represented.

- Eight muscles were included in this model. However, over 30 different muscles cross the knee joint. Including a greater number of muscles in the model would increase the accuracy of the results.

- The center of gravity of the segments defined in this model were estimated. The information included in the literature only accounts for the weights and centers of single bones.

- Several ligaments cross the knee joint and exhibit passive tension. Including the tension contribution of these ligament in the model would increase the accuracy of the results.

- The moment arm values of muscles vary according to the orientation of the bones they cross. In modeling different postures, one must take into account the change in moment arm length as a function of joint angle.

REFERENCES

V.C. Mow, W.C. Hayes (1991) *Basic Orthopedic Biomechanics*. Raven Press, Ltd., New York.

C.W. Spoor and J.L. Van Leeuwen (1992) Knee Muscle Moment Arms from MRI and from Tendon Travel. *J. Biomechanics* **25(2)**, pp. 201-206.

W. Herzog and L.J. Read (1993) Lines of Action and Moment Arms of the Major Force-Carrying Structures Crossing the Human Knee Joint. *J. Anat.* **182**, pp. 213-230.

A. Seireg and R.J. Arvikar (1973) A Mathematical Model for Evaluations of Forces in Lower Extremities of the Musculo-Skeletal System. *J. Biomechanics*, **6**, pp. 313-326.

A. Van Kampen, R. Huiskes (1990) The Three-Dimensional Tracking Pattern of the Human Patella. J. Orthopaedic Research, **8**, pp. 372-382.

Curvature Analysis for Three-Dimensional Tracking of Computer Vision Data

Adam Sanford

Cornell University

Lawrence Livermore National Laboratory
Livermore, California 94550

December 13, 1995

Prepared in partial fulfillment of the requirements of the Science and Engineering Research Semester under the direction of Dr. Shin-Yee Lu, Research Mentor, in the Lawrence Livermore National Laboratory.

* This research was supported in part by an appointment to the U.S. Department of Energy Science and Engineering Research Semester (hereinafter called SERS) program administered by LLNL under Contract W-7405-Eng-48 with Lawrence Livermore National Laboratory.

CONTENTS & THESIS

Thesis:

Markerless imaging systems could potentially track data points with an analysis of the local curvature of its acquired surfaces.

Contents:

I. Abstract 3

II. Introduction 4

A. CyberSight and its applications
B. The tracking dilemma

III. Curvature Analysis 5

A. Reasoning in choosing to investigate it
B. Mean and Gaussian curvature parameters
C. The strength of curvature analysis

IV. Methodology 6

A. PointGrab as a visualization tool
B. Virtual shapes as test of routines
    1. "Perfect" shapes
    2. Grid arrangement
C. Surface normal generation
D. Transformation about the surface normal
E. Reconstructing the orthogonal grid
F. Acquiring H and K
G. Color coding

V. Results & Conclusions 15

VI. Acknowledgments 17

VII. Bibliography 18

I. ABSTRACT

The purpose of this project is to develop a method of tracking data points for computer vision systems using curvature analysis. This is of particular interest to fellow researchers at the Lab, who have developed a markerless video computer vision system and are in need of such a method to track data points. A three dimensional viewing program was created to analyze the geometry of surface patches. Virtual surfaces were plotted and processed by the program to determine the Mean and Gaussian Curvature Parameters for each point on the surface, thus defining each point's surface geometry type. Preliminary results indicate that coordinate independent curvature analysis shows great promise and could solve the tracking dilemma faced by those in the field of markerless imaging systems.

II. INTRODUCTION

A new computer vision technology, called CyberSight, has been developed at Lawrence Livermore National Laboratory. It is capable of acquiring three-dimensional range data of moving surfaces at video speed. It was developed by LLNL researchers Lu and Johnson, with whom I worked this past semester.

CyberSight shows great promise in many fields. It has applications in biomechanics, security, entertainment, and other fields. For biomechanical analyses, CyberSight could be used for studying virtually any motion, generating precise data which could be easily reduced to yield kinematic data. For security purposes, it could be adapted for facial recognition. Movie companies are interested in the possibilities of using "virtual actors" in their films, with CyberSight's fine detail of musculature and bony prominences.

However, these applications are not yet possible for CyberSight. As a markerless data acquisition system, data tracking methods must be developed to relate different frames from concatenated movies. Though tracking has been a dilemma in computer vision for quite some time, it is the subject that was worked on in this project. The goal is to lay a foundation for future efforts in computer vision tracking.

III. CURVATURE ANALYSIS

The specific possibility of tracking that was investigated was the analysis of local curvature. This seemed a logical area of inquiry, as CyberSight is capable of generating very fine[1] surfaces to analyze.

The crux of curvature analysis lies in the ability to acquire the first and second order partial derivatives of the surface at any point of inspection. This is due to the fact the surface geometry type is governed by two parameters, the Mean Curvature and Gaussian Curvature, which are defined by these partial derivatives as follows[2]:

Mean Curvature, H:

$$H = \frac{(1+z_y^2)z_{xx} + (1+z_x^2)z_{yy} - 2z_x z_y z_{xy}}{2(1+z_x^2+z_y^2)^2}$$

Gaussian Curvature, K:

$$K = \frac{z_{xx}z_{yy} - z_{xy}^2}{(1+z_x^2+z_y^2)^2}$$

Based on the sign of H and K, the surface geometry type is then defined:

$H < 0,\ K > 0$	Peak	$H < 0,\ K < 0$	Saddle Ridge
$H > 0,\ K > 0$	Pit	$H = 0,\ K < 0$	Minimal Surface
$H < 0,\ K = 0$	Ridge	$H > 0,\ K < 0$	Saddle Valley
$H = 0,\ K = 0$	Flat	$H > 0,\ K = 0$	Valley

[1] CyberSight generates surfaces at a spatial resolution of roughly one millimeter (mm).
[2] Li, page 233.

Curvature analysis is attractive in addressing the issue of tracking. H and K are invariant to translations and rotations[1], so objects of constant surface geometry undergoing these transformations in space can still be recorded with CyberSight and still yield the same geometry type if analyzed by curvature analysis routines. As no curvature analysis packages were readily available, the research was focused on creating such a package for insertion into CyberSight's existing image processing code for later use.

IV. METHODOLOGY

A. PointGrab as a visualization tool

CyberSight's final, processed images are roughly 500 X 500 pixels, and are viewed with a graphics package called VISION. This package requires a rather complex interface, with the user inputting Lisp commands to call C code. In addition, VISION displays a set image, and cannot view data from any viewpoint. Considering these hindrances with its rather slow processing time, and the choice to write stand alone software to replace VISION was made.

A graphics program was written to carry out the research. At first written to serve basic needs, more complex routines were added to the program as required. The program, called PointGrab, has been the primary visualization tool of this research throughout the semester.

---

[1] *Ibid.*, page 233.

PointGrab has many functions, including the following:

- View a three dimensional data set from any spherical viewpoint
- Transform and stretch data sets in space
- Plot a curvature map of a data set
- Yield percentage curvature compositions of a data set

B. Virtual shapes as a test of routines

CyberSight is not a perfect system -- that is, it is not free from error. From the frame-grabbing phase to each of the processing steps, error can be introduced to the data. With this in mind, testing any curvature analysis routines on real, processed images would not be prudent. Instead, virtual shapes were created as control surfaces for the testing of any curvature algorithms.

Virtual shapes are nothing more than computer generated shapes. Since they are not "real," they need not be processed (erroneously) by any image processing routines. Therefore, they are mathematically "perfect" up to 8 decimal places[1], and serve as a natural control for any attempts at curvature analysis.

Virtual surfaces were created with a separate program for each shape, using the following process:

1) An orthogonal XY grid was created. This was usually 25 X 25, based on memory constraints.

2) For each point, its corresponding (x, y) location was found.

3) Each point's X and Y location were inserted into the equation for the shape generated by the program, yielding each point's Z value.

4) The data set was then input into a special file format that PointGrab could read, consisting of (x, y, z) points and line connections.

[1] The eight refers to the number of decimal places in a double precision floating point variable.

The goal was to generate as smooth a surface as possible, but aforementioned memory limitations prevented such surfaces from being generated for an entire shape. So a small surface patch of each shape was created for analysis.

Virtual surfaces have been the data sets directly tested with the curvature algorithms this semester. Some of the shapes include a sphere, paraboloid, cylinder, cone, and plane. Some examples are below.

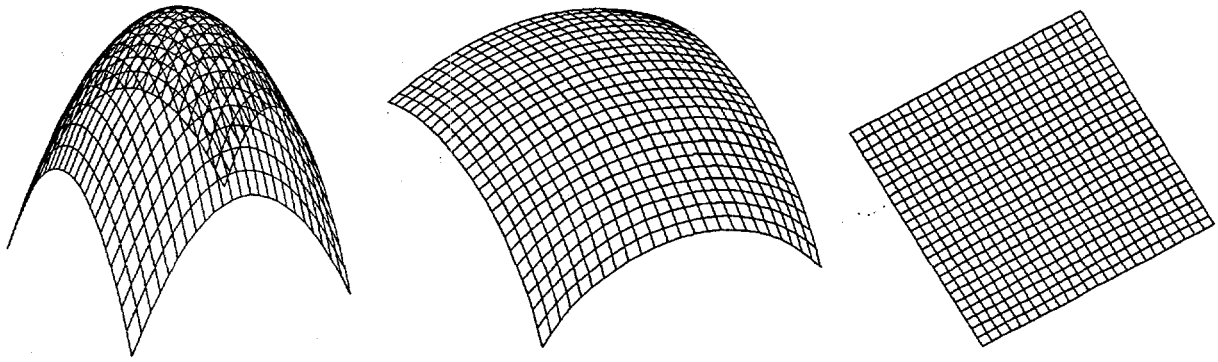

C. Surface normal generation

To achieve coordinate independent curvature analysis, a local coordinate system had to be defined for each point, with the new Z axis being each point's surface normal. Since the surface was a collection of points and not a continuous function where $z = f(x, y)$, the surface normal was not explicitly defined. So a method of generating each point's surface normal had to be devised.

As shown below, a 3 X 3 patch of points, centered about the point of interest, is generated for *every* point.

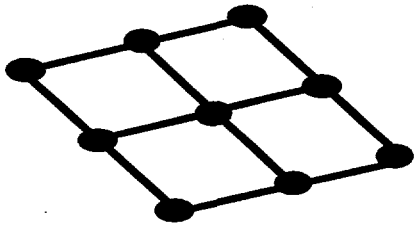

From each patch, four vectors are defined, originating from the center point and heading towards each of the four cardinal directions (one point excursions in the +/- X, Y directions) as shown.

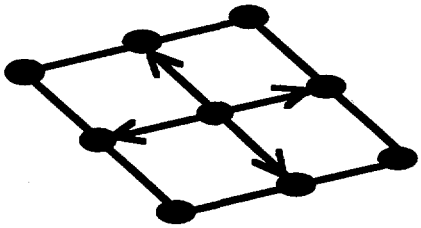

Four independent surface normals were calculated by crossing the adjacent vectors in a circular order; that is, so that the cross products always pointed outward, or always pointed inward. Whichever direction that was chosen was set as the cross product convention for the surface normal generation of each patch.

The four surface normals were then averaged to yield the final (working) surface normal vector for each point, as shown below. This method is simple and was proven effective, barring any gross outliers in the data set.

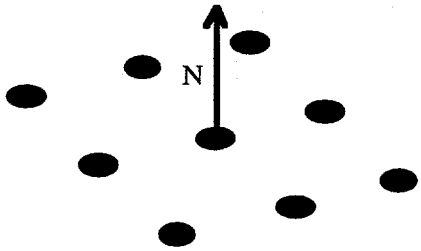

D. Transformation about the surface normal

Once the surface normal had been calculated, it was necessary to make it the new Z axis. To do so, the data points in each patch needed to be transformed about their surface normals. However, general data transformations require three new axes to transform a system.

Since curvature is coordinate independent, the only requirement for analysis with local coordinate system is the surface normal as the Z axis. Therefore, the X and Y axes can be arbitrary, as long as they define an orthogonal coordinate basis. Here a decision was made: the new X axis was chosen as the direction from the center point (x, y) to the point one unit further down the old X axis (x+1, y). The Y axis naturally followed with Z cross X, and the orthogonal coordinate basis was determined.

From this new basis, the data in each patch is transformed with the following relation[1]:

$$^{N}q = {}^{R}T_{N}^{-1}\,{}^{R}q, \text{ where}$$

^{N}q represents the new (transformed) XYZ patch as [x′ y′ z′ 1] (row vector)

^{R}q represents the old (pre-transformed) XYZ patch as [x y z 1] (column vector)

$^{R}T_{N}^{-1}$ represents the inverse transformation, which is listed below:

[1] McKerrow, page 153.

$$\begin{bmatrix} x_x & x_y & x_z & -p_x x_x - p_y x_y - p_z x_z \\ y_x & y_y & y_z & -p_x y_x - p_y y_y - p_z y_z \\ z_x & z_y & z_z & -p_x z_x - p_y z_y - p_z z_z \\ 0 & 0 & 0 & 1 \end{bmatrix}$$

where

$$x = x_x i + x_y j + x_z k$$
$$y = y_x i + y_y j + y_z k$$
$$z = z_x i + z_y j + z_z k$$
$$p = p_x i + p_y j + p_z k$$

Above, x, y, z represent the new axes, and p represents the translation vector relating the old origin with the new origin (the patch center).

E. Reconstructing the orthogonal grid

Once the patch was transformed, it no longer retained the XY orthogonality that it once had. This was expected, as only a unit normal parallel to the old Z axis could retain orthogonal patch points. So each resulting patch was a bit distorted, as shown below:

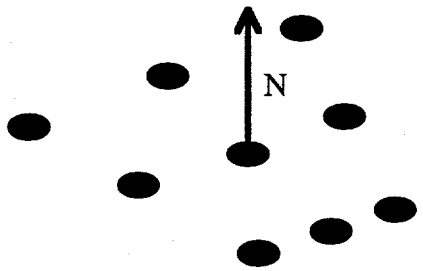

For H and K to be determined, a regular orthogonal grid needed to be reassembled in the new coordinate system. A smaller orthogonal patch, based on the new X and Y, was defined inside the old grid, with data points being separated by a distance ∂, as shown below:

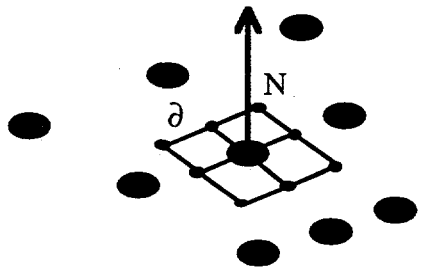

The x and y values of the grid were predetermined +/- ∂ excursions about the center point, but the Z values were unknown. To find them, a planar interpolation was used, with the following procedure:

1) The four vectors are redefined, exactly like with the surface normal generation, but with the new transformed patch. This defines four quadrants, as shown.

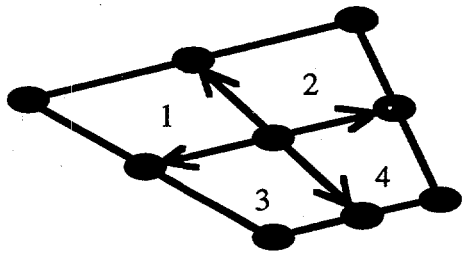

2) The vectors were crossed, to generate four normals, just as before. However, the each normal was then used to define a plane for each quadrant[1]. The equation for each plane is of the form of $Ax + By + Cz = 0$.

3) An cross product routine determined which planes the projections of the new grid points fell on with respect to the Z axis.

4) The (x, y) values of each point on the grid were inserted into its corresponding plane equation, yielding the Z value of each point's projection on the plane.

With the Z values determined, the new orthogonal data patch had been completed, and calculation of H and K could then commence.

[1] Thomas & Finney, page 734.

F. Acquiring H and K

After all of the data manipulation, acquiring H and K became a trivial task. Using grid point Z values, the partial derivatives were simply calculated. The newly constructed orthogonal grid made the calculus straightforward, as each data point was already separated an equal distance ∂.

Based on the new, transformed grid, shown below,

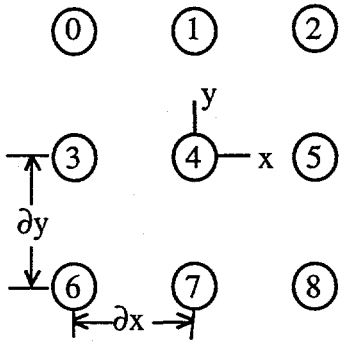

The following equations were used (z[n] equals the z value of point n):

$$z_x = \frac{(z[5]-z[4])}{\partial x} \qquad z_y = \frac{(z[1]-z[4])}{\partial y}$$

$$z_{xx} = \frac{\frac{(z[5]-z[4])}{\partial x} - \frac{(z[4]-z[3])}{\partial x}}{\partial x} \qquad z_{yy} = \frac{\frac{(z[1]-z[4])}{\partial y} - \frac{(z[4]-z[7])}{\partial y}}{\partial y}$$

$$z_{xy} = \frac{\frac{(z[2]-z[1])}{\partial x} - \frac{(z[5]-z[4])}{\partial x}}{\partial y}$$

As an aside, ∂x = ∂y = ∂ in the newly transformed grid, but the deltas have been left in their original format to clarify their usage in the equations.

These equations were applied to each patch, calculating values for each of the partial derivatives necessary to evaluate H and K. H and K were than calculated, using the equations mentioned in the Curvature Analysis section.

G. Color Coding

After H and K were determined, the surface geometry type of each point was determined from the signs of H and K, as previously mentioned. What remained was a question of how the data could be identified graphically.

A color coding scheme was chosen to identify the point's curvature. This served to facilitate curvature identification (rather than by using special dots or shapes for points), and it made groupings of a set curvature type easy to pick out.

The actual carrying out of the color coding scheme was rather simple. A color was chosen and displayed for each geometry type, and a legend was displayed at the top of the graphics window. Percentage statistics of each curvature type present in a surface were also available in a text window.

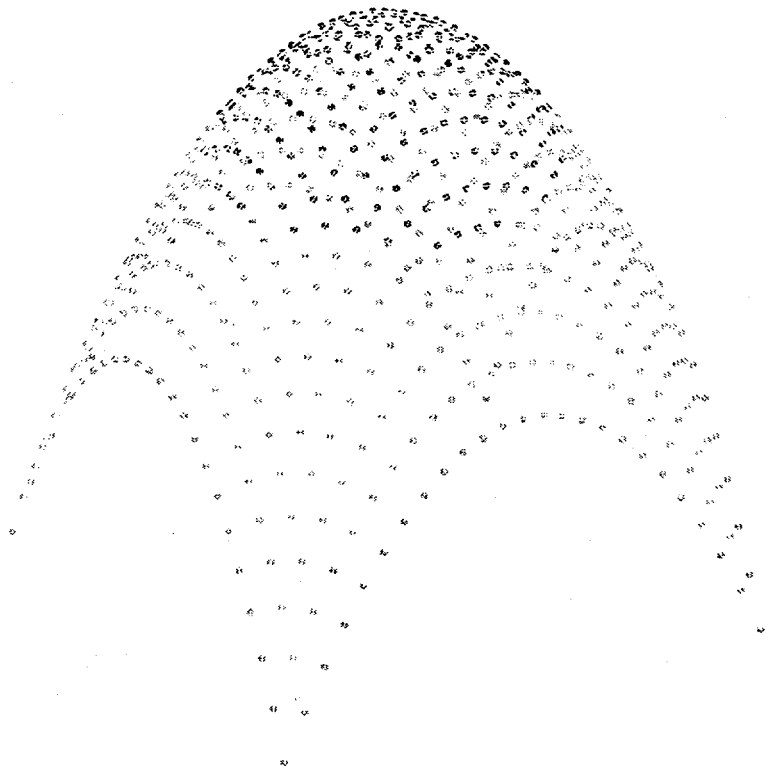

For example, in the picture above, the curvature plot for a paraboloid is shown. The darker dots surrounding the top represent peak curvature, while the dots near the bottom represent ridge curvature. This plot is typical of curvature analyses carried out this semester.

V. RESULTS & CONCLUSIONS

The fuel for the pursuit of curvature tracking was the hope that curvature data could be truly coordinate independent and invariant with rotations and translations. After all of the aforementioned routines were programmed, compiled, and carried out, this indeed was the case.

Data was correctly marked for its curvature by PointGrab, which was not of any great import. But when the data was transformed arbitrarily in space, with various rotations and changes of origin, each point's curvature remained the same. This indeed did verify that curvature analysis is invariant to data transformations.

Current work is being done to insert PointGrab's algorithms for curvature analysis directly into CyberSight's image processing code. This would provide a means to apply curvature analysis to real data acquired by CyberSight, providing the real test for curvature tracking.

With all this said and done, a basic foundation has been laid for curvature tracking of computer vision data. Hopefully it can be put to good use towards the ultimate end of automatic tracking of curvature "landmarks" on scanned surfaces.

VI. ACKNOWLEDGMENTS

I would like to thank The University of California, the Department of Energy, and Lawrence Livermore National Laboratory for giving me the opportunity to take part in this research. I would also like to thank my mentor, Shin-Yee Lu, along with Robert Van Vorhis and Robert Johnson for their guidance and assistance during the semester.

In addition, I would like to thank Stanford Professor Eric Roberts for assisting me via e-mail with my questions regarding his C libraries that I used with PointGrab.

Last but not least, I would like to offer my thanks to fellow SERS student Marc Abramowitz, who showed great patience in bringing me, a mechanical engineering student, up to speed in the world of C and UNIX.

VII. BIBLIOGRAPHY

Ammeraal, Leendert. *Programming Principles in Computer Graphics*. John Wiley & Sons, New York: 1986.

Frobin, W., Hierholzer, E., Drerup, B. "Mathematical Representation and Shape Analysis of Irregular Body Surfaces." Pages 132-139, *SPIE BioStereometrics*, Vol. 361, 1982.

Hierholzer, E., Drerup, B. "Objective Determination of a Body-Fixed Coordinate System using Back Surface Data." Pages 262-265, *SPIE BioStereometrics*, Vol. 602, 1985.

Li, S.Z. "Toward 3D Vision from Range Images: An Optimization Framework and Parallel Networks." Pages 231-260, *Computer Vision Graphics & Image Processing: Image Understanding*, Vol. 55, No. 3, May 1992.

McKerrow, Phillip John. *Introduction to Robotics*. Addison-Wesley, Reading, Massachusetts: 1993.

Roberts, Eric S. *The Art and Science of C*. Addison-Wesley, Reading, Massachusetts: 1995.

Thomas, Jr., George B., Finney, Ross L. *Calculus & Analytic Geometry*. Addison-Wesley, Reading, Massachusetts: 1992.

The China Model: Energy Modeling the Modern Dynasty

Jason Shaw
Binghamton University
Energy Research Division

In this paper a node-based microeconomic analysis is used to model the Chinese energy system. This model is run across multiple periods employing Lagrangian Relaxation techniques to achieve general equilibrium. Later, carbon dioxide emissions are added and the model is run to answer the question, "How can greenhouse gas emissions be reduced?"

December 7, 1995 Version 1.2

Introduction

The Chinese economy has been growing at an annual rate of nearly 10%. And although Chinese living standards are approximately decades behind those in the U.S, this does not make China unimportant. In fact, because of its size (nearly one billion people) and relative poverty, any small increase in the average annual income represents a proportionally larger increase in Chinese buying power. Thus, China is a "hot" topic with many economists today.

I came to Lawrence Livermore National Laboratory (LLNL) to work on an energy model of China. What I found is a generalized modeling tool, named META•Net, and a Chinese energy model built to run on it. What follows is a description of this model. Keep in mind that any feature of the Chinese economy is also a feature of META•Net.

In time, I began to learn that META•Net goes far beyond China. It is the creation of Alan Lamont, my mentor. And it is by his efforts that I found a project at LLNL. META•Net is the vanguard of his personal efforts to create a generalized modeling system, while the China model is a "racy" implementation, thereof.

In this paper, we will explore the Chinese energy system. We will explore the model at three layers of abstraction before moving on to an application of the model to a real-life policy problem.

The Model

Our model can be seen from many different levels. Starting with the highest, most abstract level, we progress down through three levels toward the deepest, most involved explanation.

Level 1 - The Black Box

At the highest level, the China Model is a black box (figure 1). Variables are passed in, manipulated in some way and are passed out. In general, users might specify the number of periods the model should run, the number of years each period represents, the economy's interest rate, and other global parameters. However, the mechanics of how the model works are completely hidden. Yet, this model can still be useful because by choosing the "proper" set of input variables, we can ask the black box questions and obtain answers by studying its final state output.

Level 2 - A Collection of Sectoral Units

Removing the opaque exterior and looking inside the box, we find our next level (figure 2). Here, the model's interior mechanism is partially revealed. Now, the China Model is a collection of sectoral units. As the figure depicts, energy resources, such as petroleum, natural gas, coal, nuclear, hydro, wind and biomass, are linked to energy demands, such as exports, industry, commerce, agriculture, transportation and residential usage.

Viewed from this second level, it's easy to associate our model with the basics of microeconomic analysis. Essentially, each link is a set of supply and demand curves specified by the input variables to the model (figure 3). Input variables include both demand and supply curves plus an initial price and quantity point. Given this information for each link, it is the interplay of these curves that will determine the model's final output state. For example, assume figure 4 represents the initial variables for the link connecting the industrial demand sector to the natural gas resource. DNG is the industrial demand curve for natural gas, SNG is the natural gas resource supply curve and point A is the initial price and quantity point. Isolated, as it is in this case, natural gas demand does not equal natural gas supply. Thus, by the law of supply and demand, this system is not in equilibrium. And, in order for our final state

output to be stable, it must be in equilibrium[1]. So, to establish equilibrium we move horizontally from initial point A to point B (figure 5). However, at point B we still aren't in equilibrium, so we move vertically to point C - then to point D and so on. This method is called "cobwebbing." Notice that each successive point brings us closer to equilibrium.

If our entire system were as simple as this single set of curves then, cobwebbing would take far longer than necessary to establish equilibrium. In fact, a simple substitution would provide the equilibrium point without confusion. However, because we are dealing with so many of these curve pairs simultaneously and across many periods, substitution for every link would be computationally monstrous. Instead, cobwebbing is a convenient, algorithmic way to find a common equilibrium.[2]

Level 3 - The Full Description

Now for the deepest level of our model. Here, in level three, we discover each sectoral unit's inner workings.

The Chinese Petroleum Sector

Consider the Chinese Petroleum Sector. Petroleum resources are either imported or produced domestically. Imported petroleum is restricted by government edict while domestic petroleum is subsidized by the government. Regardless, both compete in a market for crude oil. Here, refiners purchase crude oil with the intention of converting it into usable products. These products are then sold to demanders at a price that is inflated by government taxation.

---

1 Not all economic systems are in equilibrium, however final state stability is a hallmark of economic analysis. Without stability the model provides unreliable results. Thus, I have assumed the existence of a general equilibrium. Although this may be an oversimplification of the system, it provides many reliable results without the loss of much credibility.

2 To cobweb more than one link at a time, our model begins by surveying all its links and finding the one with the largest necessary change. Using a relaxation coefficient, the link is "relaxed" by some multiple of the full necessary change and that information is passed to all connected/related links. For instance, if the price of natural gas to industrial demanders is the largest necessary change and our cobweb algorithm increases it then, this change must be communicated to the link between natural gas and electric generation. Furthermore that change in price will affect the price of electricity and so on.

Schematically, using shape to denote function, this system maybe portrayed using a variety of nodes (figure 6). Hexagonal nodes representing energy resources, such as, imported and domestic petroleum supplies, are shown at the bottom. Rectangular "conversion" nodes for government taxes (subsidies) and restrictions are linked directly above each of these. These conversion nodes link to the oval shaped market for crude oil. The crude market "uplinks" to a commercial refinement conversion node which itself uplinks to a taxation conversion node before all refined products are deposited in the petroleum product market.

Initially, the parameters to all these nodes must be set (table 1).

Depletable resources, such as petroleum, can either be explicitly modeled or simply made part of a "price track."

Explicitly modeled resources can either be mined or extracted from a well. In either case, the model assumes that the resource will be developed or "committed," in blocks each period. The rate at which a block can produce is a function of its size and type. Once committed, a mine will produce at a constant rate until exhausted. In the case of a well, production will be equal to the demand divided by the production to reserves ratio. For each commitment there is a minimum price that must be recovered by the resource owner in order to develop it. To compute this price, the node first calculates the total production that can be obtained from the existing committed blocks. If additional commitments are required then a minimum price is modeled as an exponential function of all past commitments plus these. This "price-commitments curve" is specified by the user and specifies the minimum price that a resource owner must recover in order to commit the additional block. However, the owner will not develop the resource now if the discounted price from one of the future periods is greater than the current price.[3]

In the case our domestic petroleum resources, this depletable resource is explicitly modeled. It is extracted from a well with an initial production of 197 million tons of coal equivalent (mtce), a production to reserves ratio of 0.1, a resource life of 10 years, a

---

3 Our model assumes perfect foresight.

discount rate of 0.2, and a price-commitments curve such as the one shown in figure 7.

Foreign oil imports are different. Due to their exogenous nature, imported oil is "price tracked." Initially it costs 609 yuan/tce and simply grows at an annual rate of 2%. This maybe an oversimplification but, to a first approximation, the world oil price is independent of Chinese demands.

The nodes directly above these resource nodes represent government subsidies and import restrictions. Government subsidies, which have historically played a large part in the Chinese petroleum sector, are modeled as 950 yuan/tce. Meanwhile, import restrictions are not imposed, though the mechanism is in place for applying them later.

The crude market for petroleum is where domestic and imported petroleum complete for market share. This market node assumes that each demander buys from the supplier with the lowest *effective* cost. However, due to transportation costs, site characteristics and other local factors, the price charged to the demander is not necessarily equal to the price charged by the supplier. Consequently, the supplier with the lowest price will not necessarily have the lowest effective price for all of the buyers. Nor will the lowest priced supply dominate the market. In fact, the market share of a supplier depends on its price and the market's price sensitivity (PS), such that:

$$\text{Share of } i^{th} \text{ supplier} = \frac{\text{Price}(i) - PS}{\text{Sum from 1 to n } [\text{ Price}(j) - PS\ ]}$$

where: Price(i) is the price of the i^{th} supplier and
n is the number of suppliers to the market.

The price sensitivity for our crude market is 3.

From the crude market petroleum is passed to refineries. The refinement conversion node models the conversion of crude oil into end-use products and has several associated parameters. Refinery technology is assumed to come "on-line" in the year 1900. Refineries have a lifetime of 30 years, are available 95% of the time, with a minimum operating capacity of 70%, and an input-to-output ratio of

1.05. The Chinese economy is assumed to begin our simulation with 150 mtce of refinement capacity. Specific capital costs, the cost required to build enough capacity to produce one unit of output per year, are 483 yuan and ancillary operating costs, additional costs per unit of output beyond petroleum input prices, are 80 yuan/tce. Price calculations take into account future prices such that discounted net revenues equal discounted prices, minus the future discounted unit operating costs for future periods, plus the price minus the operating cost for the current period.

Uplinked from refinement are government taxes. For this model these taxes are zero.[4]

Finally, at the top, the Chinese petroleum sector dumps its output into an end-use product market with a market sensitivity of 5. This market links to outside demanders in every sector of the economy (level 2). More specifically, the product market links to nodes in every other sector. Links run from the petroleum product market to the industrial heat node, the industrial motor node, the agricultural stationary motor node, the agricultural mobile motor node, the commercial heat node, the rural residential heat node, the electric generation oil boiler node, the electric generation distillate turbine node, and the petroleum export node.

Other Sectors

Every other sector can be broken down into a scheme similar to that used above for the Chinese petroleum sector. In total, our model has 102 nodes and about twice as many links. Every node has parameters and every link represents a relationship. The mechanism is gigantic, however, the mechanics remain the same throughout.

---

4 This tax "hook" is left in because it will make future pricing schemes easier to update.

An Application

Today, policy-makers are worried about the threat of global warming. By including a carbon emissions module, our model can forecast Chinese carbon emissions at various levels of economic activity and vice-versa (that is, forecast economic activity at various carbon emission levels). What effect would a carbon tax have on Chinese economic activity?

To analyze the situation we run the model twice. The first run is considered the "Base Case," and is a forecast of Chinese economic activity given no government intervention. The second run is a "Taxed Case," where each ton of carbon emitted is taxed at a rate of 600 yuan, growing 3% annually.

Results begin in the year 1990 and extend through 2035. They are shown in charts 1 to 7. The Base Case is in red, the Taxed Case in dark green.

Chart 1 depicts carbon emissions under the two regimes. As expected, carbon emissions are lower when they are taxed. This gap is small to begin with (approx. 300 million tons) but grows exponentially with time (approx. 2000 million tons by 2035).

Charts 2 and 3 show that a tax on carbon will also change the energy-use composition of China. Energy demanders will move away from coal toward nuclear. Total energy-use in the Base Case is predicted to be 5.5 billion tce. While total energy-use in the Taxed Case is predicted to be 4.5 billion tce.

Meanwhile, charts 4 and 5 forecast rising prices for industrial heat and commercial electric. This is also the case for nearly every other energy demander (other energy demanders are not shown here but, include all those sectors described in level 2 of our model abstraction above). Due to the tax, the increased cost of energy increases the price to energy demanders who consequently charge a higher price for goods and services to their own customers.

Consequently (a rise in price usually signals a decline in demand), charts 6 and 7 reveal a decline in energy demand for both the industrial and commercial sectors.

Therefore, it's not too much of a step to say that a tax on carbon may adversely affect Chinese economic activity. The tax will reduce carbon emissions, change energy-use composition, increase prices, and decrease energy demand. None of this necessitates that the Chinese economy be adversely affected however, with all other things constant, economic activity is likely to slow because of this carbon tax.

Figure 1. Black Box

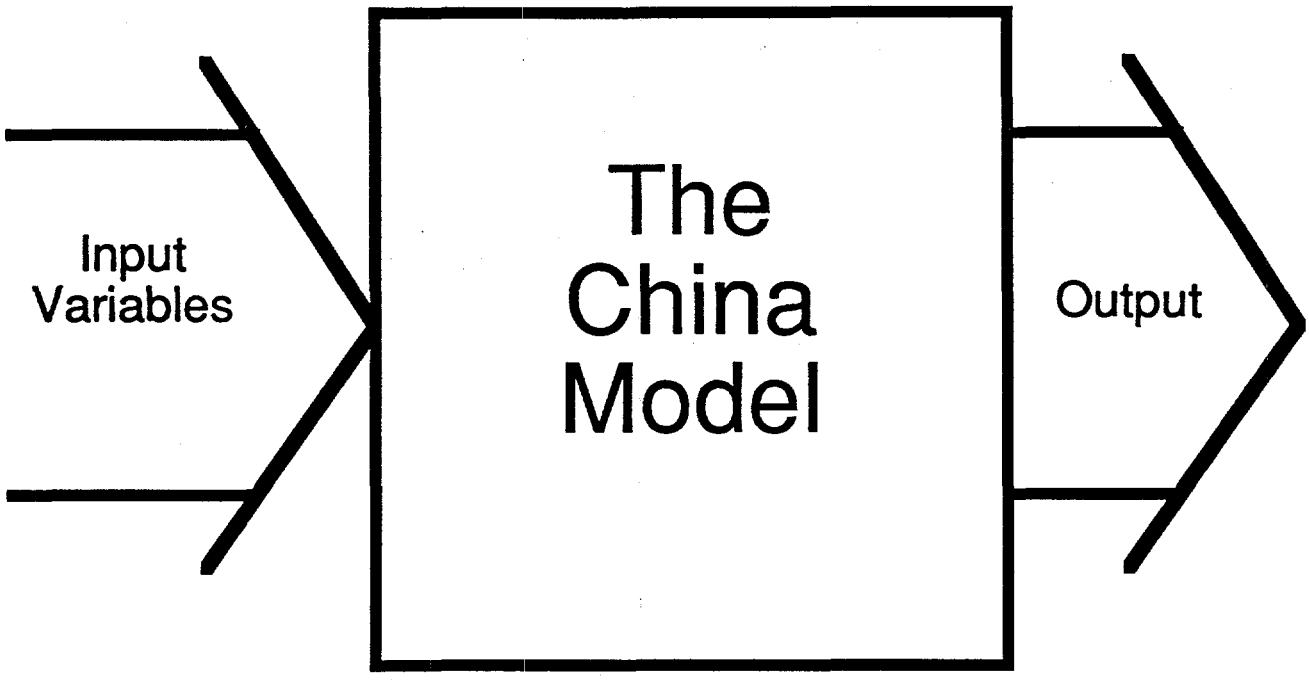

- Questions
- No Mechanics

Figure 2. A Collection of SectoralUnits

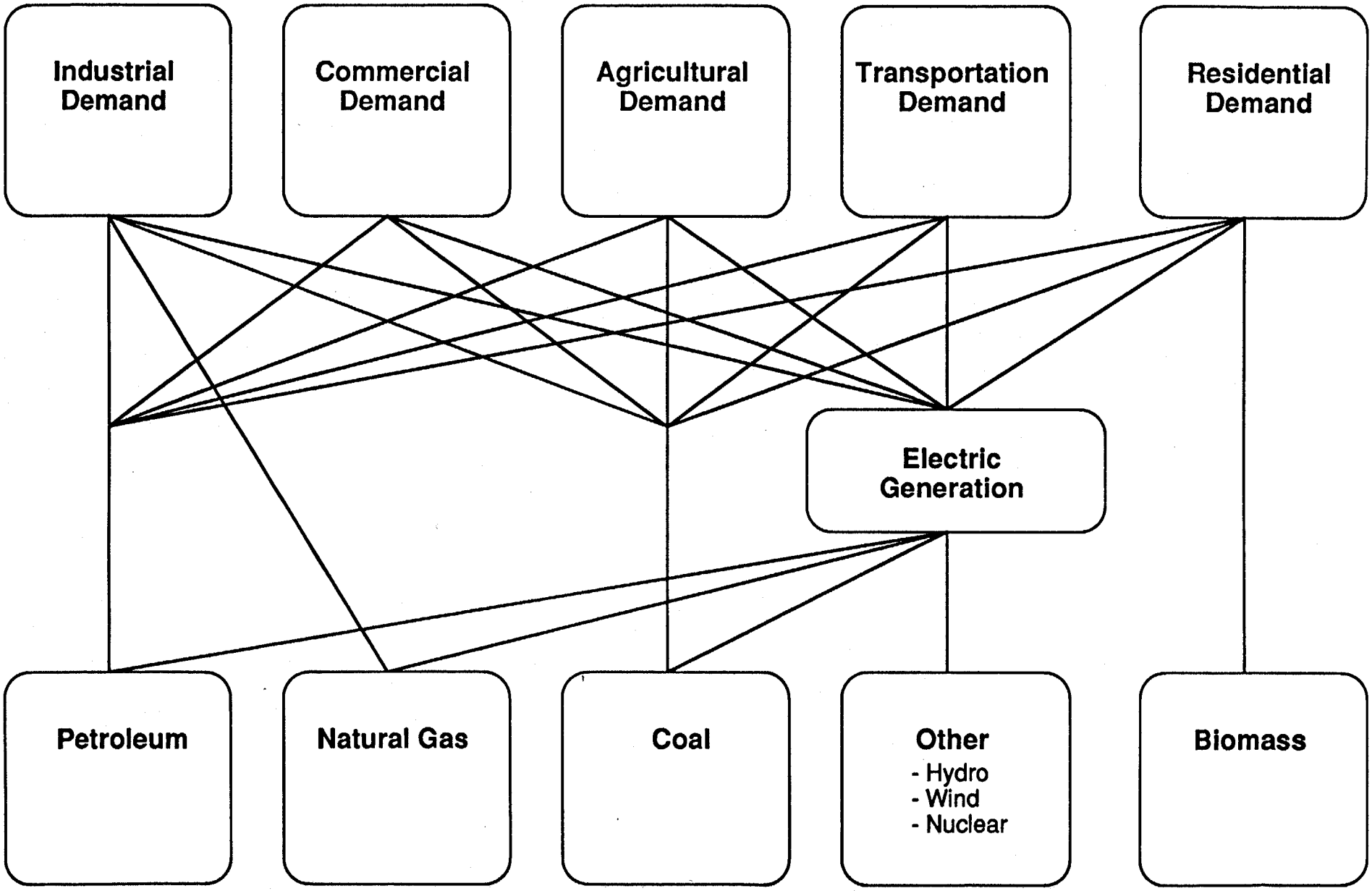

Figure 3. Microeconomic Analysis

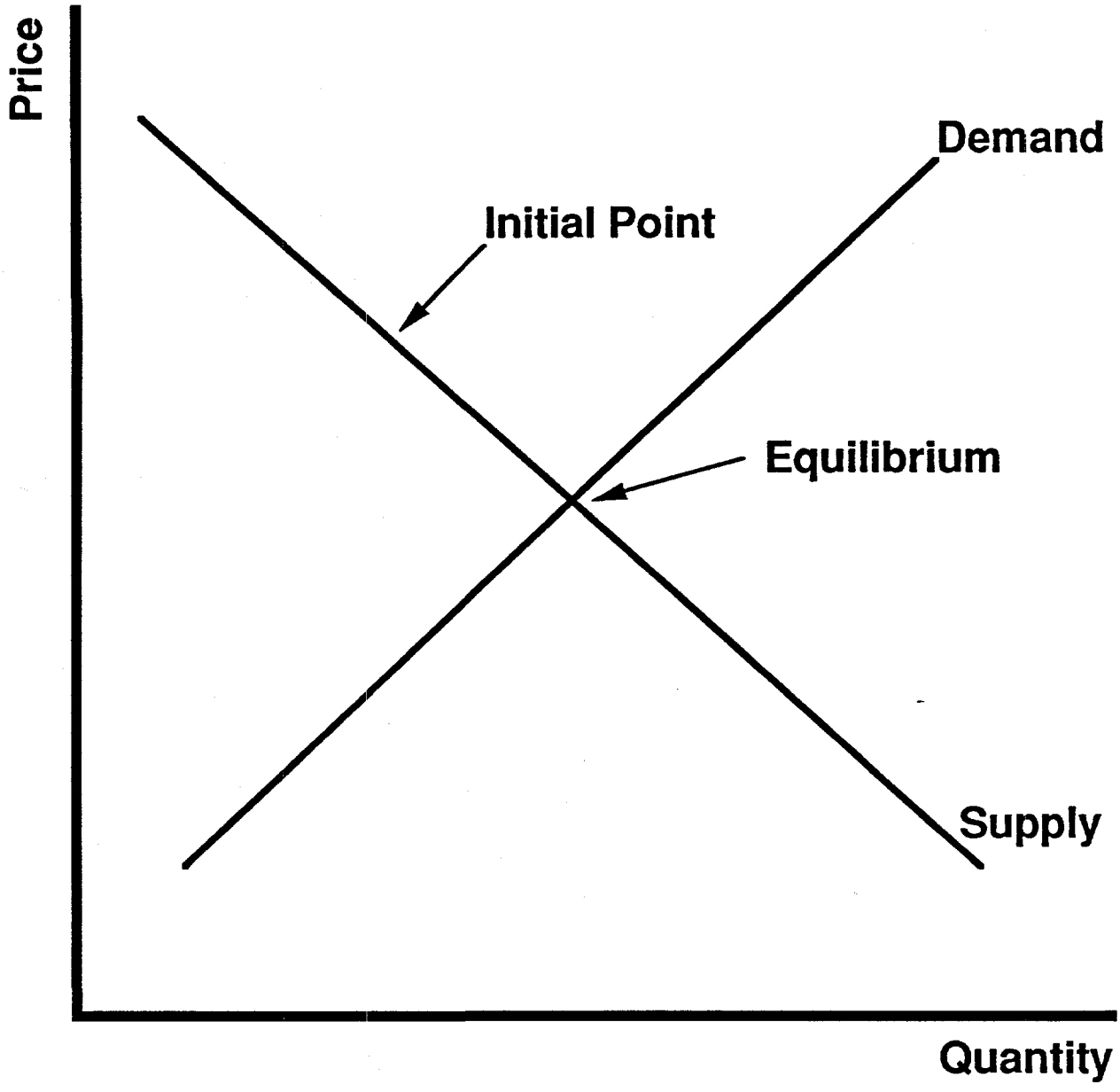

Figure 4. Industrial Demand - Natural Gas Supply Link

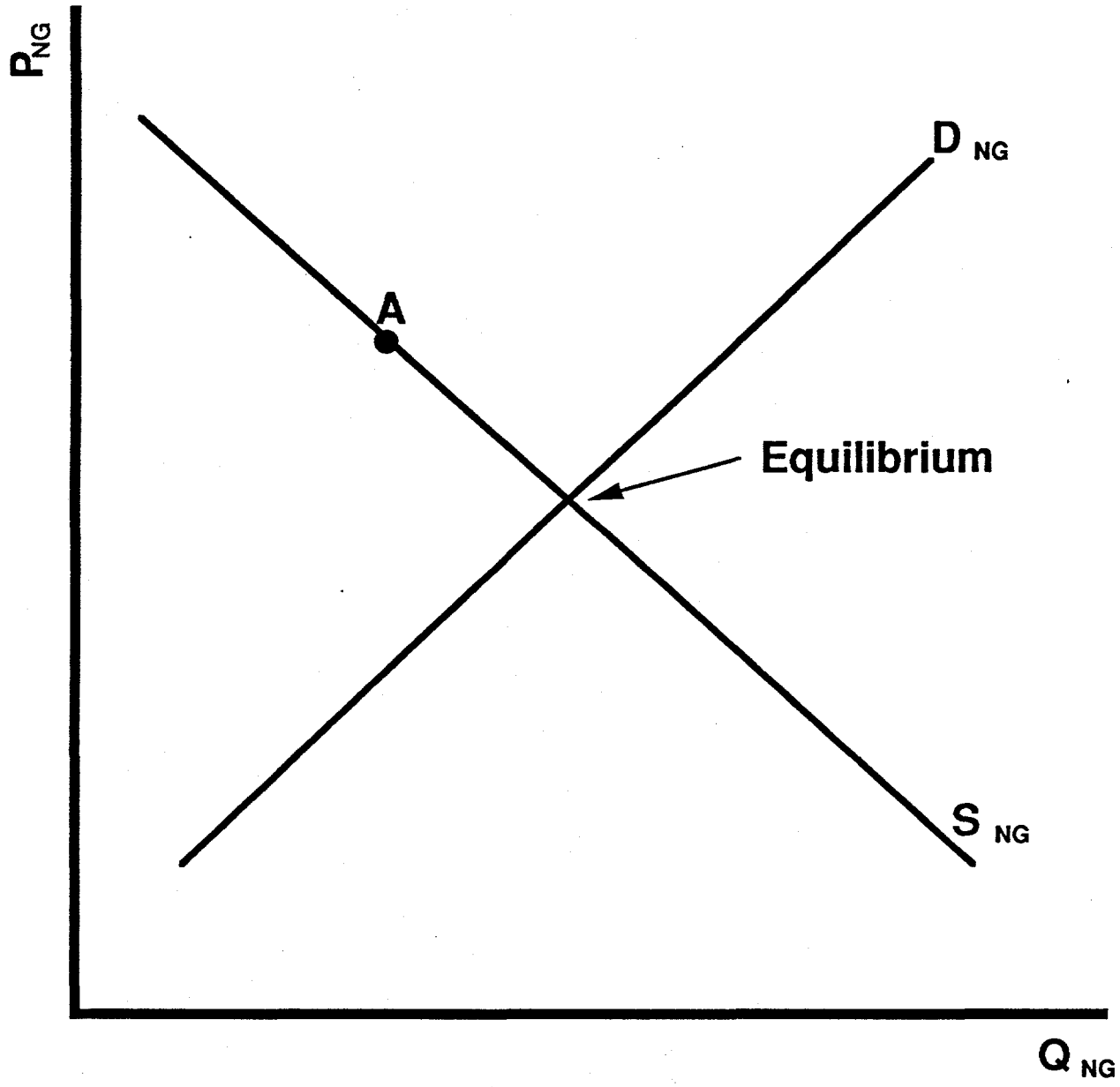

Figure 5. Cobwebbing

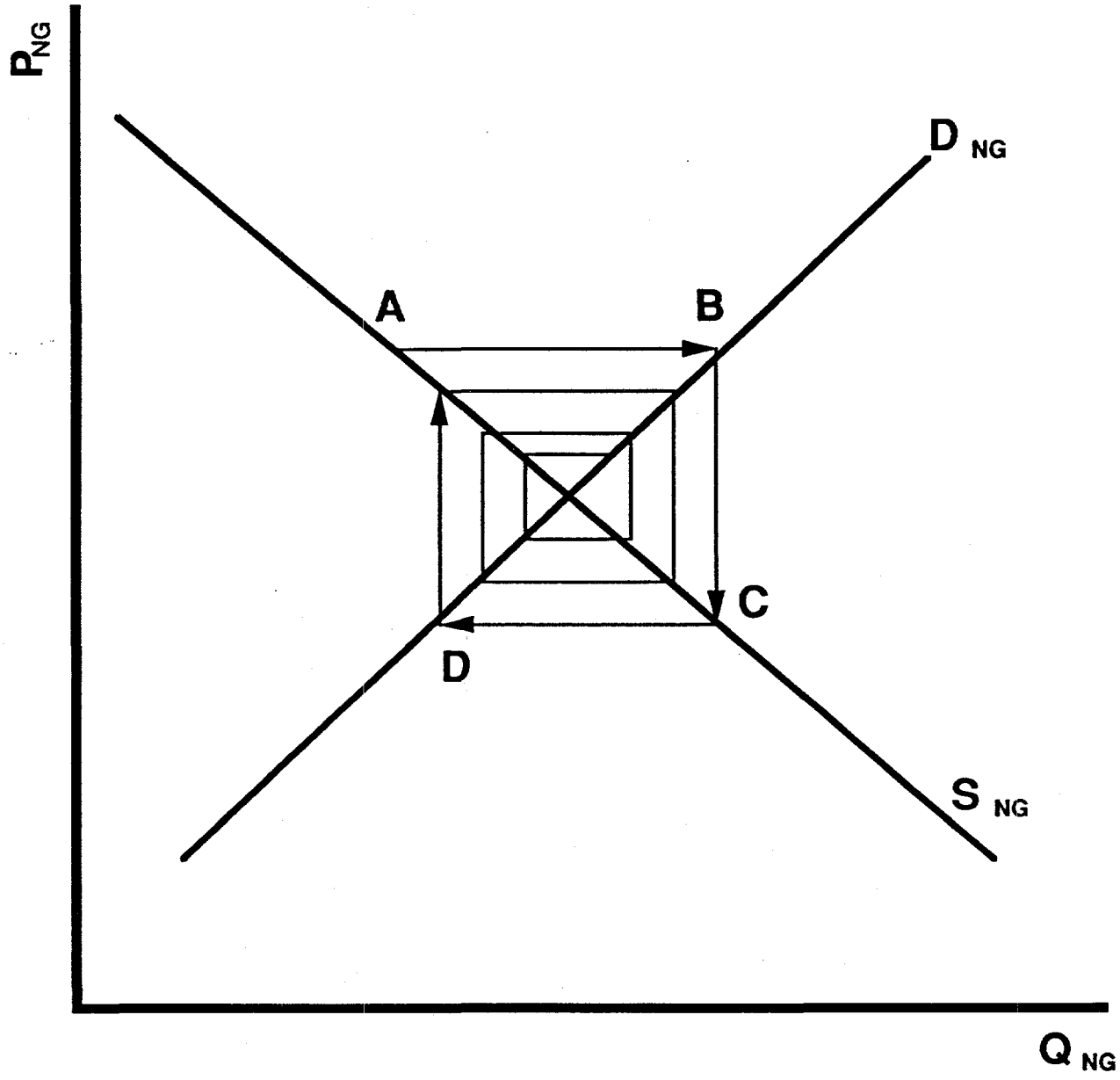

Figure 6. Chinese Petroleum Sector

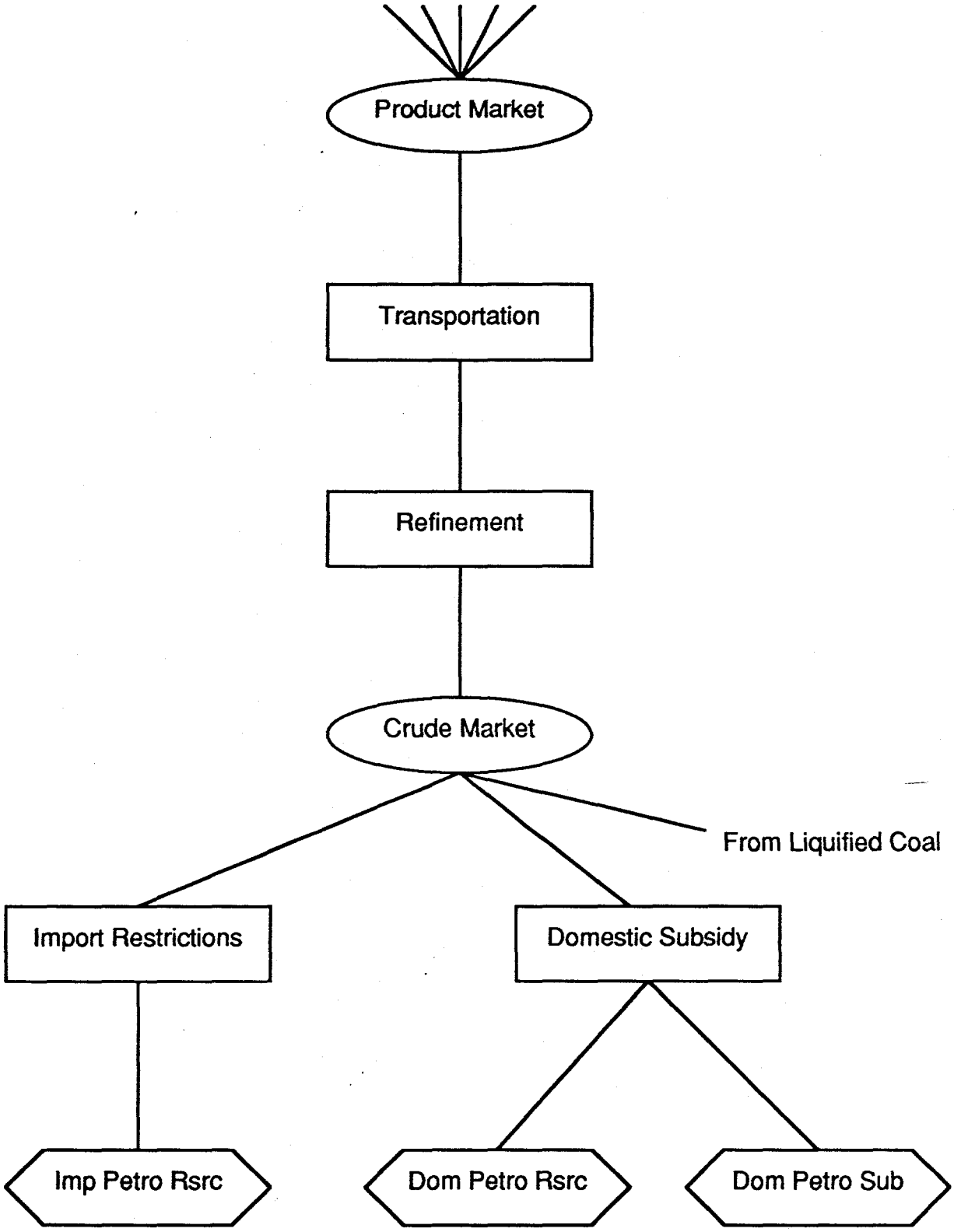

Table 1. The Chinese Petroleum Sector

Domestic Petroleum Resource

Price0	996 yuan/tce	Resource Type	well
Price1	1992 yuan/tce	Initial Production	197 tce
Commitment1	4682 mtce	Production/Reserves	0.1
Price2	2988 yuan/tce	Resource Life	10 periods
Commitment2	14,000 mtce	Discount Rate	0.2

Imported Petroleum Resource

First Period Price	609 yuan/tce	Annual Growth Rate	0.02

Government Subsidies

Annual Subsidy	950 yuan/tce

Import Restrictions

None

Crude Market

Sensitivity Rating	3

Refinement

First Year Available	1900	Availability Factor	0.95
Specific Capital Cost	483 yuan	Minimum Capacity Fa	0.7
Ancilary Operating C	80 yuan/tce	Start Capacity	150 mtce
Life	30 years	Input-Output Ratio	1.05

Taxation

None

Product Market

Sensitivity Rating	5

Figure 7. Domestic Petroleum Price-Commitments Curve

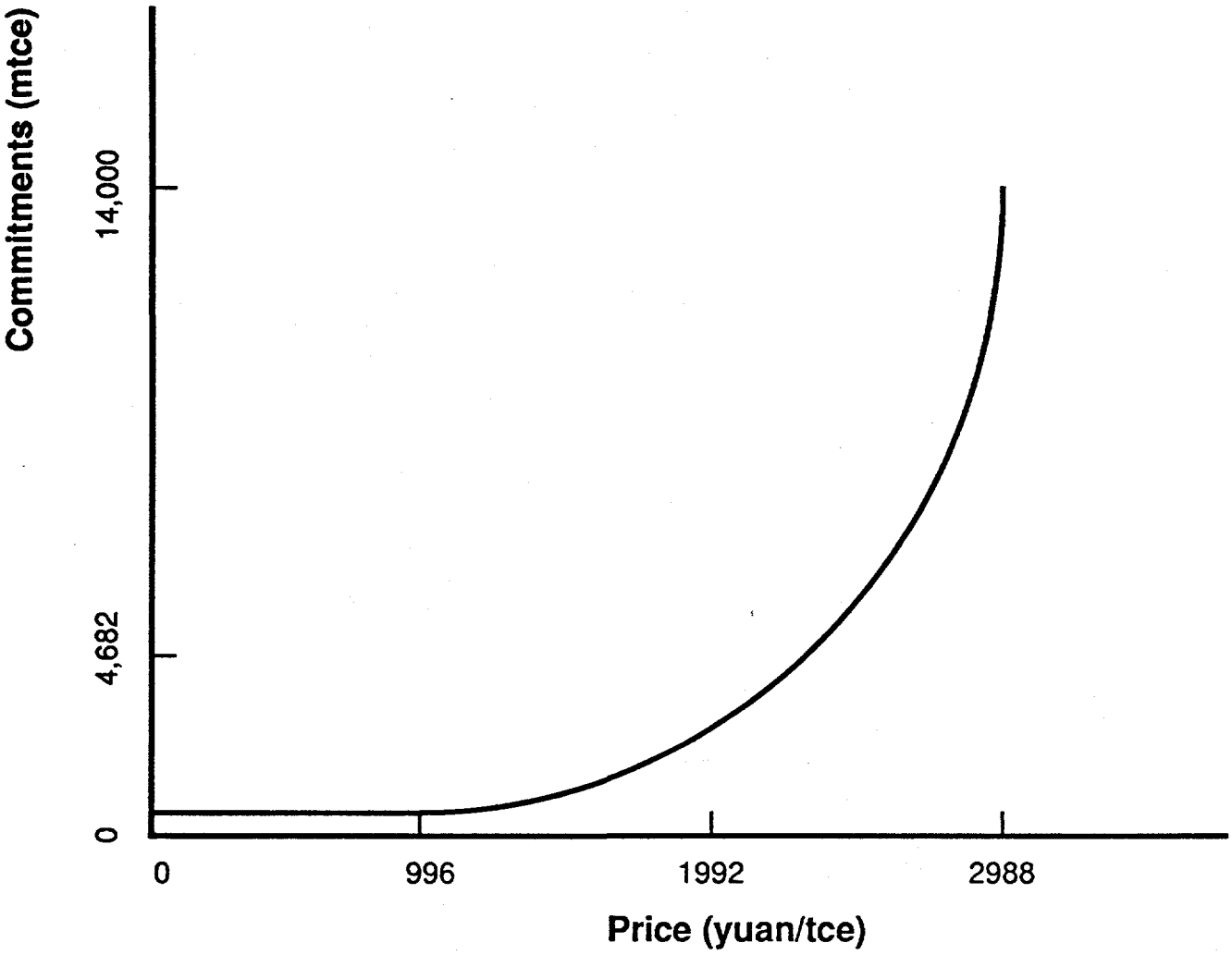

Chart 1

Carbon Emissions

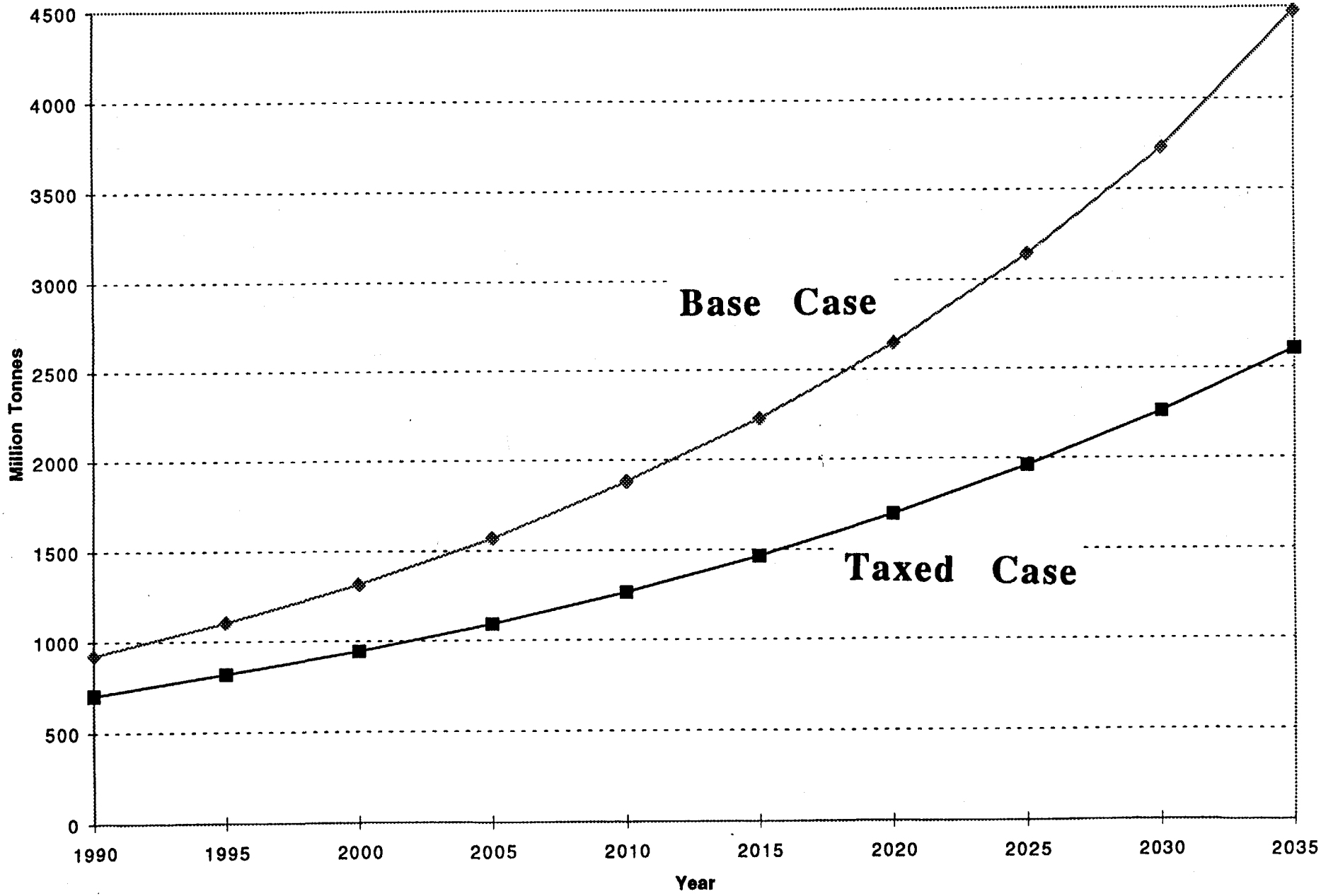

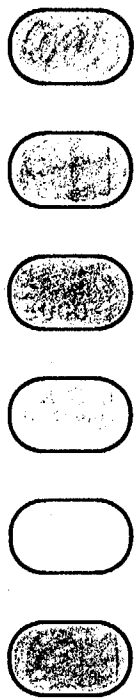
Nuclear
Biomass
Coal
Hydro
Natural Gas
Petroleum

Chart 2

Energy Use Composition (Base Case)

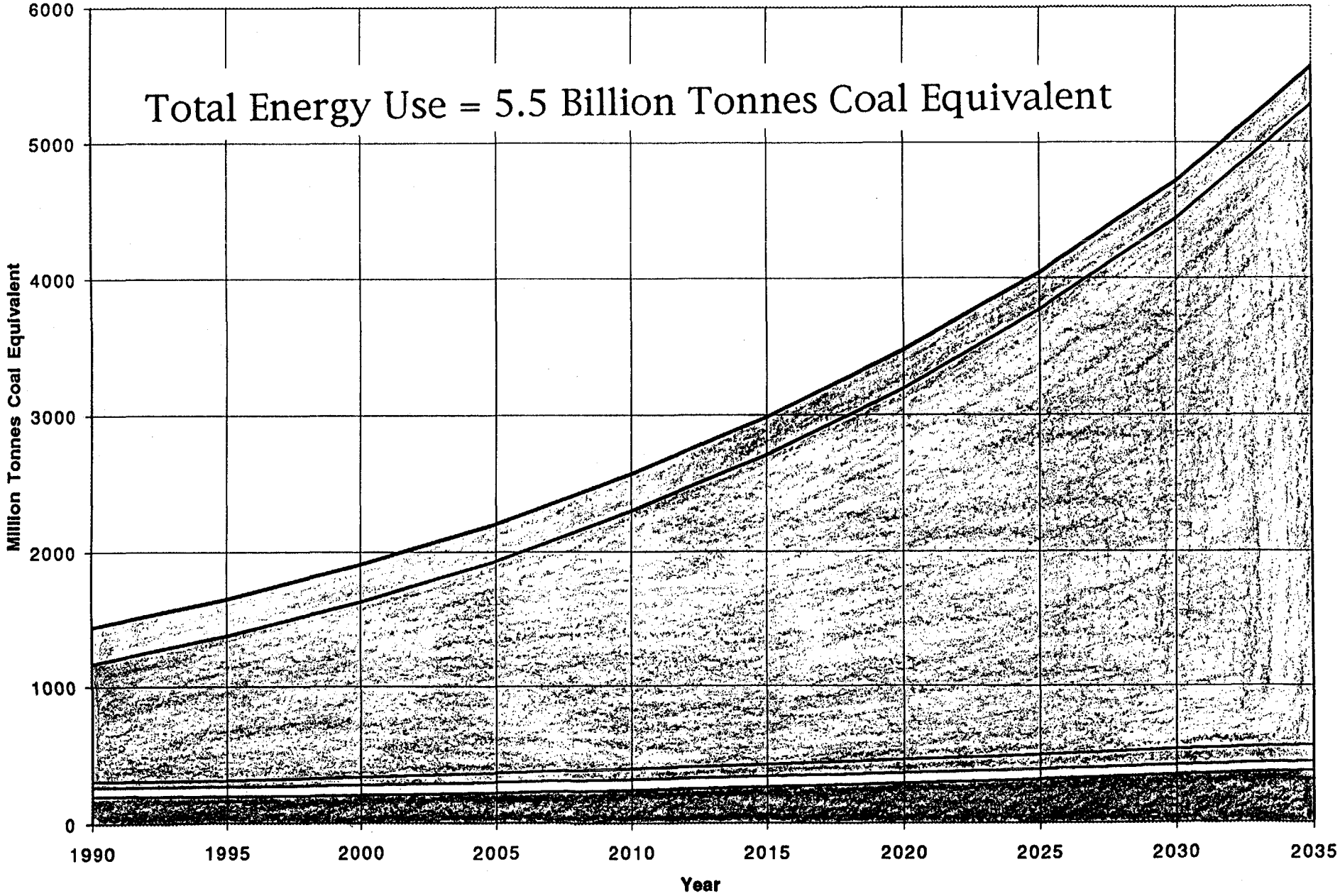

Chart 3

Energy Use Composition with Tax

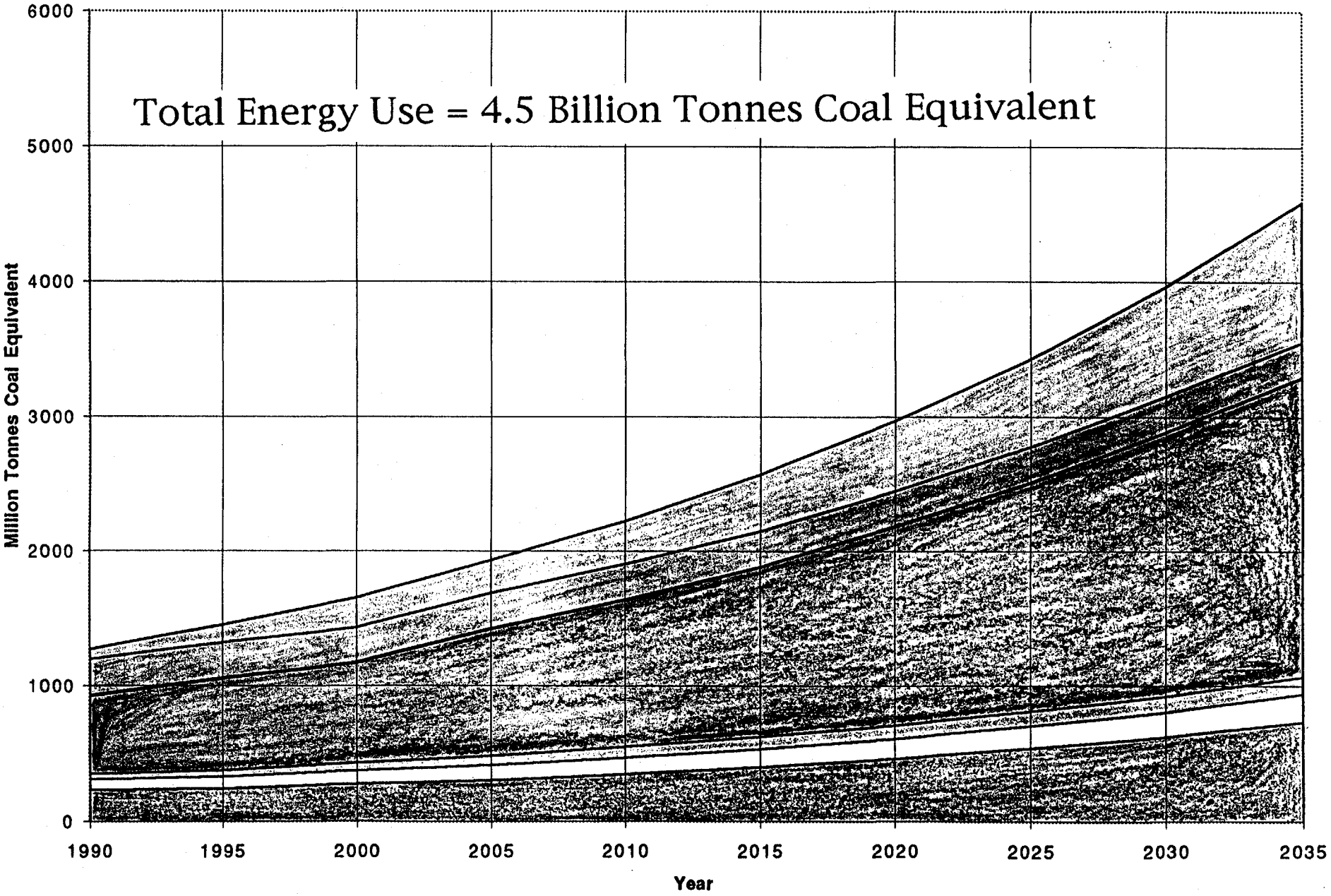

Chart 4

Industrial Heat Prices

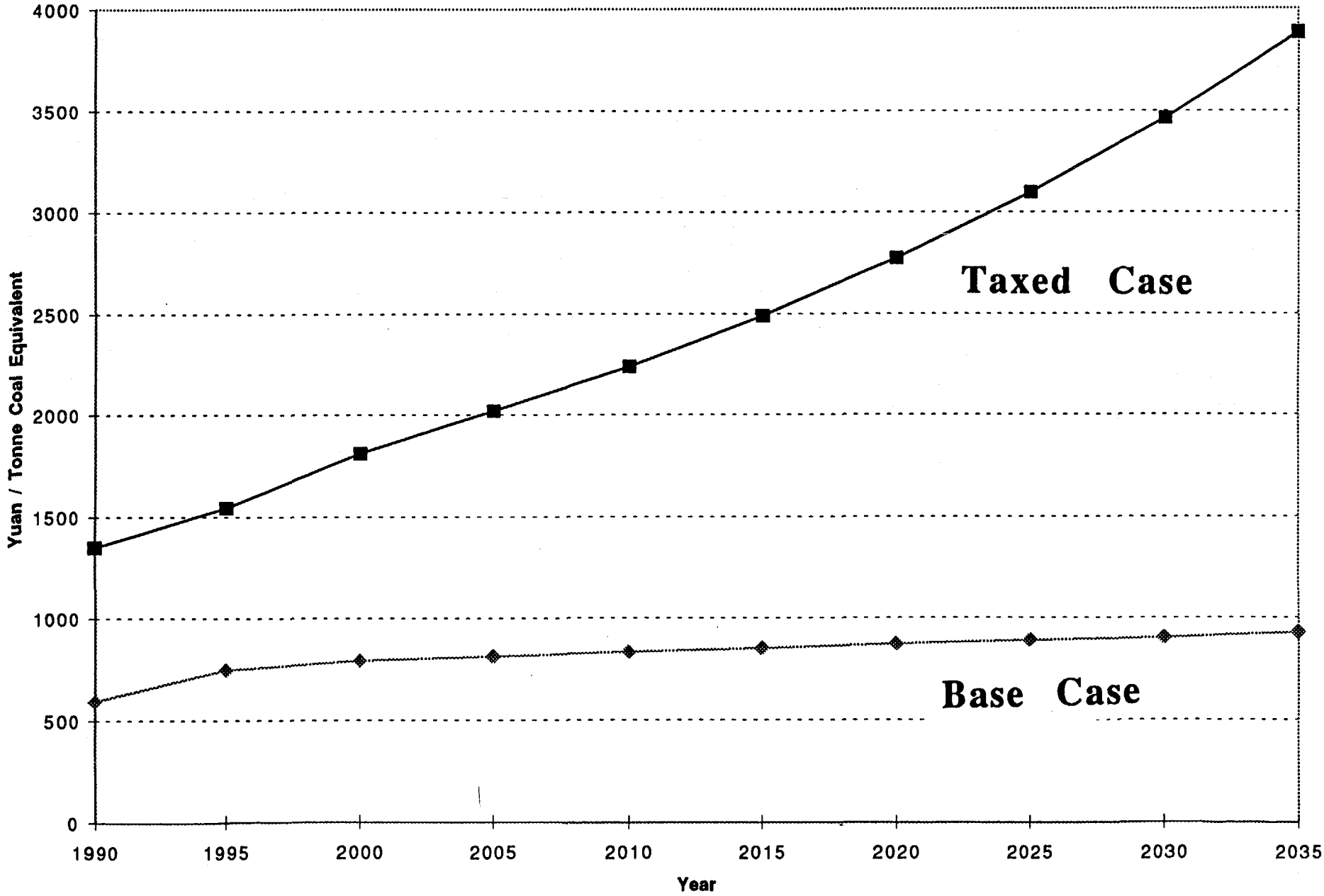

Chart 5

Commercial Electric Prices

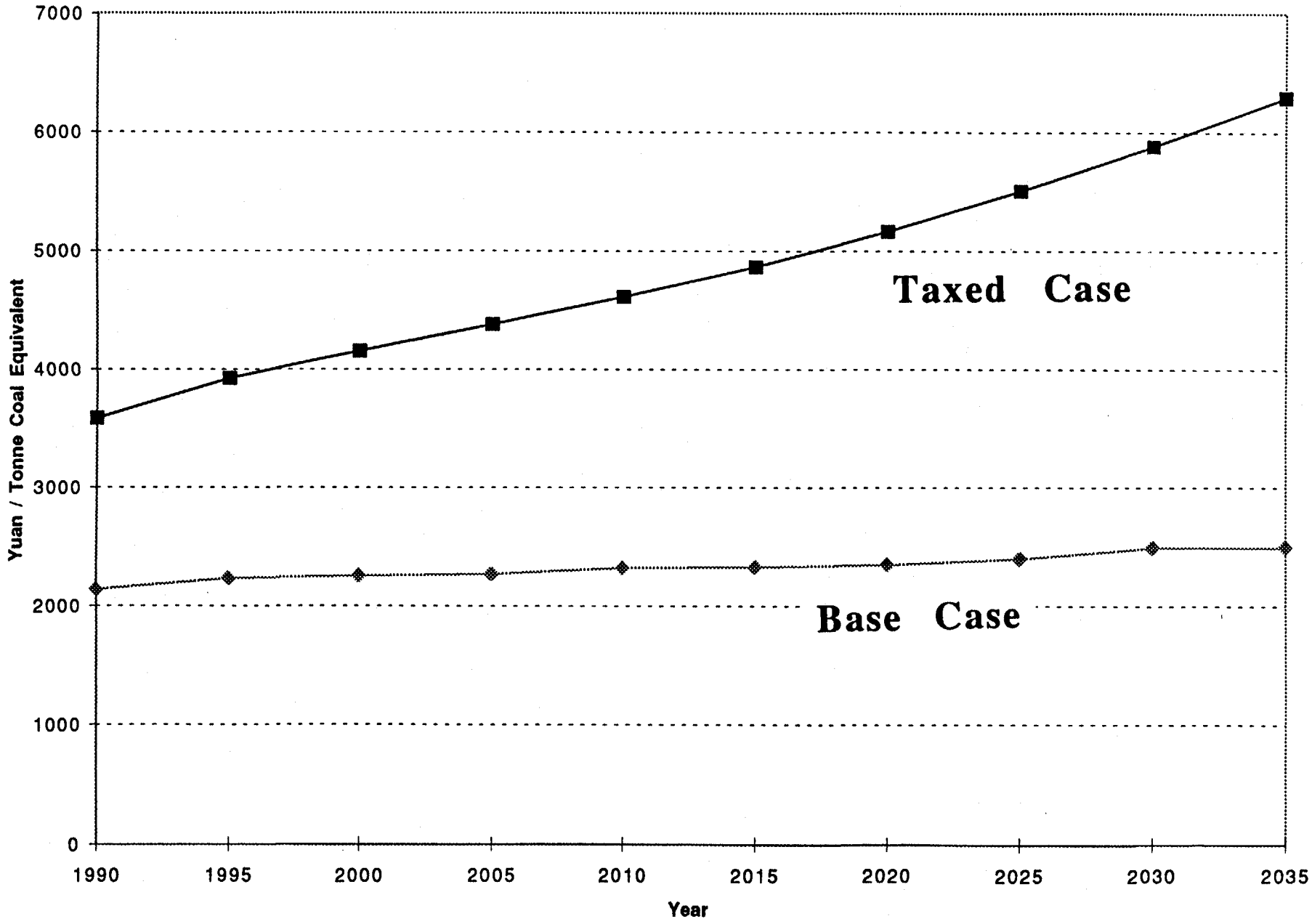

Chart 6

Industrial Energy Demand

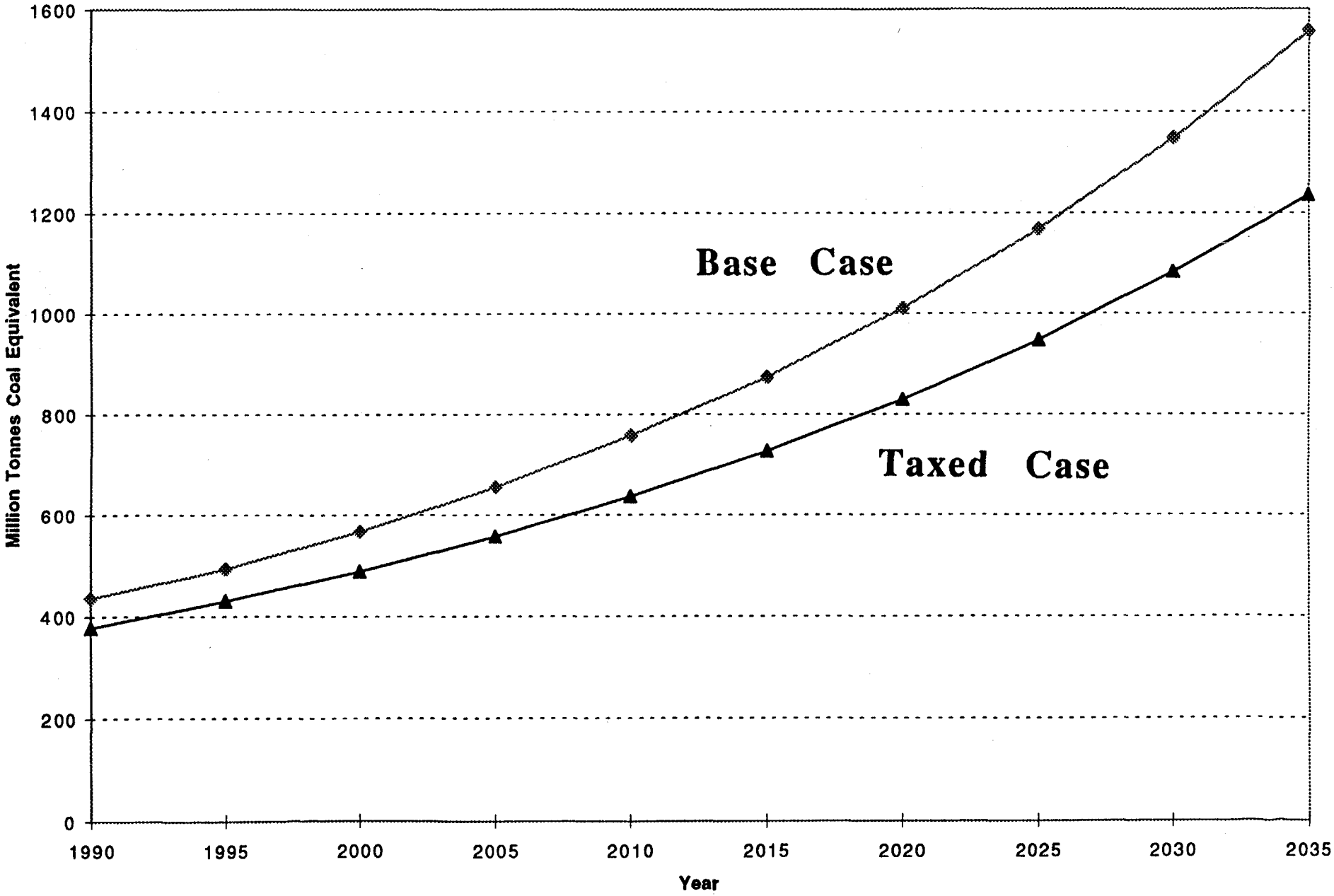

Chart 7

Commercial Energy Demand

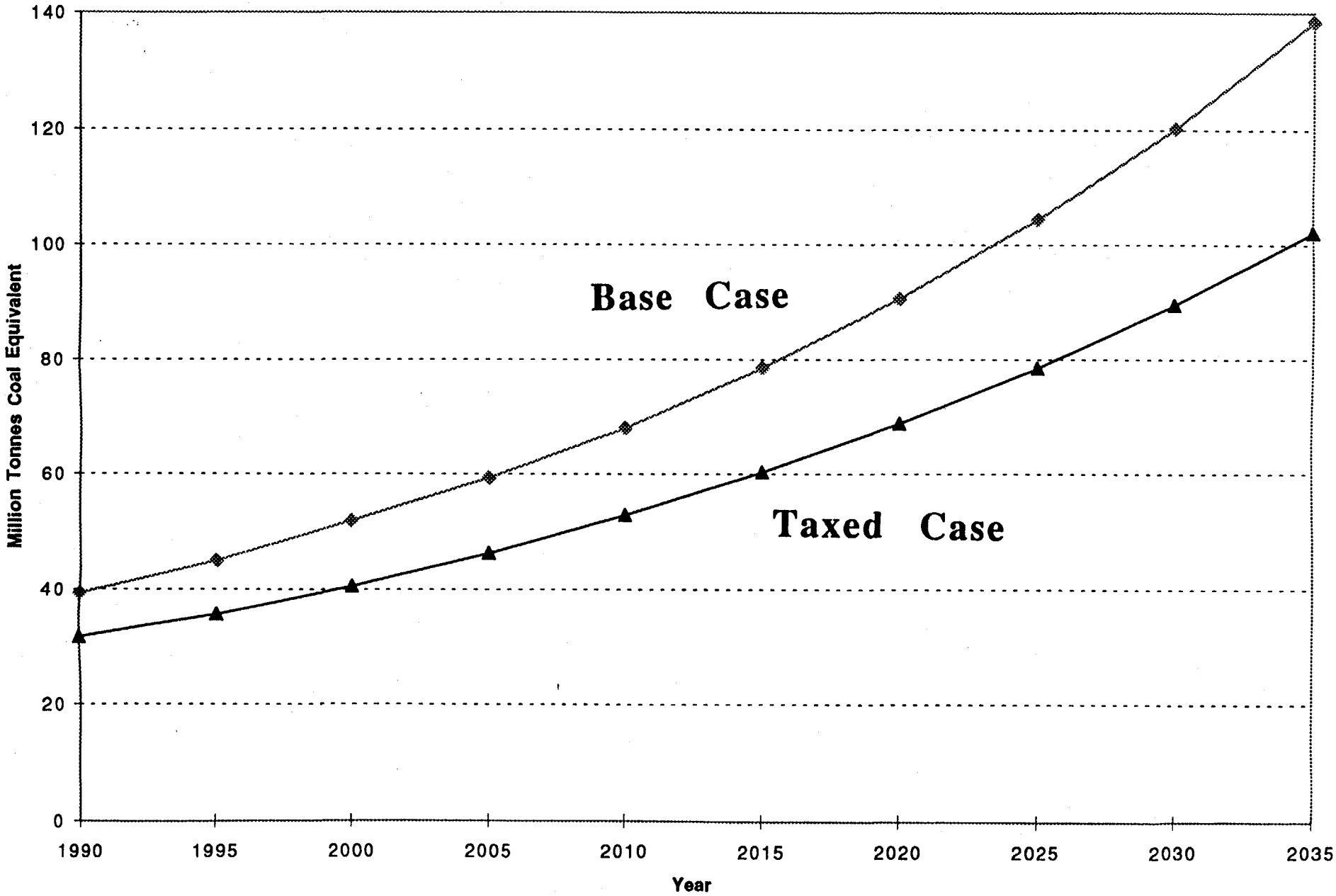

Understanding Contaminant Transport to Model and Quantify Bioremediation in the Microbial Filters Project*

Kristen Ude

University of Wisconsin - Madison

Lawrence Livermore National Laboratory
Livermore, CA 94550

December 13, 1995

Prepared in partial fulfillment of the requirements of the Science and Engineering Research Semester under the direction of Dr. Kenneth Jackson, Research Mentor, in the Lawrence Livermore National Laboratory.

*This research was supported in part by an appointment to the U.S. Department of Energy Science and Engineering Research Semester (hereinafter called SERS) program administered by LLNL under Contract W-7405-Eng-48 with Lawrence Livermore National Laboratory.

Abstract

Demonstrating biodegradation for *in situ* bioremediation processes is difficult. One aim of the microbial filters project is to evaluate the *in situ* bioremediation of chlorinated ethenes such as trichloroethylene (TCE). To meet this need, a downhole treatability tool was developed to assess field biodegradation applications. A tracer lab experiment run in a column of the downhole treatability tool combined with tracer data analyzed from a microbial filters field test were used to understand the flow of water through porous media in the lab and in the field. A spreadsheet template was written to evaluate the contaminant transport equations and predict breakthrough curves of the tracer and TCE. The data show when the contaminant should appear if there is no biodegradation; deviations from the tracer response are indications of biodegradation. The tracer curve predicted from the contaminant transport equation correlated well with experimental data and will lay the foundation for experiments performed with bacteria to assess the extent of bioremediation.

Introduction

Non-aqueous phase liquids such as gasoline, jet fuel, and chlorinated hydrocarbons are a concern in the subsurface because of their ability to contaminate large volumes of groundwater. Described as ubiquitous throughout North America, non-aqueous phase liquids have been identified at 4 out of 5 hazardous waste sites in the United States (Plumb and Pitchford, 1985). A greater understanding of the transport of these fluids, many of which are suspected carcinogens, is required in order to design and implement cost-effective, reliable clean-up strategies.

In situ bioremediation is one such strategy with advantages over the industry standard, pump-and-treat. While pump-and-treat practices usually result in a phase change of the contaminant to the atmosphere or to another medium, *in situ* bioremediation provides destruction of the contaminant in place. This results in lower costs for the duration of treatment and eliminates the need for a surface treatment facility.

Microbial filters are a type of *in situ* bioremediation developed at Lawrence Livermore National Lab (Taylor *et al.*, 1993). In the presence of the soluble methane mono-oxygenase enzyme system, a methanotrophic bacteria (*Methylosinus trichosporium* OB3b) can fortuitously transform trichloroethylene to mostly carbon dioxide and chloride ions. The first step in the implementation of the microbial filters process is to grow these microorganisms in surface bioreactors and suspend them in water for transport to the field. Once in the field, injection into the subsurface can result in a fixed bed biofilter through which groundwater flows and is bioremediated. The efficacy of this technique depends heavily on whether or not site screening criteria are met. For example, the dissolved oxygen content in the groundwater must be favorable and the aquifer material must have pore throats greater than about 20 μm to allow the transport of cells (Duba et al., 1995).

The ability to substantiate bioremediation for *in situ* applications remains one of the most difficult as well as one of the most important aspects of applying the technology. Proof that biodegradation has occurred is essential for regulator purposes.

Conservative Tracers

Conservative tracers are compounds that are not retarted in transport through the subsurface. They are not adsorbed or absorbed and do not chemically react with other species in the groundwater or sediments. These non-reactive properties of tracers make them ideal for studying water as it flows through the subsurface.

Bromide and chloride are two hydrologic tracers which have been shown to be conservative and unaffected by soil microbial processes (Groffman *et al.*, 1995). Bromide was used in a demonstration of the microbial filters technology in Chico, California to get a preliminary understanding of the subsurface around the well where the microbial filter was to be established. Figure 1 shows that a 100 ppm bromide solution was injected for eight hours prior to pumping water out. The shaded squares represent the bromide breakthrough curve and if extrapolated, the integrated area exceeds 90% of the mass of bromide injected, showing that bromide is, for all practical purposes, a conservative tracer.

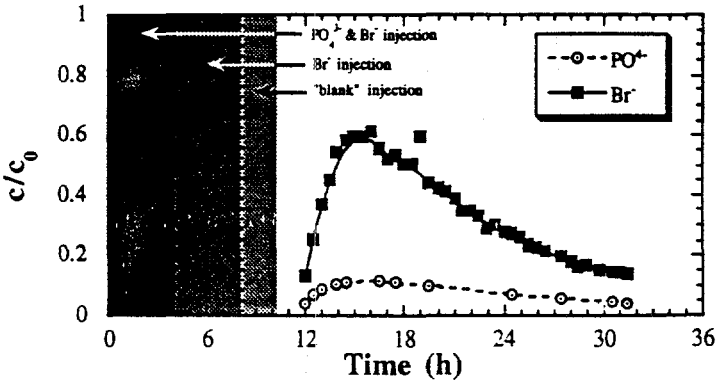

Figure 1. Field data from the Chico demonstration showing bromide recovery.

Methods

Bromide concentrations of these field samples were determined using an Orion bromide electrode (model 94-35) and an Orion Ross™ Combination pH electrode. The electrodes were connected to an Orion pH/ISE direct readout meter (model SA 720). Calibration standards prepared with KBr in deionized water were run to yield a relationship between bromide concentration in ppm and electric potential in millivolts. Samples were diluted with deionized water so that the electrode tips were adequately submerged and enough room was available for a magnetic stirrer. This optimal quantity of liquid was 12 mL: 4 mL of the sample and 8 mL of deionized water. The field samples were originally collected in 12-mL polypropylene round centrifuge tubes. The calibration standards and the samples were run in 50 mL glass beakers.

Phosphate was injected because it acts as a pH buffer for the microorganisms. Although microorganisms weren't added in this trial run, the phosphate was still injected because it was easy to analyze and mimicked what would happen in the experiment to come. For tracer purposes, it illustrates what a non-conservative tracer breakthrough curve looks like. Only about 60% of the phosphate was recovered due to its sorbing action onto the sediments.

Downhole Treatability Tool

The downhole treatability tool was developed at Lawrence Livermore National Laboratory to test remediation techniques in near - *in situ* conditions. (Duba et al., 1995) The tool consists of three 1 m. long stainless steel tubes which together fit into a 4 inch or larger well. The tubes are packed with sand or the material in the aquifer being tested and liquid is pumped through them. They can be inoculated with different population densities of bacteria so that optimal population densities can be determined.

In this study of understanding contaminant transport to quantify bioremediation, one of the columns from the tool was used to predict and study the breakthrough curve of a

tracer. Stainless steel tubes were used for the first time in this experiment (previously they had been glass).

The Contaminant Transport Equation

The first step of the tracer experiment was to develop an understanding of the governing equation: the advection-dispersion equation. Advection is the movement of the contaminant from one location to another due to the water flow (like a leaf on a stream) and dispersion takes into account small scale variations in velocity and diffusion. Diffusion is the movement of a substance due to a concentration gradient. The advection-dispersion equation is as follows:

$$R\frac{\partial c}{\partial t} = D\frac{\partial^2 c}{\partial x^2} - v\frac{\partial c}{\partial x}$$

where
R = Retardation factor
c = concentration of solute
t = time
D = Dispersion coefficient
x = spatial coordinate
v = groundwater velocity

The analytical solution to this equation was found in van Genuchten and Alves, 1982 and entered into a spreadsheet so that breakthrough curves were generated for different conditions.

The correlation between the predicted tracer breakthrough curve and the curve generated from the laboratory experiment (independent of the prediction) is represented in Figure 2. This good fit validates the equation and the way it was solved. The figure is important because it depicts how a non-reactive component flows through the column, which is a basis for then looking at how a retarded component flows through and eventually, for how a retarded component with biodegradation flows through.

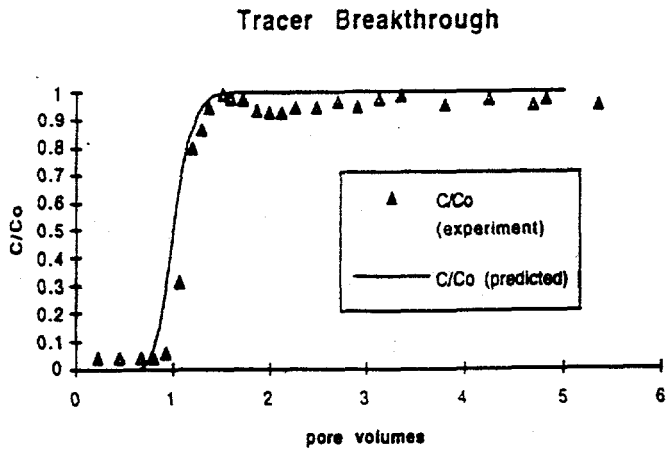

Figure 2. The lab experiment correlated well with the solid curve predicted from the contaminant-transport equation.

To further illustrate the effect of retardation, Figure 3 shows the difference between the predicted breakthrough curve for the tracer (with a retardation = 1) and TCE (with a retardation = 1.1). The retardation of trichloroethylene was found after extensive studies by the microbial filters team in previous laboratory studies. The tracer represents the fastest breakthrough of any compound (like water itself) and anything to the right of this curve represents something that is being retarded due to the chemical properties of that substance.

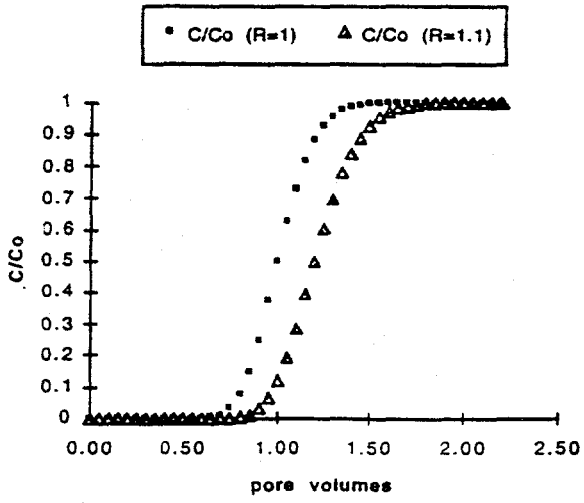

Figure 3. Breakthrough with retardation

Summary

The following cartoon (Figure 4) is an example of what a regulator might require as proof that biodegradation had occurred at a field site. In order to generate the "predicted values without biodegradation," an understanding of the contaminant-transport equation is necessary. Conservative tracers are helpful for preliminary studies of hydrogeology and for validating the contaminant-transport equation. A graph such as Figure 4 is an essential tool for the design and implementation of any bioremediation scheme. An understanding of its importance makes the microbial filters project more likely to succeed.

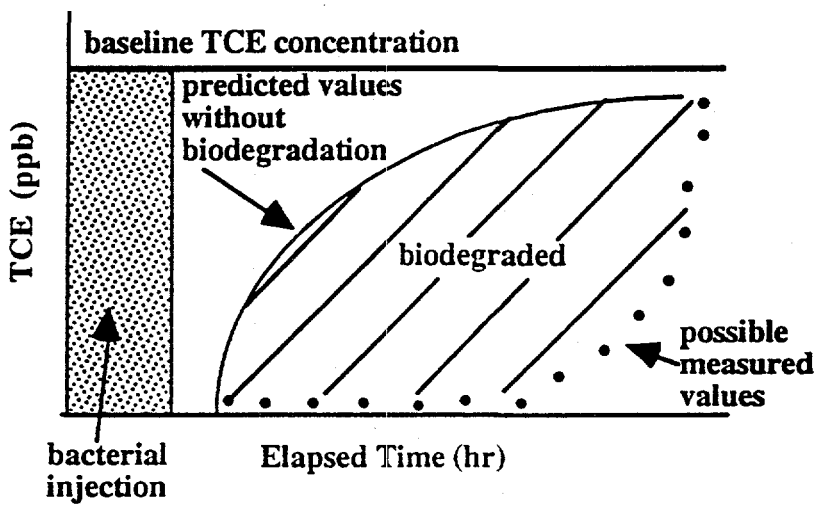

Figure 4. This work lays the foundation for quantifying biodegradation.

Bibliography

Duba, A.G., K.J. Jackson, M.C. Jovanovich, R.B. Knapp, R.T. Taylor, C.O. Boro, M. Evans, M.L. Hanna, W.E. Ralph, N.N. Shaw, 1995. "TCE Remediation Using *In Situ*, Resting-State Bioaugmentation." Manuscript in progress. Lawrence Livermore National Lab.

Duba, A.G., C.O. Boro, W.B. Durham, W.E. Ralph, 1995. "A Down-Hole Treatability Tool for Testing In Situ Ground-Water Cleanup Strategies," UCRL-JC-117581, Lawrence Livermore National Laboratory, Livermore, CA 11 pp.

Gershon, N.D., A. Nir, 1969. "Effects of Boundary Conditions of Models on Tracer Distribution in Flow through Porous Mediums,"*Water Resources Research* , August 1969, pp. 830-838.

Groffman, P.M., A.J. Gold, G. Howard, 1995. "Hydrologic Tracer Effects on Soil Microbial Activities." *Soil Sci. Soc. Am. J.*, 1995, pp. 478-481.

Jackson, K.J., A.G. Duba, M.L. Hanna, M.C. Jovanovich, R.B. Knapp, N.N. Shah, R.T. Taylor, 1994. "Field Treatability Test of the *In Situ* Microbial Filters Concept," Wilson Corners, Kennedy Space Center, Lawrence Livermore National Lab report.

Knapp, R.B., A.G. Duba, M.L. Hanna, K.J. Jackson, M.C. Jovanovich, R.T. Taylor, 1995. "Engineering an *In Situ* Microbial Filter for Ground-Water Bioremediation," Manuscript in preparation, Lawrence Livermore Naitonal Lab 25pp.

Plumb, R.H., Jr. and A.M. Pitchford, 1985. "Volatile Organic Scans: Implication for Ground-water Monitoring." *Proceedings Petroleum Hydrocarbvons and Organic Chemical in Ground Water*, National Water Well Association, November 13-15, 1985, Houston, TX, pp. 207-222.

Taylor, R.T., M.L. Hanna, N.N. Shah, D.R. Shonnard, A.G. Duba,W.B. Durham, K.J. Jackson, R.B. Knapp, A.M. Wijesinghe, J.P. Knezovich, M.C. Jovanovich, 1993. "In situ bioremediation of a trichloroethylene-contaminated water by a resting-cell methanotrophic microbial filter." *Hydrologial Sciences Journal* , August 1993, p. 323-342.

Thompson, A.F.B., R.B. Knapp, M.L. Hanna, R.T. Taylor, 1994. "Simulation of TCE migration and biodegradation in a porous medium under conditions of finite degradation capacity," *Advances in Water Resources*, 1994. pp. 241-249.

van Genuchten, M.Th., W.J. Alves, 1982. "Analytical Solutions of the One-Dimensional Convective-Dispersive Solute Transport Equation," U.S. Department of Agriculture, Technical Bulletin No. 1661, 151 pp.

Storm Water Modeling at Lawrence Livermore National Laboratory

Christopher Veis

Montana Tech

Lawrence Livermore National Laboratory
Livermore, California 94551

November 13, 1995

Prepared in partial fulfillment of the requirements of the Science and Engineering Research Semester under the direction of Erich Brandstetter, Research Mentor.

* This research was supported in part by an appointment to the US. Department of Energy Science and Engineering Research Semester (hereinafter called SERS) program administered by LLNL under Contract W-7405-Eng-48 with Lawrence Livermore National Laboratory.

Abstract

Christopher Veis
Montana Tech
Operations and Regulatory Affairs Division

This paper is primarily an overview of the methodology used for storm sewer modeling. Storm water modeling is an important component of regulatory compliance for water dischages from the Lawrence Livermore National Laboratory (LLNL). Modeling is also done to study trends in site contaminants and the available capacity of the storm sewer infrastructure. The Storm Water Management Model (SWMM) was used to simulate rainfall events at LLNL. SWMM is a comprehensive computer model simulating of urban runoff quantity and quality in storm and combined sewer systems. Due to time constraints and the extensive need for ongoing research, no comprehensive site wide modeling was completed at LLNL. With detailed information about the storm sewers, a SWMM simulation of a rainfall event on site would aid LLNL staff in the storm sewer infastructure decision making process.

Table of Contents

Abstract 1

Table of Contents 2

List of Illustrations 3

The purpose of storm water modeling 4

- Compliance 4
- Trend in pollutants 4
- Storm sewer infrastructure 5

Choosing a storm water model 5

- Picking the correct storm water model 5
- Introduction to SWMM 6

The first step to storm water modeling 8

- The runoff block 8
- Building an input file 9
- General data 9
- Precipitation data 9
- Pipe data 11
- Subcatchment data 11
- Pollutant data 15
- Print data 15

Gathering data 18

- Compatibly 18
- Climatilogical 18
- Storm Sewer Parameters 18
- Maps 18

Results 20

Summary 20

Bibliography 22

List of Illustrations

Figure 1.	Benefits and Costs as a Function of Model Complexity	6
Figure 2.	Components of the Storm Water Management Model	8
Figure 3.	Map of a storm sewer	12
Figure 4.	Examples of Subcatchments	13 & 14
Figure 5.	Typical input file for SWMM	16 & 17
Figure 6.	Map of a site broken down into subcatchments	19
Table 1.	Categorization of SWMM Input Data	10

The Purpose of Storm Water Modeling

Compliance

Environmental regulations govern the release of water from a large industrial facility, such as Lawrence Livermore National Laboratory (LLNL). The environmental regulations that govern such releases at LLNL include:

- Clean Water Act
- Porter Cologne Act
- Storm water National Pollutant Discharge Elimination System (NPDES) permit (#95-174)
- WDRs and NPDES permits for specific activities/releases
- Department of Energy (DOE) Order 5400.1
- DOE Order 5400.5
- DOE requirements regarding construction in floodplains and developing sites that impact storm water drainage systems
- LLNL's Storm Water Pollution Prevention Plan

LLNL water compliance staff use storm water modeling to demonstrate compliance. A model simulates storms or rainfall events on site. This model yields results which are used to evaluate the levels of pollutants. The level of pollutants are compared against the environmental standards to determine if an adverse environmental effect would result from rainfall events.

Trends in Pollutants

Storm water models are also used to study trends in pollutants. The result of a model is run is input to a data base. With a large enough database, trends in pollutants can be compared to the level of pollutants. If there seems to be a trend in pollutant levels above designated action levels, analysts seek to find the identified contaminant's source. Common parameters that are sampled include: pH, volatile organic compounds (VOC's), heavy metals, and radionuclides.

Storm Sewer Infrastructure

The final use of storm water modeling is to estimate a storm sewer's ability to handle a rainfall event. This is important in determining the effect of a 10 year, or larger, storm event. A 10 year storm event is a theoretical storm that is as large a storm as would occur in 10 years. Using the model, a simulation is run on a 10 year storm. If the model indicates flooding from this storm, it means that the site does not have the storm sewer flow capacity necessary to handle a 10 year storm event. Furthermore, the model can be used to identify specific components of the system that need to be upgraded in order for the system to have adequate capacity.

Choosing a Storm Water Model

Picking the Correct Storm Water Model

There are numerous storm water models that simulate industrial storm water runoff. Choosing the right model for the job is important for cost effectiveness and the best results. If a project is simple and is not necessarily needed to be highly reliable, use a simple model. When the job is complicated and the model is required to show compliance with regulations, a complex model should be used[4]. Figure 1 is a good reference for choosing a storm water model.

Figure 1. Benefits and costs as a function of model complexity[4]

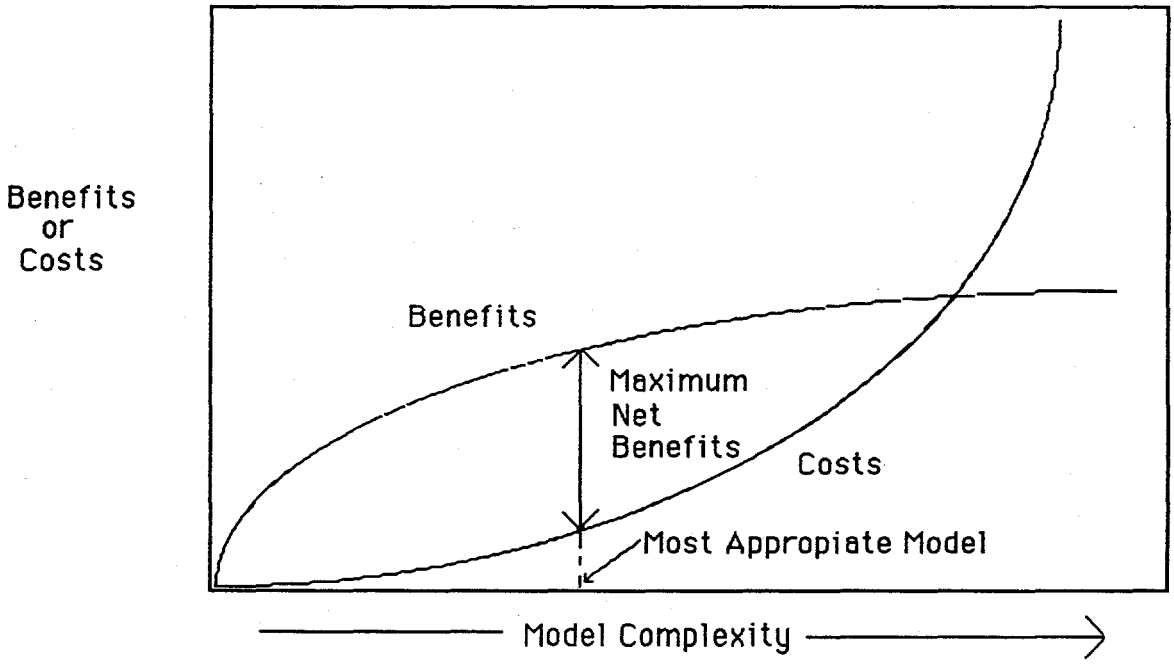

Introduction to SWMM

The storm water model chosen for this project was the Storm Water Management Model (SWMM). SWMM was developed because a need arose for a computer model which dealt with both quantity and quality problems inherent in storm water modeling. Work began at the University of Florida from 1969-71 under the sponsorship of the EPA. SWMM's effectiveness in simulating rain or storm events can be evaluated by inspection of hydrographs, pollutographs, pollutant loads, and modeled changes in receiving water quality[2].

LLNL chose SWMM because the model has been an accepted standard for a long time among the modeling community. It has

proven effective in complex modeling environments such as Livermore's highly populated dynamically changing industrial site. The model addresses all of the components needed by LLNL's staff for storm water modeling.

There are many components to SWMM, however, they can be put in to two categories. The computational blocks and the service blocks[2] (See Figure 2). The computational blocks include:

- Runoff block
- Transport block
- Extended transport block
- Storage and treatment block

The service blocks include:

- Statistics block
- Graph block
- Combine block
- Rain block
- Temperature block

All the computational and service blocks can be run together using the executive block. This project focused primarily on the runoff block . The runoff block isolates the storm sewer and has input data specific to the storm sewer.

Figure 2. Components of the Storm Water Management Model[2]

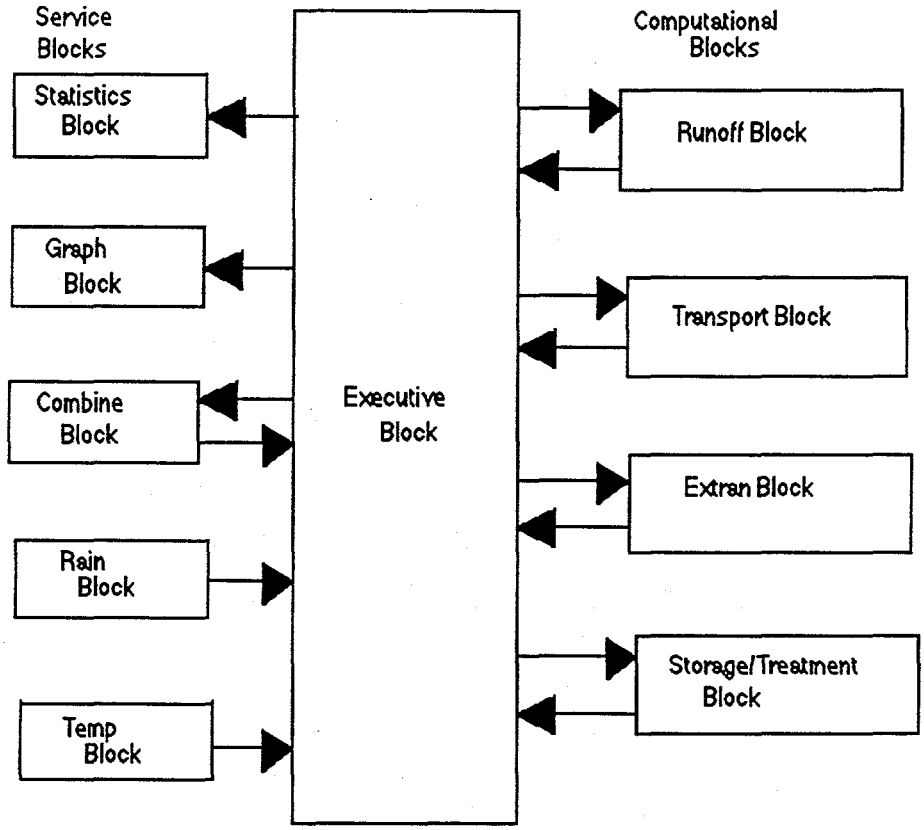

The First Steps of Storm Water Modeling

The Runoff Block

The runoff block was developed to simulate both the quantity and quality runoff phenomena of a drainage basin and the routing of flows and pollutants to the major sewer lines. It represents a site by an aggregate of idealized subcatchments and pipes. The input file accepts rainfall hyteographs and makes a step by step accounting of:

- Infiltration losses in pervious areas
- Surface detention
- Overland flow
- Pipe flow
- Constituents washed into inlets

The runoff block may be run for periods ranging from minutes to years. Simulations less than a few weeks are called single events. All events in this project are single events.

Building an input file

A PC based computer program called PCSWMM is run to begin creating files for the runoff block. PCSWMM allows for easy editing of SWMM input files. Once the files are complete, PCSWMM uses its SWMM engine to compute an output file. There are thirteen different groups of data for the runoff block and they are labeled using letters (A through M). These different categories can be broken down in to six sub-categories listed on the left side of table1.

General Data

The general data input includes all data which will stay consistent throughout the entire SWMM run and identifies the runoff block uniquely so that it can be combined with other blocks. The data which are identified under the A section are the title data. The title is usually descriptive of the type of event being simulated. The B section calls for input data which detail the units and equations used throughout the model. Section C is used to input data parameters which detail snow input data. For this project, no snow data was input. Snow doesn't fall often enough in this part of California to be considered for the model. See figure 5, sections A1 and B1-3.

Precipitation Data

Precipitation data are important in determining the quantity of water that falls on the site. This data group is simplified if snowfall is not modeled. The first step in entering data is deciding whether or not to use the rain block (Group D). The rain block is used if rainfall data are obtained from the National Weather Service (NWS). The rain block collates rainfall data and make it accessible to which ever block calls for it. The next group is identified as the E group and is used when the rain block is not called. This group calls for data from the rain gages to be input. It also contains many general type data inputs that set the units for the rainfall event. Finally this category also includes evaporation data (Group F). These data are usually obtained from climatological summaries.

Table 1. Categorization of SWMM Input Data

Type of Input	Group Name	Description of Data
General Data	A	Two title lines to describe the input file
	B	Selection of units, equations used and time of the storm
	C	Snow input data
Precipitation Data	D	Choose manual rainfall data input or call the rain block
	E	Rainfall data is input if the rain block is not called
	F	Evaporation Data
Pipe Data	G	Parameters that describe the pipes in the storm sewer
Subcatchment Data	H	Parameters that describe the subcatchments
	I	Subcatchment snow input data
Pollutant Data	J	Parameters that describe the pollutants in the storm sewer
	K	Erosion Data
	L	Subcatchment surface quality data
Print Data	M	Set print variables

Pipe Data

Channel/pipe data is a very straight forward section of the input file. The group G input section calls for pipe length, where the pipe is draining to and from, pipe shape (circular, trapezoidal), pipe slope and the Mannings roughness coefficient of the pipe. Group G also accounts for weir and orifices in the pipes. (Figure 3)

Subcatchment Data

The subcatchment data provide a comprehensive description of the ground on which the rain falls. More detail is obtained through the use of more variables. Since there is large attention to detail in this section, a site must be broken down into subcatchments. Subcatchments are smaller areas, divided up from a large area, that outline the path water will take over that small area. Examples of subcatchments are shown in figure 4.

Figure 3. Map of a typical storm sewer[1].

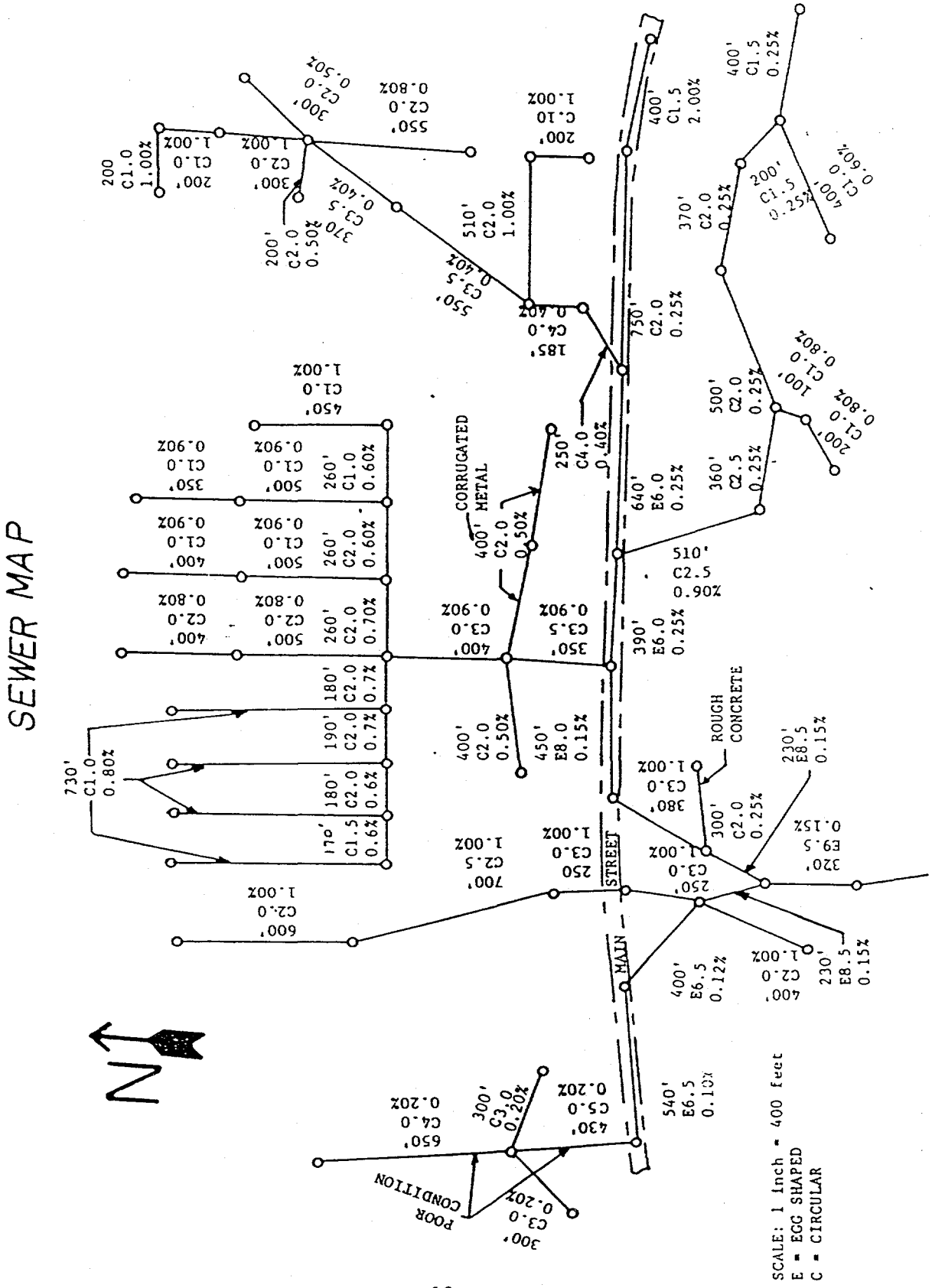

Figure 4. Examples of subcatchments[1]

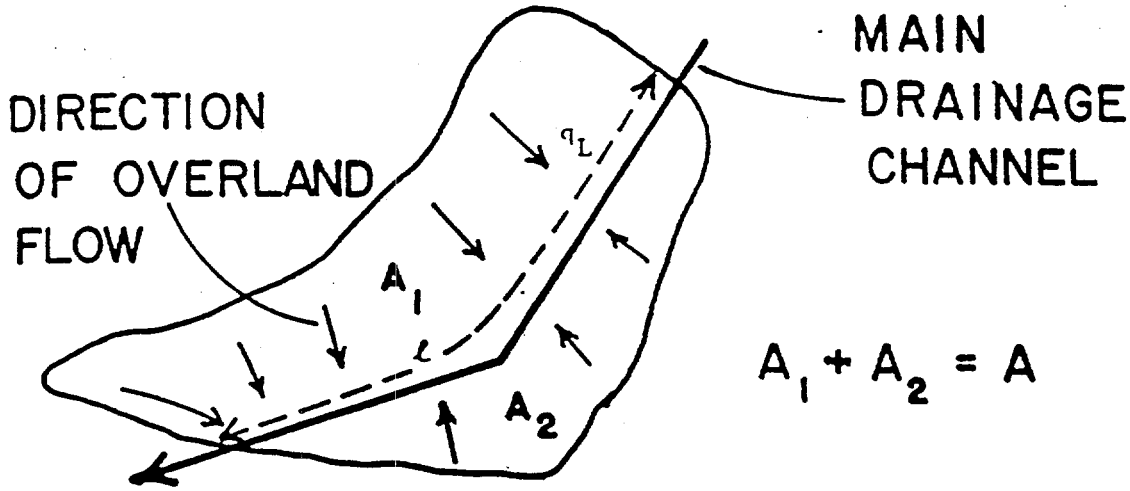

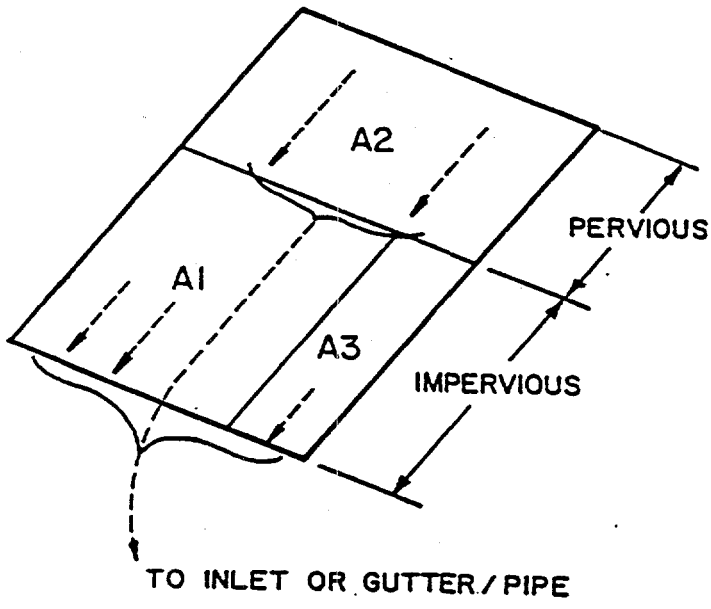

Figure 4 continued

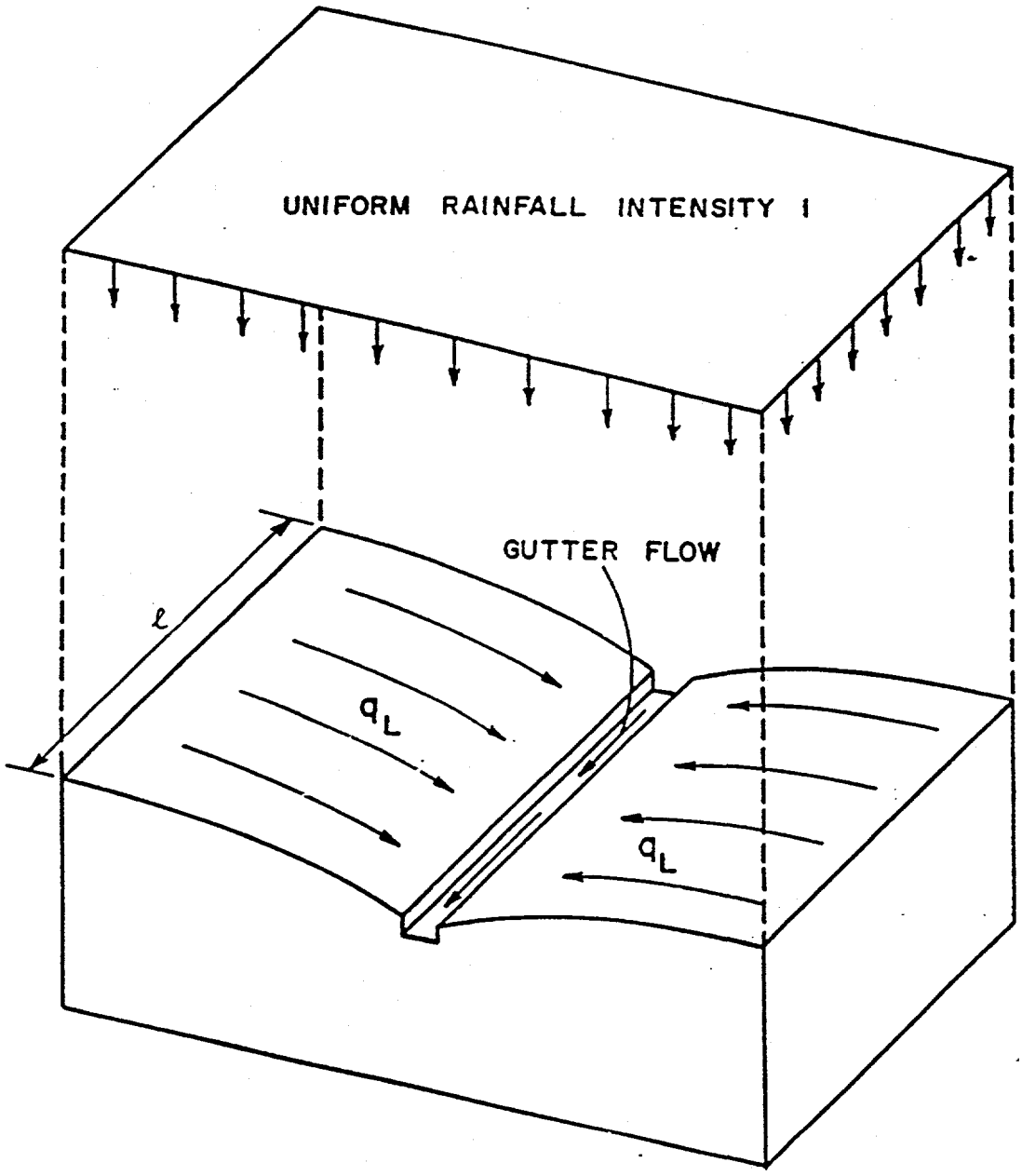

Pollutant Data

The pollutant section of the input file calls for data which describe constituents that may be found in the storm water. Selected constituents are input along with the parameters describing the action of these constituents in storm water. SWMM allows the modeler to choose four different equations that describe the behavior of consituents in storm water. Along with the eqations, constituents are largely affected by:

- Time between storms
- Street sweeping efficiency
- Erosion
- Subcatchment surface
- Site wide material handling practices
- Spill containment plans

Print Data

The print section allows control of many different print options. Printing efficiency is optimized with proper control. Printing out only the information that is essential saves on paper.

Figure 5. Typical input file for SWMM[3]

(Please note, this is not a complete file. It is an example.)

```
$RUNOFF
*
A1  'MODEL OF SIMPLE DRAINAGE NETWORK'
A1  'RUNOFF MODULE DATA SET'
*
*   GENERAL SIMULATION CONTROL
*
*    METRIC  ISNOW  NRGAG  INFILM  KWALTY  IVAP  NHR   NMN  NDAY MONTH
B1      0       0      1       0       0     0    0     0    25     0
*
*  OUTPUT CONTROL
*
*  IPRN(1)  IPRN(2)  IPRN(3)
B2   0        1         1
*
*   TIMESTEP CONTROL
*
*  WET   WETDRY   DRY   LUNIT   LONG
B3  60     120     900    2      10
*
*  ROPT
D1  0
*
*   KTYPE  KINC  KPRINT  KTHIS  KTIME  KPREP  NTHISTO THISTO  TZRAIN
E1    2       1      1        0      0      0         15     15.0      0.0
*
*   STEP-FUNCTION HYETOGRAPH
*
*   TIME=REIN(1)  RAIN=REIN(2)
*
E3     0.0              1.0
E3    15.0              1.0
E3    30.0              1.0
E3    45.0              1.0
E3    60.0              1.0
E3    75.0              1.0
E3    90.0              1.0
```

```
*      CHANNEL/PIPE DATA
*
*   NAMEG  NGTO   NPG  GWIDTH  GLEN  G3  GS1  GS2   G6     DFULL  GDEPTH
G1    100    101     2       3        300  0.1    0     0  0.014    0       0.0
G1    200    101     2       3        300  0.1    0     0  0.014    0       0.0
G1    300    101     2       3        300  0.1    0     0  0.014    0       0.0
G1    101    102     2       3        300  0.1    0     0  0.014    0       0.0
G1    201    202     2       3        300  0.1    0     0  0.014    0       0.0
G1    301    302     2       3        300  0.1    0     0  0.014    0       0.0
*
*      SUBCATCHMENT DATA
*
*   JK NAMEW  NGTO  WIDTH  WAREA %IMP   WSLP IMPN PERN IMPSTOR PSTOR
H1   1     1        100     100     10     100   0.01 0.01 0.01     0          0
H1   1     2       1000     100     10     100   0.01 0.01 0.01     0          0
H1   1     3      10000     100     10     100   0.01 0.01 0.01     0          0

*
*      PRINT CONTROL
*
*    NPRNT         INTERV
M1       3              1
*
*      NDET    STARTP(1)      STOPPR(1)
M2       1          0                  0
*
*      IPRNT(1)...
M3    102  202   302
*
$ENDPROGRAM
```

Gathering Data

Compatibility

Throughout the runoff block there are input variables which indicate the type of units or equation to be used. When a decision is made in one section of the block, that decision must remain consistent throughout the runoff block. An example is the infiltration equations. An equation chosen in the general data section and the input must match in the subcatchment data section. Before a runoff block input file is built, decisions are made on variables.

Climatological

The runoff block calls for climate related data, including:

- Rain gauge readings
- Rain intensity during a storm
- Average evaporation rate

These data are gathered and placed in the input file. Climatological conditions are gathered from a local weather station or the NWS.

Storm Sewer Parameters

Another important aspect of a runoff block is the features of the storm sewer. These data are collected from a public works office or comparable source. Both maps of the storm sewer and qualities and quantities of the storm sewer are important. Length, diameter, Manning's roughness, slope, and an identifier is needed for each pipe.

Maps

Maps of the site are used for subcatchment breakdowns. A subcatchment is defined by the storm sewer pipes that run somewhat independently through the site. A good breakdown of a site on a map will contain a group of pipes which all drain into a large drainage basin (Figure 6). Subcatchment breakdown is based upon the most likely drainage bed though that subcatchment. For the SWMM model, up to 200 subcatchments can be used in a single block. The LLNL site contained 73 subcatchments that drain into arroyo Seco and arroyo Las Positas

Figure 6. Map of a site's storm sewer broken down into subcatchments[2].

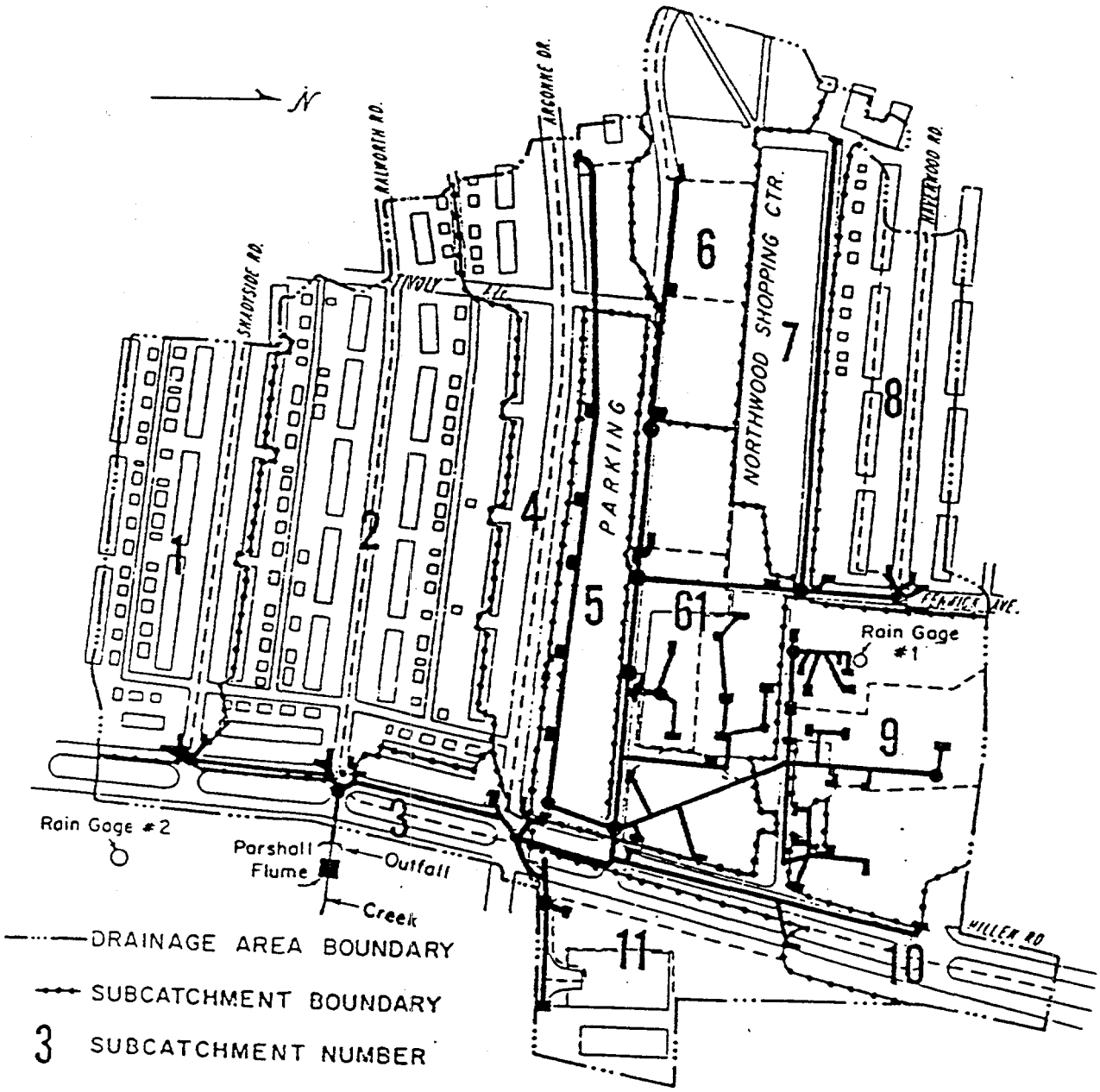

Results

Learning the SWMM model is a dynamic process. The first step in learning the model is reading and understanding the SWMM user's manual especially the section that pertains to the runoff block. The next step of this project was to model a small section of the site. The Northwest corner of the site was modeled in SWMM. Most of the input data were taken off a topographic map of the site. The measurements were taken by ruler and the rest of the data were based on the best guess. There were no hard data, thefore model results are not reliable. It was a very helpful tool in learning the model.

There are several steps involved to take the model to the next step and model a site wide storm water event. The site must also be broken down into subcatchments. Using a couple of different maps, I was able to break the site down into subcatchments. After breaking down the site, I could not complete the model because I was missing many of the needed input parameters. A detailed map of the storm sewer infastructue is required. Along with the map, there should be a database with information pertaining to the storm sewer. The map and the database need to contain information on:

- Numbering system for the storm sewer
- Length of the pipes inthe storm sewer
- Type of pipe (ie trapezoidal, circular, parabolic)
- Length of pipes
- Slope of the pipes
- The type of material that makes up the pipes
- Location of catchbasins
- Location of any weirs or orifices

Summary

All storm water modeling of LLNL has been slowed for a couple of reasons. A study is currently on going at LLNL to complete a map of the storm sewers. There is also an effort to clean the storm drains. Due to these time constraints, no modeling was completed at LLNL. When this study is complete, the information gathered will be used to simulate a rain event at LLNL. This paper is intended to be a

short summary of storm water modeling at LLNL and a guide to begin storm water modeling when all the information necessary is available.

Bibliography

[1]DiGiano, F.A., Adrian, D.D., and Mangurella, P.A., eds., "Short Course Procedings - Applicaitons of Stormwater Mangagement Models, 1976." EPA 600/2-77-065 (NTIS PB - 265321), Environmental Protection Agency, Cincinnati, OH, March, 1977.

[2]Huber, W.C., and Dickinson, R.E., "Storm Water Management Model, Version 4: User's Manual." EPA , Environmental Protection Agency, Athens, GA, August, 1988.

[3]James, W., and James, W.R.C., PCSWMM Getting Started., CHI, Guelph, Ontario, Canada., Second edition., April, 1995.

[4]Nix, Stephan J., Urban Stormwater Modeling and Simulation., CRC Press, Inc., Boca Raton, Florida, 1994.

[5]Veissman, J.W., Knspp, J.W., Lewis, G.L., and Harbaugh, T.E., Introduction to Hydrology, Harper and Row, New York, 1977.

Effect of Grain Strength Distribution on Rock Fracture

Austin Woffington

Diablo Valley College

Lawrence Livermore National Laboratory
Livermore, California 94550

December 15, 1995

Prepared in partial fulfillment of the requirements of the Science and Engineering Research Semester under the direction of Stephen C. Blair, Research Mentor, in the Lawrence Livermore National Laboratory.

* This research was supported in part by an appointment to the U.S. Department of Energy Science and Engineering Research Semester (hereinafter called SERS) program administered by LLNL under Contract W-7405-Eng-48 with Lawrence Livermore National Laboratory.

Effect of Grain Strength Distribution on Rock Fracture

Austin Woffington
Diablo Valley College
LLNL Earth Sciences Division

Abstract

This report discloses my contributions to the study of grain strength distribution and its effects on the behavior of rock in compression. This was done by simulating rock deformation using a field-theory numerical model, developed by Dr. Blair at LLNL. New data was gathered by running trials with a standardized weak grain strength. The new data set shows lattice failure to be less predictable with a higher percentage of weak sites. Strain on the lattice is affected by the distribution of grain strengths. Lattices with few weak grains tend to fracture near the same point and are more predictable. Lattices with many weak sites fracture within a high and low range of 10-70 MPa which makes these lattices less predictable. Also as the percentage of weak sites increases lattices become some what stronger and cracking becomes more spontaneous. This is an unexpected result which will be explored further in future work.

Background

This is an ongoing project headed by my mentor Dr. Stephen C. Blair on the study of rock fracture under compression. Both experimental and numerical methods are being used to further our knowledge on the mechanics of compressive rock fracture. This project will add to our understanding of the processes of rock cracking for future energy conservation techniques and environmental safety. My term at Lawrence Livermore National Lab was spent analyzing and contributing data to this project in the field of computer modeling of rock fracture and the mechanics of cracking at the grain scale.

Introduction

Rock is one of the oldest studied materials known to man. We have always wondered how to control our environment and the mechanics of rock is no exception. However, despite years of work and study with the material, rock behavior is still not fully understood. Improved understanding of rock fracture could be applied to the engineering of excavations, drilling, earthquake mechanics and other processes that involve the fracture or damage of rock.

Rock is a heterogeneous substance that is known to crack through the formation, growth, and coalescence of microcracks at the grain scale. Rock is a very unpredictable material, as far as determining fracture and strength under compression. The grains forming rock are never consistent; having different sizes, forms, types, strengths and distributions. Even the most "uniform" of rock has a diverse heterogeneity at the grain scale. This diversity affects the processes of rock cracking under stress. These fracture process are inadequately understood and are the subject of this study.

The Statistical Model

Statistical modeling is an effective technique for studying rock deformation under compression. Statistical modeling provides an easy method for introducing heterogeneity at the grain scale. It also can be used to

control factors of the rock environment (boundary conditions) for simulated testing.

In this study a uniaxial compression test on a rock sample is simulated using the two-dimensional field theory model developed by Blair, 1994 and document by Daveler and Blair, 1994. The geometry of the model as configured in this study is shown in Figure #1. The array in the trials run was 10x30, which corresponds to 300 lattice sites. Each lattice site is randomly assigned a strength using a range of bimodal site strength distributions. Stress is applied to the boundaries and the stress field is solved to determine the stress at each site. When the stress on the site exceeds the grain strength allotted to it the site is determined broken and a crack is inserted at that site. The stress is recomputed and the computer searches for another site to crack. This continues until percolation: the lattice fails when a cluster of cracks spans the lattice and the lattice is fractured from top to bottom.

Progression of Fracture

The figure #2 shows the progression of a rock cracking under compression in the statistical model. This shows results for a 30x90 array computed for this study. The first cracked sites are distributed randomly through the increase of vertical stress. As stress is increased, random cracking begins and clusters of microcracks are formed as shown in the next view of 1-200 cracks. More clusters form and group together to start the formation of a fracture (1-350 cracks). As the stress increases these cracks form fractures that will eventually percolate the lattice, or break it all the way through. The figure shows that in heterogeneous material like rock, fractures do not form by the progression of a single crack but rather by the coalescence of microcracks and clusters to form an extension of a percolating fracture.

Bimodal Distribution

Bimodal distribution is the configuring of the lattice into two types of grain strengths. One grain strength is labeled weak and the other strong. The mean site strength for each lattice, was maintained at 20 MPa. The data sets ran for this simulation had a standardized weak site strength of 2 MPa and

the strong sites varied to accommodate the mean. Table #1 shows the bimodal distributions for the data sets. The range for the group is from 25% weak sites and 75% strong, to 75% weak sites and 25% strong. Ten trials were run for each data set. A computer program named Fractool was used to produce graphical representations of the broken lattice sites. Mean Peak stress, stress-strain behavior and percolation threshold were calculated for each set of trials.

Bimodal Distributions (Table #1)

Directory	Distribution		
Weak_Strong	Weak Sites	Mean	Strong Sites
25_75	2 MPa	20 MPa	26 MPa
30_70	3		27.3
40_60	2		32
50_50	2		38
60_40	2		47
70_30	2		62
75_25	2		74

Results: *The Effect of Percent Weak Sites*

The major effort on this project involved determining how changing the percent weak sites in a bimodal strength distribution changed the behavior in the model simulations. I compared the growth of fractures in all the data sets and observed a significant change in the way the lattices broke as more weak sites were added to the data sets. Figure #3 is a representation of the first 35 cracked sites in three data sets that were the weakest in their respective sets of trials. Random cracking occurs more frequently in the beginning of the 25_75 to 50_50 trials. As the percentage of weak lattice sites increased, the cracking became more organized. Clusters of cracked sites formed quickly in the trials with more weak sites and in 75%_25% the clusters formed a fracture right away and broke the lattice very quickly. This move to greater organization can be explained as follows. The probability of

weaker sites occurring close together is higher in lattices with more weak sites. Clusters form quickly when weak sites are grouped together.

Figure #4 shows the first 35 cracked sites in the strongest trials, in their respective data sets. The progression of fracture in the data sets with few weak sites (25%_75%), again show random cracking in the beginning. As the percentage of weak sites was increase the cracking did not get as organized as the "weaker lattices" did. Clustering occurred early in the 50%_50% data sets but as more weak sites were added the lattice did not percolate at the beginning like the other trial. This 75_25 trial ended up being the strongest of all the trials in all the data sets. This is a surprising result because my original hypothesis was that as the number of weak sites increased the lattices would get weaker.

Figure #5 and #6 are the stress-strain curves for the weakest and strongest trials discussed above. This graph shows the accumulation of strain on the lattice as vertical stress is applied. The highest point on the line is the Peak stress. With figure #5 the 75_25 trial peaked at 10 MPa which is very quickly for a trial. Both the 25_75 and 50_50 trials are fairly consistent with each other. In figure #6 this consistency is present as well, however, while the 75_25 trial started to perform like the first run, it didn't go to failure and ended as the strongest trial. This shows that there is a consistency in the breaking of the lattice sets from 25_75 to 50_50 but in-between 50_50 and 75_25 a change occurs that causes a great variability in peak strength of the lattice.

Table #2 shows my results for the mean peak stress, percolation threshold, standard deviations and mean broken sites. The table shows the percolation threshold slightly decreased as percent weak sites increased. The model predicts that as the weak sites were increased the mean peak stress increased also(Figure #8). This is a reversal of the assumption made prior to this test. This is a new type of behavior that is subject to further study. The error bars are the standard deviation which is also graphed in figure #9. Figure #9 shows that as the percentage of weak sites increases the deviation of the peak stress becomes greater. When there are a few weak sites in a strong medium the overall strengths are roughly the same. Having a few strong

sites in a weak medium causes a great variability in overall strength. This substantial variability helps to explain why the Mean Peak stress decreases after 70% weak sites.

Conclusions

The results of this study show that increasing the proportions of weak sites in the simulations cause increased variability in the peak strength. with some trials fracturing at very low stress levels. Initial cracking becomes more localized as the percent weak sites increase. Percolation threshold was not strongly affected by the distribution of weak sites. Currently researchers at LLNL are conducting further testing on rock fracture which will include larger scales of lattices, different boundary conditions and other grain strength distributions. These results will be used with results of other studies to aid in understanding of fracture process in rock and other heterogeneous materials such as ceramics and concrete.

Acknowledgments

I would like to thank my mentor Stephen C. Blair for all his support in all the research I participated in. I would also like to thank Pat Berge for her input, Carolyn Bailey for her technical support, and Marty Flemming for her office support. To the Department of Energy's education staff at the Lawrence Livermore National Lab I owe a bid of gratitude for the opportunity to participate in the Science and Engineering Research Semester and all the activities they provided for our group.

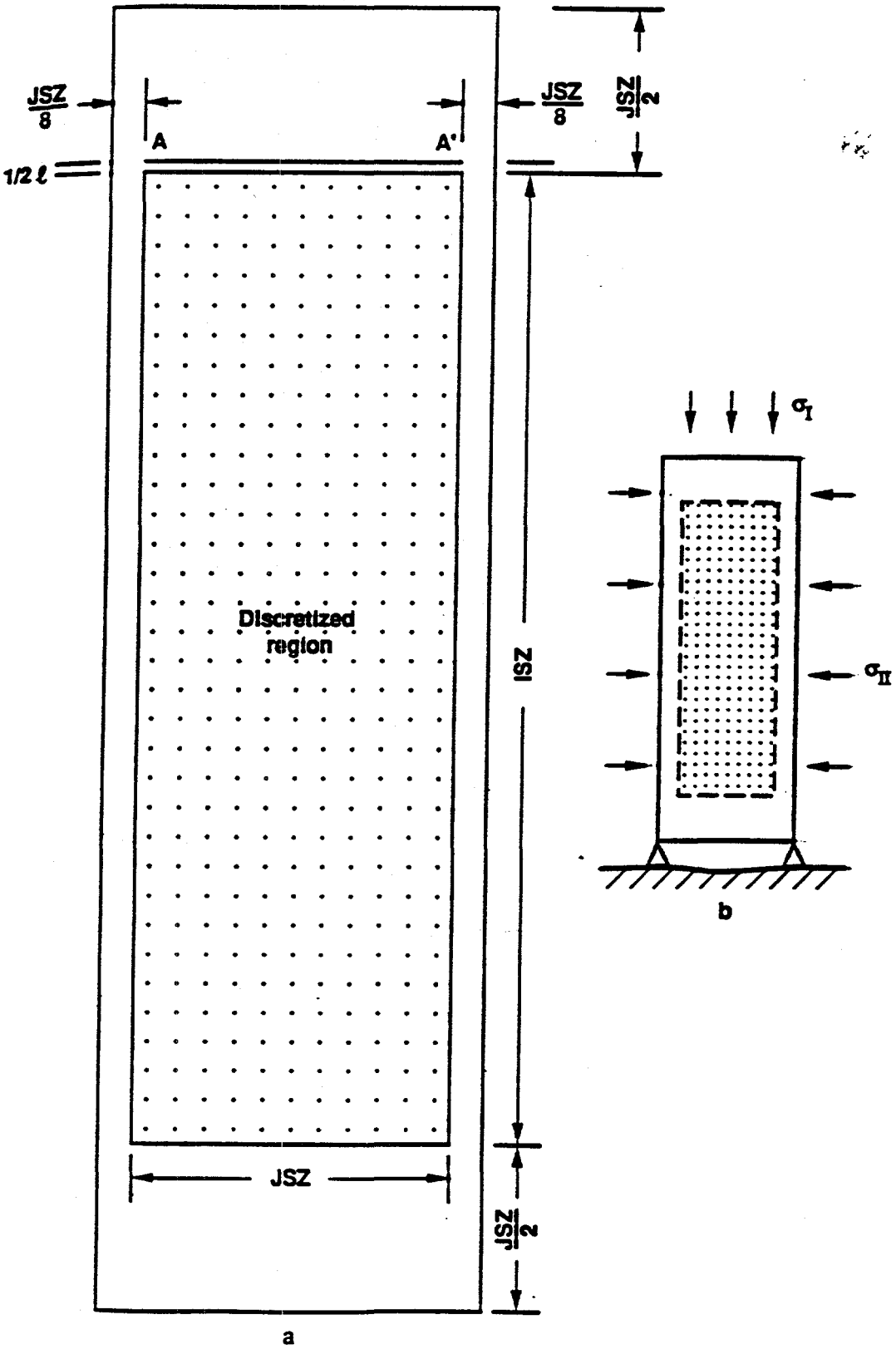

Schematic of geometry used in simulated compression tests.
a) relative array dimensions b) boundary conditions

Figure #1

Growth of a Fracture (30x90 lattice)

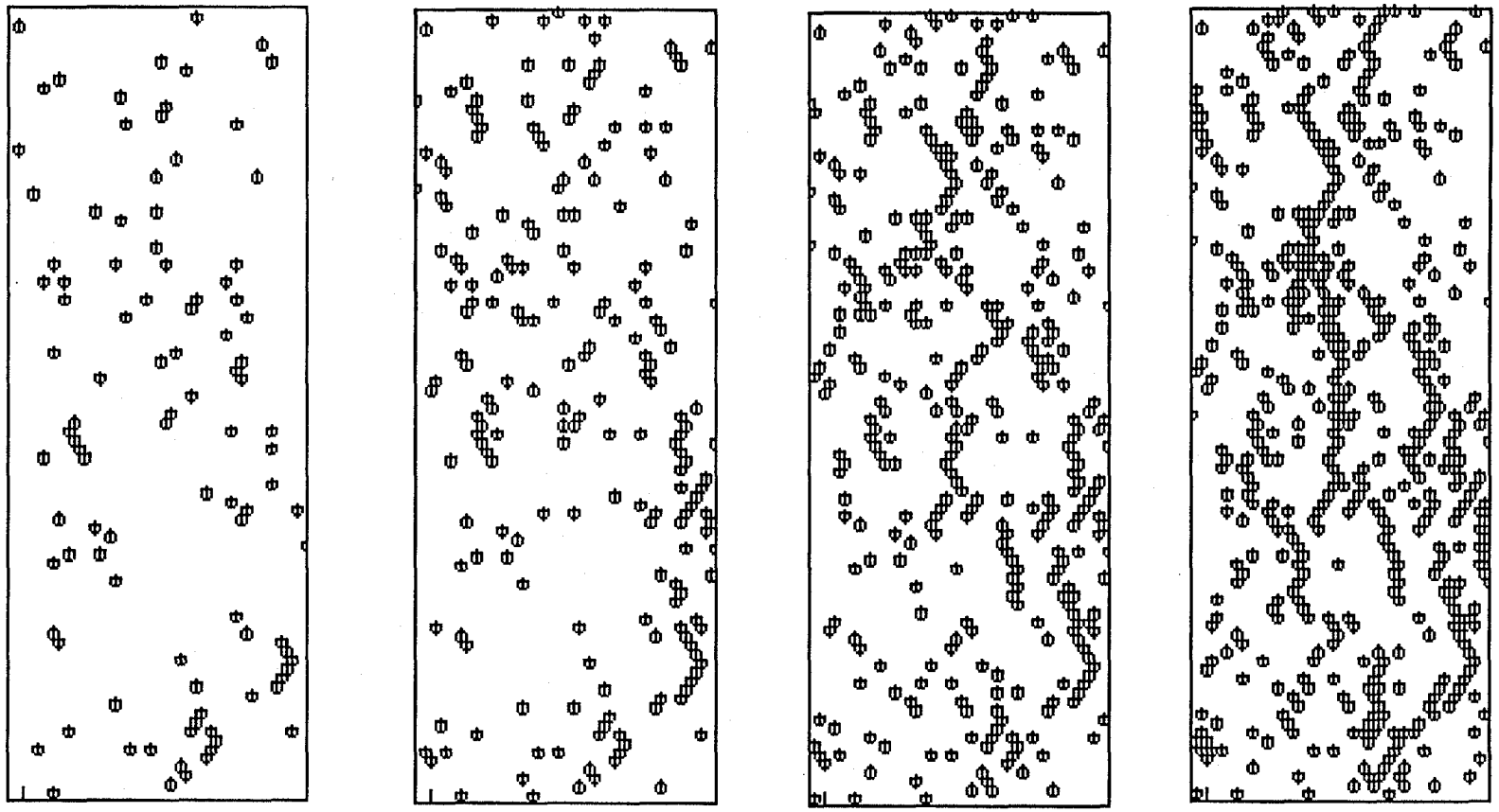

Cracks 1-100 Cracks 1-200 Cracks 1-350 Cracks 1-500

Figure #2

Distribution of the first 35 cracked sites of the weakest trials

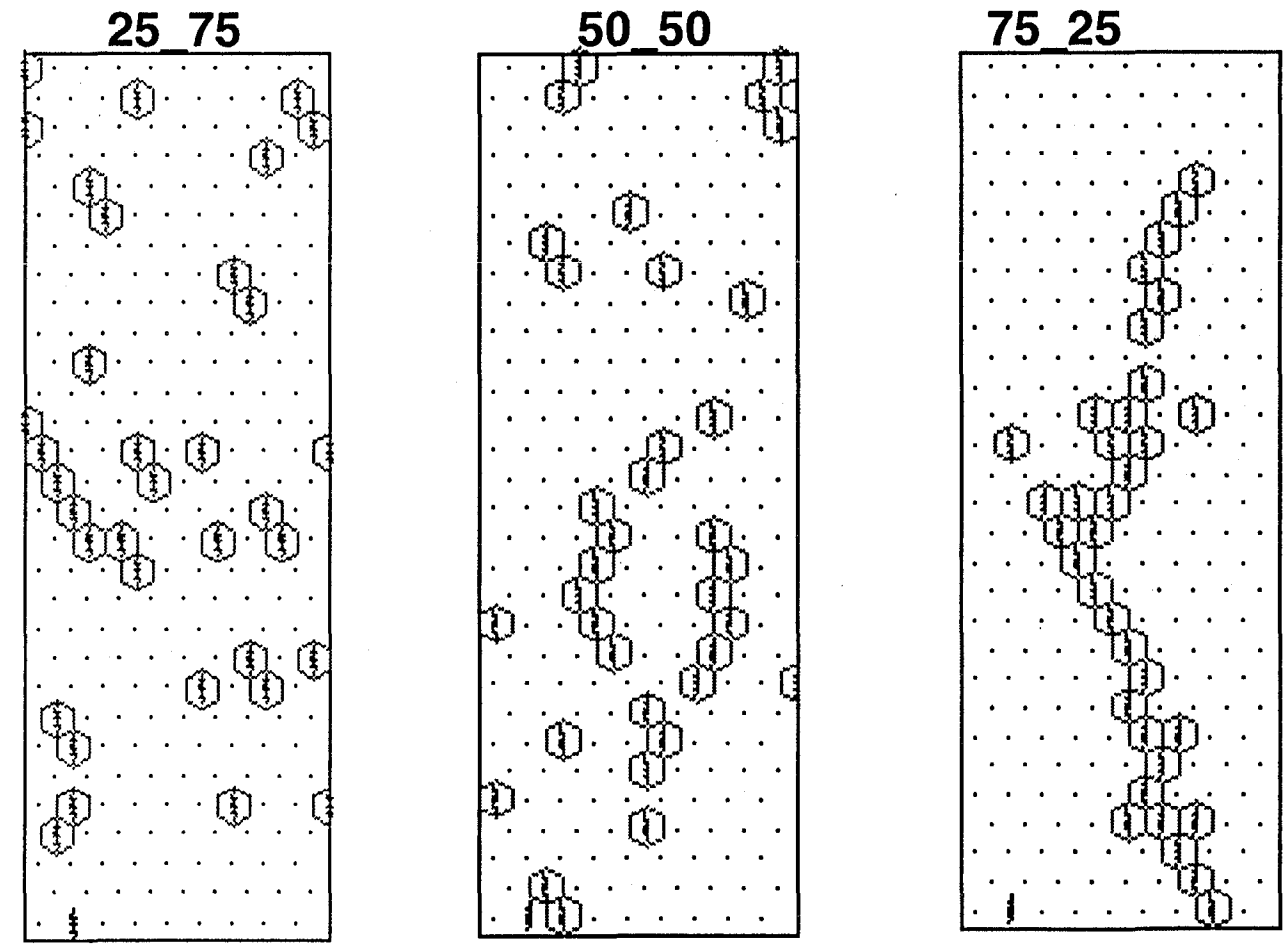

Figure #3

Distribution of the first 35 cracked sites in the strongest trials

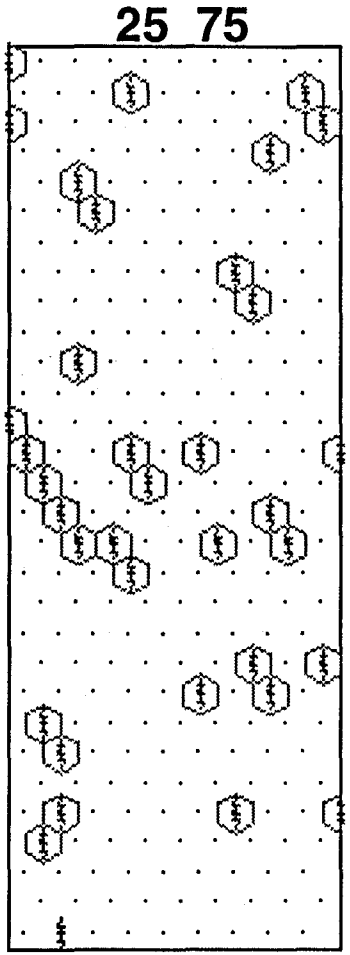

Random Cracking

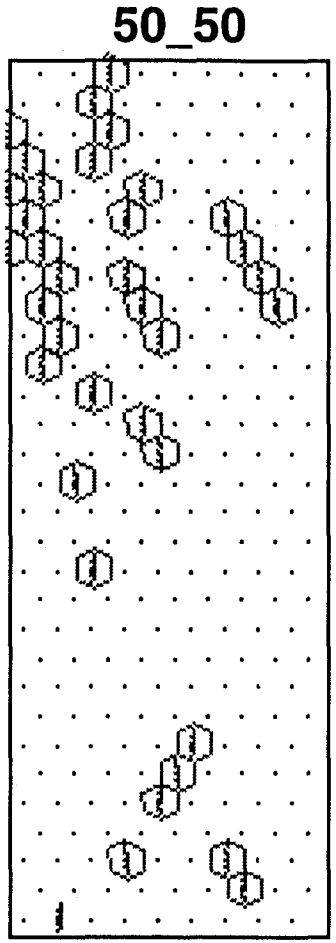

Clustering of Cracks

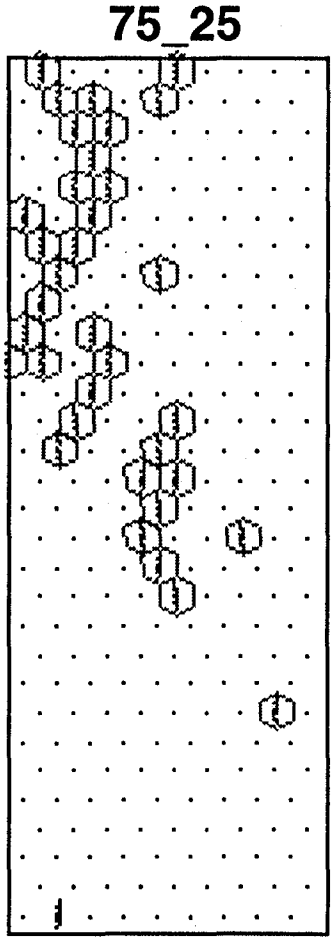

Clustering of Cracks

Figure #4

Strain V. Stress of the Weakest Trials

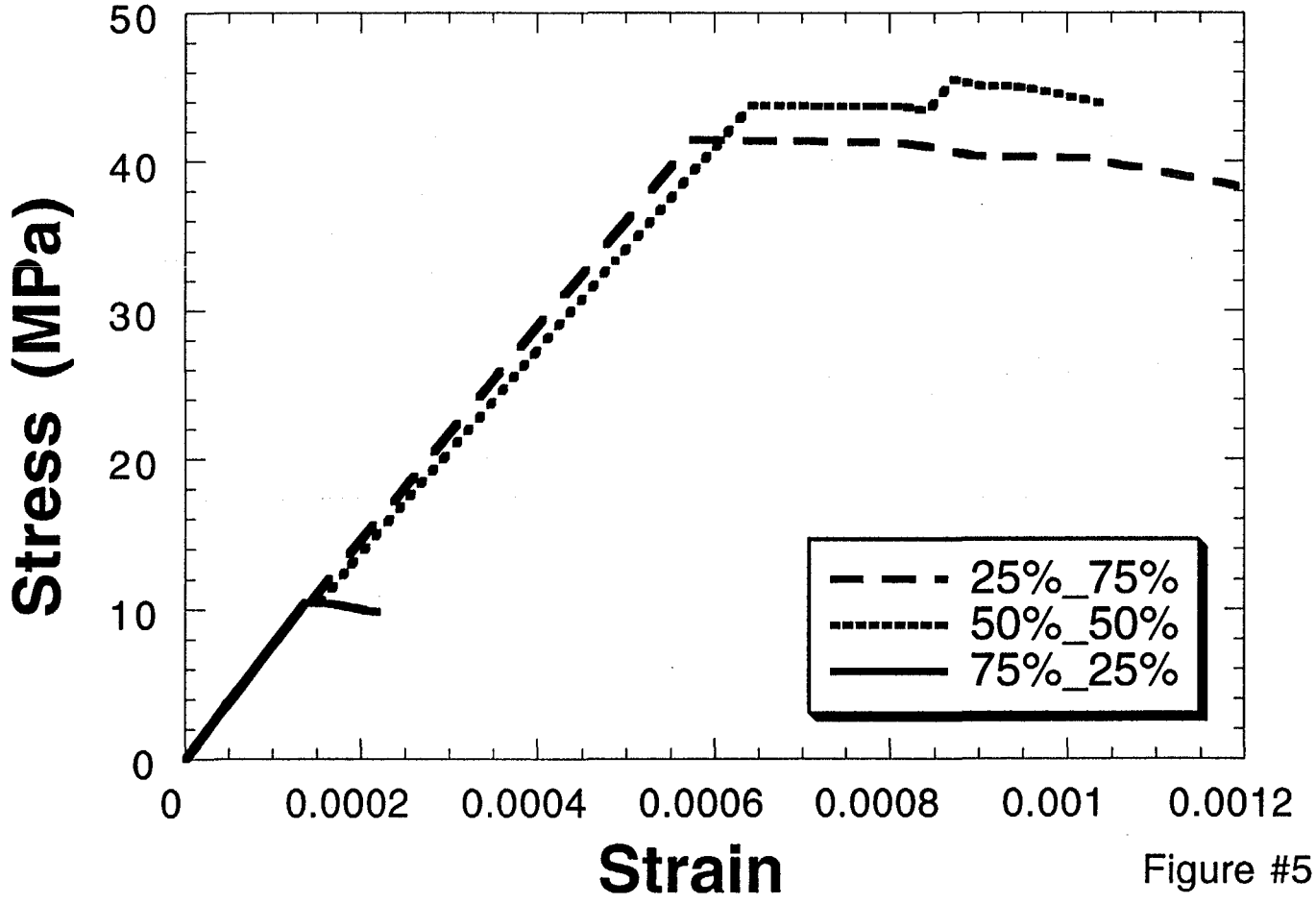

Figure #5

Strain V. Stress of the Strongest Trials

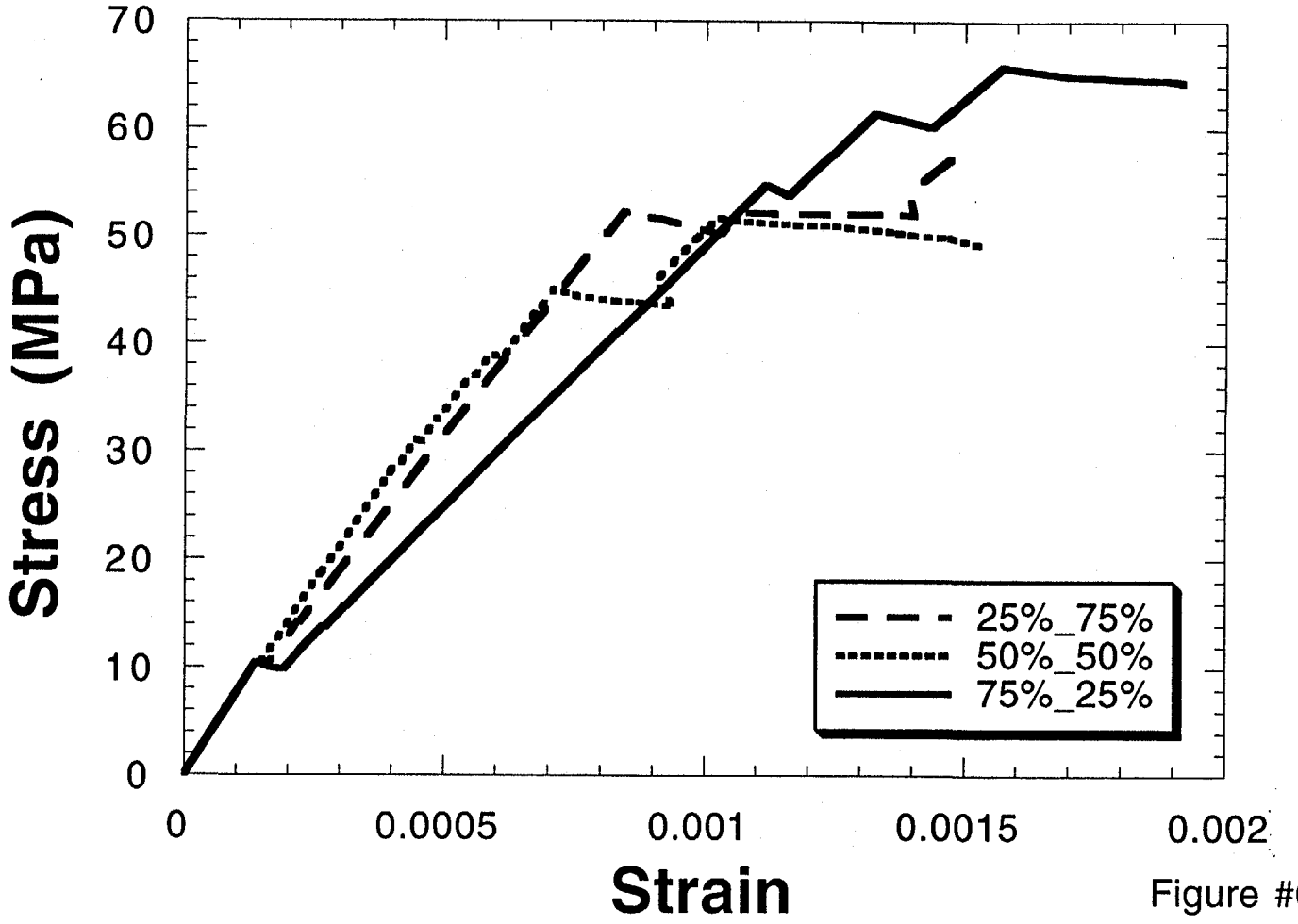

Figure #6

Results Table (Table #2)

	Mean Peak Stress	Standard Dev.	Mean Sites Broken	Mean Percolation Threshold	Standard Dev.	Mean Sites Broken
25_75	46.3	5.5	55	0.45	0.10	87
30_70	44.4	7.7	58	0.46	0.07	93
40_60	46.4	9.0	75	0.39	0.09	97
50_50	53.3	6.6	96	0.35	0.07	108
60_40	58.3	13.2	107	0.35	0.13	115
70_30	64.0	29.4	116	0.36	0.08	126
75_25	37.2	22.4	104	0.37	0.07	117

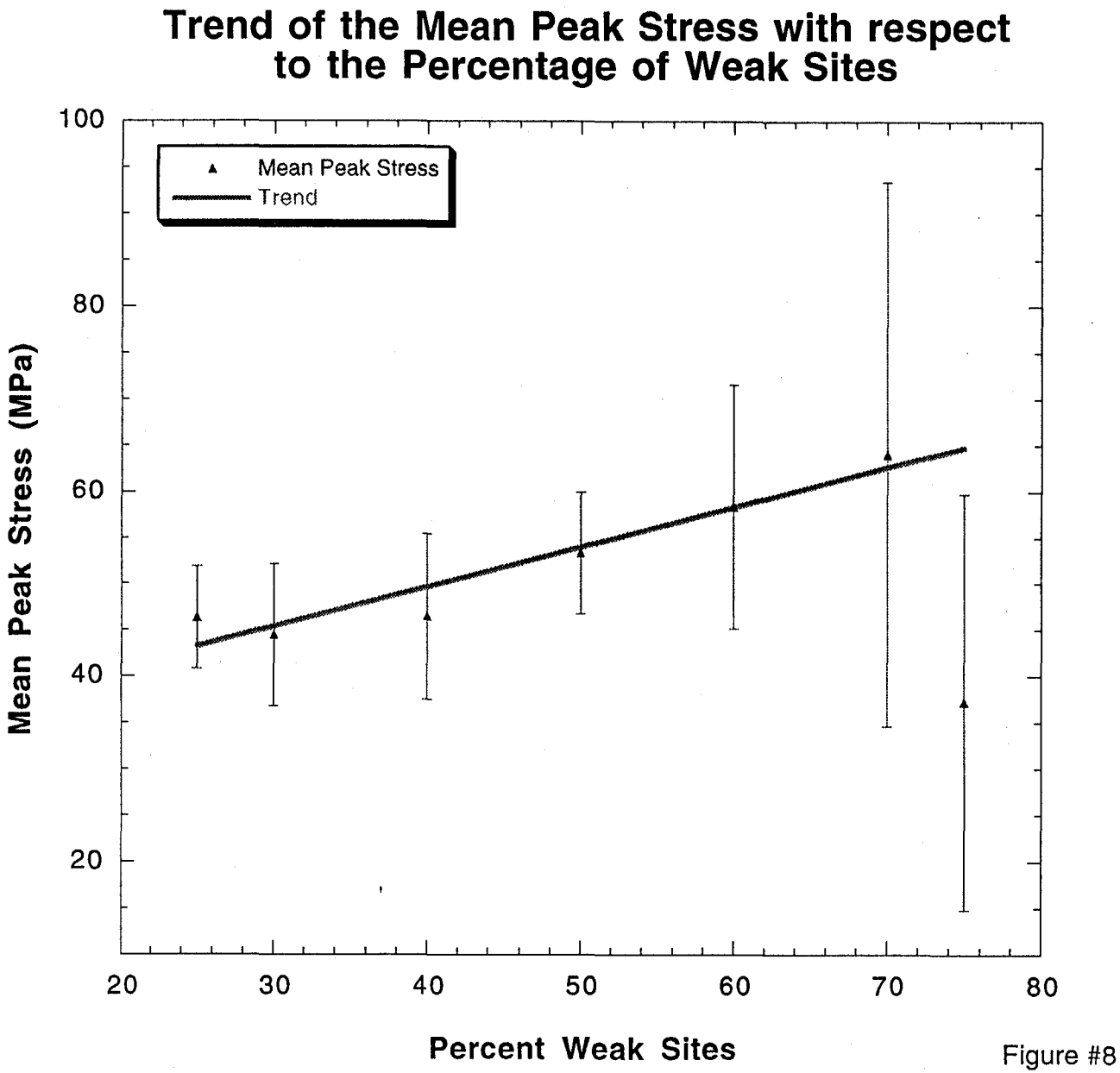
Trend of the Mean Peak Stress with respect to the Percentage of Weak Sites
Mean Peak Stress
Trend
Mean Peak Stress (MPa)
100
80
60
40
20
20
30
40
50
60
70
80
Percent Weak Sites

Figure #8

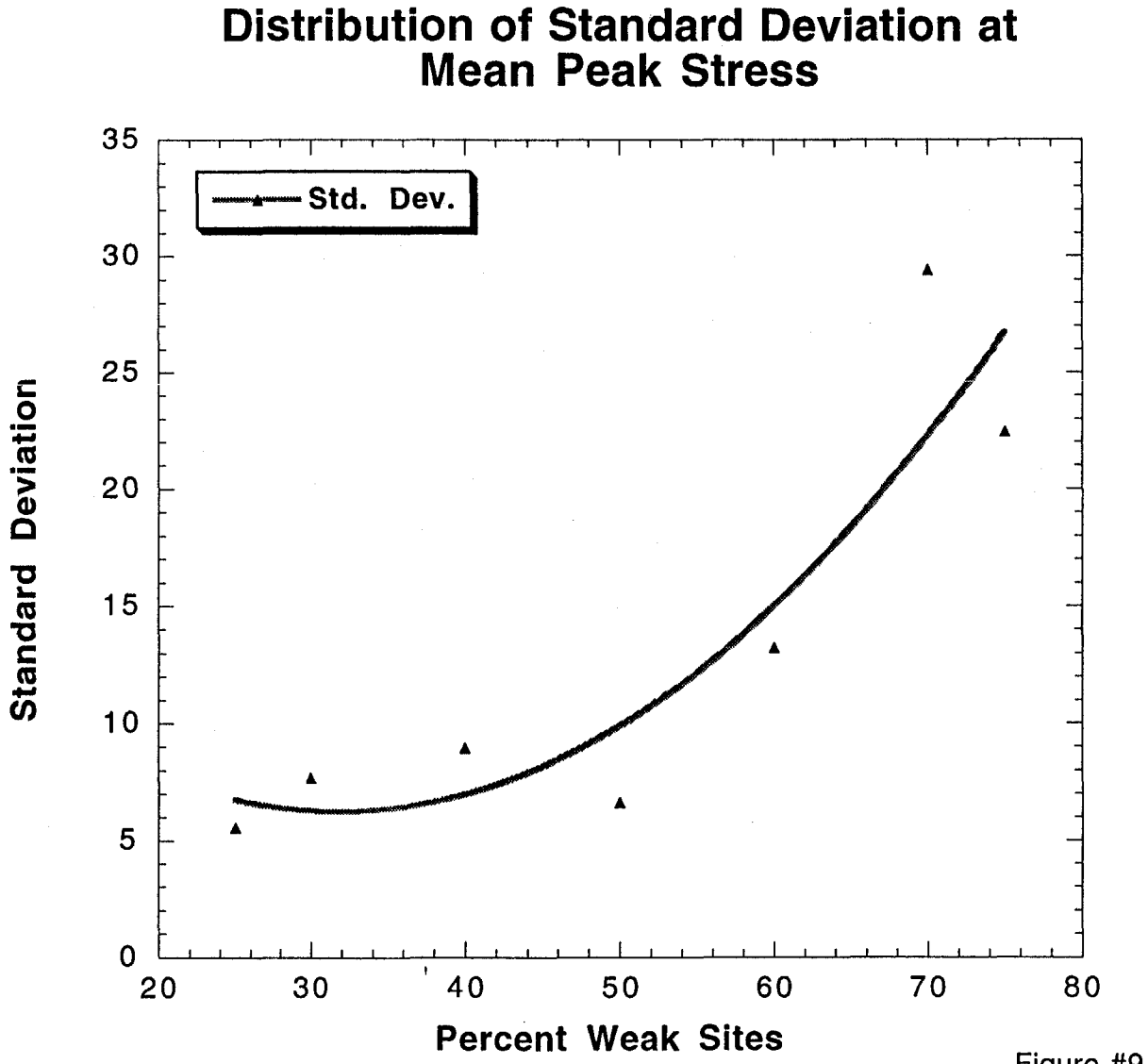
Distribution of Standard Deviation at Mean Peak Stress
Std. Dev.
Standard Deviation
Percent Weak Sites
0
5
10
15
20
25
30
35
20
30
40
50
60
70
80

Figure #9

References

Blair, S. C. (1994), *Analysis of Compressive Fracture in Rock Using Statistical Techniques (Ph.D. Thesis)*, UCRL-LR-120950, Lawrence Livermore National Laboratory, Livermore, CA.

Daveler, S. A., and S. C. Blair (1994), *Fracrock Users' Guide*, UCRL-MA-119099, Lawrence Livermore National Laboratory, Livermore, CA.